LIÈGE université
Sciences Appliquées

NATIONAL TECHNICAL UNIVERSITY OF ATHENS

Design of lattice towers from hot-rolled equal leg steel angles

A joint-thesis submitted in partial fulfillment of the requirements for the degree of Doctor of Philosophy (PhD) in Engineering Science

by

Marios-Zois BEZAS

Supervisors: Ioannis VAYAS
Jean-Pierre JASPART
Co-supervisors: Charis GANTES
Jean-François DEMONCEAU

JULY 2021

Design of lattice towers from hot-rolled equal leg steel angles

Marios-Zois BEZAS

The thesis is submitted to the School of Civil Engineering of the National Technical University of Athens and to the Doctoral college in Aerospace and Mechanics of the University of Liege in fulfilment of the requirements for the Degree of Doctor of Philosophy in Engineering Science

Members of the Examination Committee

Ioannis VAYAS, Prof. NTUA

Jean-Pierre JASPART, Prof. ULiège

Charis GANTES, Prof. NTUA

Jean-François DEMONCEAU, Prof. ULiège

Dimitrios VAMVATSIKOS, Prof. NTUA

Vincent DE VILLE DE GOYET, Prof. ULiège

Bert SNIJDER, Prof. TU Eindhoven

JULY 2021

Σχεδιασμός δικτυωτών πύργων από ελατά ισοσκελή χαλύβδινα γωνιακά

Μάριος-Ζώης Μπέζας

Η διδακτορική διατριβή υποβάλλεται στην Σχολή Πολιτικών Μηχανικών του Εθνικού Μετσόβιου Πολυτεχνείου και στο Διδακτορικό Κολλέγιο Αεροδιαστημικής και Μηχανικής του Πανεπιστημίου της Λιέγης προς εκπλήρωση των απαιτήσεων για την απόκτηση του τίτλου του Διδάκτορος Μηχανικού.

Μέλη Εξεταστικής Επιτροπής

Ιωάννης ΒΑΓΙΑΣ, Καθηγητής ΕΜΠ

Jean-Pierre JASPART, Καθηγητής ULiège

Χάρης ΓΑΝΤΕΣ, Καθηγητής ΕΜΠ

Jean-François DEMONCEAU, Καθηγητής ULiège

Δημήτριος ΒΑΜΒΑΤΣΙΚΟΣ, Καθηγητής ΕΜΠ

Vincent DE VILLE DE GOYET, Καθηγητής ULiège

Bert SNIJDER, Καθηγητής TU Eindhoven

Ιούλιος 2021

ABSTRACT

Design of lattice towers from hot-rolled equal leg steel angles

Angles profiles have been used since the very beginning of steel construction due to their easy transportation and on-site erection. However, they exhibit specific features that clearly distinguish them from other types of common sections, what inevitably leads to the need for the development of specific design provisions. In a first step, existing European specifications on hot-rolled equal angle sections were critically reviewed and then, in a second step, extensive experimental, analytical and numerical studies have been conducted to propose a complete and duly validated set of design rules covering all aspects of design for angles. These rules include cross section classification, cross section resistance for all types of loading as well as rules for member design to individual and combined internal normal forces and moments. All the proposed rules are written in Eurocode 3 format to allow a direct possible inclusion in forthcoming drafts.

Furthermore, angle profiles are extensively used in lattice towers and masts for telecommunication purposes or electric power transmission. Such types of towers are mainly designed according to EN 1993-3-1 and EN 50341-1, based on a first-order linear elastic structural analysis of a truss structure. An assessment of the current design approach is performed, where the tower has been simulated with a full non-linear finite element software, considering relevant imperfections as well as geometrical and material non-linearities. The importance of the second order effects in the analysis is underlined while the existence of an instability mode not properly covered directly by the norms, and usually therefore not checked, is highlighted. Two analytical models for the prediction of the critical load of the new buckling mode are proposed and validated numerically. Both proposed models are rather easy to apply and may fill the gap in the existing design recommendations for lattice towers.

RÉSUMÉ

Conception de tours en treillis à partir de cornières en acier à semelles égales laminées à chaud

Les profilés de type « cornière » sont utilisés depuis le début de la construction métallique en raison de leur facilité de transport et de montage sur site. Cependant, ils présentent des caractéristiques spécifiques qui les distinguent clairement des autres types de sections courantes, ce qui conduit inévitablement à la nécessité de développer des règles de dimensionnement spécifiques. Dans un premier temps, les spécifications européennes existantes pour le dimensionnement de cornières laminées à chaud à semelles égales ont fait l'objet d'une analyse critique. Ensuite, dans un second temps, des études expérimentales, analytiques et numériques approfondies ont été menées afin de proposer un ensemble complet et dûment validé de règles de dimensionnement pour la vérification de cornières. Ces règles comprennent la classification des sections transversales, le calcul de la résistance des sections transversales pour tous types de sollicitation ainsi que les règles de dimensionnement pour les membrures sous effort axial et/ou moment de flexion. Toutes les règles proposées sont écrites au format de l'Eurocode 3 afin de permettre, si souhaité, une insertion directe de celles-ci dans les versions à venir.

De plus, les cornières sont largement utilisées dans les tours et les mâts en treillis destinés aux télécommunications ou au transport d'énergie électrique. Ces tours sont principalement dimensionnées selon les normes EN 1993-3-1 et EN 50341-1, sur la base d'une analyse structurale élastique linéaire du premier ordre d'une structure en treillis. Une évaluation de l'approche de dimensionnement actuelle est effectuée via la simulation d'une tour avec un logiciel aux éléments finis non linéaires complets, en tenant compte des imperfections ainsi que des non-linéarités géométriques et matérielles. L'importance des effets du second ordre dans l'analyse est soulignée, tandis que l'existence d'un mode d'instabilité qui n'est pas couvert directement par les normes, et qui n'est donc généralement pas vérifié, est mise en évidence. Deux modèles analytiques pour la prédiction de la charge critique du nouveau mode d'instabilité sont proposés et validés numériquement. Les deux modèles proposés sont assez faciles à appliquer et peuvent combler une lacune dans les recommandations de dimensionnement existantes pour les tours en treillis.

ΠΕΡΙΛΗΨΗ

Σχεδιασμός δικτυωτών πύργων από ελατά ισοσκελή χαλύβδινα γωνιακά

Τα προφίλ γωνιακών διατομών χρησιμοποιούνται από τα πρώτα χρόνια των χαλύβδινων κατασκευών λόγω της εύκολης μεταφοράς τους και της επί τόπου συναρμολόγησής τους. Ωστόσο, παρουσιάζουν συγκεκριμένα χαρακτηριστικά που τα διαφοροποιούν από τους άλλους τύπους κοινών διατομών, γεγονός που οδηγεί αναπόφευκτα στην ανάγκη ανάπτυξης ειδικών κανόνων σχεδιασμού. Σε πρώτη φάση ελέγχθηκαν και αξιολογήθηκαν οι υφιστάμενες ευρωπαϊκές διατάξεις για τα ισοσκελή γωνιακά θερμής έλασης, και στη συνέχεια, διεξήχθησαν εκτεταμένες πειραματικές, αναλυτικές και αριθμητικές μελέτες ώστε να προταθεί ένα ολοκληρωμένο και πλήρως επικυρωμένο σύνολο κανόνων σχεδιασμού που να καλύπτει όλες τις πτυχές του σχεδιασμού των γωνιακών. Οι κανόνες αυτοί περιλαμβάνουν την ταξινόμηση της διατομής, την αντοχή της διατομής για όλους τους τύπους φόρτισης, καθώς και κανόνες για το σχεδιασμό μελών υπό μεμονωμένες ή και συνδυασμένες εσωτερικές αξονικές δυνάμεις και ροπές. Όλοι οι προτεινόμενοι κανόνες είναι γραμμένοι υπό την μορφή των διατάξεων του Ευρωκώδικα 3, ώστε να είναι δυνατή η άμεση ενσωμάτωσή τους στην επερχόμενη έκδοση.

Επιπλέον, τα γωνιακά προφίλ χρησιμοποιούνται ευρέως σε δικτυωτούς πύργους και ιστούς για τηλεπικοινωνιακούς σκοπούς ή για τη μεταφορά ηλεκτρικής ενέργειας. Τέτοιοι τύποι πύργων σχεδιάζονται κυρίως σύμφωνα με τα πρότυπα EN 1993-3-1 και EN 50341-1, βάσει μιας γραμμικής ελαστικής ανάλυσης πρώτης τάξεως όπου η κατασκευή προσομοιώνεται ως ένα δικτύωμα. Στην παρούσα εργασία πραγματοποιείται αξιολόγηση της τρέχουσας προσέγγισης σχεδιασμού, όπου ο πύργος προσομοιώνεται με ένα λογισμικό μη γραμμικών πεπερασμένων στοιχείων, λαμβάνοντας υπόψη τις αρχικές ατέλειες στην κατασκευή καθώς και τις μη γραμμικότητες του υλικού και της γεωμετρίας. Υπογραμμίζεται η σημασία των φαινομένων δευτέρας τάξεως στην ανάλυση, ενώ επισημαίνεται η ύπαρξη μιας μορφής αστάθειας που δεν καλύπτεται άμεσα από τους κανονισμούς και ως εκ τούτου, συνήθως δεν ελέγχεται. Στην συνέχεια, δύο αναλυτικά μοντέλα για την πρόβλεψη του κρίσιμου φορτίου του νέου τρόπου λυγισμού προτείνονται και επικυρώνονται αριθμητικά. Και τα δύο προτεινόμενα μοντέλα είναι εύκολα στην εφαρμογή τους και μπορούν να καλύψουν το κενό στις υπάρχουσες συστάσεις σχεδιασμού για δικτυωτούς πύργους.

ΕΚΤΕΤΑΜΕΝΗ ΕΛΛΗΝΙΚΗ ΠΕΡΙΛΗΨΗ

(EXTENDED GREEK ABSTRACT)

Εισαγωγή:

Οι δικτυωτοί πύργοι κατασκευάζονται ευρέως, τόσο στην Ευρώπη όσο και παγκοσμίως, για την εξυπηρέτηση των τηλεπικοινωνιών και της μεταφοράς ενέργειας. Οι κατασκευές που εξυπηρετούν τους σκοπούς αυτούς, συχνά εγκαθίστανται σε ορεινά εδάφη, με αποτέλεσμα η προσβασιμότητα των βαρέων οχημάτων που απαιτούνται για την μεταφορά τους να είναι περιορισμένη. Συνεπώς, οι δικτυωτοί πύργοι, που αποτελούν ένα δομικό σύστημα το οποίο μπορεί να μεταφερθεί και να ανεγερθεί με ελαφρά μηχανήματα και χωρίς ειδικό εξοπλισμό, είναι η ιδανική λύση. Η δε χρήση κοχλιωτών συνδέσεων, που ως επί το πλείστων προτιμώνται έναντι των συγκολλήσεων, διευκολύνει ακόμα περισσότερο την επί τόπου ανέγερσή τους. Παρόλο που οι δικτυωτοί πύργοι χρειάζονται περισσότερη έκταση σε σύγκριση με τα κυλινδρικά ή οκταγωνικά κελυφωτά συστήματα, αυτό δεν αποτελεί πρόβλημα καθώς ο εδαφικός χώρος είναι άφθονος σε μη ρυμοτομικές περιοχές στις περισσότερες ευρωπαϊκές χώρες. Ως εκ τούτου, οι δικτυωτοί πύργοι καθίστανται ως το κύριο δομικό σύστημα για τις τηλεπικοινωνίες και τη μεταφορά ενέργειας.

Τα μέλη τους συχνά αποτελούνται από ισοσκελείς γωνιακές διατομές, οι οποίες διακρίνονται λόγω της εύκολης παραγωγής και μεταφοράς τους, καθώς και για την εύκολή σύνδεση τους με άλλα μέλη. Διατίθενται στην αγορά ως προφίλ θερμής ή ψυχρής έλασης, ως ισοσκελή ή ανισοσκελή ανάλογα με το σχετικό μήκος των πελμάτων τους, σε ποιότητες χάλυβα έως S460, και σε μεγέθη που κυμαίνονται από μικρά έως μεγάλα (20 έως 300 mm). Η δυνατότητα σύνδεσής τους με άλλα μέλη μέσω κοχλιών στο ένα τους πέλμα, οδηγεί σε μια πολύ συμφέρουσα εφαρμογή ως αρθρωτά ή διαφραγματικά μέλη σε κτίρια και γέφυρες, αλλά και σε άλλους τύπους ειδικών κατασκευών όπως είναι οι χαλύβδινοι πύργοι και ιστοί. Επιπλέον, μπορεί ευκολά να εξασφαλισθεί η κατάλληλη προστασία τους έναντι διάβρωσης, δεδομένου ότι όλα τα μεγέθη των γωνιακών είναι πλήρως επιδεκτικά σε γαλβανισμό, σε αντίθεση με αρκετούς άλλους τύπους ανοικτών ή κλειστών διατομών.

Ωστόσο τα γωνιακά, και ιδίως τα ισοσκελή που εξετάζονται στην παρούσα διατριβή, έχουν συγκεκριμένα χαρακτηριστικά – όπως αυτά συνοψίζονται παρακάτω – τα οποία τα διαφοροποιούν πλήρως από τους άλλους τύπους κοινών διατομών: (i) είναι ανοικτά προφίλ με πολύ μικρές αντοχές τόσο σε στρέψη όσο και σε στρέβλωση, (ii) είναι μονοσυμμετρικές διατομές, (iii) η αντοχή τους σε κάμψη και η ακτίνα αδρανείας τους γύρω από τον ασθενή άξονα είναι σημαντικά μικρότερες από ό,τι γύρω από τον ισχυρό, (iv) τα πέλματά τους είναι επιρρεπή σε τοπικό λυγισμό ως εξωτερικά στοιχεία πλάκας, (v) οι πλαστικές τους αντοχές είναι σημαντικά υψηλότερες από τις ελαστικές τους και τέλος, (vi) λόγω της έκκεντρης σύνδεσης στο ένα τους πέλμα, εκτός από αξονική δύναμη υπόκεινται και σε κάμψη όταν χρησιμοποιούνται ως μεμονωμένα μέλη. Τα παραπάνω χαρακτηριστικά εξηγούν γιατί οι υφιστάμενοι κανόνες σχεδιασμού, οι οποίοι έχουν αναπτυχθεί κυρίως για τις διπλά συμμετρικές διατομές, δεν μπορούν να καλύψουν με ασφάλεια τον σχεδιασμό των γωνιακών.

Για να αντιμετωπίσουν την έλλειψη ενός ενιαίου συνόλου κανόνων σχεδιασμού για τα γωνιακά, οι ευρωπαϊκοί κανονισμοί έχουν υιοθετήσει μια εναλλακτική προσέγγιση σχεδιασμού

κατά περίπτωση, ενσωματώνοντας έτσι επιμέρους κανόνες και συστάσεις σε διάφορα μέρη του Ευρωκώδικα 3. Πιο συγκεκριμένα, στον EN 1993-1-1 [1] παρέχονται κανόνες για την κατάταξη των διατομών (κλάσεις 1 έως 4), καθώς και γενικές συστάσεις σχεδιασμού για την ευστάθεια των μελών υπό θλιπτική φόρτιση. Στον EN 1993-3-1 [2] δίδονται ειδικοί κανόνες για τον υπολογισμό της αντοχής σε λυγισμό των μελών από γωνιακά που χρησιμοποιούνται σε πύργους και ιστούς, όταν αυτά συνδέονται έκκεντρα μέσω κοχλιών στο ένα πέλμα. Στον EN 1993-1-8 [3] περιέχονται κανόνες για την αντοχή των προαναφερθέντων συνδέσεων, ενώ στον EN 1993-1-5 [4] δίνονται κανόνες για την αντοχή σε λυγισμό των γωνιακών διατομών που κατατάσσονται στην κλάση 4 και συνεπώς είναι επιρρεπή σε τοπικό λυγισμό. Ένα άλλο ευρωπαϊκό πρότυπο, το CENELEC EN 50341-1 [5], παρέχει ειδικούς κανόνες για τον έλεγχο των δικτυωτών πύργων και των μελών που τους αποτελούν, που όμως για ορισμένες πτυχές του σχεδιασμού, αποκλίνουν από τους κανόνες που προβλέπονται στον Ευρωκώδικα 3. Επιπλέον, το EN 50341-1 επιτρέπει το σχεδιασμό των δικτυωτών πύργων μέσα από δοκιμές πλήρους κλίμακας. Εξάγει έτσι συμπεράσματα για τον σχεδιασμό από μία μόνο δοκιμή, συγκρίνοντας το μέγιστο πειραματικό φορτίο με το αντίστοιχο από τους αναλυτικούς υπολογισμούς, αγνοώντας το γεγονός ότι τα αποτελέσματα μιας μεμονωμένης δοκιμής επηρεάζονται από την υπεραντοχή του υλικού, την σκλήρυνση λόγω παραμόρφωσης ή άλλες παραμέτρους, οι τιμές των οποίων συνδέονται με στατιστικές αβεβαιότητες. Κατά συνέπεια, δεν θίγει θέματα αξιοπιστίας, όπως αυτά αναφέρονται στον EN 1990 [5]. Σε αντίθεση με τους ευρωπαϊκούς κανονισμούς, οι αντίστοιχοι αμερικανικοί έχουν καταγράψει σε ένα ενιαίο έγγραφο, το AISC 2000 [6], όλους τους κανόνες που αφορούν το σχεδιασμό των γωνιακών.

Συνεπώς, γίνεται εύκολα κατανοητό ότι τόσο η ιδιαίτερη γεωμετρία και τα χαρακτηριστικά των γωνιακών, όσο και η έλλειψή ενός ενιαίου υπόβαθρου ανάμεσα στους διάφορους ευρωπαϊκούς κανονισμούς, αναπόφευκτα οδηγούν στην ανάγκη ανάπτυξης ειδικών κανόνων σχεδιασμού για τις γωνιακές διατομές.

Για τη μελέτη της συμπεριφοράς των γωνιακών διατομών έχουν διεξαχθεί εκτεταμένες αριθμητικές έρευνες, καλύπτοντας προφίλ θερμής και ψυχρής έλασης, ισοσκελή και ανισοσκελή γωνιακά, δοκούς ή υποστυλώματα που υποβάλλονται σε διάφορους τύπους φόρτισης και συνθήκες στήριξης. Οι Vayas et al. [7] υπολογίζουν την ανελαστική αντοχή γωνιακών διατομών που υποβάλλονται σε αξονική φόρτιση και διαξονική κάμψη. Ο Trahair [8] εξετάζει δοκούς γωνιακών διατομών υπό ομοιόμορφη έκκεντρη εγκάρσια φόρτιση και υπολογίζει την αντοχή της διατομής υπό συνδυασμένη διάτμηση, κάμψη και στρέψη. Οι Schillo et al. [9] εξετάζουν του κανόνες σχεδιασμού που διέπουν την αντοχή σε λυγισμό των γωνιακών διατομών θερμής έλασης σύμφωνα με τα ευρωπαϊκά πρότυπα που αναφέρθηκαν στην προηγούμενη παράγραφο (EN 1993-1-1, EN 1993-3-1 και EN 50341), και τους συγκρίνουν με πειραματικά αποτελέσματα και αριθμητικές έρευνες, λαμβάνοντας υπόψη διάφορους τύπους αρχικών ατελειών. Οι Kettler et al. [10] τονίζουν τη σημασία των συνθηκών στήριξης στις αριθμητικές τους μελέτες με γωνιακά θερμής έλασης τα οποία φορτίζονται θλιπτικά μέσω κοχλιωτών συνδέσεων στο ένα πέλμα, και συγκρίνουν τα αποτελέσματα τόσο με υφιστάμενα πειράματα όσο και με τις ισχύουσες διατάξεις των ευρωπαϊκών κανονισμών. Οι Hussain et al. [11] παρέχουν μια εξίσωση αλληλεπίδρασης στην πλαστική περιοχή για τον σχεδιασμό γωνιακών έναντι λυγισμού, που υποβάλλονται σε θλίψη και διαξονική κάμψη.

Επιπροσθέτως έχει πραγματοποιηθεί και μεγάλο πλήθος πειραμάτων με γωνιακά διαφόρων μεγεθών που υποβάλλονται σε κεντρική ή έκκεντρη φόρτιση, μερικά από τα οποία

αναφέρονται ακολούθως. Στο Πανεπιστήμιο Tsinghua του Πεκίνο [12], διεξήχθησαν πειραματικές δοκιμές θλίψης σε μεγάλες γωνιακές διατομές από L125x125x8 έως L200x200x14 που κατασκευάστηκαν από χάλυβα υψηλής αντοχής S420. Οι δοκιμές διεξήχθησαν σε αξονικά φορτισμένα υποστυλώματα με αρθρώσεις και στα δυο άκρα, προκειμένου να καθοριστεί η αλληλεπίδραση μεταξύ γενικού και τοπικού λυγισμού, δεδομένου ότι οι όλες διατομές που χρησιμοποιήθηκαν ήταν κλάσης 4. Στο Εθνικό Μετσόβιο Πολυτεχνείο πραγματοποιήθηκαν δοκιμές σε γωνιακά προφίλ L70x70x7 [13], μέσω των οποίων μελετήθηκαν οι επιδράσεις της έκκεντρης φόρτισης στην απόκριση των δοκιμίων. Επιπλέον, δοκιμές θλίψης σε προφίλ L80x80x8 και L120x120x12 διεξήχθησαν στο TU Graz [10], όπου οι οριακές συνθήκες ποικίλαν από πακτώσεις σε στηρίξεις που επέτρεπαν περιστροφή εντός ή εντός και εκτός επιπέδου. Τέλος, σειρές δοκιμών πραγματοποιήθηκαν και στο TU Braunschweig [14] σε γωνιακά L50x50x5, με διάφορα μήκη λυγισμού και οριακές συνθήκες στήριξης, όπου το εξωτερικό φορτίο επιβάλλονταν έκκεντρα μέσω ενός κοχλία στο ένα πέλμα.

Στο πλαίσιο της διατριβής και προκειμένου να διευρυνθούν οι υφιστάμενες γνώσεις για τη συμπεριφορά ευστάθειας χαλύβδινων υποστυλωμάτων από γωνιακές διατομές με χάλυβα υψηλής αντοχής (S460M) που υποβάλλονται σε θλίψη και κάμψη, πραγματοποιήθηκαν στο Πανεπιστήμιο της Λιέγης δώδεκα (12) δοκιμές λυγισμού σε τέτοια υποστυλώματα. Επιπλέον, ελέγχθηκαν και αξιολογήθηκαν οι υφιστάμενες ευρωπαϊκές διατάξεις για τα ισοσκελή γωνιακά θερμής έλασης, και στη συνέχεια, διεξήχθησαν εκτεταμένες πειραματικές, αναλυτικές και αριθμητικές μελέτες ώστε να προταθεί ένα ολοκληρωμένο και πλήρως επικυρωμένο σύνολο κανόνων σχεδιασμού που να καλύπτει όλες τις πτυχές του σχεδιασμού των γωνιακών. Οι κανόνες αυτοί περιλαμβάνουν την ταξινόμηση της διατομής, την αντοχή της διατομής για όλους τους τύπους φόρτισης, καθώς και κανόνες για το σχεδιασμό μελών υπό μεμονωμένες ή και συνδυασμένες εσωτερικές αξονικές δυνάμεις και ροπές. Όλοι οι προτεινόμενοι κανόνες είναι γραμμένοι υπό την μορφή των διατάξεων του Ευρωκώδικα 3, ώστε να είναι δυνατή η άμεση ενσωμάτωσή τους στην επερχόμενη έκδοση.

Αναφορικά με την δομική ανάλυση δικτυωτών πύργων, σύμφωνα με τα προαναφερθέντα κανονιστικά πρότυπα, ο πύργος μοντελοποιείται ως ένα απλό δικτύωμα, όπου όλες οι συνδέσεις των μελών προσομοιώνονται ως αρθρωτές. Τέτοια μοντέλα δικτυώματος δεν αντικατοπτρίζουν επαρκώς την πραγματική συμπεριφορά του πύργου, καθώς τα φορτία, και ιδίως τα φορτία ανέμου, επιβάλλονται σε όλο το μήκος των μελών και όχι στα άκρα αυτών, δημιουργώντας έτσι ροπές κάμψης στα μέλη. Επιπλέον, ο σχεδιασμός διεξάγεται μέσω μιας γραμμικής ελαστικής ανάλυσης πρώτης τάξεως, αγνοώντας τα φαινόμενα δευτέρας τάξης που αναπτύσσονται στις κατασκευές αυτές και είναι συνήθως σημαντικά. Είναι επομένως ασυνεπές και μη ασφαλές το να εκτελείται ο σχεδιασμός των μελών αυτών χωρίς να λαμβάνονται υπόψιν οι ροπές στα άκρα των μελών που οφείλονται στην εξωτερική φόρτιση καθώς επίσης και τα φαινόμενα δευτέρας τάξεως, κάτι το οποίο γίνεται συνήθως στην πράξη.

Πολλές έρευνες έχουν διεξαχθεί εδώ και χρόνια σχετικά με τη μοντελοποίηση και το σχεδιασμό των δικτυωτών πύργων. Οι Albermani et al. [15] μελέτησαν τη δομική συμπεριφορά και απόκριση πύργων μεταφοράς ενέργειας μέσω μη γραμμικών αναλύσεων και τις συνέκριναν με δοκιμές πλήρους κλίμακας. Η επιρροή του επιλεγμένου πεπερασμένου στοιχείου (στοιχείο δικτυώματος ή στοιχείο δοκού) στην τελική απόκριση της κατασκευής έχει επίσης μελετηθεί από τους Silva et al. [16]. Οι Jiang et al. [17] διερεύνησαν τη προσομοίωση των κοχλιωτών

συνδέσεων και επικύρωσαν την απόκρισή τους μέσω διαθέσιμων από τη βιβλιογραφία δοκιμών, ενώ οι Kitiponchai et al. [18] εξέτασαν την επίδραση της ολίσθησης των κοχλιών στην τελική συμπεριφορά των πύργων. Τέλος, μια συλλογή και κριτική ανασκόπηση δοκιμών πλήρους κλίμακας δικτυωτών πύργων, καθώς και πρακτικές συμβουλές για τη διεξαγωγή μελλοντικών δοκιμών, αναφέρονται από τους Nuño et al. [19].

Στην παρούσα εργασία πραγματοποιείται αξιολόγηση της τρέχουσας προσέγγισης σχεδιασμού, όπου ο πύργος προσομοιώνεται με ένα λογισμικό μη γραμμικών πεπερασμένων στοιχείων (FINELG), λαμβάνοντας υπόψη τις αρχικές ατέλειες στην κατασκευή καθώς και τις μη γραμμικότητες του υλικού και της γεωμετρίας. Ακόμη, κάθε μέλος έχει μοντελοποιηθεί κατάλληλα, όσον αφορά τον προσανατολισμό και τις εκκεντρότητες στα άκρα του. Υπογραμμίζεται η σημασία της συνεκτίμησης των φαινομένων δευτέρας τάξεως στην ανάλυση. Το επιλεγμένο λογισμικό επικυρώθηκε αρχικά μέσω των διαθέσιμων στη βιβλιογραφία δοκιμών πλήρους κλίμακας.

Η ύπαρξη μιας μορφής αστάθειας που δεν καλύπτεται άμεσα από τους κανονισμούς και ως εκ τούτου, συνήθως δεν ελέγχεται, επισημαίνεται στο πλαίσιο της διατριβής. Στην συνέχεια, δύο αναλυτικά μοντέλα για την πρόβλεψη του κρίσιμου φορτίου του νέου τρόπου λυγισμού προτείνονται και επικυρώνονται αριθμητικά. Και τα δύο προτεινόμενα μοντέλα είναι εύκολα στην εφαρμογή τους και μπορούν να καλύψουν το κενό στις υπάρχουσες συστάσεις σχεδιασμού για δικτυωτούς πύργους.

Περιεχόμενο διατριβής:

Στην συνέχεια, παρουσιάζεται αναλυτικά το περιεχόμενο και τα βασικά ερευνητικά αποτελέσματα του εκάστοτε κεφαλαίου.

Το **κεφάλαιο 1** είναι εισαγωγικό και εξηγεί τους στόχους και την δομή της εργασίας. Επιπλέον περιλαμβάνει τη βιβλιογραφική ανασκόπηση η οποία κινείται σε δυο άξονες: (i) Κανονιστικές προδιαγραφές και (ii) επιστημονικές δημοσιεύσεις. Οι προηγούμενες παράγραφοι (εισαγωγή) αποτελούν ως επί το πλείστων, την μετάφραση του κεφαλαίου 1 στα ελληνικά.

Το **κεφάλαιο 2** συνοψίζει και επεξηγεί υπό την μορφή λίστας, όλα τα σύμβολα που χρησιμοποιούνται στην διατριβή, τα οποία ακολουθούν πιστά αυτά που δίδονται και στους Ευρωκώδικες. Το Σχήμα 1 απεικονίζει αυτούς τους συμβολισμούς για τις γεωμετρικές ιδιότητες, τους γεωμετρικούς καθώς και τους κύριους άξονες της διατομής.

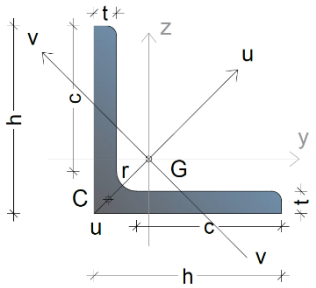

Σχήμα 1: Συμβολισμός των γεωμετρικών χαρακτηριστικών της διατομής

Στο **κεφάλαιο 3** παρουσιάζονται οι ιδιαιτερότητες των γωνιακών διατομών συγκριτικά με τις διπλά συμμετρικές διατομές, κατά τον ελαστικό λυγισμό. Τα ισοσκελή γωνιακά που εξετάζονται στη παρούσα διατριβή είναι ανοικτά προφίλ με πολύ μικρές αντοχές τόσο σε στρέψη όσο και σε στρέβλωση, είναι μονοσυμμετρικές διατομές, τα μέλη τους είναι επιρρεπή στον τοπικό λυγισμό ενώ, λόγω της έκκεντρης σύνδεσής τους, υπόκεινται και σε κάμψη μαζί με την αξονική φόρτιση. Σε αντίθεση με τις διπλά συμμετρικές διατομές, το κρίσιμο φορτίο λυγισμού των μελών με γωνιακή διατομή επηρεάζεται από τη θέση και το είδος της φόρτισης ενώ οι ιδιομορφές λυγισμού δεν είναι πλήρως αποζευγμένες στις περισσότερες περιπτώσεις. Έτσι, στο κεφάλαιο αυτό, παρουσιάζεται ο αναλυτικός υπολογισμός του κρίσιμου φορτίου λυγισμού ενός θλιπτικά φορτισμένου μέλους με ή χωρίς εκκεντρότητα (που δίνεται συνοπτικά παρακάτω), με βάση τη θεωρία λυγισμού του Euler. Διερευνώνται τα φαινόμενα στρέψης και ο αντίστοιχη ιδιομορφή λυγισμού, η οποία αποτελεί μια ειδική περίπτωση για τα γωνιακά προφίλ, ενώ αναφέρεται και η πιθανότητα αστάθειας λόγω εφελκυστικής φόρτισης. Επιπλέον, εξετάζεται η επίδραση του τύπου φόρτισης, των οριακών συνθηκών και των αρχικών ατελειών στο κρίσιμο φορτίο λυγισμού. Τέλος, οι αναλυτικές εκτιμήσεις των κρίσιμων φορτίων ενός υποστυλώματος επικυρώνονται με αριθμητικά προσομοιώματα που εκτελούνται με το λογισμικό πεπερασμένων στοιχείων FINELG μέσω γραμμικών ελαστικών αναλύσεων λυγισμού και ελαστικών αναλύσεων $2^{ας}$ τάξεως.

Το κρίσιμο φορτίο λυγισμού ενός θλιπτικά φορτισμένου μέλους προκύπτει από την επίλυση της ακόλουθης εξίσωσης:

$$A_{rp}(N_{cr,u}-P)(N_{cr,v}-P)(N_{cr,T}-P)-P^2(N_{cr,v}-P)v_P^2-P^2(N_{cr,u}-P)(u_C-u_P)^2=0$$

Προς απλοποίηση της επίλυσης, μπορούν διακριθούν δυο θεμελιώδεις περιπτώσεις αναφορικά με την θέση του επιβαλλόμενου εξωτερικού φορτίου:

1. Το φορτίο επιβάλλεται πάνω στον άξονα συμμετρίας (u_c, $u_p \neq 0$, $v_p = 0$)
2. Το φορτίο δεν επιβάλλεται πάνω στον άξονα συμμετρίας (u_c, u_p, $v_p \neq 0$)

Η επίλυση της εξίσωσης είναι ισοδύναμη με τον προσδιορισμό των σημείων τομής της τετμημένης P και των παρακάτω καμπυλών $f_1(P)$ και $f_2(P)$ για τις περιπτώσεις 1 και 2 αντίστοιχα:

$$f_1(P)=(N_{cr,u}-P)\left[\mathrm{A_{rp}}(N_{cr,v}-P)(N_{cr,T}-P)-P^2(u_C-u_P)^2\right]$$

$$f_2(P)=A_{rp}(N_{cr,u}-P)(N_{cr,v}-P)(N_{cr,T}-P)-P^2(N_{cr,v}-P)v_P^2-P^2(N_{cr,u}-P)(u_C-u_P)^2=0$$

Για τις τιμές $A_{rp}-(u_C-U_P)^2\geq 0$, η μορφή της καμπύλης $f_i(P)$ και συνεπώς η θέση των ριζών της, μπορεί να εκτιμηθεί υπολογίζοντας το πρόσημο της καμπύλης για τις τιμές 0, $N_{cr,u}$, $N_{cr,v}$, $N_{cr,T}$ και ∞. Οι ρίζες των καμπυλών επισημαίνονται ως $P_1 = N_{cr,1}$, $P_2 = N_{cr,2}$ και $P_3 = N_{cr,3}$ όπου $N_{cr,1}\leq N_{cr,2}\leq N_{cr,3}$. Αποδεχόμενοι ότι $N_{cr,u}\leq N_{cr,v}$, οι δύο θεμελιώδεις περιπτώσεις που θεωρήθηκαν παραπάνω μπορούν να διαιρεθούν στις ακόλουθες τρεις υποκατηγορίες:

a) $N_{cr,u}\leq N_{cr,v}\leq N_{cr,T}$
b) $N_{cr,T}\leq N_{cr,u}\leq N_{cr,v}$
c) $N_{cr,u}\leq N_{cr,T}\leq N_{cr,v}$

Τα Σχήματα 2, 3 και 4 απεικονίζουν τις καμπύλες $f_i(P)$ και τις ρίζες τους – όπως αναφέρονται και στο [22] – για τις δύο θεμελιώδεις περιπτώσεις, και για όλες τις διαφορετικές υποκατηγορίες που αναφέρθηκαν παραπάνω. Πρέπει να σημειωθεί ότι όλα αυτά τα σχήματα είναι σκαριφήματα και δεν αποτελούν απεικόνιση υπολογισμών. Από τα σχήματα φαίνεται ότι το κρίσιμο φορτίο λυγισμού $P_1 = N_{cr,1}$, είναι:

- το καμπτικό φορτίο λυγισμού $P_{cr,u}$ για την περίπτωση 1, υποκατηγορίες a και c,

- το στρεπτοκαμπτικό φορτίο λυγισμού σε όλες τις άλλες περιπτώσεις, με τιμή μικρότερη από αυτές των $P_{cr,u}$ και $P_{cr,T}$.

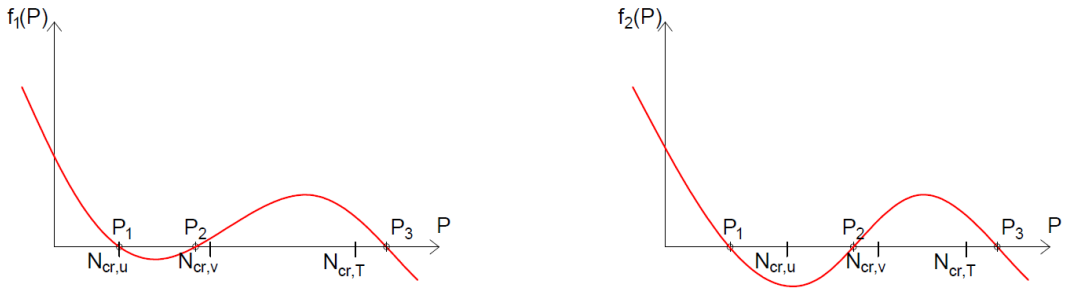

Σχήμα 2: Σκαρίφημα καμπυλών $f_i(P)$ για $N_{cr,u} \leq N_{cr,v} \leq N_{cr,T}$

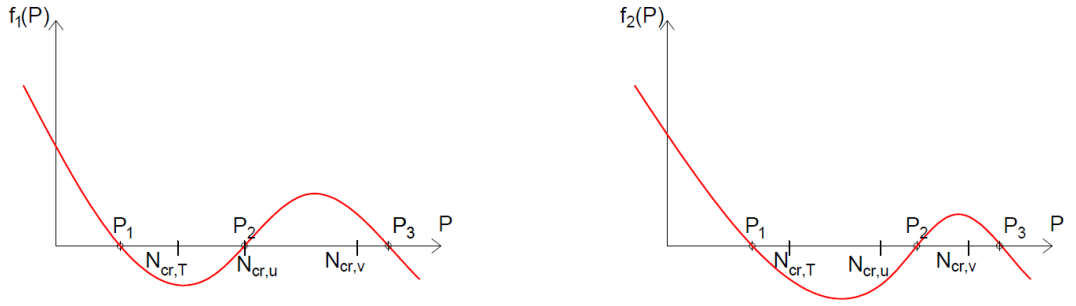

Σχήμα 3: Σκαρίφημα καμπυλών $f_i(P)$ για $N_{cr,T} \leq N_{cr,u} \leq N_{cr,v}$

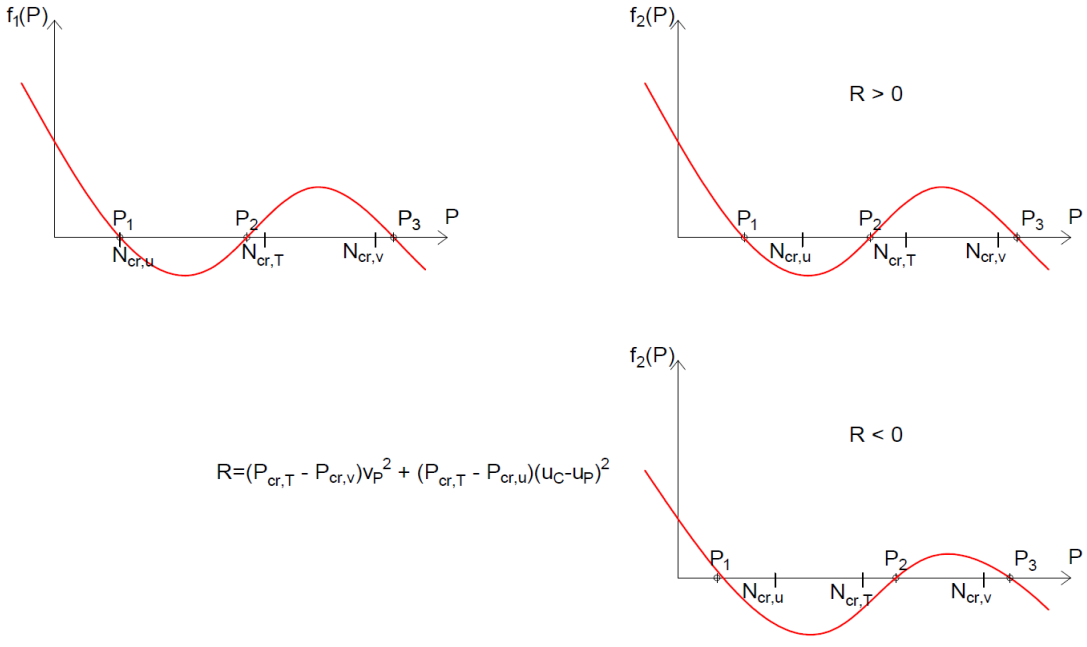

Σχήμα 4: Σκαρίφημα καμπυλών $f_i(P)$ για $N_{cr,u} \leq N_{cr,T} \leq N_{cr,v}$

Από τις αναλυτικές και αριθμητικές διερευνήσεις προκύπτει ότι:

(i) τα μέλη των γωνιακών διατομών λυγίζουν ως επί το πλείστον κατά μήκος του ασθενούς άξονά τους καμπτικά ή στρεπτικοκαμπτικά (Σχήμα 5), ανάλογα με την εκκεντρότητα του επιβαλλόμενου φορτίου,

(ii) η πλήρης αποσύνδεση των ιδιομορφών λυγισμού προκύπτει μόνο για την περίπτωση που το μέλος φορτίζεται στο κέντρο διάτμησης και όχι στο κέντρο βάρους· αυτή είναι επίσης η μόνη περίπτωση που μπορεί να εμφανιστεί μια αμιγής στρεπτική ιδιομορφή λυγισμού,

(iii) το κρίσιμο φορτίο επηρεάζεται από το είδος της φόρτισης (ροπές κάμψης, πλευρικά φορτία κ.λπ.),

(iv) ανάλογα με τη γεωμετρία της διατομής μπορεί να εμφανιστεί αστάθεια/λυγισμός ακόμη και για ένα έκκεντρο εφελκυστικό φορτίο,

(v) οι αρχικές ατέλειες του μέλους, οι οποίες στην πράξη είναι αρκετά μικρές καθώς περιορίζονται από τα πρότυπα κατασκευής των χαλύβδινων μελών, δεν επηρεάζουν σημαντικά το κρίσιμο φορτίο λυγισμού σε σύγκριση με την εκκεντρότητα του επιβαλλόμενου φορτίου.

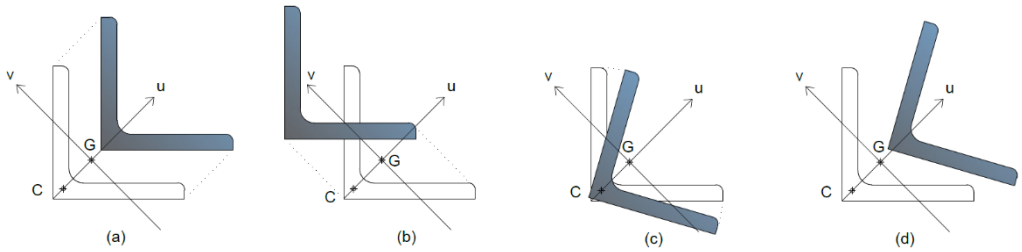

Σχήμα 5: (a),(b) Καμπτικός λυγισμός κατά μήκος του ασθενούς και του ισχυρού άξονα αντίστοιχα, (c) στρεπτικός λυγισμός, (d) στρεπτοκαμπτικός λυγισμός

Το **κεφάλαιο 4** ασχολείται με την ταξινόμηση των ισοσκελών γωνιακών διατομών. Η ταξινόμηση είναι σημαντική για την επιλογή της διαδικασίας ανάλυσης και σχεδιασμού που πρέπει να χρησιμοποιηθεί: πλαστική, ελαστική ή ελαστική με τη συνεκτίμηση του τοπικού λυγισμού. Γενικοί κανόνες για την ταξινόμηση των διατομών (κατηγορίες 1 έως 4) δίνονται στον EN 1993-1-1, σε συνδυασμό με τον EN 1993-1-5 που δίνει κανόνες για την αντοχή σε λυγισμό των γωνιακών διατομών κλάσης 4, οι οποίες είναι επιρρεπείς στον τοπικό λυγισμό. Πρόσθετοι κανόνες για την ταξινόμηση σε θλίψη υπάρχουν και στον EN 1993-3-1 για γωνιακά μέλη που χρησιμοποιούνται σε δικτυωτούς πύργους, καθώς και στο πρότυπο CENELEC EN 50341-1 που παρέχει ειδικούς κανόνες για πύργους που χρησιμοποιούνται στον τομέα των εναέριων ηλεκτρικών γραμμών. Μεταξύ αυτών των κανονιστικών προτύπων, ειδικές διατάξεις για την ταξινόμηση διατομών σε κάμψη υπάρχουν μόνο στον EN 1993-1-1, ενώ επισημαίνονται και αντιφάσεις μεταξύ αυτών, κύριως για την ταξινόμηση σε θλίψη, όπου τέσσερις διαφορετικοί λόγοι πλάτους προς πάχος μπορούν να υπολογισθούν για το ίδιο όριο κατηγορίας (κλάση 3 με κλάση 4)!

Σύμφωνα με το κανονιστικό πρότυπο EN 1993-1-1, ενότητα 5.5.2 (4), η ταξινόμηση πρέπει να γίνεται για τα θλιβόμενα τμήματα της διατομής που ορίζονται ως εξής: "Τα θλιβόμενα τμήματα περιλαμβάνουν κάθε τμήμα της διατομής που βρίσκεται είτε ολικά είτε μερικώς σε θλίψη υπό

τον εξεταζόμενο συνδυασμό φορτίων". Ωστόσο, η αυστηρή εφαρμογή αυτού του κανόνα απαιτεί ξεχωριστή ταξινόμηση της διατομής για κάθε συνδυασμό εφαρμοζόμενων δυνάμεων και ροπών. Δεδομένου ότι ο κανόνας αυτός δεν είναι πρακτικός για το σχεδιασμό, προτείνεται εδώ μια απλούστερη προσέγγιση, όπου η διατομή ταξινομείται χωριστά για θλίψη, κάμψη ισχυρού άξονα και κάμψη ασθενούς άξονα. Για την τελευταία περίπτωση, η κλάση της διατομής μπορεί να είναι διαφορετική για θετικές ή αρνητικές ροπές λόγω της μονοαξονικής συμμετρίας της διατομής, που οδηγεί σε διαφορετικές κλάσεις όταν το άκρο βρίσκεται σε θλίψη ή εφελκυσμό.

Συνεπώς, στο κεφάλαιο 4 συζητούνται και επαναπροσδιορίζονται μέσω αναλυτικών θεωρήσεων και εκτεταμένων αριθμητικών υπολογισμών τα όρια των λόγων πλάτους προς πάχος (c/t) για τα θλιβόμενα τμήματα ισοσκελών γωνιακών διατομών υπό θλίψη και κάμψη περί του ισχυρού ή του ασθενούς τους άξονα. Οι αναλυτικές προσεγγίσεις ακολουθούν πάντα τις βασικές αρχές των Ευρωκωδίκων και ειδικότερα του EN 1993-1-1, ενώ οι αριθμητικές μελέτες έχουν πραγματοποιηθεί με το λογισμικό μη γραμμικών πεπερασμένων στοιχείων ABAQUS και βρίσκονται σε πολύ καλή συμφωνία με τις αναλυτικές διερευνήσεις. Αξίζει να σημειωθεί ότι στην τελευταία έκδοση του EN 1993-1-1, δηλαδή στο prEN 1993-1-1 [25], δεν προβλέπεται καμία τροποποίηση όσον αφορά την ταξινόμηση των διατομών.

Πίνακας 1: Μέγιστα όρια των λόγων πλάτους προς πάχος (c/t) για θλιβόμενα τμήματα ισοσκελών γωνιακών

	Διατομή υπό θλίψη	**Διατομή υπό κάμψη ισχυρού άξονα M_u**	**Διατομή υπό κάμψη ασθενούς άξονα M_v – άκρο σε θλίψη**	**Διατομή υπό κάμψη ασθενούς άξονα M_v – άκρο σε εφελκυσμό**
Κλάση 1 – 2	---	$\frac{c}{t} \leq 16\,\varepsilon$	$\frac{c}{t} \leq 14\,\varepsilon$	$\frac{c}{t} \leq 27\,\varepsilon$
Κλάση 3	$\frac{c}{t} \leq 13{,}9\,\varepsilon$	$\frac{c}{t} \leq 26{,}3\,\varepsilon$	$\frac{c}{t} \leq 26{,}9\,\varepsilon$	---
όπου $\varepsilon = \sqrt{235/f_y[\frac{N}{mm^2}]}$				

Το πλήρες σύνολο των προτεινόμενων και πλήρως επικυρωμένων κριτηρίων ταξινόμησης συνοψίζεται στον Πίνακα 1. Μπορεί να διαπιστωθεί ότι οι προτεινόμενοι κανόνες:

(i) σε αντίθεση με τους ισχύοντες Ευρωκώδικες, χρησιμοποιούν τις ίδιες γεωμετρικές παραμέτρους, c και t, για όλες τις καταστάσεις φόρτισης της διατομής,

(ii) είναι γραμμένοι με τη μορφή του Ευρωκώδικα 3,

(iii) καλύπτουν όλες τις κατηγορίες διατομών,

(iv) αίρουν τις ασυνέπειες μεταξύ των υφιστάμενων κανονισμών.

Στο **κεφάλαιο 5**, προτείνονται σχέσεις υπολογισμού για την αντίσταση σχεδιασμού ισοσκελών γωνιακών διατομών που βασίζονται σε θεωρητικές προσεγγίσεις και εν συνεχεία επικυρώνονται πλήρως μέσω των αριθμητικών αποτελεσμάτων που προέκυψαν από το κεφάλαιο 4. Οι σχέσεις αυτές βασίστηκαν στις αντίστοιχες σχέσεις που δίνονται στον

Ευρωκώδικα 3 και προσαρμόστηκαν κατάλληλα όπου χρειάσθηκε, ώστε να καλύπτουν την συμπεριφορά των γωνιακών διατομών. Περιλαμβάνουν όλες τις σημαντικές συνθήκες φόρτισης, όπως θλίψη, κάμψη ασθενούς και ισχυρού άξονα. Με βάση τα αποτελέσματα που προέκυψαν στο κεφάλαιο 4, υιοθετείται μια γραμμική μετάβαση μεταξύ πλαστικής και ελαστικής αντίστασης της διατομής σε κάμψη. Αυτή η ομαλή μετάβαση έχει ήδη προταθεί και επικυρωθεί για διπλά συμμετρικές διατομές στο πλαίσιο του ευρωπαϊκού έργου SEMI-COMP [32] ενώ πρόκειται πλέον να υιοθετηθεί και για τις γωνιακές διατομές στην επικείμενη νέα έκδοση του Ευρωκώδικα 3 (prEN 1993-1-1).

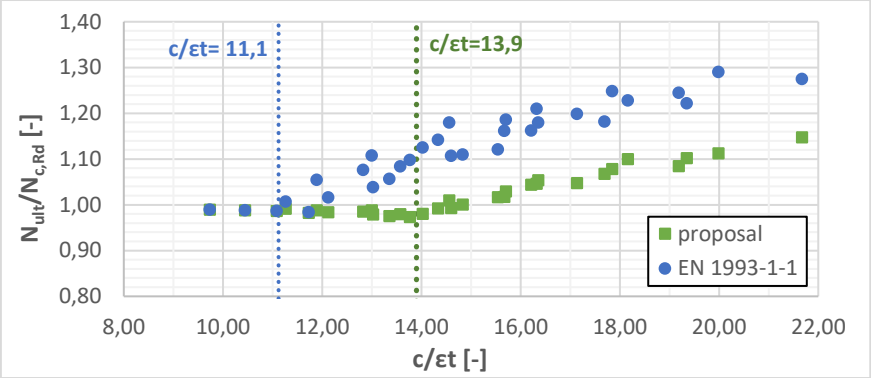

Σχήμα 6: Αντοχή διατομής σε θλίψη. Λόγος μεταξύ των αριθμητικών αποτελεσμάτων και της αντοχής σχεδιασμού που προκύπτει από Ευρωκώδικα 3- Μέρος 1 συναρτήσει του λόγου c/εt

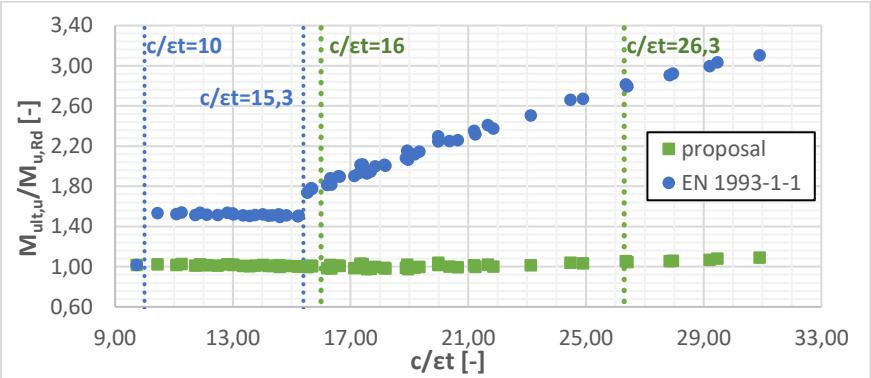

Σχήμα 7: Αντοχή διατομής κάμψη ισχυρού άξονα. Λόγος μεταξύ των αριθμητικών αποτελεσμάτων και της αντοχής σχεδιασμού που προκύπτει από Ευρωκώδικα 3- Μέρος 1 συναρτήσει του λόγου c/εt

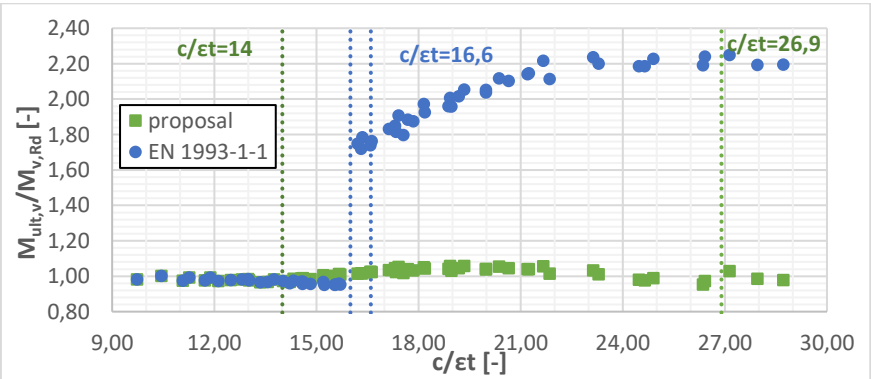

Σχήμα 8: Αντοχή διατομής κάμψη ασθενούς άξονα. Λόγος μεταξύ των αριθμητικών αποτελεσμάτων και της αντοχής σχεδιασμού που προκύπτει από Ευρωκώδικα 3- Μέρος 1 συναρτήσει του λόγου c/εt

Όπως φαίνεται και από τα παραπάνω διαγράμματα (Σχήματα 6, 7 και 8) για τις διάφορες φορτιστηκές καταστάσεις, οι προτεινόμενοι κανόνες σχεδιασμού είναι λιγότερο συντηρητικοί από τους ισχύοντες, όπως αυτοί περιγράφονται στον Ευρωκώδικα 3.

Για να διευρυνθούν οι γνώσεις σχετικά με τη συμπεριφορά και την ευστάθεια των χαλύβδινων υποστυλωμάτων που αποτελούνται από γωνιακές διατομές με χάλυβα υψηλής αντοχής (S460M) και υποβάλλονται σε θλίψη και κάμψη, πραγματοποιήθηκαν δώδεκα (12) δοκιμές λυγισμού σε τέτοια υποστυλώματα στο Πανεπιστήμιο της Λιέγης, οι οποίες και παρουσιάζονται αναλυτικά στο **κεφάλαιο 6**. Τα πειράματα περιορίστηκαν μόνο σε χάλυβα υψηλής αντοχής, δεδομένου ότι στη βιβλιογραφία υπήρχαν ήδη αρκετές δοκιμές θλίψης σε γωνιακά με χαμηλότερες κατηγορίες χάλυβα [10]-[12]-[13]-[14]. Η επιλογή των δοκιμίων, οι λεπτομέρειες σχετικά με την πειραματική καμπάνια, όπως οι μετρήσεις πριν ή και κατά τη διάρκεια των δοκιμών, καθώς και τα πειραματικά αποτελέσματα, παρουσιάζονται στο κεφάλαιο αυτό.

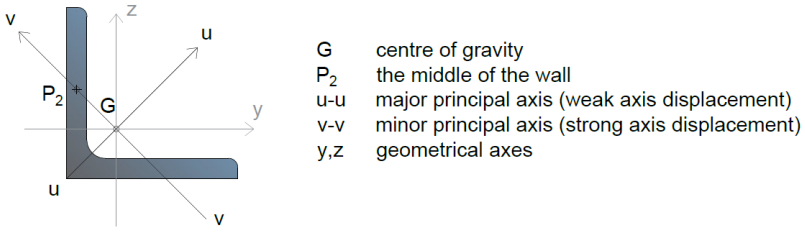

Σχήμα 9: Θέσεις των σημείων εφαρμογής του φορτίου (G και P_2)

Για τα πειράματα επιλέχθηκαν δύο (2) προφίλ από μεγάλες γωνιακές διατομές (L150x150x18 και 200x200x16) και χάλυβα αντοχής S460M. Για κάθε προφίλ, πραγματοποιήθηκαν έξι (6) δοκιμές με τρία (3) διαφορετικά μήκη ανά προφίλ και δύο (2) θέσεις εφαρμογής του φορτίου για κάθε μήκος (Σχήμα 9):

(i) το κέντρο βάρους, το οποίο αντιστοιχεί σε καθαρή θλίψη στη διατομή και

(ii) το σημείο τομής του δευτερεύοντος κύριου άξονα v-v με τη μέση γραμμή του πάχους του μέλους, το οποίο αντιπροσωπεύει τη θέση υλοποίησης της κοχλίωσης σε γωνιακά.

Τα χαρακτηριστικά των δοκιμίων συνοψίζονται στον Πίνακα 2. Το όνομα κάθε δοκιμίου αποτελείται από δύο αριθμούς Sp## (π.χ. Sp12):

- ο πρώτος αριθμός υποδηλώνει το προφίλ: 1 για L150x150x18 και 2 για 200x200x16,
- ο δεύτερος είναι ο αύξων αριθμός του δοκιμίου (1 έως 6 ανά προφίλ).

Για όλες τις δοκιμές, έχουν επιλεγεί σταθερές διαστάσεις για τις ακραίες πλάκες (Σχήμα 10), οι οποίες συγκολλούνται στα άκρα των γωνιακών μελών, προκειμένου να απλοποιηθεί η διαδικασία τοποθέτησης του δοκιμίου στην πειραματική διάταξη. Ως εκ τούτου, η θέση του επιβαλλόμενου φορτίου είναι πάντα η ίδια για το έμβολο της πρέσας. Η ποιότητα χάλυβα όλων των ακραίων πλακών είναι S355. Οι συγκολλήσεις έχουν σχεδιαστεί σύμφωνα με τον EN 1993-1-8. Για όλα τα δοκίμια, το ελάχιστο απαιτούμενο πάχος συγκόλλησης είναι 6 mm, εκτός από τα δοκίμια Sp11 και Sp21 που απαιτούν ελάχιστο πάχος 8 mm.

Πίνακας 2: Χαρακτηριστικά των δοκιμίων

Ονομασία δοκιμίου	Διατομή	Κατηγορία χάλυβας	Μήκος [mm]	Εκκεντρότητα φορτίου [mm]
Sp11	L 150x150x18	S460M	2500	0,00
Sp12	L 150x150x18	S460M	2500	$e_v = 48,74$
Sp13	L 150x150x18	S460M	3000	0,00
Sp14	L 150x150x18	S460M	3000	$e_v = 48,74$
Sp15	L 150x150x18	S460M	3500	0,00
Sp16	L 150x150x18	S460M	3500	$e_v = 48,74$
Sp21	L 200x200x16	S460M	3000	0,00
Sp22	L 200x200x16	S460M	3000	$e_v = 66,64$
Sp23	L 200x200x16	S460M	3500	0,00
Sp24	L 200x200x16	S460M	3500	$e_v = 66,64$
Sp25	L 200x200x16	S460M	4000	0,00
Sp26	L 200x200x16	S460M	4000	$e_v = 66,64$

Πριν την διεξαγωγή των πειραμάτων, μετρήθηκαν σε κάθε δοκίμιο οι πραγματικές του διαστάσεις (μήκος δοκιμίου, πλάτος και πάχος διατομής σε 3 θέσεις κατά μήκος αυτού). Επιπλέον καταγράφηκαν οι αρχικές ατέλειες και στα δυο πέλματα κατά μήκος των δοκιμίων, ενώ για τον προσδιορισμό των πραγματικών ιδιοτήτων του υλικού, πραγματοποιήθηκαν δοκιμές εφελκυσμού σύμφωνα με το πρότυπο ISO 6892-1:2016 [35], τα αποτελέσματα των οποίων συνοψίζονται στον Πίνακα 3. Μπορεί να παρατηρηθεί ότι ενώ η πραγματική οριακή τάση ήταν πάνω από τις ονομαστικές τιμές για όλα τα δοκίμια, αυτό δεν συνέβη για την τάση διαρροής.

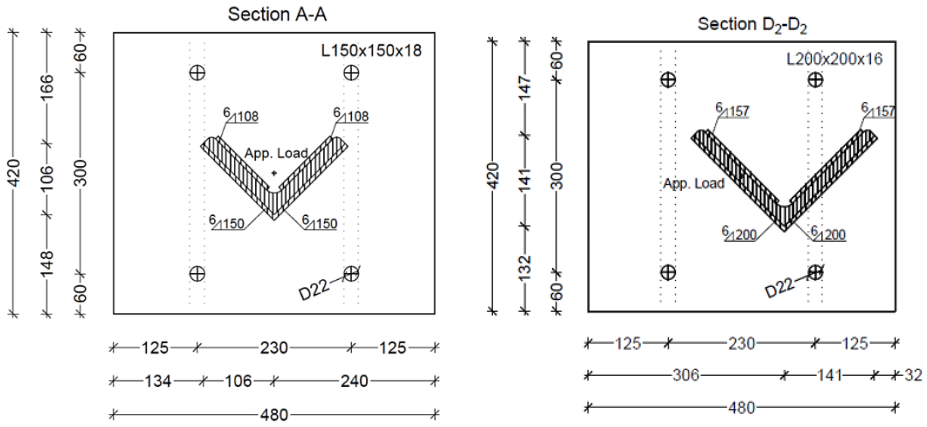

Σχήμα 10: Κατασκευαστική λεπτομέρεια των ακραίων πλακών για δοκίμια με κεντρική (αριστερά) και έκκεντρη (δεξιά) φόρτιση

Πίνακας 3: Αποτελέσματα δοκιμών εφελκυσμού

Ονομασία δείγματος	**E [MPa]**	**f_y [MPa]**	**f_{ult} [MPa]**	**Παραμόρφωση κατά την αστοχία [%]**	**$f_{y,nom}$ [MPa]**	**$f_y/f_{y,nom}$ [-]**	**Χαρακτηριζόμενα δείγματα**
S 460/1	203155	425,8	572,50	14,3	460,0	0,93	Sp12, Sp13, Sp14, Sp15, Sp16
S 460/2	208947	487,6	604,64	13,7	460,0	1,06	Sp21, Sp22, Sp23, Sp25, Sp26
S 460/3	197317	417,2	560,87	14,3	460,0	0,91	Sp11
S 460/4	203797	472,6	587,21	13,8	460,0	1,03	Sp24

Οι δοκιμές θλίψης πραγματοποιήθηκαν με την μηχανική πρέσα Amsler 500, η οποία είχε μέγιστη ικανότητα επιβολής θλιπτικού φορτίου ίσο με 5000 kN. Η διάταξη έχει δύο σφαιρικές αρθρώσεις άνω και κάτω (Σχήμα 12), έτσι ώστε οι περιστροφές γύρω από τον δευτερεύοντα και τον κύριο άξονα να μπορούν να αναπτυχθούν ελεύθερα, χωρίς ωστόσο να μπορεί να εμφανιστεί συστροφή ή στρέβλωση στα άκρα του δοκιμίου. Κατά τη διάρκεια των δοκιμών μετρήθηκαν διάφορες μετατοπίσεις, όπως αυτές απεικονίζονται στο Σχήμα 11 και συνοψίζονται ακολούθως:

- κατακόρυφη μετατόπιση C_1 (χρησιμοποιώντας δύο LVDT's, έναν στην μπροστινή και έναν στην πίσω όψη του δοκιμίου),
- τέσσερις οριζόντιες μετατοπίσεις C_2, C_3, C_4 και C_5 στη διατομή του μέσου ύψους του δοκιμίου (1η θέση),
- τέσσερις οριζόντιες μετατοπίσεις C_6, C_7, C_8 και C_9 στη διατομή που βρίσκεται στο ¼L από την βάση (2η θέση).

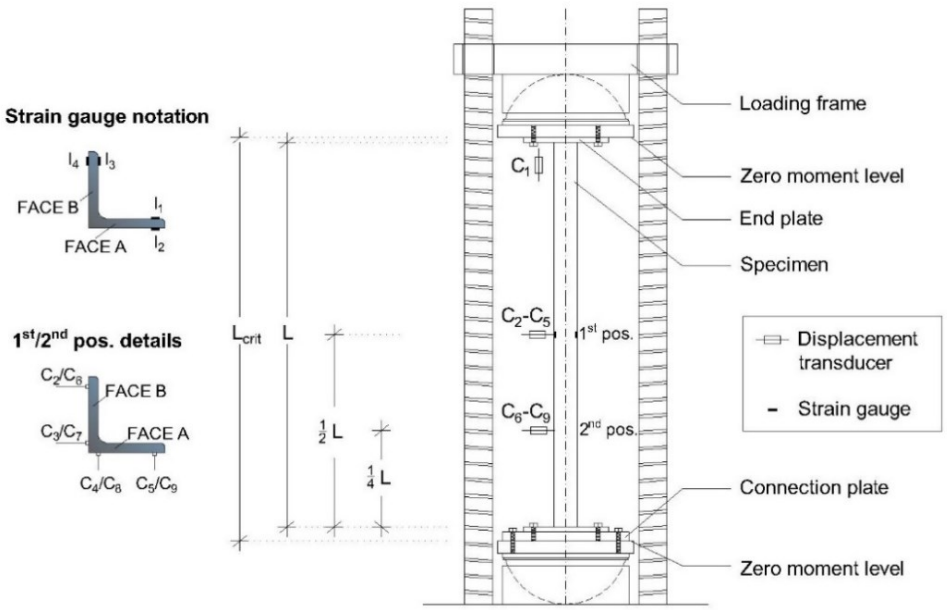

Σχήμα 11: Σκαρίφημα της διάταξης Amsler 500 και απεικόνιση των μετρήσεων που πραγματοποιήθηκαν κατά την διάρκεια των δοκιμών

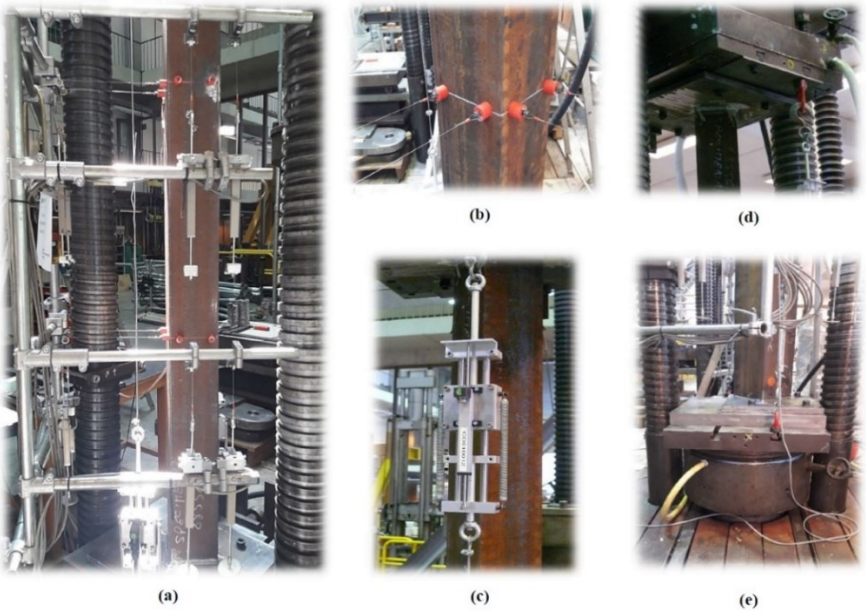

Σχήμα 12: (a) Γενική εικόνα της διάταξης με τις συσκευές μέτρησης, (b) σημεία σύνδεσης των LVDT's στη διατομή, (c) LVDT για την μέτρηση της αξονικής μετακίνησης, (d) λεπτομέρεια της άνω πλάκας έδρασης και (e) λεπτομέρεια της κάτω πλάκας έδρασης

Όλες οι μετρήσεις (αρχικές γεωμετρικές ατέλειες, περιστροφές, τάσεις και παραμορφώσεις) για κάθε δοκίμιο είναι διαθέσιμες στη σχετική τεχνική έκθεση [33]. Τα αποτελέσματα των δοκιμών παρουσιάζονται συνοπτικά στην συνέχεια μέσω διαγραμμάτων (Σχήμα 13, Σχήμα 14, Σχήμα 15 και Σχήμα 16) και στον Πίνακα 4.

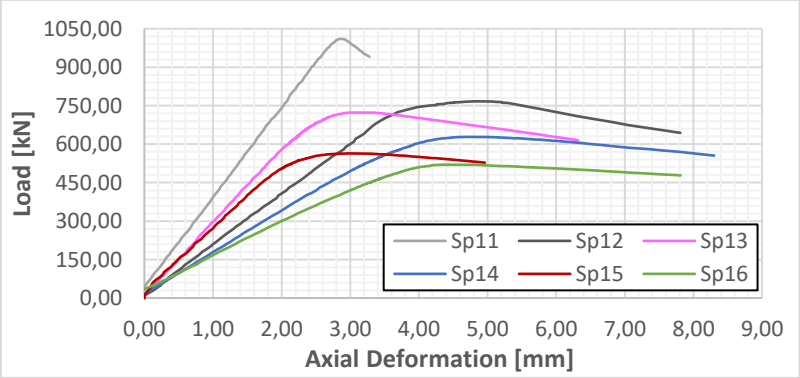

Σχήμα 13: Καμπύλες φορτίου – αξονικής παραμόρφωσης για τα προφίλ L 150x150x18

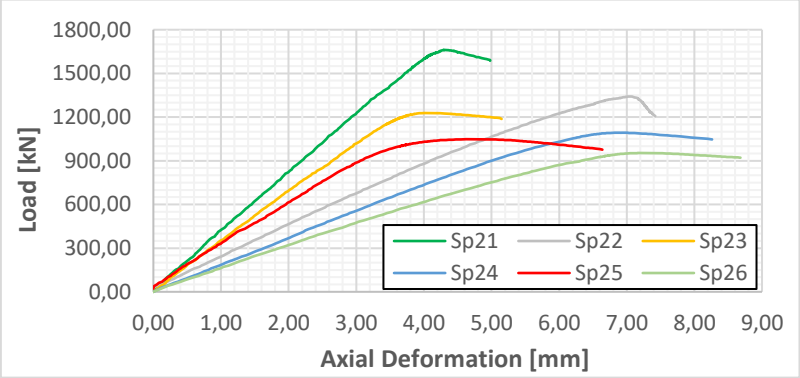

Σχήμα 14: Καμπύλες φορτίου – αξονικής παραμόρφωσης για τα προφίλ L 200x200x16

Τα κεντροβαρικά φορτισμένα δοκίμια Sp11, Sp13, Sp15 αστόχησαν με καμπτικό λυγισμό κατά μήκος του ασθενούς άξονά τους ενώ τα έκκεντρα φορτισμένα δοκίμια Sp22, Sp24, Sp26 με στρεπτοκαμπτικό λυγισμό. Επιπλέον, τα κεντροβαρικά φορτισμένα δοκίμια Sp21, Sp23, Sp25 και τα έκκεντρα φορτισμένα δοκίμια Sp12, Sp14, Sp16 αστόχησαν κυρίως σε στρεπτοκαμπτικό λυγισμό, ο οποίος ήταν λιγότερο έντονος.

Θα πρέπει επίσης να αναφερθεί ότι δεν παρατηρήθηκε τοπικός λυγισμός σε κανένα από τα πειράματα, παρόλο που όλα τα δοκίμια Sp2# κατατάσσονται στην κατηγορία 4 σύμφωνα με τις ισχύουσες διατάξεις του EN 1993-1-1.

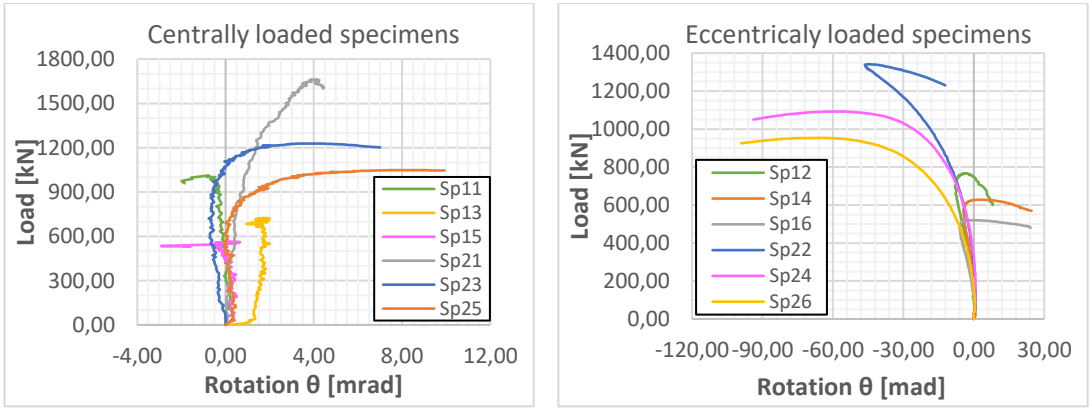

Σχήμα 15: Καμπύλες φορτίου - περιστροφής στο μέσο ύψος του δοκιμίου για κεντρικά φορτισμένα (αριστερά) και έκκεντρα φορτισμένα (δεξιά) δοκίμια

Σχήμα 16: Τελική παραμορφωμένη μορφή του (a) Sp15 λόγω καμπτικού λυγισμού (b) Sp26 λόγω στρεπτοκαμπτικού λυγισμού και (c) Sp14 λόγω μικτής αστοχίας μεταξύ καμπτικού και στρεπτοκαμπτικού λυγισμού

Πίνακας 4: Παραμορφώσεις και στροφές στη διατομή μέσου ύψους για το φορτίο αστοχίας

Ονομασία δοκιμίου	Διατομή	N_{exp} [kN]	u_O [mm]	v_O [mm]	θ [mrad]
Sp11	150x150x18	1010,6	8,88	-0,01	-0,82
Sp12		767,3	-15,28	-16,39	-3,94
Sp13		723,2	-28,22	0,53	1,71
Sp14		628,3	-16,35	-17,05	2,05
Sp15		563,9	-31,53	-0,95	0,39
Sp16		519,8	-17,78	-17,03	-1,81
Sp21	200x200x16	1661,5	10,89	1,52	3,96
Sp22		1341,4	2,48	-17,07	-44,92
Sp23		1228,0	20,49	1,53	3,51
Sp24		1092,3	16,87	-18,09	-59,51
Sp25		1048,1	-38,43	0,62	7,77
Sp26		953,6	16,31	-22,11	-62,95

Οι δοκιμές συνοδεύτηκαν από αριθμητικά προσομοιώματα, τα οποία πραγματοποιήθηκαν λαμβάνοντας υπόψη τις σχετικές ατέλειες καθώς και τις γεωμετρικές και υλικές μη γραμμικότητες, ενώ τα αριθμητικά αποτελέσματα συγκρίθηκαν και επικυρώθηκαν με τα πειραματικά. Οι αναλύσεις πραγματοποιήθηκαν με το λογισμικό μη γραμμικών πεπερασμένων στοιχείων FINELG χρησιμοποιώντας στοιχεία δοκού. Η επιλογή των στοιχείων δοκού δικαιολογείται από το γεγονός ότι κατά τη διάρκεια των δοκιμών δεν παρατηρήθηκε τοπικός λυγισμός. Μόνο το υποστύλωμα προσομοιώθηκε, ενώ η συμπεριφορά των πλακών στα άκρα λήφθηκαν έμμεσα υπόψιν. Τα υποστυλώματα θεωρήθηκαν αρθρωτά στα άκρα τους, αναπαριστώντας έτσι αρκετά καλά τις πραγματικές πειραματικές συνθήκες.

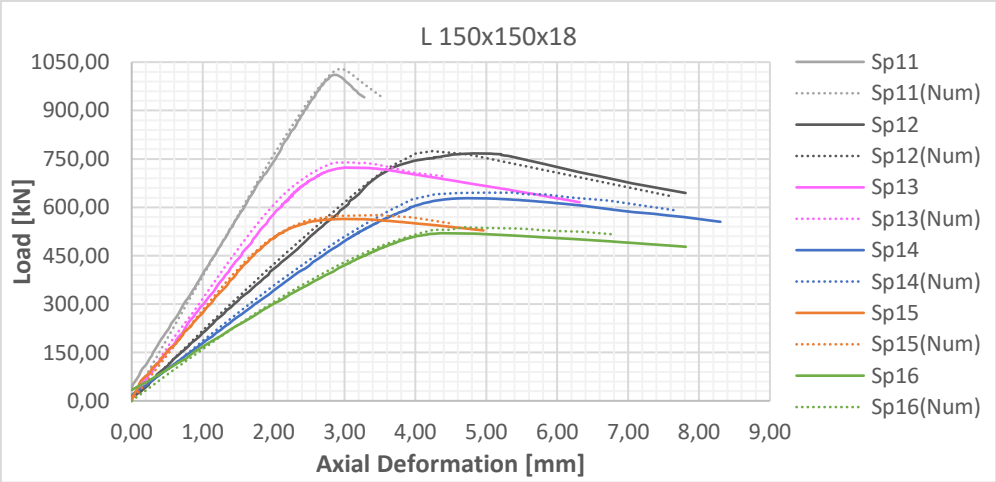

Σχήμα 17: Σύγκριση μεταξύ πειραμάτων και αριθμητικών αναλύσεων για τα δοκίμια Sp1#

Πίνακας 5: Οριακές αντοχές που προέκυψαν από πειραματικές δοκιμές και αριθμητικά μοντέλα

Ονομασία δοκιμίου	Διατομή	Μήκος λυγισμού [mm]	Πραγματική εκκεντρότητα φορτίου [mm]	Επιπρόσθετη εκκεντρότητα αναλύσεων GMNIA [mm]	N_{exp} [kN]	N_{FEM} [kN]	N_{exp}/N_{FEM}
Sp11	150x150x18	2607	0,00	$e_u = 1,50$	1010,6	1028,6	0,98
Sp12		2607	$e_v = 48,71$	$e_u = 0,50$	767,3	774,1	0,99
Sp13		3107	0,00	$e_u = -2,00$	723,2	739,3	0,98
Sp14		3107	$e_v = 48,72$	$e_u = -1,10$	628,3	645,9	0,97
Sp15		3607	0,00	$e_u = -2,00$	563,9	575,8	0,98
Sp16		3607	$e_v = 48,70$	$e_u = -1,00$	519,8	536,0	0,97
Sp21	200x200x16	3107	0,00	$e_u = -1,50$	1661,5	1690,6	0,98
Sp22		3107	$e_v = 66,60$	$e_u = -0,80$	1341,4	1361,0	0,99
Sp23		3607	0,00	$e_u = -2,00$	1228,0	1267,4	0,97
Sp24		3607	$e_v = 66,65$	$e_u = -0,50$	1092,3	1107,6	0,99
Sp25		4107	0,00	$e_u = -1,70$	1048,1	1082,2	0,97
Sp26		4107	$e_v = 66,63$	$e_u = 0,00$	953,6	959,1	0,99

Στα Σχήματα 17 και 18 παρουσιάζονται οι αξονικές παραμορφώσεις (βράχυνση) των δοκιμίων συναρτήσει του φορτίου τόσο για τις πειραματικές δοκιμές (συνεχείς γραμμές) όσο και για τα αριθμητικά προσομοιώματα (διακεκομμένες γραμμές). Στον Πίνακα 5 συνοψίζονται και συγκρίνονται οι τελικές πειραματικές και αριθμητικές αντοχές για κάθε δοκίμιο. Από τα γραφήματα και τον πίνακα μπορεί κανείς να δει ότι υπάρχει πολύ καλή συμφωνία μεταξύ των αριθμητικών προσομοιωμάτων και των πειραματικών δοκιμών όσον αφορά την αξονική δυσκαμψία και τη φέρουσα ικανότητα. Η μέση τιμή του λόγου N_{exp} / N_{FEM} είναι ίση με 0,98 με τυπική απόκλιση 1%.

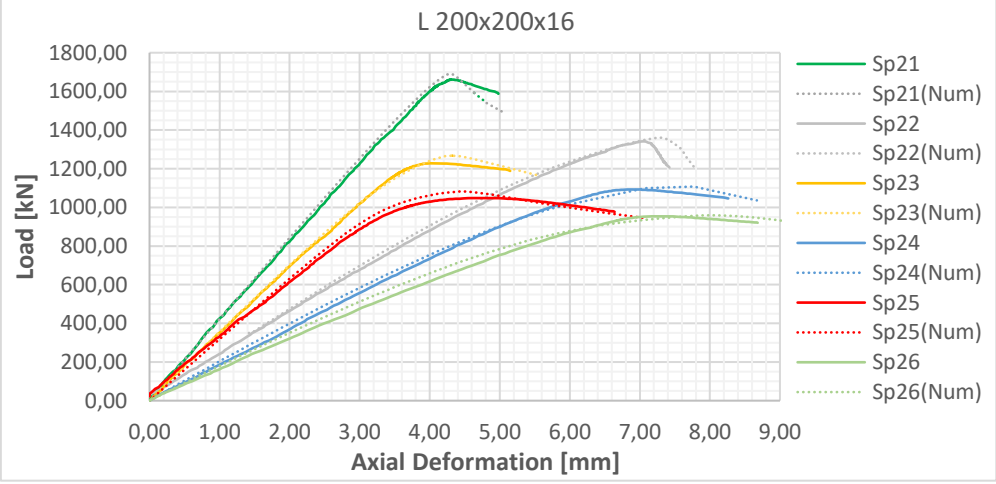

Σχήμα 18: Σύγκριση μεταξύ πειραμάτων και αριθμητικών αναλύσεων για τα δοκίμια Sp2#

Τέλος, από τις αναλύσεις προκύπτει ότι μια μικρή εκκεντρότητα της θέσης του φορτίου εφαρμογής μπορεί να επηρεάσει την αντοχή του μέλους, σε σχέση με την τέλεια περίπτωση του κεντρικά φορτιζόμενου μέλους. Από την παρούσα μελέτη προέκυψε ότι μια εκκεντρότητα ίση με 1,5 mm μπορεί να μεταβάλλει την τελική αντοχή κατά περίπου 6%.

Όπως εξηγήθηκε και στην εισαγωγή, οι ιδιαιτερότητες των γωνιακών διατομών δικαιολογούν τους λόγους που οι υφιστάμενοι κανόνες σχεδιασμού που εφαρμόζονται για άλλους τύπους διατομών δεν μπορούν να καλύψουν με ασφάλεια τα γωνιακά, γεγονός που οδηγεί αναπόφευκτα στην ανάγκη ανάπτυξης ειδικών κανόνων σχεδιασμού για τις διατομές αυτές. Στο **κεφάλαιο 7** προτείνονται σχέσεις σχεδιασμού για την αντοχή και την ευστάθεια ισοσκελών γωνιακών μελών υπό κάμψη και θλίψη, τονίζοντας τις διαφορές με τις υφιστάμενες διατάξεις του Ευρωκώδικα 3. Οι προτεινόμενοι κανόνες επικυρώνονται πλήρως μέσω αριθμητικών ερευνών και πειραματικών δοκιμών.

Οι εκτεταμένες αριθμητικές παραμετρικές μελέτες πραγματοποιήθηκαν με το μη γραμμικό λογισμικό πεπερασμένων στοιχείων ABAQUS. Σε όλα τα προσομοιώματα, όλα τα εφαρμοζόμενα φορτία αυξάνονται ταυτόχρονα μέχρι την αστοχία (ή τουλάχιστον μέχρι να φτάσουν στο μέγιστο οριακό φορτίο). Στις περιπτώσεις όπου τα φαινόμενα δευτέρας τάξης επηρεάζουν σημαντικά την απόκριση, το τελικό φορτίο ορίζεται όπως στην §3.6. Το μοντέλο είναι παρόμοιο με αυτό που χρησιμοποιήθηκε στις αριθμητικές μελέτες για την κατάταξη των διατομών. Οι αναλύσεις πραγματοποιήθηκαν λαμβάνοντας υπόψη τόσο τις αρχικές ατέλειες των μελών όσο και τις παραμένουσες τάσεις που προκύπτουν από τη διαδικασία θερμής έλασης. Ενδεικτικά αναφέρονται στην συνέχεια κάποια αποτελέσματα.

Στο Σχήμα 19 απεικονίζονται τα αριθμητικά αποτελέσματα για κεντροβαρικά θλιβόμενα μέλη, σε σύγκριση με τις καμπύλες λυγισμού a και b, όπως αυτές ορίζονται στον prEN 1993-1-1. Σύμφωνα με τον prEN 1993-1-1, τα αριθμητικά αποτελέσματα που προκύπτουν για χάλυβα S355 πρέπει να συγκρίνονται με την καμπύλη λυγισμού b, ενώ για χάλυβα S460 με την καμπύλη a. Μπορεί εύκολα να παρατηρηθεί ότι όλα τα αποτελέσματα που πρέπει να συγκριθούν με την καμπύλη b είναι πάνω από αυτήν, ενώ τα αποτελέσματα που πρέπει να συγκριθούν με την καμπύλη a είναι είτε πάνω στην καμπύλη είτε λίγο χαμηλότερα, γεγονός που είναι αποδεκτό δεδομένης της απόκλισης 2% που λαμβάνεται υπόψη.

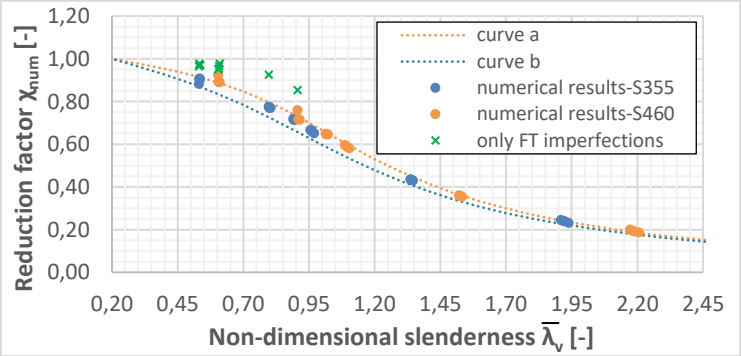

Σχήμα 19: Σύγκριση αριθμητικών αποτελεσμάτων για κεντρικά θλιβόμενα μέλη με τις καμπύλες λυγισμού του prEN 1993-1-1

Στο Σχήμα 20 παρουσιάζεται ο λόγος μεταξύ της αριθμητικής αντοχής υπό κάμψη ισχυρού άξονα του μέλους ($M_{ult,u}$) και της αντίστοιχης αναλυτικής ($M_{u,Rd}$), σε σχέση με τη λυγηρότητα.

Είναι εμφανές ότι οι σχέσεις υπολογισμού της αντοχής σε κάμψη που προτείνονται στο πλαίσιο της διατριβής είναι αποδεκτές και επικυρώνονται πλήρως αριθμητικά.

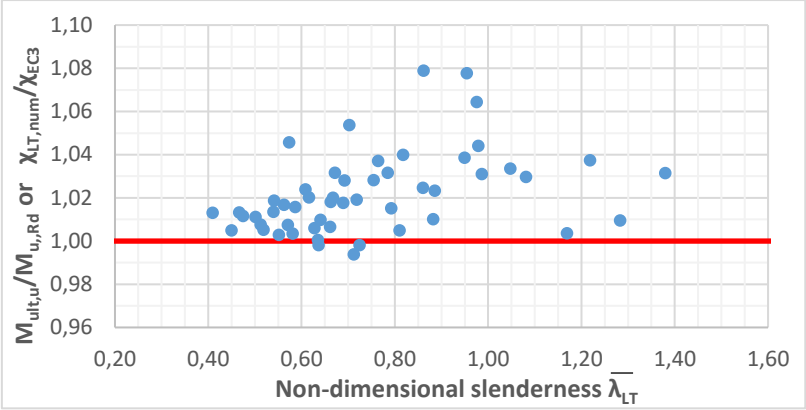

Σχήμα 20: Σύγκριση αριθμητικών και αναλυτικών αποτελεσμάτων της αντοχής σε κάμψη ισχυρού άξονα

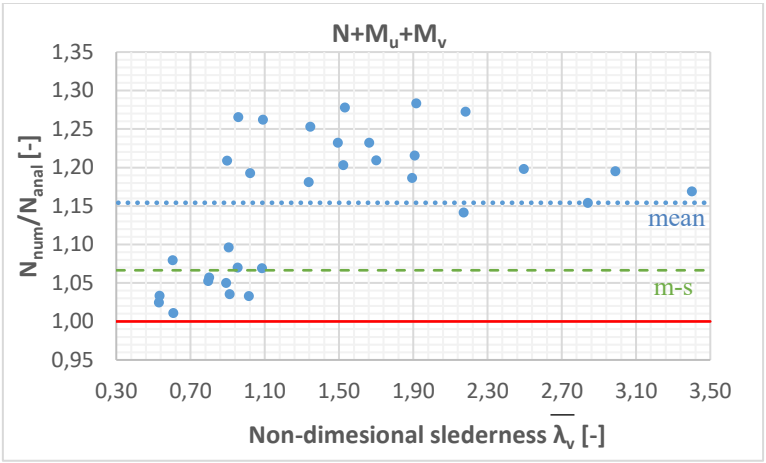

Σχήμα 21: Λόγος αριθμητικών και αναλυτικών φορτίων για συνδυασμένη φόρτιση $N+M_u+M_v$

Για την περίπτωση που το μέλος υποβάλλεται σε συνδυασμένη αξονική φόρτιση και κάμψη, τα αποτελέσματα φαίνονται στο σχήμα 21, όπου η αξονική δύναμη εφαρμόζεται στο μέσο του ύψους του πέλματος και στη μέση γραμμή του πάχους του. Η μέση τιμή του λόγου N_{num}/N_{anal} είναι ίση με 1,15 και η τυπική απόκλιση 8,77%. Είναι προφανές ότι οι αναλυτικές προβλέψεις για την αντοχή του μέλους σε συνδυασμένη φόρτιση είναι προς την μεριά της ασφάλειας, επικυρώνοντας έτσι τις αναλυτικές προτεινόμενες σχέσεις.

Τα πειραματικά αποτελέσματα προέρχονται από τις δοκιμές που πραγματοποιήθηκαν στο πλαίσιο της διατριβής (κεφάλαιο 6), καθώς και από προηγούμενες πειραματικές έρευνες που βρέθηκαν στη βιβλιογραφία. Τα πειραματικά αποτελέσματα συγκρίθηκαν επίσης με τις υφιστάμενες διατάξεις του Ευρωκώδικα 3 και μερικά από τα αποτελέσματα φαίνονται στα παρακάτω διαγράμματα (Σχήματα 22-25).

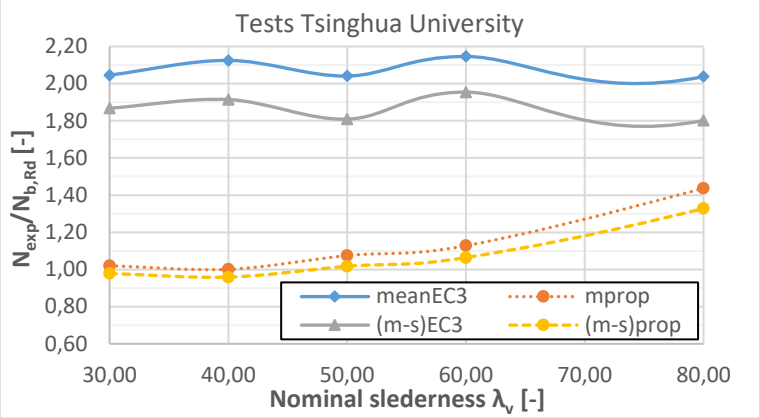

Σχήμα 22: Λόγος αριθμητικών και αναλυτικών φορτίων για τα πειράματα σε κεντροβαρικά θλιβόμενα υποστυλώματα που έγιναν στο Tsinghua University, μέσες τιμές και σύγκριση με τον prEN 1993-1-1

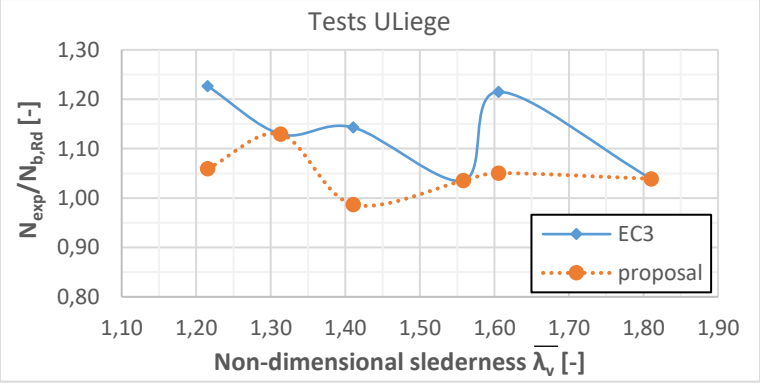

Σχήμα 23: Λόγος αριθμητικών και αναλυτικών φορτίων για τα πειράματα σε κεντροβαρικά θλιβόμενα υποστυλώματα που έγιναν στο Liege University και σύγκριση με τον prEN 1993-1-1

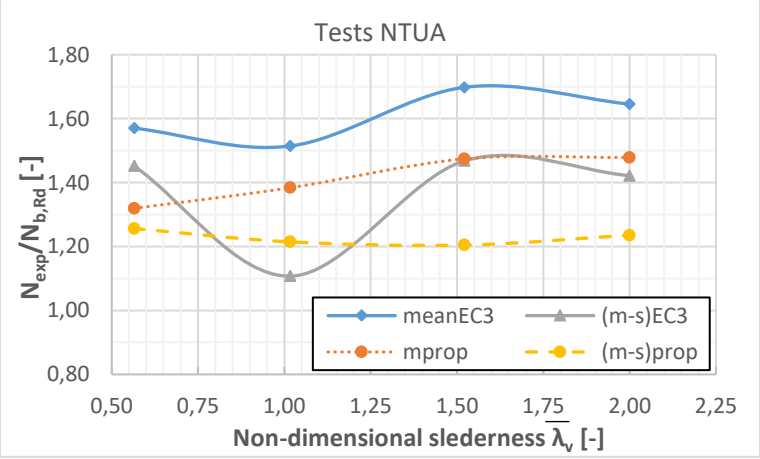

Σχήμα 24: Λόγος αριθμητικών και αναλυτικών φορτίων για τα πειράματα σε έκκεντρα θλιβόμενα υποστυλώματα που έγιναν στο NTUA, μέσες τιμές και σύγκριση με τον prEN 1993-1-1

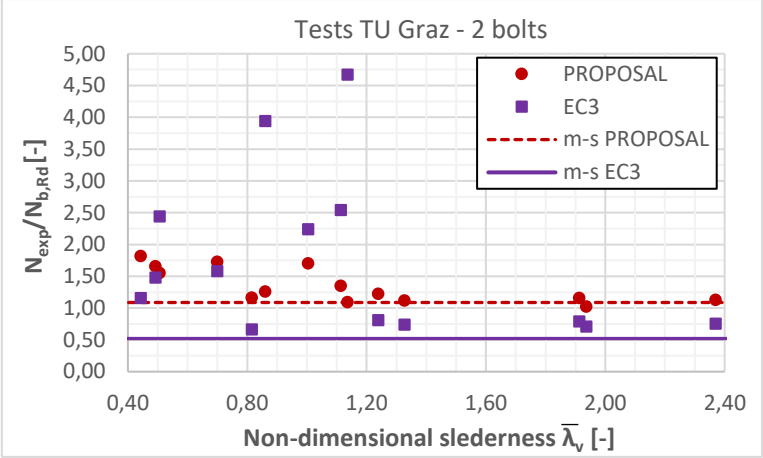

Σχήμα 25: Λόγος αριθμητικών και αναλυτικών φορτίων για τα πειράματα σε θλιβόμενα υποστυλώματα συνδεδεμένα με δυο κοχλίες στα άκρα τους που έγιναν στο TU Graz και σύγκριση με τον EN 1993-3-1

Στο **κεφάλαιο 8** παρουσιάζονται συνοπτικά οι τυπολογίες (Σχήμα 26) και οι λειτουργίες των πύργων μεταφοράς ενέργειας, καθώς και γενικά οι τυπολογίες των δικτυωτών πύργων με την σχετική τους ορολογία.

(a) **(b)** **(c)** **(d)**

Σχήμα 26: Τυπική μορφή (a) ξύλινου πυλώνα, (b) πυλώνα από σκυρόδεμα, (c) κελυφωτού μεταλλικού πύργου και (d) δικτυωτοί πύργου

Στο **κεφάλαιο 9**, επιλέχθηκε ένας τυπικός δικτυωτός μεταλλικός πύργος μεταφοράς ηλεκτρικής ενέργειας κατασκευασμένος από ισοσκελή γωνιακές διατομές, η γεωμετρία του οποίου φαίνεται στο Σχήμα 27. Ο πύργος σχεδιάστηκε αρχικά με ένα εμπορικό λογισμικό (TOWER) σύμφωνα με τις ισχύουσες κανονιστικές διατάξεις, δηλαδή βάσει μιας γραμμικής ελαστικής ανάλυσης πρώτης τάξεως όπου η κατασκευή προσομοιώνεται ως ένα δικτύωμα.

Στη συνέχεια, πραγματοποιήθηκε αξιολόγηση του σχεδιασμού με εκ νέου προσομοίωση του πύργου με το λογισμικό μη γραμμικών πεπερασμένων στοιχείων δοκού (FINELG), λαμβάνοντας υπόψη τις σχετικές ατέλειες καθώς και γεωμετρικές και υλικές μη γραμμικότητες. Το τρισδιάστατο προσομοίωμα του πύργου απεικονίζεται στο Σχήμα 28. Κάθε

στοιχείο/ράβδος μοντελοποιείται με την κατάλληλη εκκεντρότητα, περιστροφή και προσανατολισμό, ώστε να προσομοιώνεται όσο το δυνατόν καλύτερα η πραγματική του θέση στην κατασκευή. Ως αποτέλεσμα, τα μέλη του πύργου δεν υπόκεινται μόνο σε αξονικές δυνάμεις αλλά και σε ροπές κάμψης. Για το προσομοίωμα έγιναν οι ακόλουθες παραδοχές:

- οι τέσσερεις κύριοι ορθοστάτες (πόδια) του πύργου μοντελοποιούνται ως συνεχή στοιχεία σε όλο το μήκος τους,
- οι οριζόντιες και κύριες διαγώνιοι ράβδοι πλήρωσης θεωρούνται αρθρωτά στα άκρα τους,
- τα δευτερεύοντα στοιχεία στήριξης (διαγώνιες πλήρωσης) θεωρούνται επίσης αρθρωτά στα άκρα τους.

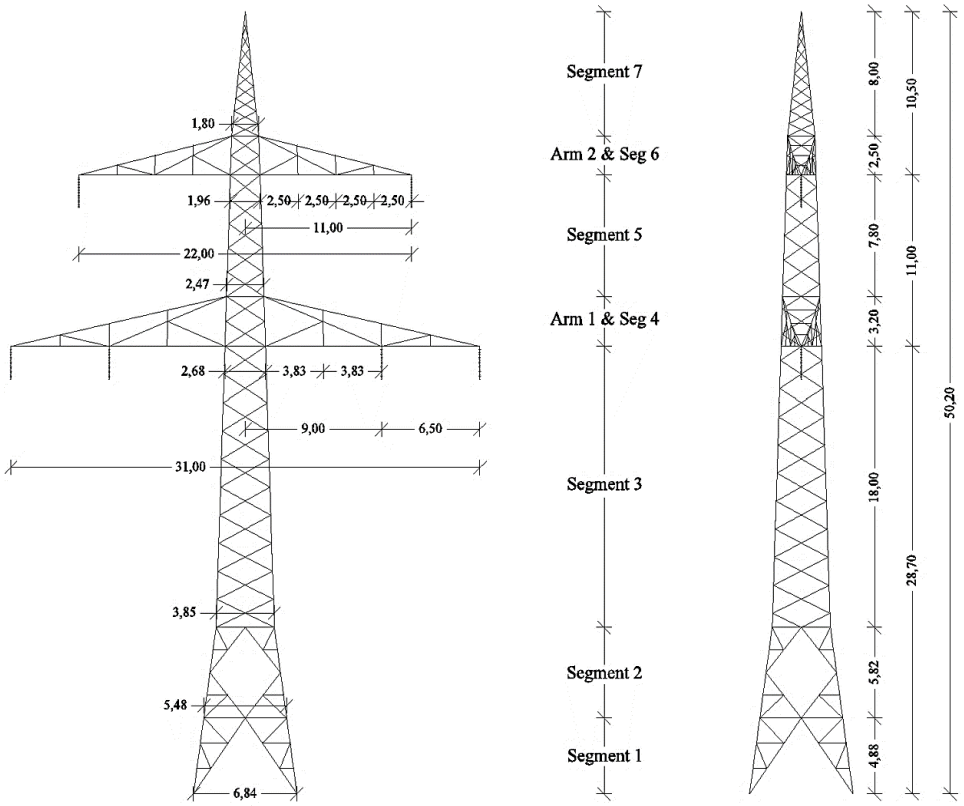

Σχήμα 27: Γεωμετρία και διακριτοποίηση των διαφόρων τμημάτων του μελετώμενου Danube tower

Όλα τα μέλη του πύργου είναι κατασκευασμένα από χάλυβα κατηγορίας S355J2. Τα καλώδια και οι και οι μονωτήρες δεν έχουν προσομοιωθεί. Ωστόσο, τα φορτία ανέμου που ασκούνται σε αυτά, καθώς και το ίδιο βάρος τους έχουν υπολογιστεί ξεχωριστά και έχουν εισαχθεί στο πρόγραμμα ως σημειακά φορτία που ασκούνται στην κορυφή των μονωτήρων.

Για τον αρχικό σχεδιασμό του πύργου εξετάστηκαν δώδεκα διαφορετικοί συνδυασμοί φορτίων αναφορικά με τη διεύθυνση του ανέμου και τον ορισμό των δράσεων (ευνοϊκές / δυσμενείς). Μεταξύ αυτών, επιλέχθηκαν για την αξιολόγηση του σχεδιασμού οι δύο πιο κρίσιμοι, οι οποίοι αντιστοιχούν σε δυσμενείς δράσεις και είναι:

Διεύθυνση Χ: φορτία βαρύτητας (G) και δυνάμεις ανέμου κάθετες στους βραχίονες (W_x).

Διεύθυνση Υ: φορτία βαρύτητας (G) και δυνάμεις ανέμου παράλληλες προς τους βραχίονες (W_y).

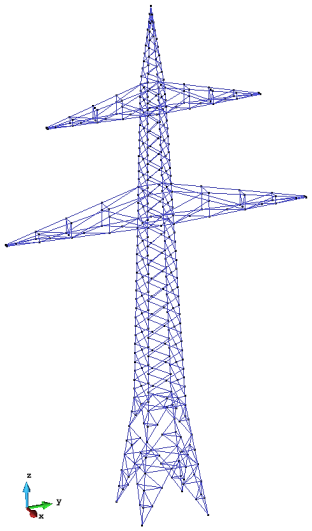

Σχήμα 28: Τρισδιάστατο προσομοίωμα του πύργου με το λογισμικό FINELG

Τα δύο λογισμικά αρχικά συγκρίθηκαν στο πλαίσιο μιας γραμμικής ελαστικής ανάλυσης (ίδιο βάρος, μετακινήσεις, δυσκαμψία). Οι διαφορές τους είναι αποδεκτές καθώς είναι μικρότερες από 5%. Στη συνέχεια, και για να υπάρχει μια συνολική εικόνα της πραγματικής απόκρισης του πύργου, πραγματοποιήθηκε μια ανάλυση ελαστικού λυγισμού, η οποία συμπληρώθηκε – επικυρώθηκε από μια γραμμική ελαστική ανάλυση δεύτερης τάξης. Μέσα από την δεύτερη, υπογραμμίζεται και η σημασία της συνεκτίμησης των φαινομένων δεύτερης τάξης στην ανάλυση. Τα αποτελέσματα της ανάλυσης ελαστικού λυγισμού συνοψίζονται στον Πίνακα 6, ενώ η πρώτη ιδιομορφή λυγισμού για τους δυο συνδυασμούς φόρτισης φαίνονται στο Σχήμα 29. Ο τρόπος αστάθειας που παρατηρείται στο Σχήμα 29 (δεξιά) ονομάστηκε "αστάθεια τμήματος" και διερευνάται περαιτέρω στο κεφάλαιο 10, όπου προτείνονται δύο αναλυτικά μοντέλα υπολογισμού.

Πίνακας 6: Αποτελέσματα ανάλυσης ελαστικού λυγισμού

Συνδυασμός φόρτισης	**1,35G+ α_{cr}1,35W_x**		**1,35G+ α_{cr}1,35W_y**	
Ιδιομορφή	**α_{cr}**	**Μορφή αστάθειας**	**α_{cr}**	**Μορφή αστάθειας**
1st	3,056	Member	1,015	Segment
2nd	5,853	Member	1,179	Member

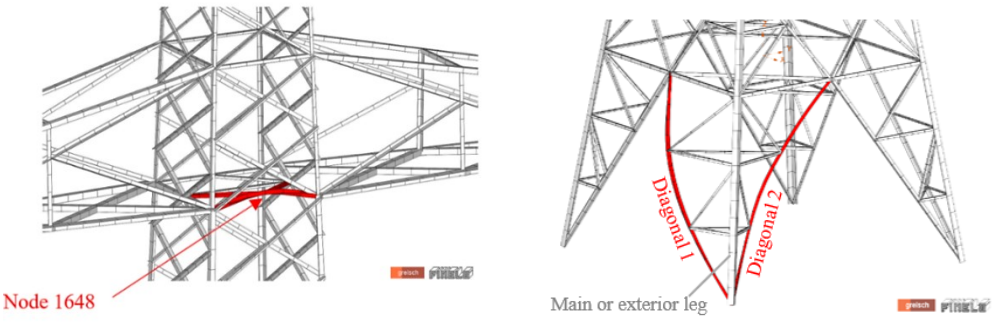

Σχήμα 29: Πρώτη ιδιομορφή λυγισμού για συνδυασμό φορτίου 1,35G+ α_{cr}1,35W_x (αριστερά) και 1,35G+ α_{cr}1,35W_y (δεξιά)

Τα αποτελέσματα της γραμμικής ελαστικής ανάλυσης δεύτερης τάξης, στη οποία έχει θεωρηθεί ελαστικός νόμος υλικού, αλλά χωρίς να έχουν ληφθεί υπόψη οι αρχικές ατέλειες (συνεχής γραμμή), συνοψίζονται για κάθε κατεύθυνση στα διαγράμματα παρακάτω (Σχήμα 30). Η διακεκομμένη γραμμή αναπαριστά τα αποτελέσματα της ανάλυσης ελαστικού λυγισμού.

Είναι αξιοσημείωτο το γεγονός ότι το κρίσιμο φορτίο λυγισμού που προέκυψε από την ανάλυση αστάθειας είναι σημαντικά υψηλότερο από αυτό που προέκυψε από την γραμμική ελαστική ανάλυση δευτέρας τάξεως. Ωστόσο, αν παρατηρήσει κανείς τα εντατικά μεγέθη των ράβδων που αστοχούν στις δυο διαφορετικές αναλύσεις, διαπιστώνει ότι η αστοχία εμφανίζεται για δύο διαφορετικές τριπλέτες σχετικής αξονικής δύναμης και ροπών κάμψης. Αυτό οφείλεται στο γεγονός ότι στην ανάλυση αυτή, τα φαινόμενα δευτέρας τάξεως επηρεάζουν σημαντικά τα εντατικά μεγέθη των μελών. Αυτό έχει παρατηρηθεί επίσης και για μεμονωμένα γωνιακά μέλη, αλλά στην περίπτωση αυτή, η πολυπλοκότητα και η κλίμακα της κατασκευής ενισχύουν πραγματικά τα φαινόμενα P-δ.

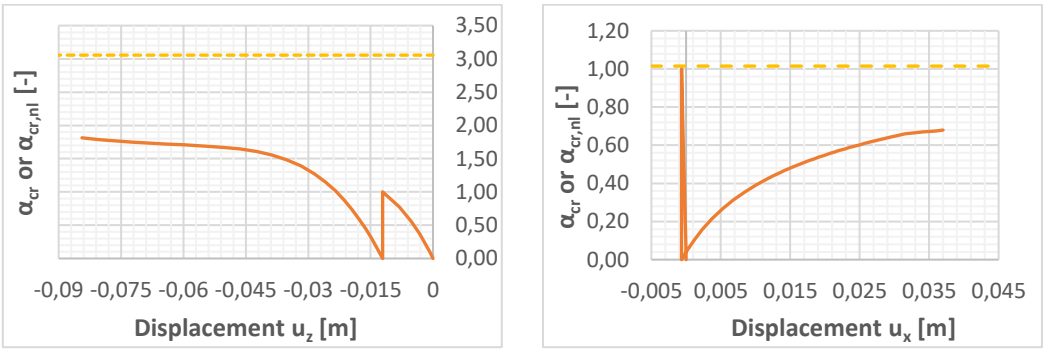

Σχήμα 30: Μετατόπιση συναρτήσει του συντελεστή φόρτισης για διαφορετικούς τύπους αναλύσεων - άνεμος κάθετος (αριστερά) και παράλληλος (δεξιά) με βραχίονες

Τέλος, εκτελέστηκε μια πλήρης μη γραμμική ανάλυση για να ελεγχθεί η εγκυρότητα του αρχικού σχεδιασμού αναφορικά με την αντοχή και την ευστάθεια του πύργου. Τα αποτελέσματα παρουσιάζονται στο Σχήμα 31.

Για τον συνδυασμό φόρτισης 1,35G+α_u1,35W_x, η αστοχία εμφανίζεται στην ίδια ράβδο όπως και στις προηγούμενες αναλύσεις, ενώ φαίνεται ότι ο αρχικός σχεδιασμός είναι ασφαλής. Επιπλέον, παρατηρείται ότι ο πύργος παραμένει στην ελαστική περιοχή για συντελεστές φόρτισης $\alpha_u \leq 1,0$, επιβεβαιώνοντας έτσι τις παραδοχές του αρχικού σχεδιασμού.

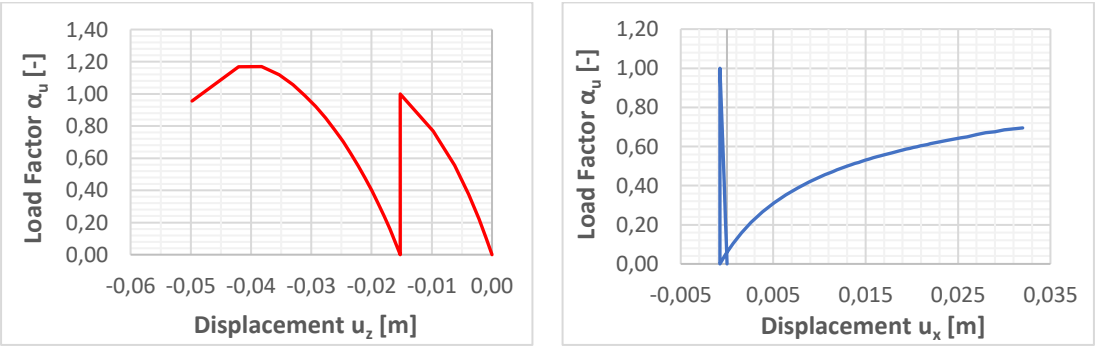

Σχήμα 31: Μετατόπιση σε σχέση με τον συντελεστή οριακού φορτίου – 1,35G+1,35W_x (αριστερά) και 1,35G+1,35Wy (δεξιά)

Σε αντίθεση με προηγουμένως, για τον συνδυασμό φόρτισης $1,35G+\alpha_u 1,35W_y$, ο αρχικός σχεδιασμός του πύργου από το λογισμικό TOWER θεωρείται ανεπαρκής και μη συντηρητικός. Αυτό μπορεί να εξηγηθεί από την ανάπτυξη μιας μορφής λυγισμού του πύργου, η οποία ονομάστηκε "αστάθεια τμήματος", η οποία δεν διασαφηνίζεται πλήρως από τα ισχύοντα ευρωπαϊκά πρότυπα, και συνεπώς δεν έχει ελεγχθεί κατά τον αρχικό σχεδιασμό.

Στο **κεφάλαιο 10** αναλύεται η νέα μορφή λυγισμού που εντοπίσθηκε από τις αριθμητικές αναλύσεις του κεφαλαίου 9. Ως "αστάθεια τμήματος" ορίζεται μια συνολική κατάσταση αστάθειας που συνδέεται με τον λυγισμό περισσότερων του ενός μελών που σχηματίζουν ένα τμήμα. Όπως φαίνεται στο Σχήμα 29 (δεξιά), στην παρούσα περίπτωση η αστάθεια σχετίζεται με τον λυγισμό των δύο διαγώνιων του ποδιού του πύργου. Πιο συγκεκριμένα, το πόδι αποτελείται από τρία κατακόρυφα μέλη: τον ορθοστάτη, ή κύριο ή "εξωτερικό" μέλος και τις δύο διαγώνιες που συνδέονται με έναν αριθμό οριζόντιων ράβδων πλήρωσης, σχηματίζοντας έτσι τριγωνικά επίπεδα. Κάθε μία από τις δύο διαγώνιες και τον ορθοστάτη που αποτελούν το τμήμα, είναι μεμονωμένα σταθερά και μπορούν να φέρουν τα μέγιστα φορτία για τα οποία έχουν αρχικά σχεδιαστεί. Ωστόσο, ο ταυτόχρονος λυγισμός των δυο διαγωνίων σε όλο το ύψος του ποδιού, που συνεπάγεται με την περιστροφή του ορθοστάτη, αντιπροσωπεύει μια νέα μορφή αστοχίας/λυγισμού, η οποία έχει διαπιστωθεί ότι είναι κρίσιμη σε αρκετές φορτιστηκές καταστάσεις.

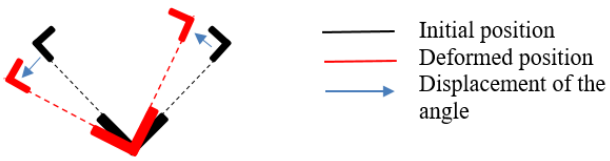

Σχήμα 32: Παραμόρφωση των μελών όπως προκύπτει από οριζόντια τομής στο πόδι

Το Σχήμα 32 φαίνεται μια οριζόντια τομή του ποδιού του ιστού που απεικονίζει πώς παραμορφώνονται τα διάφορα μέλη του κατά τον λυγισμό. Παρατηρείται ότι οι δυο διαγώνιοι κινούνται πλευρικά και κάμπτονται γύρω από έναν από τους γεωμετρικούς άξονες τους, ο ορθοστάτης περιστρέφεται γύρω από τον άξονά του, ενώ τα στοιχεία πλήρωσης δεν υφίστανται καμία παραμόρφωση, και απλώς μετατοπίζονται.

Στη συνέχεια προτείνονται και επικυρώνονται αριθμητικά δύο αναλυτικά μοντέλα (ένα απλουστευμένο και ένα βελτιωμένο), για την πρόβλεψη του κρίσιμου φορτίου της νέας μορφής λυγισμού. Τα προτεινόμενα μοντέλα σχεδιασμού είναι εύκολα στην εφαρμογή και καλύπτουν το κενό στις υφιστάμενες διατάξεις των ευρωπαϊκών κανονιστικών εγγράφων.

Στο **κεφάλαιο 11** παρουσιάζονται τα γενικά συμπεράσματα καθώς και οι προτάσεις της διατριβής για μελλοντική έρευνα. Οι επόμενες παράγραφοι (γενικά συμπεράσματα) αποτελούν ως επί το πλείστων, την μετάφραση του κεφαλαίου 11 στα ελληνικά.

Το παράρτημα Α (**κεφάλαιο 12**) περιλαμβάνει τυπολόγιο για τον υπολογισμό των γεωμετρικών ιδιοτήτων των ισοσκελών γωνιακών που δεν αναφέρονται στους εμπορικούς καταλόγους διατομών, όπως η ελαστική και η πλαστική ροπή αντίστασης ως προς τον ισχυρό και τον ασθενή κύριο άξονα, καθώς και οι σταθερές στρέψης και στρέβλωσης.

Στο παράρτημα Β (**κεφάλαιο 13**), το λογισμικό πεπερασμένων στοιχείων FINELG χρησιμοποιείται για να προβλέψει την αντοχή και τον τρόπο αστοχίας δοκιμών πλήρους κλίμακας που πραγματο-ποιήθηκαν σε δικτυωτούς πύργους στο Εθνικό Μετσόβιο Πολυτεχνείο, με σκοπό την επικύρωσή του.

Γενικά Συμπεράσματα:

Τα γωνιακά προφίλ, και πιο συγκεκριμένα τα ισοσκελή που εξετάζονται στην παρούσα διατριβή, έχουν ορισμένα χαρακτηριστικά που τα διαφοροποιούν από τα περισσότερα κοινά προφίλ διατομών. Είναι γνωστό ότι, για μια διπλά συμμετρική διατομή, το κρίσιμο φορτίο λυγισμού δεν επηρεάζεται από την εκκεντρότητα του φορτίου, ενώ οι ιδιομορφές του λυγισμού είναι πάντα αποσυζευγμένες μεταξύ τους, με κρίσιμη αυτή την καμπτική. Ωστόσο, αυτό δεν ισχύει και για τις γωνιακές διατομές, καθώς λυγίζουν ως επι το πλείστον κατά μήκος του ασθενούς άξονά τους είτε καμπτικά είτε στρεπτοκαμπτικό, ανάλογα πάντα με την εκκεντρότητα του επιβαλλόμενου φορτίου. Η πλήρης αποσύζευξη των ιδιομορφών λυγισμού συμβαίνει μόνο στην πολύ συγκεκριμένη περίπτωση όπου το μέλος φορτίζεται στο κέντρο διάτμησής του. Αυτή είναι επίσης η μόνη περίπτωση στην οποία μπορεί να εμφανιστεί ένας καθαρά στρεπτικός λυγισμός. Επιπλέον, το κρίσιμο φορτίο επηρεάζεται από τον τύπο της φόρτισης, ενώ δε, μπορεί να εμφανιστεί λυγισμός ακόμη και για ένα έκκεντρο εφελκυστικό φορτίο, ανάλογα με τη γεωμετρία της διατομής.

Αυτές οι ιδιαιτερότητες δείχνουν ότι οι υφιστάμενοι κανόνες σχεδιασμού που έχουν αναπτυχθεί κατά βάση για τις διπλά συμμετρικές διατομές, δεν μπορούν να καλύψουν με ασφάλεια τα γωνιακά, γεγονός που αναπόφευκτα οδηγεί στην ανάγκη ανάπτυξης ειδικών κανόνων σχεδιασμού για τις διατομές αυτές. Η ανάγκη αυτή ενισχύεται σημαντικά και από την έλλειψη ενιαίων και συνεπών κανόνων σχεδιασμού στα υφιστάμενα ευρωπαϊκά κανονιστικά πρότυπα. Διατάξεις και κανόνες σχεδιασμού για τις γωνιακές διατομές υπάρχουν σήμερα στα EN 1993-1-1, EN 1993-3-1, EN 1993-1-5 και EN 50341-1, όπως εξηγείται και στην εισαγωγή, αλλά αυτά τα πρότυπα είναι μερικές φορές αντιφατικά μεταξύ τους. Στο πλαίσιο της διατριβής, οι υπάρχουσες ευρωπαϊκές προδιαγραφές που διέπουν τον σχεδιασμό των ισοσκελών γωνιακών θερμής έλασης επανεξετάστηκαν και αναπτύχθηκε ένα ολοκληρωμένο και πλήρως επιστημονικά επικυρωμένο σύνολο κανόνων σχεδιασμού που καλύπτει όλες τις πτυχές του σχεδιασμού. Έτσι, τίθεται πλέον μια τάξη και μια οργανωμένη διαδικασία σχεδιασμού για τα γωνιακά, εν αντιθέσει με τις προσεγγίσεις των υφιστάμενων διατάξεων.

Αναπτύχθηκε και επικυρώθηκε μέσω εκτεταμένων αριθμητικών ερευνών και αναλυτικών μεθόδων μια πρόταση για την κατάταξη των ισοσκελών γωνιακών διατομών, η οποία συνάδει πλήρως με τα κανονιστικά έγγραφα του Ευρωκώδικα 3. Οι αριθμητικές έρευνες πραγματοποιήθηκαν με το μη γραμμικό λογισμικό ABAQUS, χρησιμοποιώντας στοιχεία όγκου, και βρίσκονται σε πολύ καλή συμφωνία με τις αναλυτικές διερευνήσεις. Οι γωνιακές διατομές έχουν ταξινομηθεί χωριστά για διάφορες φορτιστηκές καταστάσεις όπως θλίψη, κάμψη ισχυρού και ασθενούς άξονα, ενώ τα όρια κατάταξης από την κατηγορία 3 στην 4 έχουν καθοριστεί μέσω της πλαστιμότητας/διαρροής του θλιβόμενου πέλματος και όχι της στρεπτικής ιδιομορφής λυγισμού, όπως θεωρείται για τα άλλα κοινά προφίλ. Επιπλέον, έχουν αναπτυχθεί και επικυρωθεί αριθμητικά, κανόνες για τις αντιστάσεις σχεδιασμού των διατομών που περιλαμβάνουν όλες τις σημαντικές συνθήκες φόρτισης (θλίψη, κάμψη ασθενούς και ισχυρού άξονα). Οι κανόνες αυτοί επιτρέπουν την ομαλή μετάβαση της αντοχής σε κάμψη

μεταξύ των κατηγοριών 2 και 3 των διατομών, καταργώντας κάθε τεχνητή σταδιακή πρόβλεψη της αντίστασης των υφιστάμενων διατάξεων, όπως ήδη προτείνεται στον Ευρωκώδικα 3 για τις διπλά συμμετρικές διατομές. Είναι επίσης λιγότερο συντηρητικοί από τους ισχύοντες κανόνες σχεδιασμού που προτείνει ο ισχύων Ευρωκώδικας 3.

Επίσης, έχουν προταθεί και επικυρωθεί μέσω αριθμητικών ερευνών και πειραματικών δοκιμών, κανόνες σχεδιασμού για την πρόβλεψη της ευστάθειας και της αντοχής των μελών που κατασκευάζονται από προφίλ ίσων γωνιών θερμής έλασης, που υπόκεινται σε συνδυασμένες δυνάμεις και ροπές. Οι εκτεταμένες αριθμητικές παραμετρικές μελέτες πραγματοποιήθηκαν και πάλι με το λογισμικό ABAQUS χρησιμοποιώντας στοιχεία όγκου. Τα πειραματικά αποτελέσματα προέρχονται από δοκιμές που πραγματοποιήθηκαν στο πλαίσιο της παρούσας διατριβής σε μεγάλα γωνιακά προφίλ από χάλυβα υψηλής αντοχής, καθώς και από προηγούμενες πειραματικές έρευνες που βρέθηκαν στη βιβλιογραφία. Εντοπίστηκαν και προτάθηκαν κατάλληλες ευρωπαϊκές καμπύλες λυγισμού για τον καμπτικό και τον πλευρικό λυγισμό των γωνιακών. Από τα πειραματικά αποτελέσματα αποδείχθηκε ότι οι προτεινόμενες σχέσεις επιτρέπουν την ασφαλή πρόβλεψη της φέρουσας ικανότητας του μέλους και είναι λιγότερο συντηρητικές από τις υπάρχουσες διατάξεις του Ευρωκώδικα 3.

Επιπλέον, έχει πραγματοποιηθεί μέσω αριθμητικών μελετών, αξιολόγηση της τρέχουσας προσέγγισης σχεδιασμού που χρησιμοποιείται για τους δικτυωτούς πύργους μεταφοράς ενέργειας. Από τα αριθμητικά αποτελέσματα φαίνεται ότι το κρίσιμο φορτίο λυγισμού που προκύπτει από μια ελαστική ανάλυση $2^{ας}$ τάξης είναι μικρότερο από το αντίστοιχο που προκύπτει από μια γραμμική ελαστική ανάλυση λυγισμού. Ο λόγος είναι ότι τα εντατικά μεγέθη που ασκούνται στα μέλη και στις δύο περιπτώσεις διαφέρουν, επηρεάζοντας έτσι το φορτίο λυγισμού του μέλους στην περίπτωση των μη συμμετρικών διατομών. Κατά συνέπεια, οι τα φαινόμενα δευτέρας τάξεως πρέπει να λαμβάνονται υπόψη στην στατική ανάλυση, καθώς επηρεάζουν τη συνολική απόκριση του πύργου αλλά και την οριακή του κατάσταση αστοχίας. Επιπλέον, εντοπίστηκε ένας τρόπος αστάθειας για δικτυωτούς πύργους που δεν καλύπτεται πλήρως από τους ισχύοντες κανονισμούς. Προτάθηκαν και επικυρώθηκαν αριθμητικά δύο αναλυτικά μοντέλα (ένα απλουστευμένο και ένα βελτιωμένο), για την πρόβλεψη του κρίσιμου φορτίου της νέας μορφής λυγισμού. Και τα δύο προτεινόμενα μοντέλα σχεδιασμού είναι εύκολα στην εφαρμογή, υποδεικνύουν σαφώς τον απαιτούμενο έλεγχο που πρέπει να γίνει και καλύπτουν το κενό στις υφιστάμενες διατάξεις των ευρωπαϊκών κανονιστικών προτύπων.

Όλοι οι προτεινόμενοι κανόνες και μέθοδοι σχεδιασμού είναι απλοί στην εφαρμογή και έχουν συνταχθεί στη μορφή του Ευρωκώδικα 3. Παρόλο που έχουν επικυρωθεί μόνο για ισοσκελή γωνιακά που χρησιμοποιούνται κυρίως σε πυλώνες, μπορούν να γενικευθούν και να εφαρμοσθούν και σε άλλου τύπου κατασκευές. Ωστόσο, μια πρόταση για μελλοντική έρευνα είναι να διεξαχθούν περαιτέρω αναλύσεις για να διαπιστωθεί εάν οι προτεινόμενοι κανόνες μπορούν να εφαρμοστούν και για ανισοσκελείς γωνιακές διατομές. Επιπλέον, όλοι οι κανόνες σχεδιασμού έχουν αναπτυχθεί για αρθρωτά γωνιακά μέλη. Επομένως, απαιτούνται ακόμη έρευνες για να ληφθεί καλύτερα υπόψη η ευεργετική δράση των κοχλιωτών συνδέσεων στα άκρα των μελών, η οποία επί του παρόντος καλύπτεται από τις διατάξεις του EN 1993-3.

Τέλος, ο τρόπος αστάθειας του τμήματος που ανιχνεύεται εδώ χρειάζεται περαιτέρω διερεύνηση. Πρώτον, η επιλογή της καμπύλης λυγισμού θα μπορούσε να βελτιωθεί, καθώς τώρα προτείνεται η χρήση της χαμηλότερης καμπύλης λόγω έλλειψης μελετών που να αποδεικνύουν ότι μπορεί να χρησιμοποιηθεί με ασφάλεια μια υψηλότερη. Επιπλέον, ο τρόπος

αυτός συνδέθηκε με μια συγκεκριμένη γεωμετρία πύργου και έχει παρατηρηθεί στο πόδι. Κατά συνέπεια, το ερώτημα είναι να ελεγχθεί εάν μια αστάθεια τμήματος θα μπορούσε να εμφανιστεί και σε άλλα μέρη του πύργου (για παράδειγμα στους βραχίονες) και πώς αυτό θα μπορούσε να επηρεαστεί από την μορφολογία του πύργου.

This project would not have been possible without the support of many people.

First, I am extremely grateful to my supervisors, Prof. Jean-Pierre Jaspart and Prof. Ioannis Vayas and my co-supervisor Prof. Jean-François Demonceau for their invaluable advice, continuous support, and patience during my PhD study. Their immense knowledge and plentiful experience have encouraged me in all the time of my academic research.

I would like to thank again Prof. Jean-Pierre Jaspart and Prof. Jean-François Demonceau, as well as Mrs. Laurence Defrere and my colleagues who make my stay in Liege happy, easy, and pleasant.

I would like to thank all the members in the "Laboratoire de Mécanique des Matériaux et Structures" of Liège University and especially Nicola Labeye for his technical support, help and the excellent cooperation during the experimental campaign.

Finally, the thesis is dedicated to my parents and my girlfriend for their unconditional, unequivocal, and loving support. Without their tremendous understanding and encouragement in the past few years, it would be impossible for me to complete my study.

This study was carried under the financial assistance of the European Research project entitled ANGELHY "Innovative solutions for design and strengthening of telecommunications and transmission lattice towers using large angles from high strength steel and hybrid techniques of angles with FRP strips", with a financial grant from the Research Fund for Coal and Steel (RFCS) of the European Community.

TABLE OF CONTENTS

1. INTRODUCTION

Lattice towers are extensively built in Europe and worldwide to serve telecommunication or power transmission purposes. Such towers are often installed in mountainous terrains with very limited access to heavy vehicles. Consequently, a lattice tower structural system, which may be transported and erected by light machinery and equipment, is almost the only possible solution. The in situ modular construction of the tower is simplified using bolted connections and gusset plates. On the other hand, lattice towers need more ground space compared to cylindrical, octagonal or similar shell-type systems. However, ground space is plentifully available in remote places outside the densely populated regions for most of the European countries. Therefore, lattice towers are rendered as the main structural system for telecommunication and power transmission. The main typologies of the transmission towers are reported in chapter 8.

The members of such towers are frequently composed of equal leg angle sections; their easy production and transportation, together with an excellent connectivity discern them from other profiles. They are available as hot-rolled or cold-formed profiles, as equal or unequal sections depending on the relative length of their legs, in steel grades up to S460, in sizes ranging from small to large, 20 to 300 mm. They are employed either as single or as built-up sections in a back-to-back or star battened configuration. The preferred bolted connection of one leg to gusset plates leads to a most advantageous application as truss or diaphragm members in buildings, bridges or any other structural application and, as already said, steel towers and masts. Appropriate long life corrosion protection is additionally ensured since all angle sizes are fully amenable to hot dip galvanizing in contrast to several other types of open or closed sections.

However, angles, and especially equal angle profiles considered here, exhibit some properties that clearly distinguish them from other common steel profiles: (i) they are open profiles with very small section constants in both torsion and warping, (ii) they are monosymmetrical sections, (iii) their bending capacity and radius of gyration around the weak axis are substantially lower than around strong axis, (iv) their legs are prone to local buckling as external plate elements, (v) their plastic resistances are substantially higher than their elastic ones and (vi) due to the eccentric connection in one leg, they are subjected to some bending in addition to axial force when used as single members. The particularities of the angle sections in comparison with the doubly symmetric well-known ones in terms of elastic instability are presented in chapter 3.

These features explain that existing design rules for other types of sections, mostly doubly symmetric ones, cannot safely cover angles, what inevitably leads to the need for the development of specific design provisions for angle sections. Facing the lack of unified consistent rules for angles, European specifications have adopted a case-by-case approach, embedding individual rules and recommendations in various parts of Eurocode 3. More specifically, EN 1993-1-1 [1] provides rules for cross-section classification (classes 1 to 4) and general design recommendations for the verification of the stability in compression. EN 1993-3-1 [2] presents specific rules for the buckling resistance of angle members used in towers, when connected eccentrically with bolts in one leg. EN 1993-1-8 [3] contains rules for resistance to tension for the above-mentioned connection configuration, while EN 1993-1-5 [4] gives rules for buckling resistance of class-4 angle sections prone to local buckling. Another European specification, the CENELEC standard EN 50341-1 [5] provides specific rules for lattice towers used in the field of overhead electrical lines, addressing specific problems linked to such applications; but it also provides specific rules for the verification

of the lattice tower and its constituting parts. But for some aspects, the EN 50341-1 design methods for angle sections may diverge from the rules provided in the Eurocodes. Moreover, EN 50341-1 allows design of lattice towers by full scale testing. However, it draws design conclusions from a single test comparing the ultimate load achieved in the test with the corresponding one from calculations, neglecting the fact that the results of an individual test are influenced by potential material overstrength, strain hardening or other parameters, the values of which are associated with statistical uncertainties Consequently, it does not touch reliability issues as it is done in the structural Eurocodes, in accordance with EN 1990 [6]. In contrast to the European Codes, American Codes have written down in a single document, AISC 2000 [7], all rules concerning angle design.

Extensive numerical and experimental research has been carried out to study the behaviour of angle sections. It covers hot-rolled and cold-formed profiles, equal and unequal sections, beams or columns subjected to various types of loading, as well as different connection conditions. Vayas et al. [8] give the inelastic capacity of angle sections to combined axial forces and biaxial bending. Trahair [9] examines angle section beams to uniform eccentric transverse loading and gives the section capacity to combined shear, bending and torsion. Schillo et al. [10] examine the buckling resistance rules of rolled angles to European standards discussed before, compare them to test results and numerical investigations considering various types of initial imperfections. Kettler et al. [11] highlight the importance of the end support conditions in their numerical study of rolled angles loaded in compression through bolted connections in one leg and comparisons with experimental results and provisions of European standards. Hussain et al. [12] provide an interaction equation in the plastic range for the stability design of angles subjected to compression and biaxial bending. Compression tests on large angle sections ranging from L125x125x8 to L200x200x14 in high strength steel S420 were conducted in Tsinghua University at Beijing [13]. The tests were carried out on axially loaded pin-ended columns in order to define global-local buckling interactions since cross-sections were class-4 ones. Tests on L70x70x7 profiles were performed at NTUA in Athens [14], where the effects of eccentric loading were studied. Compression tests on L80x80x8 and L120x120x12 profiles were carried out at TU Graz [11] in which the boundary conditions were varying from clamped supports to supports allowing in-plane or in- and out-of-plane rotation. Tests series on L50x50x5 profiles were carried out at the Technical University of Braunschweig [15] with various specimen lengths and end support conditions, while the load was introduced eccentrically through one bolt M12 in one leg.

In the perspective of the thesis and in order to extend the knowledge for the stability behaviour of steel columns from high strength steel (S460M) angle cross-sections subjected to compression and bending, twelve buckling tests on such columns have been performed at Liège University and presented in chapter 6. Furthermore, existing European specifications on rolled equal angle sections were reviewed, extensive experimental, analytical and numerical studies have been conducted and a complete set of design rules covering all aspects of design has been developed and duly validated. They include cross section classification (chapter 4), cross section design for all ranges of response, plastic, elastic-plastic or elastic including local buckling (chapter 5), as well as corresponding rules for member design to individual and combined internal forces and moments (chapter 7). Details for the geometrical properties of angles are given in chapter 12 (Annex A), while the notations and symbols that are used in the whole document, are summarized in chapter 2.

Concerning the structural analysis, in the above-mentioned normative documents, the tower is modelled as a simple truss structure where all the steel element connections are considered as hinged. Such models do not adequately reflect the actual structural behaviour of the tower, as loads and

especially wind ones are directly imposed on the entire member length and introduce bending moments in members. Furthermore, the design of lattice towers is usually carried out through a first order linear elastic analysis, neglecting the significant second order effects developing in these structures. It is therefore inconsistent, and sometimes not safe, to perform member design by neglecting moments due to both local and overall loading, as well as the second order effects, as it is usually done in practice. A critical assessment of the current design approach is performed in chapter 9, where the tower is simulated with the full non-linear finite element software named FINELG using beam elements, considering relevant imperfections as well as geometrical and material non-linearities. In these simulations, every single member has been properly modelled, in terms of orientation and eccentricities at its extremities. The importance of considering the second order effects in the analysis is underlined. The selected software has been firstly validated through comparisons to full-scale tests available in the literature, as presented in chapter 13 (Annex B).

A lot of research has been performed through years on the modelling and the design of lattice towers. Albermani et al. [16] have studied the structural behaviour of the transmission towers through full non-linear analysis and compared them with full scale tests. The influence of the selected element (truss or beam) in the final response of the tower have been reported also by Silva et al. [17]. Jiang et al. [18] investigated the modelling of the bolted connections and validate their response through available tests from the literature, while Kitiponchai et al. [19] examined the effect of bolt slippage on the ultimate behaviour of lattice structures. Finally, a collection and critical review of full-scale tests on lattice towers as well as practical advice for conducting future tests are reported in Ref. [20]. However, the existence of an instability mode not properly covered by the European normative documents is highlighted in the framework of the thesis. Therefore, two analytical models for the prediction of the critical load of the new buckling mode are proposed in chapter 10, followed by their numerical validation through FEM simulations. Comparisons with the existing normative predictions are presented too.

Finally, chapter 11 presents the general conclusions as well as the perspectives of the thesis for future research.

2. NOTATIONS, SYMBOLS AND ABBREVIATIONS

The notations, symbols and abbreviations that used hereafter in this document are defined below; they mainly follow those given in EN 1993-1-1. Figure 2.1 illustrates these notations for the geometrical properties, the geometrical axes as well as the principal axes.

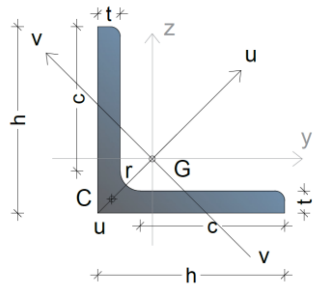

Figure 2.1: Notations for geometrical properties and axes

2.1 Conventions for member axes

For angle sections, the axes are defined as follows:

- x-x – axis along the member
- y-y – geometric axis of the cross-section parallel to the leg
- z-z – geometric axis of the cross-section parallel to the leg
- u-u – major/strong principal axis (associated to weak axis displacement)
- v-v – minor/weak principal axis (associated to strong axis displacement)

2.2 Symbols

2.2.1 Latin upper-case symbols

A	cross-sectional area
A_{eff}	effective area of a cross-section
A_G	normal area of a cable of a lattice tower
A_{ref}	reference area normal to the face of a bar/beam
C	shear centre of the cross-section
C_T	torsion constant
C_u, C_v	equivalent uniform moment factors
C_w	warping constant
E	Young's modulus of elasticity
$F_c(z)$	mean wind load in wind's direction on a cable of a lattice tower at height z
$F_{m,W}(z)$	mean wind load in wind's direction on a segment of a lattice tower at height z
G	centre of gravity of the cross-section and shear modulus
I_u, I_v	moment of inertia about u-u axis and v-v axis, respectively
$I_v(z)$	turbulence intensity at height z

I_y, I_z	moment of inertia about y-y geometrical axis and z-z geometrical axis, respectively
L	length of the member
L_{crit}	buckling length of the member
M_{cr}	elastic critical bending moment based on the gross cross-sectional properties
$M_{el,u}$, $M_{el,v}$	elastic resistance to bending of the gross cross-section about u-u and v-v axis, respectively
$M_{pl,u}$, $M_{pl,v}$	plastic resistance to bending of the gross cross-section about u-u and v-v axis, respectively
M_T	tortional moment
$M_{u,Ed}$, $M_{v,Ed}$	is the bending moment about u-u and v-v axis respectively
$M_{ult,u}$, $M_{ult,v}$	ultimate test resistance to bending of the cross-section about u-u and v-v axis, respectively
$M_{u,Rd}$, $M_{v,Rd}$	design value of the resistance to bending moment about u-u and v-v axis respectively
$M_{u,Rk}$, $M_{v,Rk}$	characteristic value of the resistance to bending moment about u-u and v-v axis respectively
$N_{bu,Rd}$	design value of the buckling resistance of a member in compression about u-u axis
$N_{bv,Rd}$	design value of the buckling resistance of a member in compression about v-v axis
N_{cr}	elastic critical axial force for the relevant buckling mode based on the gross cross-sectional properties
$N_{cr,FT}$	elastic critical axial force for flexural-torsional buckling
$N_{c,Rd}$	design value of the resistance to uniform compression axial force of the cross-section
$N_{c,Rk}$	characteristic value of the resistance to compression axial force
$N_{cr,T}$	elastic critical axial force for torsional buckling
$N_{cr,u}$, $N_{cr,v}$	elastic critical axial force for flexural buckling about u-u axis and v-v axis, respectively, based on the gross cross-section properties
N_{Ed}	is the axial force
$N_{t,Rd}$	design value of the resistance to uniform tension axial force of the cross-section
$N_{t,Rk}$	characteristic value of the resistance to tension axial force
N_{pl}	design value of the plastic resistance to axial force of the gross cross-section
N_{ult}	ultimate test resistance to axial force of the cross-section
$V_{c,i}$	self-weight of the i conductor or cable of a lattice tower
$W_{eff,u}$, $W_{eff,v}$	elastic section modulus of the effective area of a cross-section for bending about u-u and v-v axis, respectively
$W_{el,u}$, $W_{el,v}$	elastic section modulus for bending about u-u axis and v-v axis, respectively
$W_{pl,u}$, $W_{pl,v}$	plastic section modulus for bending about u-u axis and v-v axis, respectively

2.2.2 Latin lower-case symbols

$\bar{b}$	appropriate width, that is equal to h for angle sections according to EN 1993-1-5
c	outstand flange width (c=h-t-r)
c_f, $c_{f,G}$	wind force coefficient
d	diameter of a cable, index for diagonal
f_y	yield strength
h	width of the cross-section
i_v	radius of gyration about v axis
k_σ	plate buckling coefficient
m_l	mass per unit length
$q_p(z)$	peak wind pressure at the effective height z;
r	radius of root fillet
t	thickness of the cross-section
v_m	mean wind velocity

2.2.3 Greek upper-case symbols

Δ	displacement
Φ	value to determine the reduction factor χ for flexural buckling
Φ_{LT}	value to determine the reduction factor χ_{LT} for lateral torsional buckling

2.2.4 Greek lower-case symbols

α	imperfection factor
α_{cr}	critical load factor/amplifier
α_{LT}	imperfection factor for lateral torsional buckling
γ_{M0}	partial factor for resistance of cross-sections that equals 1,0 as recommended by EN 1993-1-1
γ_{M1}	partial factor for resistance of members to instability assessed by member checks
ε	material parameter depending on f_y
$\bar{\lambda}$	relative slenderness for flexural buckling
λ_{LT}	relative slenderness for lateral torsional buckling
$\overline{\lambda_{op}}$	relative slenderness for out-of-plane buckling
$\overline{\lambda_p}$	relative plate slenderness for plate buckling
ξ	interaction factor depends on the cross-section class
ρ, ρ_u, ρ_v	reduction factors for plate buckling

ρ_{air}	air density equal to 1,25 Kg/m^3
σ_1, σ_2	end stresses in a member
σ_{cr}	elastic critical plate buckling stress
χ_{LT}	reduction factor for lateral torsional buckling
χ_u	reduction factor due to flexural buckling about u-u axis
χ_v	reduction factor due to flexural buckling about v-v axis
ψ	ratio of end moments in a segment of beam, stress ratio, angle

Symbols that are used only in a specific case or example, are not defined in this chapter but they will be defined individually where it is necessary hereafter.

3. ELASTIC INSTABILITY OF SINGLE ANGLE MEMBERS

Equal leg angles exhibit some properties that distinguish them from other common steel profiles. They are open profiles with very small constants in both torsion and warping, are monosymmetric sections, their legs are prone to local buckling as external elements and finally, due to the eccentric connection in one leg, they are also subjected to bending when used as single members. In contrast with the well-known doubly symmetric cross-sections, the critical loads of angle profile members are affected by the position and the type of the loading and the buckling modes are not fully decoupled, as explained below, in the most of the loading cases.

The analytical derivation of the critical load of an axially – centric or eccentric – loaded member, based on Euler's buckling theory, is presented in this chapter. The torsional effects and the corresponding buckling mode, which consists a specific case for angle profiles, are investigated, and the possibility of an instability due to a tensile load is reported. Furthermore, the influence of the loading type, the boundary conditions and the initial imperfections to the critical load are also addressed. Then, the analytical evaluations of the critical loads of a column are validated by numerical simulations performed with the finite element software named FINELG through elastic instability and 2nd order linear elastic analyses. This chapter consists a summary of the existing knowledge aims to highlight the specificities of angle profiles, before going further in new developments and analyse the classification, the cross-section resistance as well as the stability of members made of angle profiles.

3.1 Analytical derivation of the critical load of a column by Euler's theory

The analytical derivation of the critical load of a single angle pin-end column that is loaded by a compression load *P*, can be found in literature [21]-[22] and is presented below. The axial load is applied with an eccentricity at both axes (u_P, v_P). The cross-section is placed in such a way that its local axes (*u, v*) coincide with the global ones (U, V) of the 3D Cartesian system and the static system is schematized in Figure 3.1. The boundary conditions are:

- At node 1: $x_1 = u_1 = v_1 = \theta_1 = 0$;
- At node 2: $u_2 = v_2 = \theta_2 = 0$;
- The warping restraint is free for both nodes.

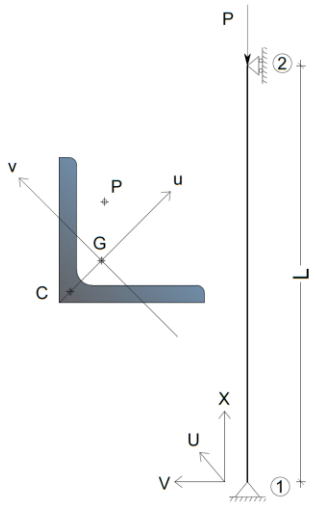

Figure 3.1: Static system (right) and horizontal cut at the mid-height (left) for the analytical derivation of the critical load

The internal axial force resulting from a first order linear elastic analysis is:

$$N_{Ed} = -P \quad \text{(Eq. 3.1)}$$

According to the elastic buckling theory of Euler, the three equations of equilibrium for an equal leg angle column, where (u_c, u_p, $v_p \neq 0$ *and* $v_c = 0$), are the following:

$$EI_v \frac{d^4u(x)}{dx^4} + P\frac{d^2u(x)}{dx^2} - P(u_C - u_P)\frac{d^2\theta(x)}{dx^2} = 0 \quad \text{(Eq. 3.2)}$$

$$EI_u \frac{d^4v(x)}{dx^4} + P\frac{d^2v(x)}{dx^2} - Pv_P\frac{d^2\theta(x)}{dx^2} = 0 \quad \text{(Eq. 3.3)}$$

$$GC_T\frac{d^2\theta(x)}{dx^2} - EC_w\frac{d^4\theta(x)}{dx^4} - P\left[\frac{I_u+I_v}{A} + u_C^2\right]\frac{d^2\theta(x)}{dx^2} - Pu_P\left(\frac{I_{ur2}}{I_v} - 2u_C\right)\frac{d^2\theta(x)}{dx^2} - P(u_P - u_C)\frac{d^2u(x)}{dx^2} + Pv_P\frac{d^2v(x)}{dx^2} = 0 \quad \text{(Eq. 3.4)}$$

where:

$$I_{ur2} = \int_A u(u^2+v^2)dA \approx \frac{\sqrt{2}}{2}(h-0{,}5t)\left(\frac{(h-0{,}5t)^3t}{12} - \frac{(h-0{,}5t)t^3}{12}\right) \quad \text{(Eq. 3.5)}$$

3.1.1 Column loaded at the shear centre

It can be seen that the full decoupling between flexural and torsional buckling modes can occur only in the case where the axial load is applied to the shear centre ($u_C = u_P$; $v_P = 0$); then the three equations of equilibrium become:

$$EI_v \frac{d^4u(x)}{dx^4} + P\frac{d^2u(x)}{dx^2} = 0 \quad \text{(Eq. 3.6)}$$

$$EI_u \frac{d^4v(x)}{dx^4} + P\frac{d^2v(x)}{dx^2} = 0 \quad \text{(Eq. 3.7)}$$

$$GC_T\frac{d^2\theta(x)}{dx^2} - EC_w\frac{d^4\theta(x)}{dx^4} - P\left[\frac{I_u+I_v}{A} + u_C^2\right]\frac{d^2\theta(x)}{dx^2} - Pu_P\left(\frac{I_{ur2}}{I_v} - 2u_C\right)\frac{d^2\theta(x)}{dx^2} = 0 \quad \text{(Eq. 3.8)}$$

It is assumed that the column buckles with a half-sine deformation shape. This being, the following deformations are adopted:

$$u(x) = A_1\sin\left(\frac{\pi x}{L}\right) \;;\; v(x) = A_2\sin\left(\frac{\pi x}{L}\right) \;;\; \theta(x) = A_3\sin\left(\frac{\pi x}{L}\right) \quad \text{(Eq. 3.9)}$$

By solving the above system, one founds that the constants A_1, A_2 and A_3 are not zero for the critical loads:

$$P = N_{cr,u} = \frac{\pi^2 EI_v}{L^2} \quad \text{(Eq. 3.10)}$$

$$P = N_{cr,v} = \frac{\pi^2 EI_u}{L^2} \quad \text{(Eq. 3.11)}$$

$$P = N_{cr,T} = \frac{1}{A_{rc}}\left(GC_T + \frac{\pi^2 EC_w}{L^2}\right) \quad \text{(Eq. 3.12)}$$

where,

$$A_{rc} = \frac{I_u+I_v}{A} + u_C^2 + u_C\left(\frac{I_{ur2}}{I_v} - 2u_C\right) \quad \text{(Eq. 3.13)}$$

The first two loads indicate a flexural buckling along U and V axis respectively while the third one indicates a pure torsional buckling mode. Obviously, the critical load of the column is the smallest one among these loads.

3.1.2 Column loaded with a random eccentricity

In the general case where the load is applied with an eccentricity at both axes (u_P, v_P), but not at the shear centre, the three equations of equilibrium transform into the following ones, by using eq. (3.9):

$$A_1\left(\frac{\pi^2 EI_v}{L^2} - P\right) + A_3 P v_P = 0 \quad \text{(Eq. 3.14)}$$

$$A_2\left(\frac{\pi^2 EI_u}{L^2} - P\right) - A_3 P(u_C - u_P) = 0 \quad \text{(Eq. 3.15)}$$

$$A_1 P v_P + A_2 P(u_C - u_P) + A_3\left(\frac{\pi^2 EC_w}{L^2} + GC_T - PA_{rp}\right) = 0 \quad \text{(Eq. 3.16)}$$

where

$$A_{rp} = \frac{I_u + I_v}{A} + u_C^2 + u_P\left(\frac{I_{ur2}}{I_v} - 2u_C\right) \quad \text{(Eq. 3.17)}$$

The column will buckle for the minimum load P that satisfies eq. (3.14) – (3.16) when the constants A_1, A_2 and A_3 are not zero; this can be written in a matrix format as:

$$\begin{bmatrix} N_{cr,u} - P & 0 & Pv_P \\ 0 & N_{cr,v} - P & P(u_C - u_P) \\ Pv_P & P(u_C - u_P) & A_{rp}(N_{cr,T} - P) \end{bmatrix} = 0 \quad \text{(Eq. 3.18)}$$

Therefore, the critical load can be found by solving eq. (3.19).

$$A_{rp}(N_{cr,u} - P)(N_{cr,v} - P)(N_{cr,T} - P) - P^2(N_{cr,v} - P)v_P^2 - P^2(N_{cr,u} - P)(u_C - u_P)^2 = 0 \quad \text{(Eq. 3.19)}$$

It should be noted that the value of $N_{cr,T}$ should be calculated according to the eccentricity of the applied load by using eq. (3.12) and replacing A_{rc} with A_{rp}.

To simplify the solution of eq. (3.19), two fundamental cases may be distinguished in terms of the position of the applied load:

1. the load is applied on the axis of symmetry (u_c, $u_p \neq 0$, $v_p = 0$);
2. the load is not applied on the axis of symmetry (u_c, u_p, $v_p \neq 0$);

To find the roots of eq. (3.19) is equivalent to the determination of the intersection points between the abscissa P and the curves $f_i(P)$; this writes as follows for case 1 and case 2, respectively:

$$f_1(P) = (N_{cr,u} - P)\left[\mathrm{A_{rp}}(N_{cr,v} - P)(N_{cr,T} - P) - P^2(u_C - u_P)^2\right] \quad \text{(Eq. 3.20)}$$

$$f_2(P) = A_{rp}(N_{cr,u} - P)(N_{cr,v} - P)(N_{cr,T} - P) - P^2(N_{cr,v} - P)v_P^2 - P^2(N_{cr,u} - P)(u_C - u_P)^2 = 0 \quad \text{(Eq. 3.21)}$$

For the values such that $A_{rp} - (u_C - U_P)^2 \geq 0$, the form of the curve $f_i(P)$ and therefore the position of its roots, can be estimated by calculating the sign of the curve for the values 0, $N_{cr,u}$, $N_{cr,v}$, $N_{cr,T}$ and ∞. The roots of the curve can be noted as $P_1 = N_{cr,1}$, $P_2 = N_{cr,2}$ and $P_3 = N_{cr,3}$ where $N_{cr,1} \leq N_{cr,2} \leq N_{cr,3}$. By the acceptance that $N_{cr,u} \leq N_{cr,v}$, the two fundamental cases considered above can be additionally divided into three sub-groups:

d) $N_{cr,u} \leq N_{cr,v} \leq N_{cr,T}$
e) $N_{cr,T} \leq N_{cr,u} \leq N_{cr,v}$
f) $N_{cr,u} \leq N_{cr,T} \leq N_{cr,v}$

Figure 3.2, Figure 3.3 and Figure 3.4 illustrate the curves $f_i(P)$ and their roots – as they are also reported in Ref. [22] – for the two fundamental cases for all the different sub-groups mentioned above. It should be noted that these figures are all illustrative and do not present explicit results of a calculation. It can be seen that the critical load $P_1 = N_{cr,1}$, is:

- the flexural buckling load $P_{cr,u}$ for the case 1, subgroups a and c;

- the flexural-torsional buckling load in all the other cases with a value lower than $P_{cr,u}$ and $P_{cr,T}$.

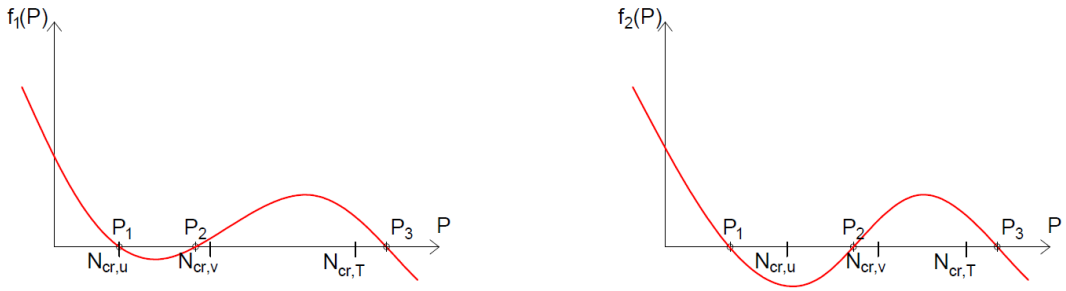

Figure 3.2: Schematized form of the curves $f_i(P)$ when $N_{cr,u} \leq N_{cr,v} \leq N_{cr,T}$

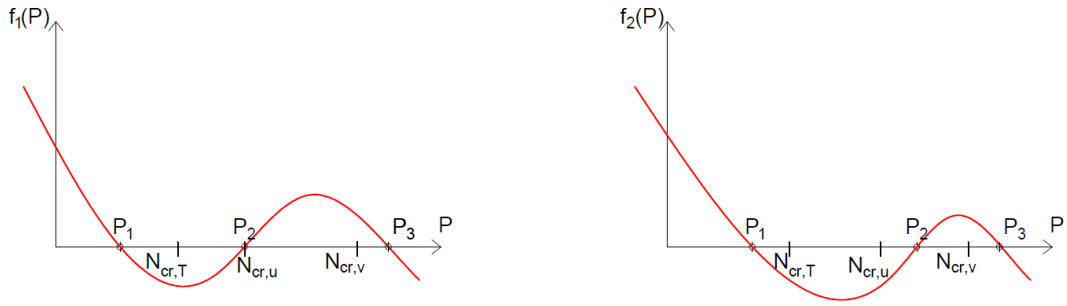

Figure 3.3: Schematized form of the curves $f_i(P)$ when $N_{cr,T} \leq N_{cr,u} \leq N_{cr,v}$

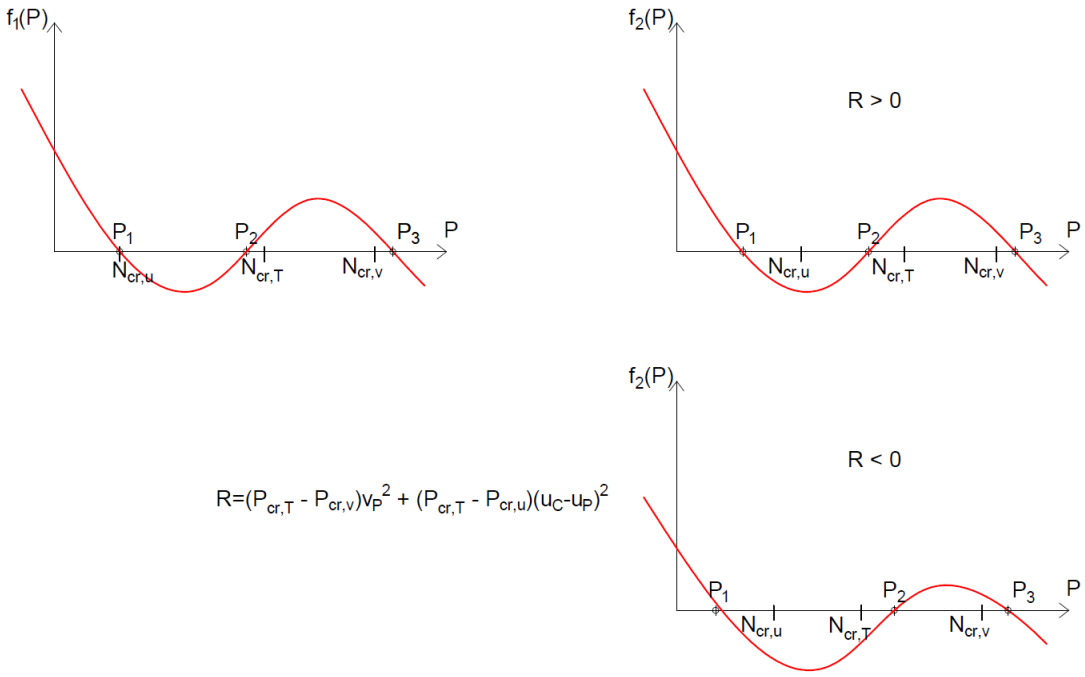

Figure 3.4: Schematised form of the curves $f_i(P)$ when $N_{cr,u} \leq N_{cr,T} \leq N_{cr,v}$

3.1.3 Summary

There are three ways in which an angle member can buckle, if local plate buckling does not occur: flexural buckling, torsional buckling, and flexural-torsional buckling.

Flexural buckling (FB) can occur in any compression member that experiences a deflection caused by bending without any torsion or the cross section along the member. Flexural buckling occurs about the axis with the largest slenderness ratio and the smallest radius of gyration. Therefore, it can occur in direction of u or v axis as it shown if the Figure 3.5(a)-(b), but for pin-ended members it happens along weak axis u, as it has been also shown through the analytical calculation.

Torsional buckling (TB), that it is caused by a rotation about the longitudinal axis (see Figure 3.5(c)), occurs almost never in hot rolled angle cross-sections, except the case where the section is loaded at the shear centre (see §3.3 for more details). In all the other cases, a flexural-torsional buckling occurs.

Flexural-torsional buckling (FTB) is the simultaneous bending and twisting of a member (see Figure 3.5(d)) and it is a very common buckling mode for angle sections. If this type of buckling occurs, two possible buckling modes can appear: one in which the flexural deflection is predominated, accompanied by a small torsion of the cross-section and another one in which the torsion is predominant is accompanied by a small deflection, depending on the member length.

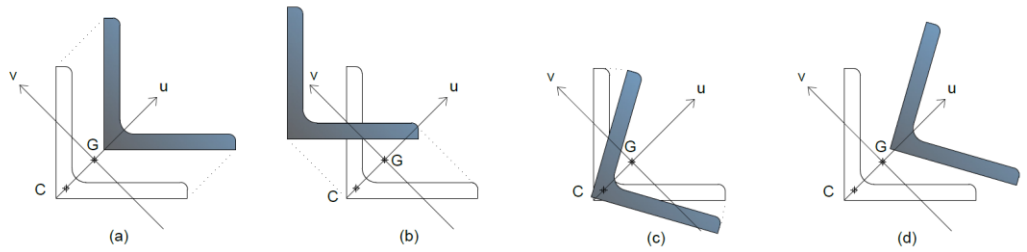

Figure 3.5: (a),(b) Deflections due to flexural buckling along u,v axis, (c) deflections due to torsional buckling, (d) deflections due to flexural-torsional buckling

3.2 Higher buckling modes

In the case where the critical load of a higher buckling mode needs to be calculated, eq. (3.20) or (3.21) may be accordingly used, where the following parameters are applied:

$$N_{cr,u,n} = n^2 \frac{\pi^2 E I_v}{L^2} \quad \text{(Eq. 3.22)}$$

$$N_{cr,v,n} = n^2 \frac{\pi^2 E I_u}{L^2} \quad \text{(Eq. 3.23)}$$

$$N_{cr,T,n} = \frac{1}{A_{rp}} \left(G C_T + n^2 \frac{\pi^2 E C_w}{L^2} \right) \quad \text{(Eq. 3.24)}$$

where n=2,3,4,...,n, for the second, third, fourth, .. n^{th} buckling mode.

It should be also noticed that as the shear centre is located at the intersection of the two legs, there is practically no warping rigidity and the warping constant C_w can be assumed to be zero. Therefore, it may be assumed that the torsional buckling mode is not affected by the member length.

3.3 Instability due to tensile load

Depending on the cross-section geometry and the load eccentricity, instability may be occurred even for a tensile load, as reported in [22]. Indeed, Vlassov [23] shows that a cross-section can be unstable

under a tensile force, if this one is applied outside of a circle defined by the coordinates of its centre (u_s, v_s) and by its radius R (see Figure 3.6), that for an equal leg angle profile are:

$$(u_S, v_S) = \left(\frac{I_{ur2}}{2I_v}, 0\right) \quad \text{(Eq. 3.25)}$$

$$R = \sqrt{\frac{I_u + I_v}{A} + u_S^2} \quad \text{(Eq. 3.26)}$$

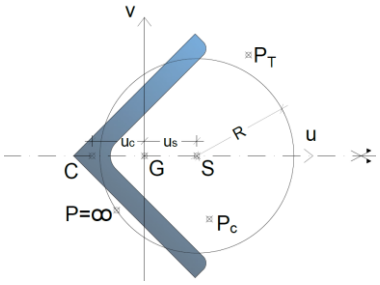

Figure 3.6: Schematized illustration of the circle according to Vlassov

Obviously if the load is applied inside the circle defined above, then it should be a compression one to cause instability. For the specific case where the load is applied at the boundary of the circle, independently if it is a compression or a tensile one, the critical load become significantly high (≈∞).

Therefore, a pure torsional mode can be obtained when the load is applied at the shear centre C as it has been shown in §3.1, but depending on the cross-section geometry, this load could be either a compression or a tensile one. The flexural-torsional buckling mode where the torsion is predominated (usually $N_{cr,3}$) is accordingly affected. In the latter mode, the critical load should be calculated for a compression load P_c that is applied inside the above-mentioned circle or a tension one P_T that is outside of the circle. If the load is applied at the boundary, then the critical load become significantly high.

3.4 Influence of the boundary conditions

Equation given in §3.1 have been developed and therefore can be applied only for pin-ended columns. Inevitably, some end restraints are usually present when an angle member is connected to other members in a structure. As the connection is often achieved on one leg only, the modelling of the end-restraint effect become complicated. A few analytical solutions are available as those proposed by Trahair et al. [24]. An acceptable design solution is to use effective-length factors K_i, (see Figure 3.7) so that eq. (3.20) or (3.21) may be applied by using the following parameters:

$$N_{cr,u} = \frac{\pi^2 E I_v}{(K_u L)^2} \quad \text{(Eq. 3.27)}$$

$$N_{cr,v} = \frac{\pi^2 E I_u}{(K_v L)^2} \quad \text{(Eq. 3.28)}$$

$$N_{cr,T} = \frac{1}{A_{rp}}\left(GC_T + \frac{\pi^2 E C_w}{(K_T L)^2}\right) \approx \frac{1}{A_{rp}} GC_T \quad \text{(Eq. 3.29)}$$

In fact, an effective length defines the portion of the deflected shape between points of zero curvature. In other words, K_iL is the length of an equivalent pin-ended column buckling which would exhibit the same elastic buckling load than the end-restrained column.

The K_i factors reported in Figure 3.7 could be used to evaluate K_u and K_v factors so as to estimate the flexural critical loads, but not to evaluate the K_T one. Nevertheless, as explained before, the warping constant C_w of angle sections can be assumed as zero and then, the torsional critical load can be estimated only by the first term of the eq. (3.29), without determining the K_T factor.

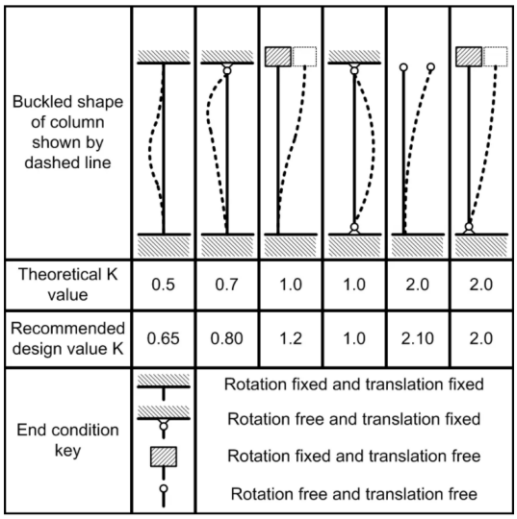

Figure 3.7:Effective-length factors K_u, K_v for axially loaded columns with various end condition [21]

When there is a need to take into account the positive effect of the restraints in the design, then the formulas proposed in EN 1993-3-1 [2] where an angle is connected through different numbers of bolts at its extremities, may be applied. In those formulas, a modified slenderness is proposed per axis (u-u, v-v, z-z) depending on the boundary conditions (i.e. single/ doubled bolted at both ends member, etc). In the present thesis, this aspect is not addressed and only pin-ended angles are so considered.

3.5 Influence of the loading type

In contrast with other common profiles, the critical load of an angle section is affected from the position of the axial load. The analytical solution for a centrally or eccentrically axial loaded member is given in §3.1. If the member is loaded with an eccentric axial force (e_N) and a bending moment, this can be translated to an axial force with a fictitious eccentricity ($e_{fic}=e_N+M/N$), and therefore same equations may be used; at least as long as M and N vary proportionally.

But angles that are used in pylons, towers and masts are also subjected to lateral loads (wind forces) additionally to their axial force. A few numerical simulations on single angle axially loaded members subjected to lateral loads have been performed, and it is clear that the critical load of the column is affected, especially when the lateral load increases. However, it can be seen (see §9.2.2) that the wind force acting on a bar is rather small compared with the axial one. Therefore, it will be assumed in the thesis that lateral loads remain quite modest and that M and N forces in the angle members vary proportionally.

3.6 Second order elastic buckling analyses

Besides the first order linear elastic theory that is presented in §3.1, the critical load of a member can be also evaluated by a second order elastic analysis using a non-linear software, as reported through an example in section §3.7. In this case, if the column is perfectly straight and the load is applied at the centre of gravity, the straight position becomes unstable when the load exceeds the critical value

and a slight increase of the load leads to large displacements of the member and, finally, to the collapse due to buckling. The critical point, after which the deflections of the member become very large, is defined as the "bifurcation point" $N_{cr,\delta o=0}$ of the system; this is illustrated in Figure 3.8, for $\delta_o = 0$. On the contrary, if the column is not initially straight – as it happens often in practise – or it is eccentrically loaded, deflection starts from the beginning of the loading and there is no sudden buckling by bifurcation (Figure 3.8). If the bow imperfections or the eccentricities remain low, then the critical load tends to reach the critical one and a small plateau appears in the curve corresponding to the critical load multiplier. However, if the loading eccentricity is high, there is a continuous increase of the displacements since *P-δ* effects become significant. The initial imperfections cannot become rather high so as to affect the member's response because they are limited due to fabrication standards. This phenomenon is called "divergence of the equilibrium" and sometimes there is no strict stability limit. For those cases (dotted line in Figure 3.8), the critical load factor can be determined by the point where the curvature changes. The intersection points of the small horizontal red lines and the 2nd order displacement curves shown in Figure 3.8, indicate the critical load multipliers for the two main cases described above.

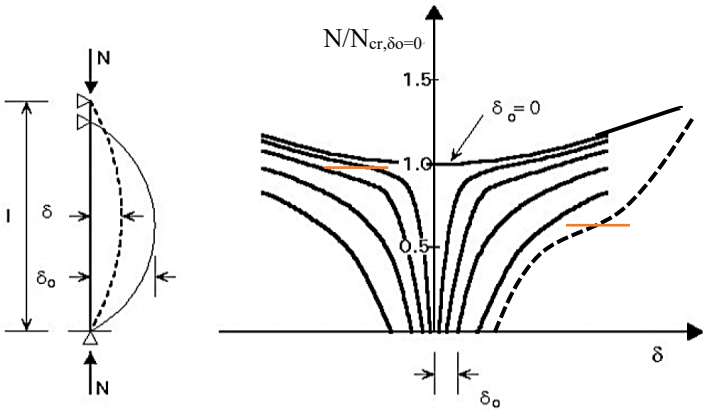

Figure 3.8: Load-displacement 2nd order elastic curves of a compressed column (in the case of a bow imperfection) [21]

3.7 Numerical and analytical studies

A pin-ended perfectly straight column with 2,0 m length is assumed. Its cross-section consists of an angle profile L70x70x7 made of S235 and the Young's modulus equals 210000 N/mm^2. The geometry properties of the profile are reported in Table 3.1. For the studied section, the parameters of the Vlassov's circle described in §3.3 are also calculated; the coordinates of its centre are (22,87 ; 0) and its radius is *R=37,67 mm*.

Table 3.1: Geometry properties of the cross-section L70x70x7

h [mm]	t [mm]	A [mm^2]	i_u [mm]	i_v [mm]	I_T [mm^4]	I_w [mm^6]	u_c [mm]	v_c [mm]	I_{ur2} [mm^5]
70	7	939,691	26,665	13,605	14601,1	5603850,0	-22,842	0	7956200,0

The column is loaded with an eccentric axial load of 100kN. Two main cases are distinguished and studied in terms of the load eccentricity:

(a) the load is applied on the major axis U ($u_p \neq 0$, $v_p = 0$);
(b) the load is applied on the minor axis V ($u_p = 0$, $v_p \neq 0$);

Table 3.2: Analytical and numerical load factors for eccentrically loads on U axis

u_P [m]	$\alpha_{cr,1}$ [-]	$\alpha_{cr,2}$ [-]	$\alpha_{cr,3}$ [-]	$\alpha_{cr,anal}$ [-]	$\alpha_{cr,FINELG}$ [-]	$\alpha_{NL\text{-}el}$ [-]
-0,2	0,901	1,52	-0,556	-0,556	-0,5561	---
-0,15	0,901	1,85	-0,773	-0,773	-0,7738	---
-0,1	0,901	2,36	-1,26	0,901	0,9015	0,7621
-0,07	0,901	2,79	-2,03	0,901	0,9015	0,7722
-0,05	0,901	3,13	-3,35	0,901	0,9015	0,7992
-0,04	0,901	3,30	-4,89	0,901	0,9015	0,8051
-0,03	0,901	3,42	-8,66	0,901	0,9015	0,8452
-0,02284	0,901	3,46	-17,59	0,901	0,9015	0,8654
-0,01	0,901	3,29	36,68	0,901	0,9015	0,8892
-0,005	0,901	3,11	20,42	0,901	0,9015	0,8970
-0,001	0,901	2,94	16,38	0,901	0,9015	0,9010
0	**0,901**	**2,89**	**15,74**	**0,901**	**0,9015**	**0,9014**
0,001	0,901	2,85	15,24	0,901	0,9015	0,9010
0,005	0,901	2,66	13,96	0,901	0,9015	0,8970
0,01	0,901	2,43	13,42	0,901	0,9015	0,8892
0,015	0,901	2,21	13,59	0,901	0,9015	0,8821
0,02	0,901	2,02	14,30	0,901	0,9015	0,8782
0,025	0,901	1,86	15,54	0,901	0,9015	0,8621
0,03	0,901	1,71	17,43	0,901	0,9015	0,8452
0,04	0,901	1,47	24,60	0,901	0,9015	0,8052
0,05	0,901	1,29	46,31	0,901	0,9015	0,7992
0,07	0,901	1,03	-49,48	0,901	0,9015	0,7831
0,08	0,901	0,933	-23,72	0,901	0,9015	0,7722
0,1	0,901	0,787	-11,46	0,787	0,7869	0,7621
0,15	0,901	0,563	-4,92	0,563	0,5637	0,6411
0,2	0,901	0,439	-3,11	0,439	0,4386	0,5372

For each considered eccentricity, three load factors are calculated analytically ($a_{cr,1}$, $a_{cr,2}$, $a_{cr,3}$) by using eq. (3.19), and the smallest one among them, indicates the critical one ($a_{cr,anal}$). Then, and in order to evaluate numerically the critical load multiplier ($a_{cr,FINELG}$), an elastic instability analysis is performed with FINELG [25] finite element software. The column is meshed in 16 beam elements along its length and the boundary conditions are those described in Figure 3.1. Finally, a second order linear elastic analysis without initial imperfections, but with the relevant eccentricity, is performed with FINELG, and the $a_{cr,NL\text{-}el}$ is evaluated according to §3.6. Only for the specific case where the column is loaded at the centre of gravity, a rather small imperfection has been implemented so as to the convergence of the FINELG calculations. The analytical and numerical load multipliers for different load eccentricities are illustrated graphically in Figure 3.9 and Figure 3.10 while their values are reported in Table 3.2 and Table 3.3 for eccentrically loads on U and V axis respectively.

Table 3.3: Analytical and numerical load factors for eccentrically loads on V axis

v_P [m]	$\alpha_{cr,1}$ [-]	$\alpha_{cr,2}$ [-]	$\alpha_{cr,3}$ [-]	$\alpha_{cr,anal}$ [-]	$\alpha_{cr,FINELG}$ [-]	α_{NL-el} [-]
-0,2	0,382	3,43	-0,718	0,382	0,3823	0,4061
-0,15	0,464	3,41	-1,08	0,464	0,4648	0,4720
-0,1	0,587	3,35	-2,06	0,587	0,5867	0,6048
-0,07	0,687	3,27	-4,09	0,687	0,6867	0,7124
-0,05	0,764	3,18	-9,45	0,764	0,7641	0,7633
-0,04	0,803	3,11	-20,92	0,803	0,8036	0,8021
-0,02284	0,864	2,99	38,08	0,864	0,8642	0,8499
-0,01	0,894	2,91	17,76	0,894	0,8938	0,8785
-0,005	0,899	2,90	16,20	0,90	0,8995	0,8909
-0,001	0,901	2,89	15,76	0,901	0,9014	0,9013
0	**0,901**	**2,89**	**15,74**	**0,901**	**0,9015**	**0,9014**
0,001	0,901	2,89	15,76	0,901	0,9014	0,9013
0,005	0,899	2,90	16,20	0,899	0,8995	0,8909
0,01	0,894	2,91	17,76	0,894	0,8938	0,8785
0,02284	0,864	2,99	38,08	0,864	0,8642	0,8499
0,04	0,803	3,11	-20,92	0,803	0,8036	0,8021
0,05	0,764	3,18	-9,45	0,764	0,7641	0,7633
0,07	0,687	3,27	-4,09	0,687	0,6867	0,7124
0,1	0,587	3,35	-2,06	0,587	0,5867	0,6048
0,15	0,464	3,41	-1,08	0,464	0,4648	0,4720
0,2	0,382	3,43	-0,718	0,382	0,3823	0,4061

When the member is loaded on U axis, three load factors are calculated analytically. One ($a_{cr,1}$) which is related with flexural buckling of the member along U axis, one ($a_{cr,2}$) which is associated to flexural-torsional buckling along V axis when the flexural deflection predominates and finally one ($a_{cr,3}$), which corresponds to flexural-torsional buckling along V axis when the torsion predominates. Similarly, when the member is loaded on V axis, $a_{cr,2}$ and $a_{cr,3}$ are correlated again with the flexural-torsional buckling along V axis as before, but $a_{cr,1}$ relates now to a flexural-torsional buckling towards U axis, that becomes a pure flexural one when the load approaches the centre of gravity. It can be seen through both graphs that out of the Vlassov's circle – its boundaries are reported with dot lines in the figures – a tensile load is requested to reach the flexural-torsional buckling where the torsion prevails. Additionally, as the load is approaching the circle's boundaries, the corresponding critical load tends to become rather high (infinity). The Vlassov theory is therefore validated through this study. Furthermore, from Figure 3.9 it can be easily observed that the curves are not symmetrical relatively to V axis because the critical load of an angle section increases when the point of application of the load approaches the shear centre. However, thanks to U axis of symmetry, the critical loads are identical (see Figure 3.10) whether the force is applied on (u_p, v_p) or (u_p, $-v_p$).

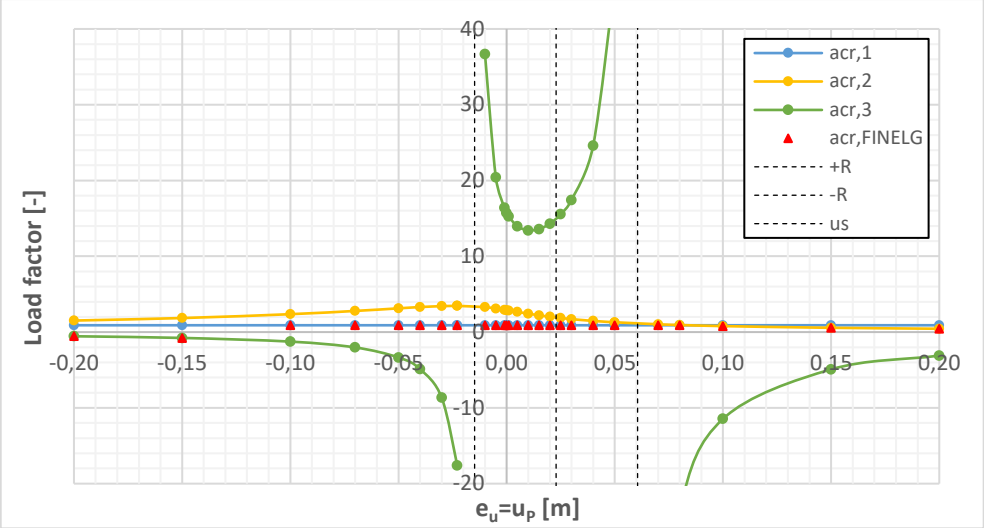

Figure 3.9: Analytical and numerical instability load factors for eccentrically loads on U axis

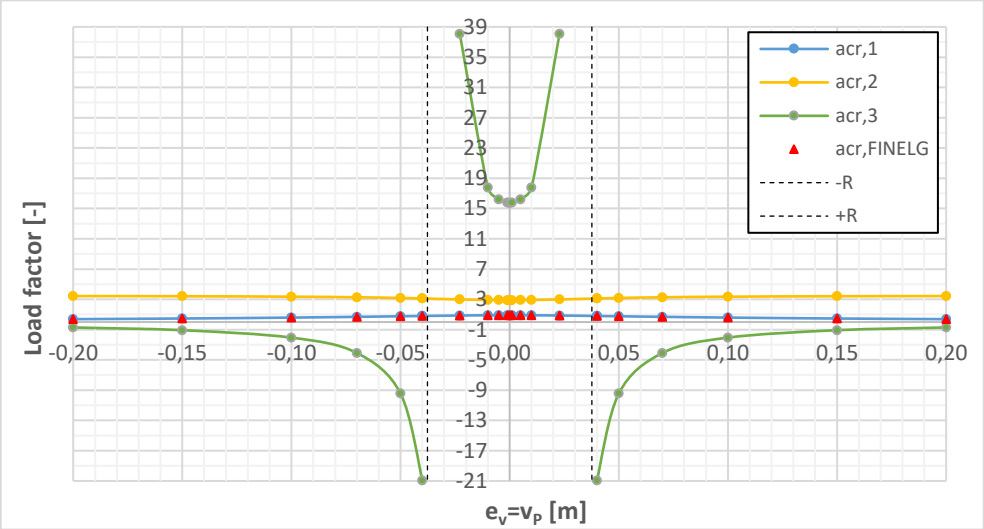

Figure 3.10: Analytical and numerical instability load factors for eccentrically loads on V axis

The results obtained analytically and numerically, through the elastic instability critical analysis, are in very close agreement, as seen from both graphs and tables. From the comparison between the analytical results and those estimated through the 2nd order elastic analysis (Table 3.2 and Table 3.3), one sees a very good agreement for small load eccentricities, but slight differences when the load eccentricity increases. This difference is explained by the "divergence of the equilibrium" phenomenon, as there is not always strict stability limit, and it seems to be more relevant for an eccentric load on U axis than V.

Figure 3.11 shows the load factor vs displacement curves obtained through a 2nd order linear elastic analysis for eccentrically loads on U axis. All the curves compared with the load factor obtained for the centrally loaded column through the elastic instability analysis ($N_{cr,u}/N = 0{,}9015$) that is illustrated with the orange horizontal line. The curves that correspond to the eccentricities u_p equal to 0,1, 0,15 and 0,2 are not shown in this graph due to the fact that their relevant buckling mode is a flexural-torsional one along V axis. The values of all the load factors $\alpha_{cr,NL\text{-}el}$ are reported in Table 3.2. For the cases where instability occurs due to a tensile load (i.e for $u_p = -0{,}15$ or $-0{,}2$) according to Vlassov's theory (§3.3), even if the analytical solutions and the corresponding results from an

elastic first order instability analysis are identical, it is not possible to verify their load multipliers through a non-linear elastic analysis with a tensile load, because the member just elongates in these cases.

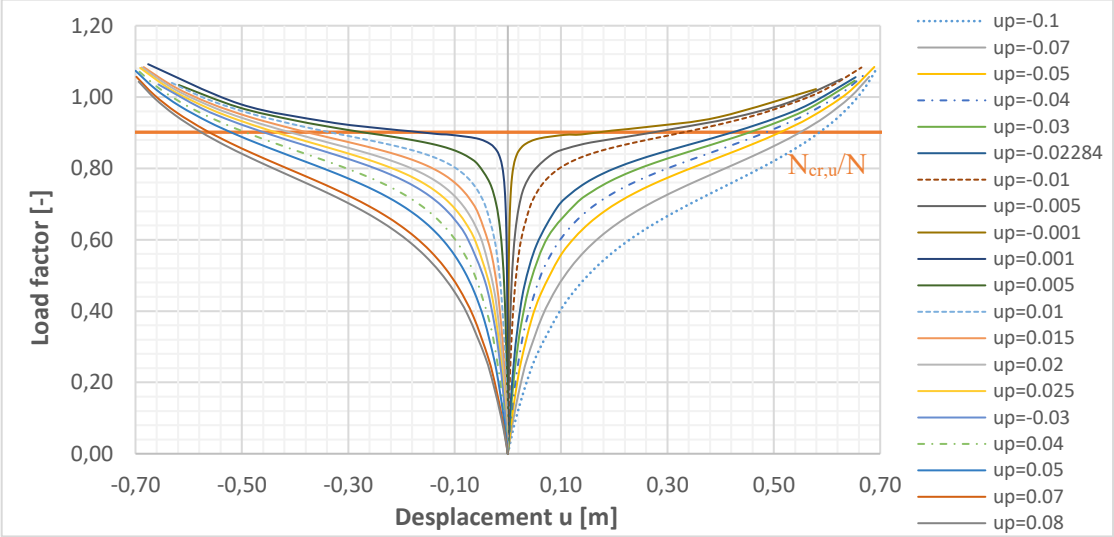

Figure 3.11: Load factor – displacement curves obtained through a 2nd order linear elastic analysis for eccentrically loads on U axis

Figure 3.12 shows the load factor vs displacement curves obtained through a 2nd order linear elastic analysis for eccentrically loads on V axis. In this case, the curves compared with the relevant load factor obtained through the elastic instability analysis, that is illustrated with a dot horizontal line with same colour with the displacement curve that should compared. As the section is symmetrical in this direction, the curves are identical for the same absolute value of the applied eccentricity.

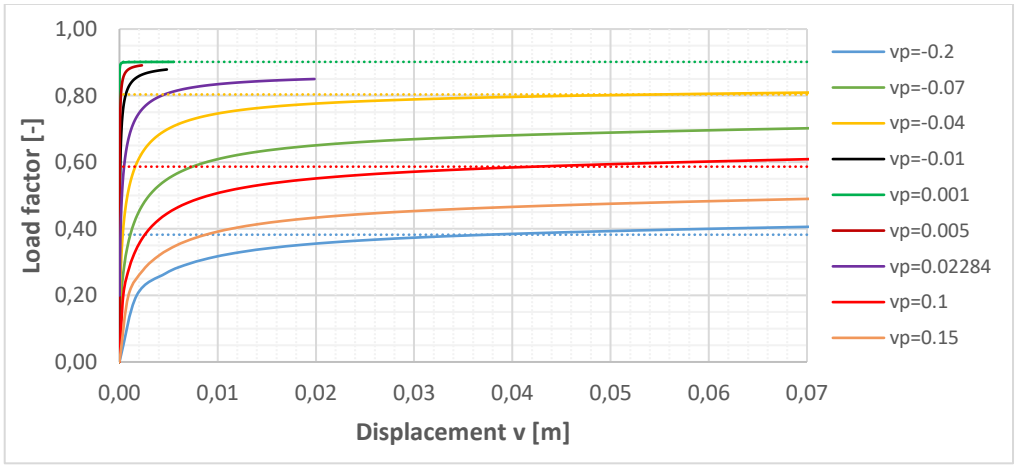

Figure 3.12: Load factor – displacement curves obtained through a 2nd order linear elastic analysis for eccentrically loads on V axis

Complementary analyses have been finally performed in order to investigate the influence of the out-of-straightness of the column to its critical load. Eight load eccentricities on U axis have been considered, three positive and four negatives (see Figure 2.1 for the definition of the sine), and for each eccentricity, an initial bow imperfection with shape similar to the first instability mode (a deflection along U axis) is implemented. In terms of the imperfection's magnitude, four cases are also considered: ± *L[mm]/1000* and ± *L[mm]/200*. Then, 2nd order linear elastic analyses were

performed and the load factor – displacement curves are shown in Figure 3.13 and Figure 3.14 for negative and positive eccentricities on U respectively.

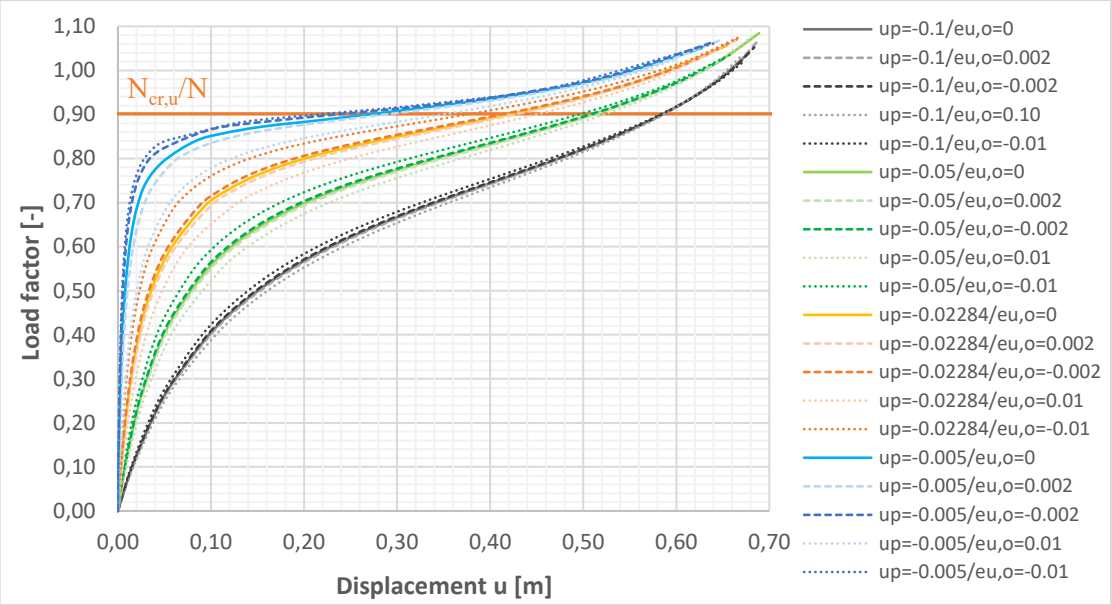

Figure 3.13: Load factor – displacement curves obtained through a 2nd order linear elastic analysis (with negative eccentricity on U axis and initial imperfections)

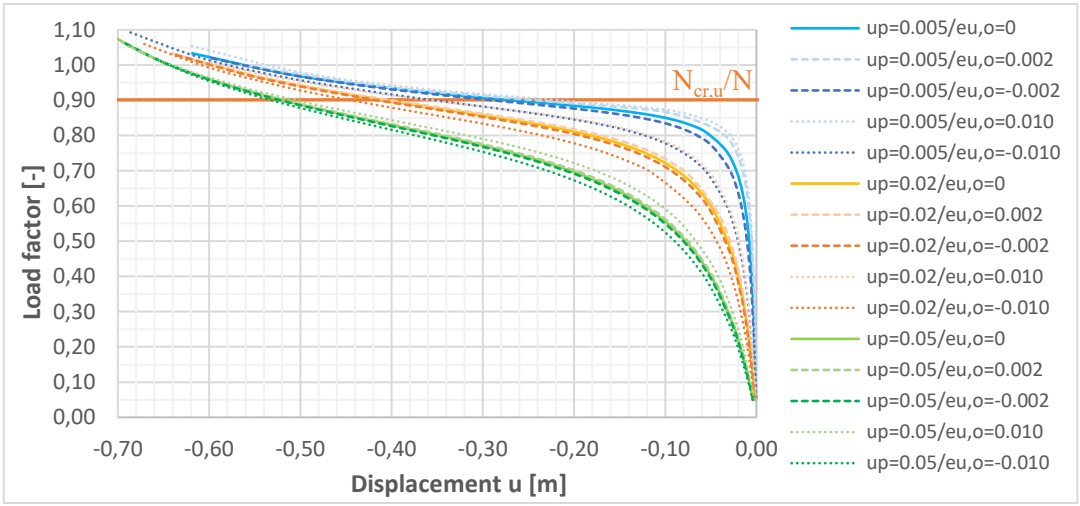

Figure 3.14: Load factor – displacement curves obtained through a 2nd order linear elastic analysis (with positive eccentricity on U axis and initial imperfections)

It can be seen that for the same loading eccentricity, the initial imperfections do not affect the critical load of the column so much, but they have an impact at its stiffness, that tends to be negligible as the load eccentricity increases. Roughly, if $u_P < 5e_{u,o}$ then the influence of the initial out-of-straightness becomes relevant for the response of the member until it reaches its critical load. On the contrary, the critical load of the column is affected much more by the loading eccentricity and becomes smaller as far as the eccentricity increases.

3.8 Conclusions

Angle profiles, and more specifically the equal leg ones investigated in the present thesis, exhibit some properties that distinguish them from the well-known profiles. It is known that, for a double-

symmetric cross-section, the critical load is not affected by the load eccentricity while the buckling modes are always decoupled and the critical one is a flexural one. This is different for angle sections; their particularities are summarized below:

- They mostly buckle along their weak axis with a flexural or a flexural-torsional mode, depending on the load eccentricity.
- The full decoupling of the buckling modes happens only for a very specific case, where the member is loaded at the shear centre; this is also the only case that a pure torsional buckling mode can be appeared.
- The critical load is affected by the type of the loading (bending moments, lateral loads, etc).
- Depending on the cross-section geometry, an instability may be occurred even for an eccentric tensile load.
- The initial imperfections of the member, that in practise are rather small as they are limited by fabrication standards, do not significantly affect the critical load in comparison with an eccentricity of the applying load. However, they influence the stiffness of the member until it reaches its critical load, as results from a 2^{nd} order linear elastic analysis.

4. CLASSIFICATION OF EQUAL LEG ANGLES PROFILES

Cross-section classification is of importance for the selection of the analysis and design procedures to employ: plastic, elastic or elastic with due account for local buckling. General rules for cross-section classification (classes 1 to 4) are given in EN 1993-1-1, in combination with EN 1993-1-5 that gives rules for buckling resistance of class-4 angle sections prone to local buckling. Additional rules for classification to compression can be found in EN 1993-3-1 for angle members used in lattice towers, as well as in the CENELEC standard EN 50341-1 that provides specific rules for lattice towers used in the field of overhead electrical lines. Amongst these normative documents, specific provisions for classification to bending can be found only in EN 1993-1-1, while inconsistencies between them are highlighted and presented for classification to compression, where four different width-to-thickness ratios can be evaluated for a same class limit!

According to EN 1993-1-1, clause 5.5.2 (4) classification should be done for the compression parts of the cross-section that are defined as follows: “Compression parts include every part of the cross-section which is either totally or partially in compression under the load combination considered”. However, a strict application of this rule requires a separate classification of the cross-section for each combination of applied forces and moments. Since this rule is unpractical for design, a simpler approach is proposed here, where the cross-section is classified separately for compression, strong axis and weak axis bending. For the latter, the cross-section class may be different for positive or negative moments due to the mono-symmetric shape of the profile, that leads to different classes when the tip is in compression or in tension.

In the following, the limiting width-to-thickness ratios for compression parts of equal leg angle sections are discussed and redefined through analytical considerations and numerical calculations, for the above-referred loading conditions. The analytical derivations always follow the main principles of Eurocodes, and especially EN 1993-1-1. As in the latest version of EN 1993-1-1, namely prEN 1993-1-1 [26], no modification is contemplated regarding the classification of the cross-sections, the former is used hereafter when a reference is made.

4.1 Description of the numerical model

The numerical models for the parametrical numerical studies were created with ABAQUS non-linear finite element software [27] using volume elements. The samples have been modelled as pin-ended with at least three volume linear elements over the thickness (see Figure 4.1). The selection of the elements (linear instead of quadratic) does not influence the results. A denser mesh (i.e four volume elements per thickness) gives better results by 1-2%, but increases substantially the required time of the analysis, that is not desirable in combination with the high number of the numerical studies to be performed. At the extremities, fictitious end plates have been introduced through a specific constraint, so as to distribute uniformly the external applied loads but also to avoid any local failure at the point of application of the load.

The finite element analyses were performed considering:

- a local leg imperfection equal to *h/100* (*h* is the width of the cross-section), based on the tolerances defined in EN 10056-2 [28], with imperfection shape affine to the lower relevant elastic instability mode obtained through an elastic instability analysis, that has been performed with an axial force or a bending moment for compression or bending cases respectively;

- a linear elastic – perfectly plastic material behaviour law without strain hardening in accordance with EN 1993-1-14,§4.3.2-(1a) [29], as it is shown in Figure 4.2.

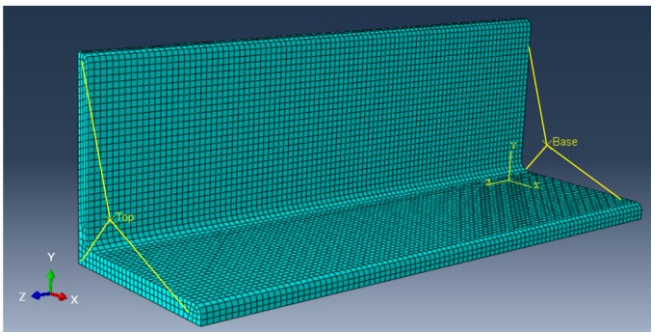

Figure 4.1: Sample of the 3-D model used for the numerical analyses

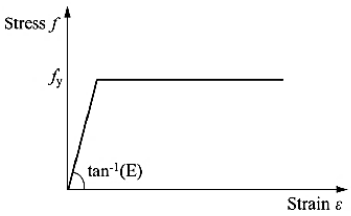

Figure 4.2: Material law in accordance with [29]

Subsequently, parametrical numerical investigations on short column subjected to compression, strong axis bending, and weak axis bending will be conducted in view of deriving appropriate classification criteria. In all the numerical simulations, the applied load increasing up to failure. All nominal dimensions of the cross-sections used in these studies are in *mm*.

4.2 Classification to compression

The resistance of sections subjected to compression is identical for classes 1, 2 or 3. Accordingly, there is a need to define only the limit between classes 3 and 4. The failure modes on each side of this limit are respectively the yielding of the cross section and the local buckling of the legs. Often, but erroneously, local buckling for class 4 sections is associated to torsional buckling while it is known from §0 that a pure torsional buckling mode can only be obtained when the load application point is the shear centre, which does not coincide with the centroid in case of angles sections. Accordingly, the relevant failure mode for class 1 to 3 angle sections is yielding, while, for class 4 sections, local plate buckling occurs in the legs.

Table 4.1: Samples for the analyses of the cross-section subjected to compression

No	Cross-Section	Steel grades
1	L45x45x3	S355 / S460 / S550 / S690
2	L45x45x4	S355 / S460 / S550 / S690
3	L70x70x5	S355 / S460 / S550 / S690
4	L70x70x6	S355 / S460 / S550 / S690
5	L250x250x17	S355 / S460 / S550 / S690
6	L250x250x20	S355 / S460 / S550 / S690
7	L250x250x22	S355 / S460 / S550 / S690
8	L250x250x26	S355 / S460 / S550 / S690

Table 4.1 presents the cross-sections and the steel grades that have been used for the analyses in which the samples are subjected to compression. These samples have been selected in order to cover a wide range of cross-section leg slenderness. In particular, even if steel grade S690 is not available on the market, it has been selected so as to reach higher slenderness ratios.

In order to prevent flexural buckling, the length of the samples was selected in such a way that $\bar{\lambda} \leq 0{,}2$, a slenderness below which the European buckling curves assume that no reduction associated to buckling is required. This limitation leads to a value of the length of the samples equal to $18{,}5 \cdot \varepsilon \cdot i_v$:

$$\bar{\lambda} \leq 0{,}2 \quad \Rightarrow \quad \frac{L_{cr}}{i_v} \cdot \frac{1}{\lambda_1} \leq 0{,}2 \quad \Rightarrow \quad L_{cr} \leq 18{,}75 \cdot \varepsilon \cdot i_v \quad \Rightarrow \quad \boldsymbol{L_{cr} = 18{,}5 \cdot \varepsilon \cdot i_v} \qquad \text{(Eq. 4.1)}$$

Figure 4.3 and Figure 4.4 show the ratio between the numerically obtained cross-section (CS) resistance (N_{ult}) and the plastic characteristic resistance ($N_{pl} = A \cdot f_y$), versus the $h/\varepsilon t$ and $c/\varepsilon t$ ratio respectively. It can be easily observed that the scatter is bigger when the results are correlated with the $h/\varepsilon t$ ratio than the $c/\varepsilon t$ one, that makes the latter ratio more suitable for classification purposes.

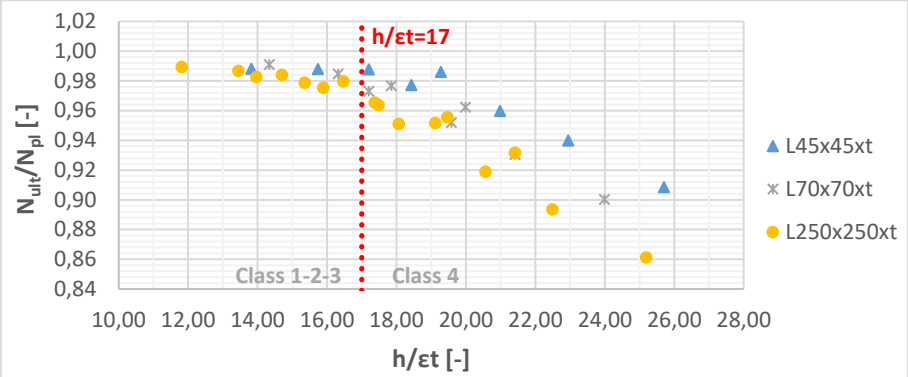

Figure 4.3: Compression. Ratio between numerical results and plastic resistance vs. h/εt ratio

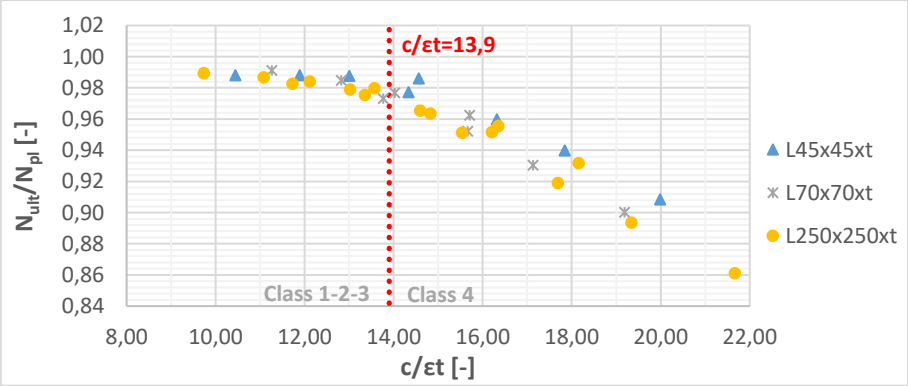

Figure 4.4: Compression. Ratio between numerical results and plastic resistance vs. c/εt ratio

The samples that reach their plastic characteristic resistance even with a 3% deviation, that is assumed as acceptable due to the selected mesh density, can be categorized as class 1 to 3. Therefore, based on the numerical results, the class-3 limit for equal leg angles subjected to compression may be set as $c/t \leq 13{,}9\varepsilon$.

In EN 1993-1-1, table 5.2 (sheet 3), two conditions are provided to distinguish Class 3 from Class 4 sections for equal leg angles:

$$h/t \leq 11{,}5\varepsilon \quad \text{and} \quad h/t \leq 15\varepsilon \quad \text{so} \quad h/t \leq 11{,}5\varepsilon \qquad \text{(Eq. 4.2)}$$

For the available hot-rolled equal leg angles, it can be seen that the mean value for parameter *c* is equal to *0,8h*. So, in this case, eq. (4.2) may be rewritten and becomes $c/t \leq 9{,}2\varepsilon$. This value is seen to be quite conservative when compared to the obtained numerical results.

In the same table 5.2 (sheet 3) of EN 1993-1-1, a cross reference to sheet 2 is made for "outstand elements", from which the class-3 limit is:

$$c/t \leq 14\varepsilon \qquad \text{(Eq. 4.3)}$$

This limit may be also determined analytically by considering the risk of local plate buckling resistance of the leg. Indeed, the reduction factor for outstand plated elements due to local buckling is given in EN 1993-1-5 as below:

$$\rho = \begin{cases} 1{,}0 & \text{for } \bar{\lambda}_p \leq 0{,}748 \\ \frac{\bar{\lambda}_p - 0{,}188}{\bar{\lambda}_p^2} & \text{for } \bar{\lambda}_p > 0{,}748 \end{cases} \qquad \text{(Eq. 4.4)}$$

where:

$$\bar{\lambda}_p = \sqrt{\frac{f_y}{\sigma_{cr}}} = \frac{\bar{b}/t}{28{,}4\varepsilon\sqrt{k_\sigma}} \qquad \text{(Eq. 4.5)}$$

In this case, the condition for class 3 to 4 limit is that the resistance should not be reduced due to local buckling, which may be expressed as $\bar{\lambda}_p \leq 0{,}748$, i.e. $\rho = 1$. In table 4.2 of EN 1993-1-5, the buckling factor for outstand elements in compression ($\psi = 1$) is defined as $k_\sigma = 0{,}43$. Additionally, for equal leg angles EN 1993-1-5 defines $\bar{b} = h$. Introducing the above values in the expression for the limit slenderness, the class-3 limit in respect to local buckling may be calculated as:

$$h/t \leq 13{,}9\varepsilon \qquad \text{corresponding approximatively to} \qquad c/t \leq 11{,}1\varepsilon \qquad \text{(Eq. 4.6)}$$

But in fact, looking to the obtained numerical results, it appears clearly now that $\bar{b}$ should be selected as equal to *c*, and not to *h* as suggested in EN 1993-1-5.

As a conclusion, the class-3 to class-4 limit for equal leg angles subjected to compression may be preferably set equal to:

$$c/t \leq 13{,}9\varepsilon \qquad \text{(Eq. 4.7)}$$

This condition is in line with:

- the numerical studies;
- the current provisions of Eurocode 3 and more specifically with EN 1993-1-1, table 5.2, sheet 2 for class-3 limit of outstand elements ($c/t \leq 14\varepsilon$);
- EN 1993-1-5, in which $\bar{b} = c$ instead of *h* ($c/t \leq 13{,}9\varepsilon$);
- the standard EN 50341, mainly used in practice in central Europe for the design of lattice towers made of angles ($c/t \leq 13{,}9\varepsilon$);
- the recommendations of EN 1993-3-1 ($c/t \leq 13{,}9\varepsilon$) in which the *c/t* ratio for angles defined in EN 1993-1-1, table 5.2, may be replaced by the ratio *(h-2t)/t*, in which the nominator is not so far from the exact value *c=h-t-r*.

4.3 Classification to strong axis bending

The stress distribution for strong axis bending M_u is such that only one leg is under compression and needs classification. It may be seen from EN 1993-1-1 that the design resistance for classes 1 and 2

is identical, the plastic one. The two classes differ in the possibility to apply plastic methods of analysis for class 1 sections, while for class 2 sections elastic methods shall be employed. However, plastic methods of analysis are rarely used in towers composed of angle sections according to the existing norms. Therefore, the two classes 1 and 2 are merged in the following and only limits between classes 2 and 3 and 3 and 4 have been derived. Table 4.2 presents the cross-sections and the steel grades that have been used for the numerical studies in which the samples are subjected to strong axis bending moment M_u. The selected parameters lead to $c/\varepsilon t$ ratios below 25. However, in order to extend the results to higher ratios, additional analyses were carried out for two cross-sections (L 120x120x7 and L 130x130x8) with non-commercially available higher steel grades (S800, S900, S1000 and S1100). In order to prevent lateral torsional buckling, the length of all samples has been each time adapted so as the relative slenderness remains $\lambda_{LT} \leq 0,4$ which is the limit slenderness under which LTB does not reduce the bending strength according to EN 1993-1-1.

Table 4.2: Samples for the analyses of the cross-section subjected to weak axis bending M_u

No	Cross-Section	Steel grades
1	L45x45x3	S355 / S460 / S550 / S690
2	L45x45x4	S355 / S460 / S550 / S690
3	L70x70x5	S355 / S460 / S550 / S690
4	L70x70x6	S355 / S460 / S550 / S690
5	L120x120x7	S355 / S460 / S550 / S690
6	L120x120x8	S355 / S460 / S550 / S690
7	L130x130x8	S355 / S460 / S550 / S690
8	L130x130x9	S355 / S460 / S550 / S690
9	L150x150x10	S355 / S460 / S550 / S690
10	L150x150x12	S355 / S460 / S550 / S690
11	L250x250x17	S355 / S460 / S550 / S690
12	L250x250x20	S355 / S460 / S550 / S690
13	L250x250x22	S355 / S460 / S550 / S690
14	L250x250x26	S355 / S460 / S550 / S690

Figure 4.5 shows the ratio between the numerical results for the cross-section resistance ($M_{ult,u}$) and the plastic characteristic resistance ($M_{pl,u}=W_{pl,u}\cdot f_y=1,5\cdot W_{el,u}\cdot f_y$), versus the $c/\varepsilon t$ ratio. Details about the evaluation of the elastic/plastic modulus in respect to the strong u axis can be found in Annex A.

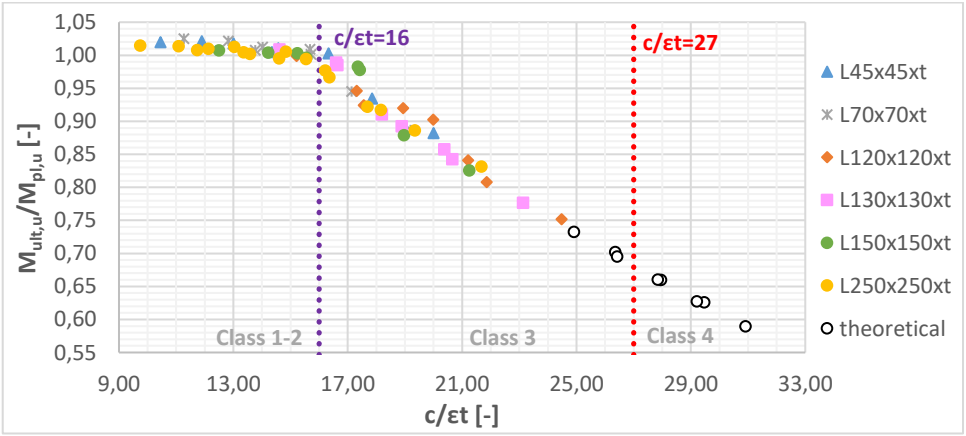

Figure 4.5: Strong axis bending. Ratio between numerical results and plastic resistance vs. c/εt ratio

The samples that reach their plastic characteristic resistance ($M_{pl,u}=1,5 \cdot M_{el,u}$), even with a 3% deviation, can be categorized as class 1-2, while the class-3 limit can be easily found when $M_{ult,u}$ is equal to $M_{el,u}$ and then $M_{ult,u} / M_{pl,u} = 0,66$. Subsequently, from the numerical results, the class-2 limit for equal leg angles subjected to strong axis bending may be adopted as $c/t \leq 16\varepsilon$, while the class-3 limit can be set to $c/t \leq 27\varepsilon$.

In the plastic domain, the leg is an outstand element subjected to uniform compression and then class-2 limit may be obtained from EN 1993-1-1, Table 5.2, sheet 2 as $c/t \leq 10\varepsilon$. The background of this value may be found in ESDEP [30] where it is indicated that a class-2 limit can be obtained by defining the value of the reduced plate slenderness $\overline{\lambda_{p,min}}$ by eq. (4.8) as equal to 0,6:

$$\overline{\lambda_p} = \frac{c/t}{28,427\varepsilon\sqrt{k_\sigma}} = \overline{\lambda_{p,min}} \Rightarrow \frac{c}{t} = 17,06\varepsilon\sqrt{k_\sigma} \qquad \text{(Eq. 4.8)}$$

The buckling factor k_σ is equal to 0,43 for simply supported boundary conditions. So, a c/t value of $11,2\varepsilon$ is found (rounded to 10ε in Table 5.2, sheet 2). If clamped boundary conditions are now assumed, $k_\sigma = 1,25$ (see Ref.[31]-[32]) and this leads to $c/t \leq 19,1\varepsilon$. By observing the numerical and analytical results, it can be concluded that the actual class-2 limit is between the above two extreme cases and finally the following limit may be adopted:

$$\frac{c}{t} \leq 16\varepsilon \qquad \text{(Eq. 4.9)}$$

which defines the limit between classes 2 and 3. In fact, the leg in tension is seen to bring a torsional restraint to the leg in compression, with an intermediate efficiency between fully pinned and fully fixed boundary conditions.

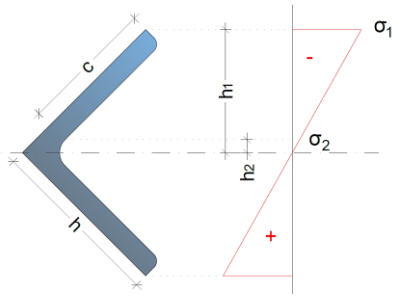

Figure 4.6: Elastic stress distribution for strong axis bending (M_u)

For elastic behaviour (Figure 4.6), the compression leg is an outstand element subjected to a stress ratio $\psi = \frac{\sigma_2}{\sigma_1} = \frac{h_2}{h_1} = \frac{h-c}{h} \approx \frac{h-0,8h}{h} \approx 0,20$. Based on EN 1993-1-1, Table 5.2, sheet 2, the class-3 limit is equal to $c/t \leq 15,3\varepsilon$, which is smaller than the proposed class-2 limit. Again, it is based on an assumption of simply supported boundary condition (i.e $k_\sigma = 0,54$). If, now, clamped boundary conditions are assumed, the corresponding buckling factor [31]-[32] may be taken as equal to $k_\sigma = 1,57$. Then, the class-3 limit may be obtained from the general formula of EN 1993-1-1, Table 5.2, sheet 2:

$$\frac{c}{t} \leq 21\varepsilon\sqrt{1,57} = 26,3\varepsilon \qquad \text{(Eq. 4.10)}$$

This value is quite close to the numerically obtained one (27ε) and is selected here as the proposed class-3 limit.

4.4 Classification to weak axis bending

When the cross-section is subjected to weak axis bending M_v, the stress conditions for the two legs are identical and then, classification refers to both legs. As before, only limits between classes 2 and 3 and 3 and 4 have been derived. Two cases are defined and checked afterwards: the leg tip is under compression and under tension.

4.4.1 Tip in compression

Table 4.3 presents the cross-sections and the steel grades that have been used for the numerical studies in which the samples are subjected to weak axis bending moment M_v, with the tip in compression. As before, the last 8 analysis, i.e. 15* and 16* in Table 4.3, are theoretical so as to address slenderer cross-sections.

Table 4.3: Samples for the analyses of the cross-section subjected to weak axis bending M_v

No	Cross-Section	Steel grades
1	L45x45x3	S355 / S460 / S550 / S690
2	L45x45x4	S355 / S460 / S550 / S690
3	L70x70x5	S355 / S460 / S550 / S690
4	L70x70x6	S355 / S460 / S550 / S690
5	L120x120x7	S355 / S460 / S550 / S690
6	L120x120x8	S355 / S460 / S550 / S690
7	L130x130x8	S355 / S460 / S550 / S690
8	L130x130x9	S355 / S460 / S550 / S690
9	L150x150x10	S355 / S460 / S550 / S690
10	L150x150x12	S355 / S460 / S550 / S690
11	L250x250x17	S355 / S460 / S550 / S690
12	L250x250x20	S355 / S460 / S550 / S690
13	L250x250x22	S355 / S460 / S550 / S690
14	L250x250x26	S355 / S460 / S550 / S690
15*	L120x120x7	S700 / S800 / S900 / S950
16*	L130x130x8	S700 / S800 / S900 / S950

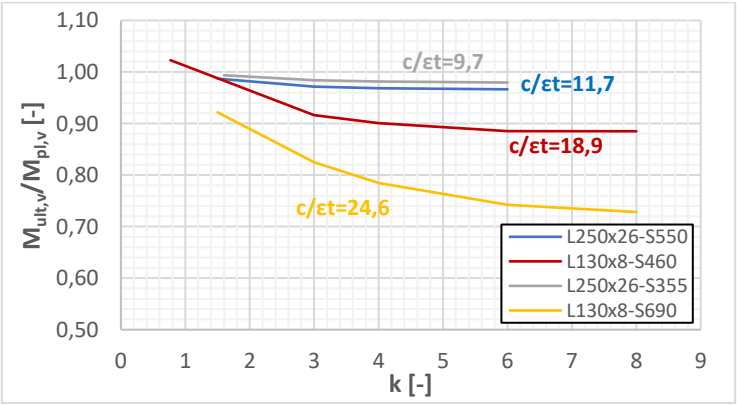

Figure 4.7: Weak axis bending – tip in compression. Ratio between numerical results and plastic resistance vs. the length parameter k

A number of numerical simulations have been performed to evaluate an optimal length value ($L = k \cdot h$), so that yielding develops freely along the member while the cross-section resistance is

independent of the length. It has been found that the value of the sample length $L = 6 \cdot h$ [mm], is working quite well (see Figure 4.7):

- for small $c/\varepsilon t$ ratios which corresponds to class 1 or 2 profiles, the difference between $L = 4 \cdot h$ and $L = 6 \cdot h$ is less than 0,5%, what is acceptable.
- for large $c/\varepsilon t$ ratios which corresponds to class 3 and 4 profiles, the difference between $L = 6 \cdot h$ and $L = 8 \cdot h$ is less than 1,8%, what is also acceptable.

The details and results of this specific parametric study are summarized in Table 4.4.

Table 4.4: Samples of the numerical simulations about the optimal length value

No	h [mm]	f_y [N/mm²]	t [mm]	c/εt	k	L=k·h [mm]	$M_{ult,v}$ [kNm]	$M_{pl,v}$ [kNm]	$M_{ult,v}/M_{pl,v}$ [-]
1	250	355	26	9,7	1,6	400	183,17	184,34	0,99
					3	750	181,43	184,34	0,98
					3,5	875	181,16	184,34	0,98
					4	1000	180,94	184,34	0,98
					6	1500	180,57	184,34	0,98
2	250	550	26	11,7	1,5	375	281,90	285,6	0,99
					3	750	277,57	285,6	0,97
					4	1000	276,54	285,6	0,97
					6	1500	275,98	285,6	0,97
3	130	460	8	18,9	0,77	100	21,42	20,94	1,02
					3	390	19,19	20,94	0,92
					4	520	18,86	20,94	0,90
					6	780	18,54	20,94	0,89
					8	1040	18,53	20,94	0,88
4	130	690	8	24,6	1,5	195	28,96	31,42	0,92
					3	390	25,92	31,42	0,82
					4	520	24,65	31,42	0,78
					6	780	23,32	31,42	0,74
					8	1040	22,88	31,42	0,73

Figure 4.8 shows the ratio between the numerical results for the cross-section resistance ($M_{ult,v}$) and the plastic characteristic resistance ($M_{pl,v}=W_{pl,v} \cdot f_y$), versus the $c/\varepsilon t$ ratio. The analytical expressions for the evaluation of $W_{pl,v}$ can be found in Annex A. From the numerical results, one can observe that the class-2 limit, where the samples reach their $M_{pl,v}$ even with a 3% deviation, is $c/t \leq 14\varepsilon$, while the class-3 limit (samples that reach their elastic resistance) is $c/t \leq 26,9\varepsilon$.

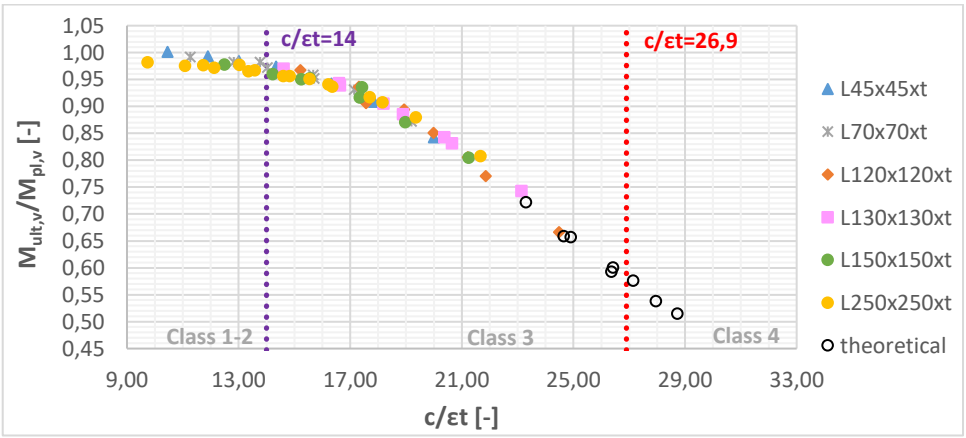

Figure 4.8: Weak axis bending – tip in compression. Ratio between numerical results and plastic resistance vs. c/εt ratio

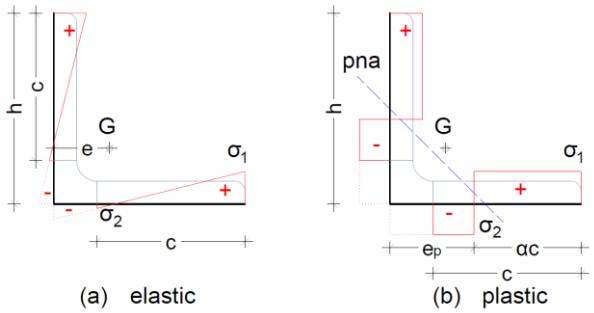

Figure 4.9: Stress distribution (compression taken as positive) for weak axis bending (M_v) – tip in compression

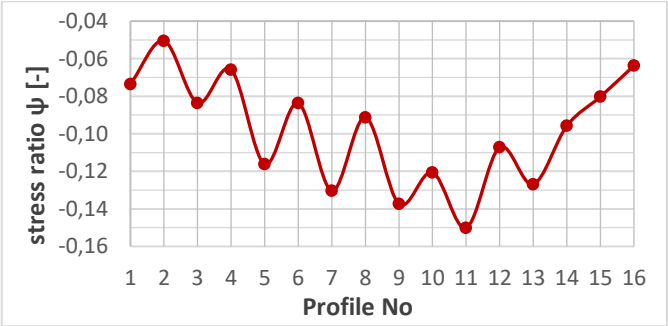

Figure 4.10: Stress ratio ψ for elastic stress distribution – tip in compression (angles from 70 to 300)

The stress ratio for elastic stress distribution (see Figure 4.9-a) is given by $\psi = \frac{\sigma_2}{\sigma_1} = -\frac{e-(h-c)}{h-e}$. As is shown in Figure 4.10, the stress ratio $\psi \approx -0,1$ for usual angle sections. Therefore, the buckling factor may be conservatively set equal to $k_\sigma = 0,57$ (valid for $\psi = 0$) and according to EN 1993-1-1, Table 5.2, sheet 2, the class-3 limit is:

$$c/t \leq 15,9\varepsilon \qquad \text{(Eq. 4.11)}$$

If now clamped boundary conditions are considered, as done for strong axis bending, the buckling factor is equal to $k_\sigma = 1,65$ (for stress ratio $\psi \approx -0,1$). Then, the class-3 limit may be obtained again from the general formula of EN 1993-1-1, Table 5.2, sheet 2 as follows:

$$\frac{c}{t} \leq 21\varepsilon\sqrt{k_\sigma} = 21\varepsilon\sqrt{1,65} = 26,9\varepsilon \qquad \text{(Eq. 4.12)}$$

The class-3 limit may so be defined accordingly as it is in agreement with the numerical results.

For the plastic stress distribution, the proportion of the leg in compression is $a = 1 - \frac{e_p - t - r}{h - t - r}$. By considering all the available angle sections, it can be seen that the value of α is ranging between 0,50 to 0,62 with a mean value of approximately 0,58 and a standard deviation of 2%, and therefore, a value of 0,60 is adopted. The class 2 limit may be accordingly obtained from the general formula of EN 1993-1-1, Table 5.2, sheet 2, from:

$$\frac{c}{t} \leq \frac{10\varepsilon}{a} = \frac{10\varepsilon}{0,6} = 16,6\varepsilon \qquad \text{(Eq. 4.13)}$$

The classification limits proposed currently by Eurocode 3, i.e. eq. (4.11) and eq. (4.13), are not at all consistent as the c/t-ratio for class 3 ($c/t \leq 15,9\varepsilon$) is lower than the one obtained for class 2 ($c/t \leq 16,6\varepsilon$). The reason is that the mechanical model for class 2 sections in Eurocode 3, when the tip is in compression, is not correct because the outstand elements partially in compression are treated as

elements fully in compression with a reduced width αc. This means that the hinge support is introduced exactly at the position where the compression starts. This is questionable since tension is beneficial to local buckling. For that reason, it is proposed here to keep the c/t limit for class 2 equal to:

$$\frac{c}{t} \leq 14\varepsilon \qquad \text{(Eq. 4.14)}$$

which is in good agreement with the numerical results.

4.4.2 Tip in tension

Table 4.5 presents the cross-sections and the steel grades that have been used for the analyses in which the pin-ended samples are subjected to weak axis bending moment *Mv*-tip in tension. As already explained for the previous cases, the last 8 analysis, i.e. 3* and 4* in Table 4.5, are theoretical so as to investigate the behaviour of the cross-section and validate the limit between class 2 and class 3. The value $L = 6 \cdot h$ [mm] for the length has been adopted in this case too, as explained in section 4.4.1.

Table 4.5: Details for the analyses of the cross-section subjected to weak axis bending Mv-tip in tension

No	Cross-Section	Steel grades
1	L120x120x7	S355 / S460 / S550 / S690
2	L120x120x8	S355 / S460 / S550 / S690
3*	L130x130x8	S720 / S850 / S1050 / S1250
4*	L130x130x9	S820 / S990 / S1200 / S2000

Figure 4.11 shows the ratio between the numerically obtained values of the cross-section resistance ($M_{ult,v}$) and the plastic resistance, according to the $c/\varepsilon t$ ratio.

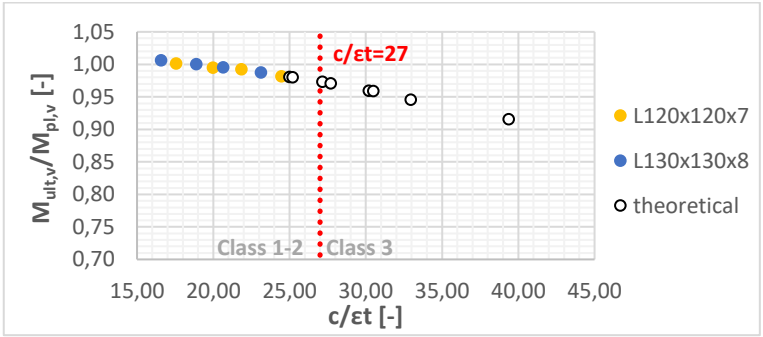

Figure 4.11: Weak axis bending – tip in tension. Ratio between numerical results and plastic resistance vs. c/εt ratio

From the numerical results, one can observe that the class-2 limit for equal leg angles subjected to weak axis bending when the tip is in tension, equals $c/t \leq 27\varepsilon$.

In the plastic domain, the proportion of the leg subjected to compression is $\alpha = \frac{e_p - t - r}{h - t - r}$ and taking $r = t$ as an approximation, it may be shown (Figure 4.12) that, for usual angle sections, it is $\alpha \approx 0{,}4$. Then, the class-2 limit may be obtained from the general formula of EN 1993-1-1, Table 5.2, sheet 2:

$$\frac{c}{t} \leq \frac{10\varepsilon}{\alpha\sqrt{\alpha}} = \frac{10\varepsilon}{0{,}4\sqrt{0{,}4}} = 39{,}52\varepsilon \qquad \text{(Eq. 4.15)}$$

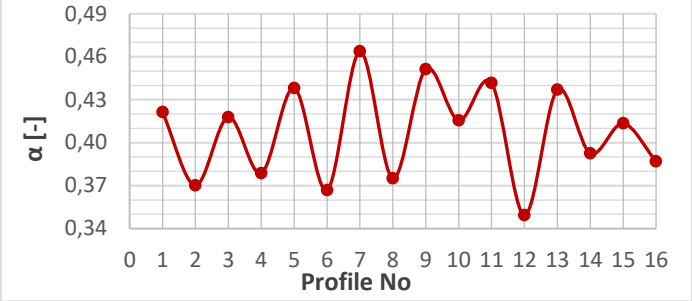

Figure 4.12: Ratios α for tip in tension (angles from 70 to 300)

At the end, the class-2 limit may be kept as provided by the numerical results ($c/t \leq 27\varepsilon$), which is on the safe side concerning the normative approach. In any case, both limits are far from the highest $c/\varepsilon t$ ratios obtained for available angles and steel grades. Therefore, all angle sections may practically always develop their plastic moment for weak axis bending when the tip is in tension.

4.5 Summary of classification for equal leg angle sections

The complete set of the proposed duly validated classification criteria is summarized in Table 4.6. It may be seen that, unlike in the current Eurocodes, the same geometric parameters, c and t, are used for all cross-section loading situations.

Table 4.6: Maximum width-to-thickness ratios for compression parts of equal leg angle sections

	Section in compression	**Section in strong axis bending M_u**	**Section in weak axis bending M_v – tip in compression**	**Section in weak axis bending M_v – tip in tension**
Class 1 – 2	---	$\frac{c}{t} \leq 16\,\varepsilon$	$\frac{c}{t} \leq 14\,\varepsilon$	$\frac{c}{t} \leq 27\,\varepsilon$
Class 3	$\frac{c}{t} \leq 13{,}9\,\varepsilon$	$\frac{c}{t} \leq 26{,}3\,\varepsilon$	$\frac{c}{t} \leq 26{,}9\,\varepsilon$	---
where $\varepsilon = \sqrt{235/f_y[\frac{N}{mm^2}]}$				

4.6 Conclusions

From the present study, involving numerical and analytical approaches, the following conclusions may be drawn:

- A proposal for the classification of equal leg angles, fully consistent with the Eurocode normative documents, is presented and validated numerically and analytically.
- Angle cross-sections are classified separately for compression, strong and weak axis bending.
- The numerical investigations have been performed with ABAQUS software using volume elements and are in very good agreement with the analytical developments.
- The classification boundary from class 3 to 4 of an angle cross-section subjected to different loadings, is determined through the slenderness of the compression leg and not the torsional instability mode as usually considered for other common profiles.
- The proposed classification rules are written in the format of the existing Eurocode 3, cover all cross-section classes and remove inconsistencies of existing specifications.

5. DESIGN RESISTANCES OF ANGLE CROSS-SECTIONS

In the following paragraphs, formulae for the evaluation of the cross-section design resistance of equal leg angles are proposed and validated through the numerical results obtained in chapter 4 concerning the classification. The formulae were based on those given in EN 1993-1-1 and were adjusted appropriately for angles sections when required. The notations for the material properties, safety factors and other properties follow those given in chapter 2, and therefore no further definitions are given here, unless it is necessary. Finally, based on the results obtained in the previous chapter of classification, a linear transition between plastic and elastic bending resistances is adopted. This smooth transition has been proposed and validated for double symmetric cross-sections in the SEMI-COMP European funded project [33] and will be adopted for these sections in the forthcoming new version of Eurocode 3 Part 1-1 (pr EN 1993-1-1 [26]).

5.1 Cross-section resistance to tension

The cross-section design resistance for axial tension may be determined from:

$$N_{t,Rd} = \frac{Af_y}{\gamma_{M0}} \qquad \text{(Eq. 5.1)}$$

The corresponding characteristic resistance $N_{t,Rk}$ is given by eq. (5.1), removing γ_{M0} from the equation. No modification is recorded here from the existing Eurocode 3, but is reported just for sake of completeness.

5.2 Cross-section resistance to compression

The proposed cross-section design resistance for axial compression may be determined from:

$$N_{c,Rd} = \begin{cases} \frac{Af_y}{\gamma_{M0}} & \text{for class 1,2 and 3 profiles} \\ \frac{A_{eff}f_y}{\gamma_{M0}} & \text{for class 4 profiles} \end{cases} \qquad \text{(Eq. 5.2)}$$

where,

A_{eff} is the area of the effective cross-section defined as:

$$A_{eff} = A - 2ct(1-\rho) \qquad \text{(Eq. 5.3)}$$

ρ is the reduction factor accounting for plate buckling, equal to:

$$\rho = \begin{cases} 1{,}0 & \text{for } \bar{\lambda}_p \le 0{,}748 \\ \frac{\bar{\lambda}_p - 0{,}188}{\bar{\lambda}_p^2} & \text{for } \bar{\lambda}_p > 0{,}748 \end{cases} \qquad \text{(Eq. 5.4)}$$

considering a reduced plate slenderness of the legs equal to:

$$\bar{\lambda}_p = \sqrt{\frac{f_y}{\sigma_{cr}}} = \frac{c/t}{28{,}4\varepsilon\sqrt{0{,}43}} = \frac{c/t}{18{,}6\varepsilon} \qquad \text{(Eq. 5.5)}$$

The corresponding characteristic resistance $N_{c,Rk}$ is given by eq. (5.2), removing γ_{M0} from the equation.

In order to be in line with the classification limits as derived in section 4.2, the geometric property $\bar{b}$ must be defined differently than in the current Eurocode provisions. Consequently, the statement of EN 1993-1-5, §4.4(2) that $\bar{b} = h$ for equal leg angles should be replaced for this type of section by

$\bar{b} = c$. This constitutes the only difference between the current proposal and the existing Eurocode 3 provisions.

Figure 5.1 shows the ratio between the numerically determined cross-section resistance (N_{ult}), and the characteristic resistance ($N_{c,Rk}$), versus the $c/\varepsilon t$ ratio. It may be seen that the response is not influenced by the cross-section size. Furthermore, it may be seen that, for stocky class 1 to 3 legs, there is a small overestimation of resistance by the proposed formulae. However, this is largely counterbalanced by strain hardening effect that is not considered in the numerical analysis. For class-4 sections the proposed rules are largely on the safe side.

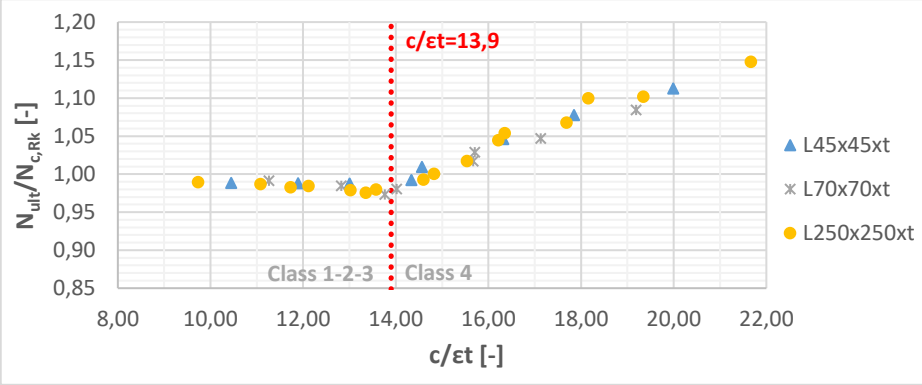

Figure 5.1: Cross-section resistance to compression. Ratio between numerical results and characteristic compression resistance vs. c/εt ratio

Figure 5.2 illustrates the ratio between the numerically determined cross-section resistance (N_{ult}), and the design resistance ($N_{c,Rd}$), versus the $c/\varepsilon t$ ratio. The design resistances have been evaluated firstly with the current proposal and then based on the existing provisions of EN 1993-1-1 in combination with EN 1993-1-5 for class-4 sections. The vertical dot lines represent the class-3 limit as suggested in chapter 4 ($c/t \leq 13{,}9\varepsilon$) and the one calculated using Eurocode 3 provisions ($c/t \leq 11{,}1\varepsilon$ – eq. (4.6)). It can be easily seen that the proposed model is less conservative for class-4 profiles while still remaining on the safe side.

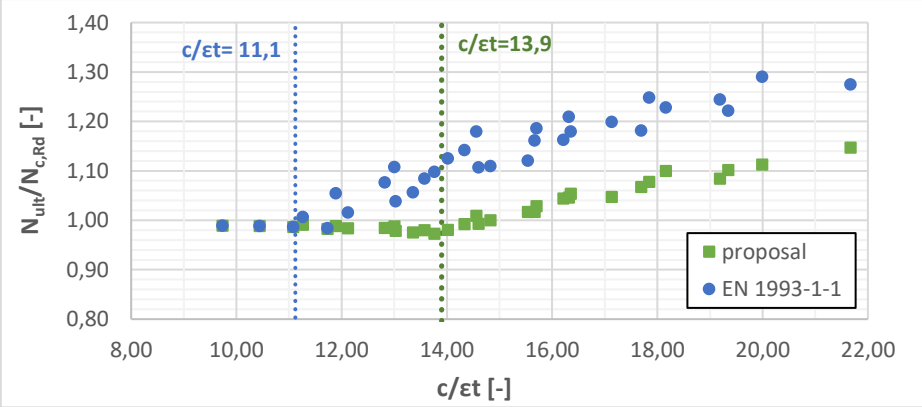

Figure 5.2: Cross-section resistance to compression. Ratio between numerical results and design compression resistance obtained from the current proposal and Eurocode 3 vs. c/εt ratio

5.3 Cross-section resistance to strong axis bending

The proposed cross-section design resistance to strong axis bending M_u may be determined from:

$$M_{u,Rd} = W_u \frac{f_y}{\gamma_{M0}} \qquad \text{(Eq. 5.6)}$$

where,

W_u is the section modulus about u axis that equals:

$$W_u = \alpha_{i,u} W_{el,u} \text{ with } i = 2, 3, 4 \quad \text{(Eq. 5.7)}$$

where,

$\alpha_{2,u} = 1{,}5$ for class 1 or 2 (Eq. 5.8)

$\alpha_{3,u} = \left[1 + \left(\frac{26{,}3\varepsilon - c/t}{26{,}3\varepsilon - 16\varepsilon}\right) \cdot (1{,}5 - 1)\right]$ for class 3 (Eq. 5.9)

$\alpha_{4,u} = W_{eff,u} / W_{el,u} = \rho_u^2$ for class 4 (Eq. 5.10)

ρ_u is the reduction factor for plate buckling, determined from eq. (5.4) considering a plate slenderness of legs expressed by:

$$\bar{\lambda}_p = \sqrt{\frac{f_y}{\sigma_{cr}}} = \frac{c/t}{28{,}4\varepsilon\sqrt{1{,}57}} = \frac{c/t}{35{,}6\varepsilon} \quad \text{(Eq. 5.11)}$$

For strong axis bending of class-4 sections, the effective cross-section becomes non-symmetric due to the fact that only one leg is in compression (see Figure 5.3(b)). This changes the position of the centroid, the directions of the principal axes and all cross-section properties. In order to avoid such laborious calculation, an approximate solution for the effective section modulus is envisaged. This may be achieved by reducing equally the other leg too, an approach that is on the safe side (see Figure 5.3(c)). The comparison of the ratio between the initial and the approximate effective cross-section, is shown in Figure 5.4. It may be seen that the proposed approach, applied to a large number of cross-sections, is on the safe side.

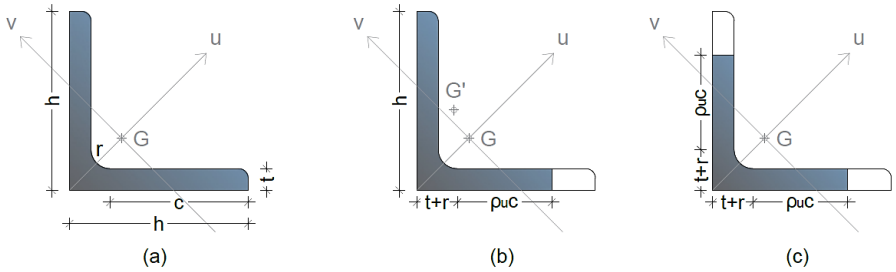

Figure 5.3: (a) Initial cross-section, (b) actual effective cross-section and (c) Approximate effective cross-section

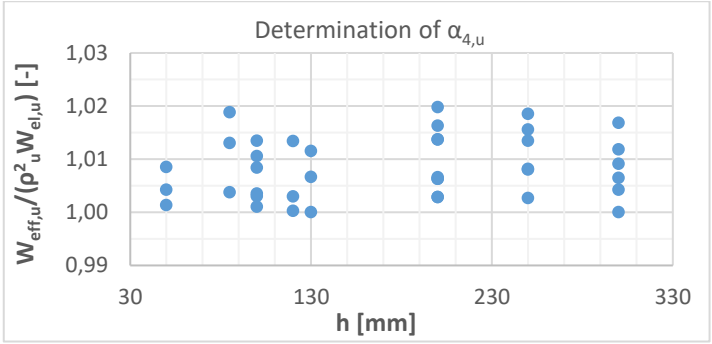

Figure 5.4: Ratio of the strong axis moduli between the initial and the effective cross-section

Figure 5.5 shows the ratio between the numerically determined cross-section resistance ($M_{ult,u}$), and the characteristic resistance ($M_{u,Rk}$), versus the $c/\varepsilon t$ ratio. It may be seen that the response is not

influenced by the cross-section size. For stocky class 1 and 2 legs, the proposed formulae predict almost exactly the resistance. For class-3 sections there is a small overestimation of resistance in a very limited range of $c/\varepsilon t$-ratios, while for class-4 sections the proposed rules are always on the safe side.

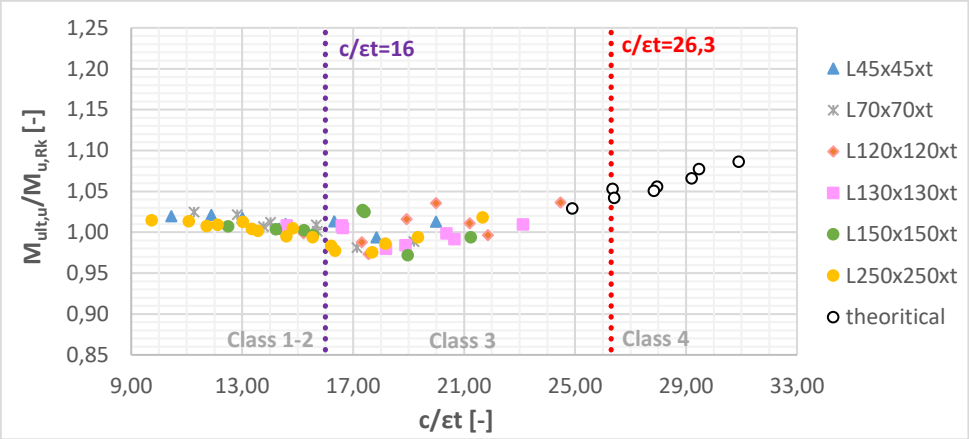

Figure 5.5: Cross-section resistance to strong axis bending. Ratio between numerical results and characteristic moment resistance vs. c/εt ratio

Figure 5.6 illustrates the ratio between the numerically determined cross-section resistance ($M_{ult,u}$), and the design resistance ($M_{u,Rd}$), versus the $c/\varepsilon t$ ratio. The design resistances have been evaluated both with the current proposal and the existing provisions of EN 1993-1-1. The vertical green and blue dot lines represent respectively the class limits as suggested in chapter 4 (i.e $c/t \leq 16\varepsilon$ for class 2 to 3 and $c/t \leq 26{,}3\varepsilon$ for class 3 to 4) and as calculated using EN 1993-1-1 provisions (i.e $c/t \leq 10\varepsilon$ for class 2 to 3 and $c/t \leq 15{,}3\varepsilon$ for class 3 to 4). The benefits and the improvements coming from the proposals in terms of classification and cross-section resistance on the design of the cross-sections under strong axis bending may be clearly observed.

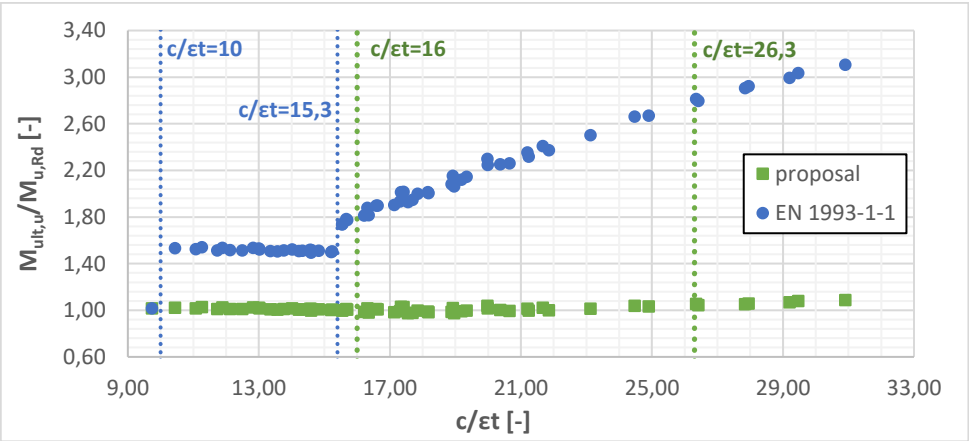

Figure 5.6: Cross-section resistance to strong axis bending. Ratio between numerical results and design resistance obtained from the current proposal and Eurocode 3 vs. c/εt ratio

5.4 Cross-section resistance to weak axis bending

5.4.1 Tip in compression

The design characteristic resistance of angle cross-sections to weak axis bending M_v –when the tip is in compression – may be determined from:

$$M_{v,Rd} = W_v \frac{f_y}{\gamma_{M0}} \quad \text{(Eq. 5.12)}$$

where,

W_v is the section modulus about v axis that equals:

$$W_v = \alpha_{i,v} W_{el,v} \text{ with } i = 2, 3, 4 \quad \text{(Eq. 5.13)}$$

where,

$\alpha_{2,v} = W_{pl,v}/W_{el,v}$ for class 1 or 2 (Eq. 5.14)

$\alpha_{3,v} = \left[1 + \left(\frac{26{,}9\varepsilon - c/t}{26{,}9\varepsilon - 14\varepsilon}\right) \cdot \left(\alpha_{2,v} - 1\right)\right]$ for class 3 (Eq. 5.15)

$\alpha_{4,v} = W_{eff,v}/W_{el,v} = 0{,}94 \cdot \rho_v^2$ for class 4 (Eq. 5.16)

ρ_v is the reduction factor for plate buckling, determined from eq. (5.4) considering a plate slenderness of legs expressed by:

$$\bar{\lambda}_p = \sqrt{\frac{f_y}{\sigma_{cr}}} = \frac{c/t}{28{,}4\varepsilon\sqrt{1{,}65}} = \frac{c/t}{36{,}5\varepsilon} \quad \text{(Eq. 5.17)}$$

It should be noted that, for weak axis, $W_{pl,v} \neq 1{,}50 \cdot min(W_{el,v}^{tip}, W_{el,v}^{toe})$, in contrast with the case of strong axis bending. However, based on the numerically tested samples, it appears that $W_{pl,v} = (1{,}65 \sim 1{,}95) \cdot min(W_{el,v}^{tip}, W_{el,v}^{toe})$ and so, a value $\alpha_{2,v} = 1{,}75$ could be possibly adopted as a rough estimation for a preliminary design.

For class 4 cross-sections, a similar procedure than for strong axis bending is followed. Figure 5.7 shows that the modulus of the effective cross section is approximately equal to the modulus of the initial cross-section multiplied with the factor $0{,}94 \cdot \rho_v^2$. Therefore, $\alpha_{4,v}$ is fixed accordingly.

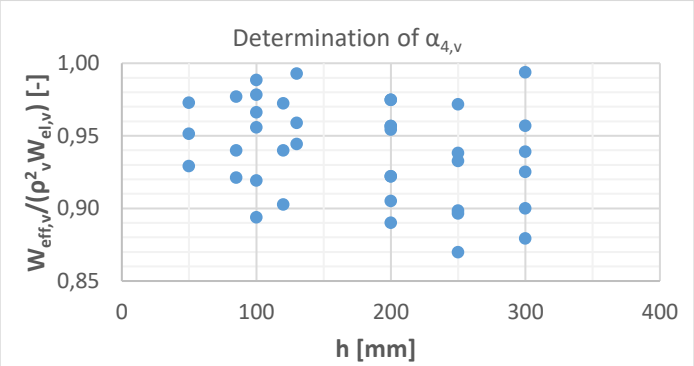

Figure 5.7: Ratio of the weak axis section moduli between the full and the effective cross-section

Figure 5.8 shows the ratio between the numerically determined cross-section resistance ($M_{ult,v}$), and the characteristic resistance ($M_{v,Rk}$ using the exact value of $W_{pl,v}$), versus the $c/\varepsilon t$-ratio. It may be seen that the response is not influenced by the cross-section size. For stocky legs of class 1 and 2, entering even in class-3, there is a small overestimation of resistance. This may be counterbalanced by strain hardening effect not considered here. This is also observed for large $c/\varepsilon t$-ratios in the border between class 3 and 4. However, such ratios are not corresponding to existing hot-rolled angle profiles.

Figure 5.9 illustrates the ratio between the numerically determined cross-section resistance ($M_{ult,v}$), and the design resistance ($M_{v,Rd}$), versus the $c/\varepsilon t$ ratio. The design resistances have been evaluated

both with the current proposal and the existing provisions of EN 1993-1-1. The vertical green and blue dot lines represent respectively the class limits as suggested in chapter 4 (i.e $c/t \leq 14\varepsilon$ for class 2 to 3 and $c/t \leq 26{,}9\varepsilon$ for class 3 to 4) and as calculated using EN 1993-1-1 provisions (i.e c/t ≤ 16,6ε for class 2 to 3 and $c/t \leq 16\varepsilon$ for class 3 to 4 as explained in section 4.4.1, the profiles in between 26 and 16,6 are treated as class 4 sections for the calculations). The benefits and the improvements brought from the current proposals (classification and cross-section resistance) on the design of the sections is again clearly observed.

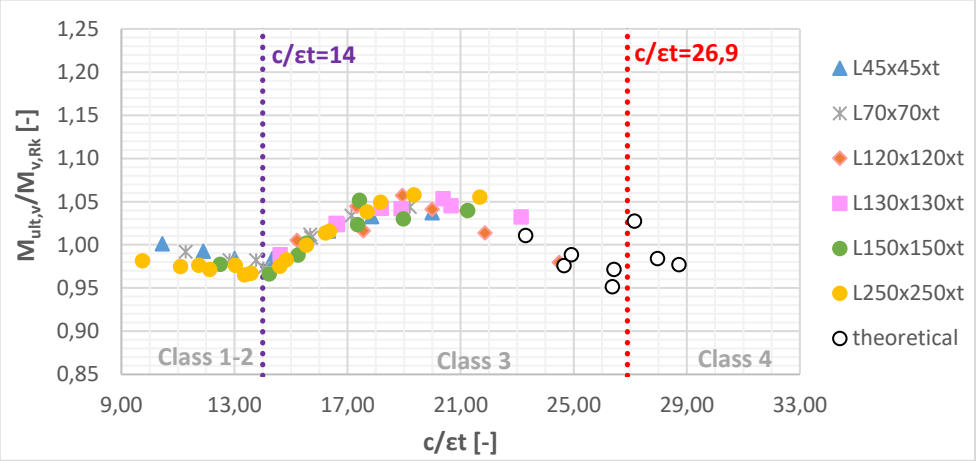

Figure 5.8: Cross-section resistance to weak axis bending – tip in compression. Ratio between numerical results and characteristic moment resistance vs. c/εt ratio Tip in tension

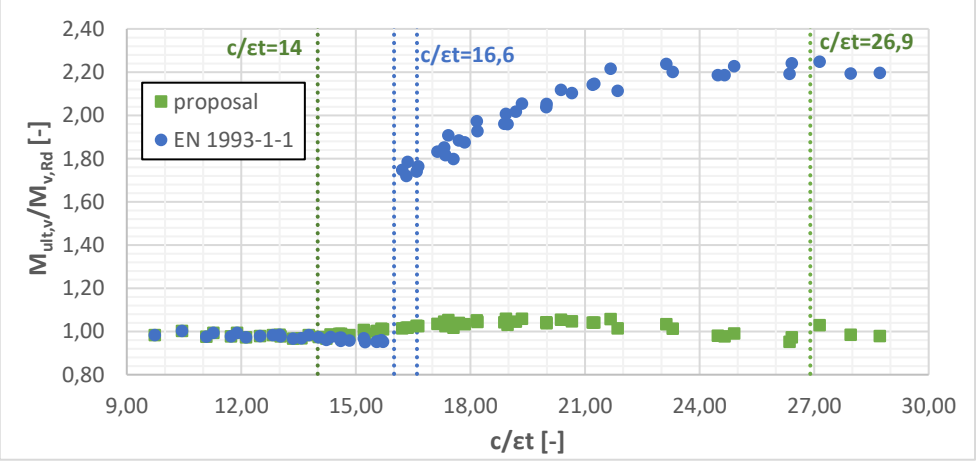

Figure 5.9: Cross-section resistance to weak axis bending– tip in compression. Ratio between numerical results and design resistance obtained from the current proposal and Eurocode 3 vs. c/εt ratio

5.4.2 Tip in tension

The design resistance of angle cross-sections to weak axis bending M_v – tip in tension – may be determined from:

$$M_{v,Rd} = W_{pl,v} \frac{f_y}{\gamma_{M0}} \qquad \text{(Eq. 5.18)}$$

As it is shown in Figure 4.11 for $c/\varepsilon t$ ratio less than 27, the analytical approach for the cross-section resistance subjected to weak axis bending, when the tip is in tension, is in good agreement with the numerical results.

5.5 Conclusions

The main features of the proposed design rules are summarized below:

- The proposed design rules are based on theoretical-analytical considerations and are duly validated through extensive numerical investigations.
- They are written respecting the format of the existing Eurocode 3 specifications.
- They are simple to apply.
- They include all important loading conditions such as compression, weak and strong axis bending.
- They allow a smooth transition between cross-section classes, removing any artificial stepwise prediction of resistance.
- They are less conservative than the current design rules proposed by Eurocode 3.

6. COMPRESSION TESTS ON HIGH STRENGTH STEEL COLUMNS

To extend the knowledge for the stability behaviour of steel columns from high strength steel (S460M) angle cross-sections subjected to compression and bending, twelve buckling tests on such columns have been performed at Liège University. The experiments have been limited to high strength steel only, given the fact that several compression tests on angles with lower steel grades were already available in the literature [11]-[13]-[14]-[15]. The selection of the specimens, the details about the experimental campaign such as measurements before and during the tests, as well as the test results, are presented in this chapter. The tests have been accompanied by numerical simulations, performed considering relevant imperfections as well as geometrical and material non-linearities. The numerical results have been then compared and validated with the experimental ones.

6.1 Details of the tested specimens

For the experimental program, two profiles from large angle cross-sections (L150x150x18 and 200x200x16) made of S460M steel grade have been selected. For each profile, six column tests have been performed with three different lengths per profile and two positions of load application for each length. The selected points are (see Figure 6.1) the centre of gravity (G), which corresponds to pure compression in the angle cross-section and the intersection point of minor principal axis v-v with the middle line of the leg thickness (P_2), which represents the position of the connecting bolt for angles in structures.

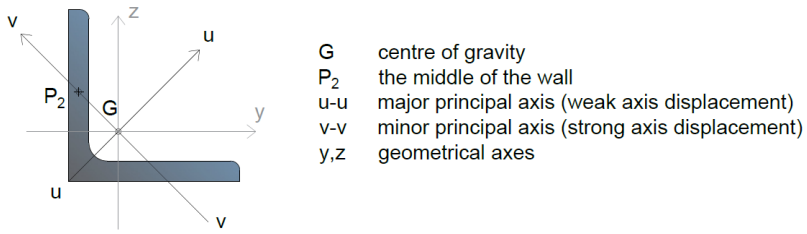

Figure 6.1: Definition of the axes and position of the load application points (G and P_2)

Table 6.1: Details about the specimens

ID of Specimen	Profile	Steel grade	Length of angle member L [mm]	Eccentricity [mm]
Sp11	L 150x150x18	S460M	2500	0,00
Sp12	L 150x150x18	S460M	2500	e_v = 48,74
Sp13	L 150x150x18	S460M	3000	0,00
Sp14	L 150x150x18	S460M	3000	e_v = 48,74
Sp15	L 150x150x18	S460M	3500	0,00
Sp16	L 150x150x18	S460M	3500	e_v = 48,74
Sp21	L 200x200x16	S460M	3000	0,00
Sp22	L 200x200x16	S460M	3000	e_v = 66,64
Sp23	L 200x200x16	S460M	3500	0,00
Sp24	L 200x200x16	S460M	3500	e_v = 66,64
Sp25	L 200x200x16	S460M	4000	0,00
Sp26	L 200x200x16	S460M	4000	e_v = 66,64

Table 6.1 summarizes all the details about the specimens. The reported length is the one of the angle member, without considering the end plates. The system length is defined in §6.4. The name of each specimen consists of two numbers Sp## (e.g. Sp12):

- the first number indicates the profile: 1 for L150x150x18 and 2 for 200x200x16;
- the second one is the serial number of the specimen (1 to 6 per profile).

For all tests, constant dimensions have been selected for the end plates welded at the extremities of the angle members, in order to simplify the placement procedure of the specimen in the test rig. Therefore, the position of the applied load is always the same for the machine and the eccentricity is introduced by moving the profile on the end plates. The steel grade of all end plates is S355. The welds have been designed according to EN 1993-1-8 [3]. For all specimens, the minimum required weld thickness is 6 mm, except for specimens Sp11 and Sp21 which require a minimum thickness of 8 mm. Figure 6.2 shows the details of such end plates on which the specimens have been welded.

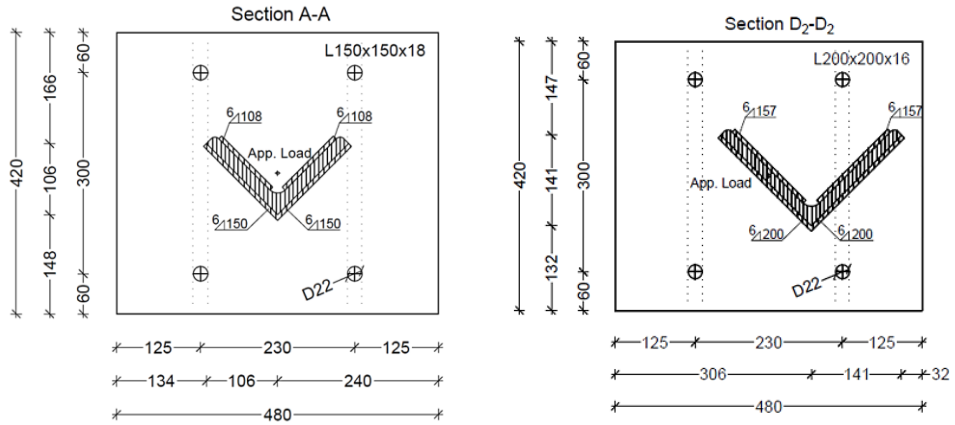

Figure 6.2: Detail of end plates in case of centrally (left) and eccentrally (right) loaded specimens.

6.2 Test measurements

6.2.1 Actual dimensions of the cross-sections

The actual geometrical dimensions of each angle section – the width (h_i) and the thickness (t_i) of each leg – have been measured at 3 points along the member: at 1/4, 1/2 and 3/4 of the angle member length (L). The mean values of the measurements are reported in Table 6.2; the notations can be found in chapter 2, while indexes A and B are determined in Figure 6.3. The length of the angle member and the load eccentricity of each specimen has been also measured and reported in Table 6.2.

Table 6.2: Measurements of the actual geometry and dimensions of the cross-sections

ID of specimen	L [mm]	Eccentricity [mm]	h_A [mm]	h_B [mm]	t_A [mm]	t_B [mm]
Sp11	2500	0,00	149,97	150,09	18,16	18,14
Sp12	2500	e_v = 48,71	150,07	150,12	18,18	18,04
Sp13	3000	0,00	150,11	149,92	18,04	18,16
Sp14	3000	e_v = 48,72	150,09	150,10	18,04	18,17
Sp15	3500	0,00	150,07	150,11	18,17	18,07
Sp16	3500	e_v = 48,70	150,11	149,95	18,16	18,19

ID of specimen	L [mm]	Eccentricity [mm]	h_A [mm]	h_B [mm]	t_A [mm]	t_B [mm]
Sp21	3000	0,00	200,31	200,41	16,32	16,34
Sp22	3000	e_v = 66,60	200,36	200,39	16,39	16,29
Sp23	3500	0,00	200,25	199,92	16,32	16,28
Sp24	3500	e_v = 66,65	200,05	200,01	16,42	16,10
Sp25	4000	0,00	199,96	200,27	16,33	16,35
Sp26	4000	e_v = 66,63	200,06	200,39	16,32	16,31
$h_i = 1/3(h_{iL1/4}+h_{iL1/2}+h_{iL3/4})$ (i = A, B) ; $t_i = 1/3(t_{iL1/4}+t_{iL1/2}+t_{iL3/4})$ (i = A, B)						

6.2.2 Measurement of initial geometrical imperfections along the member length

Two displacement measurements (M1 & M2) on each external face (Face A & Face B) and along the column length have been performed to evaluate the initial imperfections of the specimens. Figure 6.3 shows the details of the set-up. Due to the end plates and the measurement system itself, it was not possible to take measurements quite close to the ends of the specimens. As a result, all the measurements start at 140 mm from the top end plate and finish at 140 mm from the bottom one. A measurement has been taken every 50 mm along the column. It has been reasonably assumed that the columns are straight close to the end plates (140 mm).

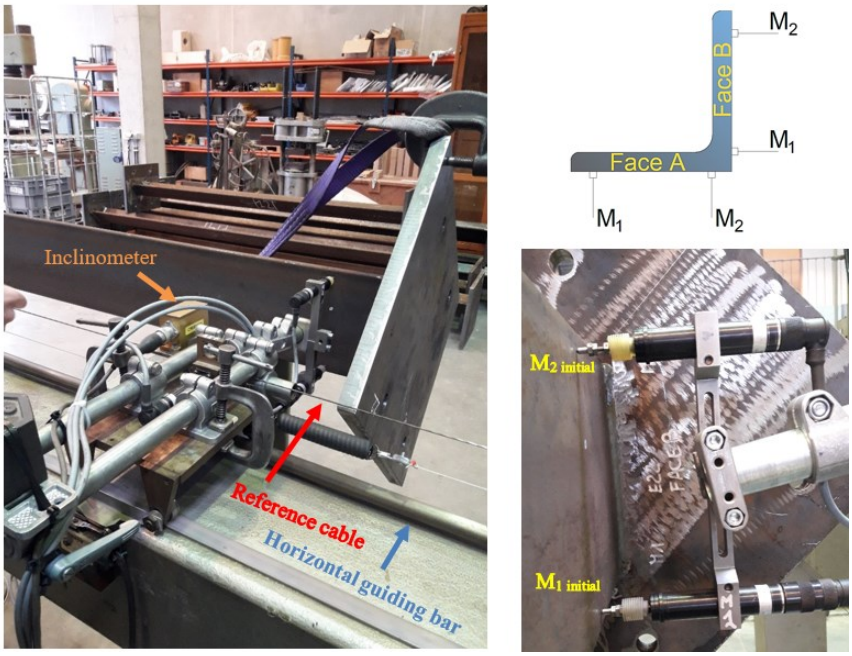

Figure 6.3: Measurement system for geometrical imperfections (left), detail and position of the displacement transducers (right)

Different corrections had to be made on the so-obtained raw measurements:

- As the chariot supporting the displacement transducers was moving onto a horizontal guiding bar (see Figure 6.3), a small rotation of the metric system was occurring; this one has been measured with an inclinometer, so allowing correcting the measurements accordingly.
- In addition, the specimen was not perfectly parallel to the set-up. To account for this effect, the relative position of the specimen from a prestressed reference cable (see Figure 6.3) was measured.

- Finally, a last correction has been done in order to assume a zero imperfection at the extremities of the column to account for the fact that the first and last measurements are realised at 140 mm from the end plate.

This procedure has been followed for face A and face B. All the results from the measured geometrical imperfections can be found in the relevant technical report [34]. An example of the initial measurements and of the corrected geometrical imperfections for Sp15 are presented in Figure 6.4 and Figure 6.5 respectively.

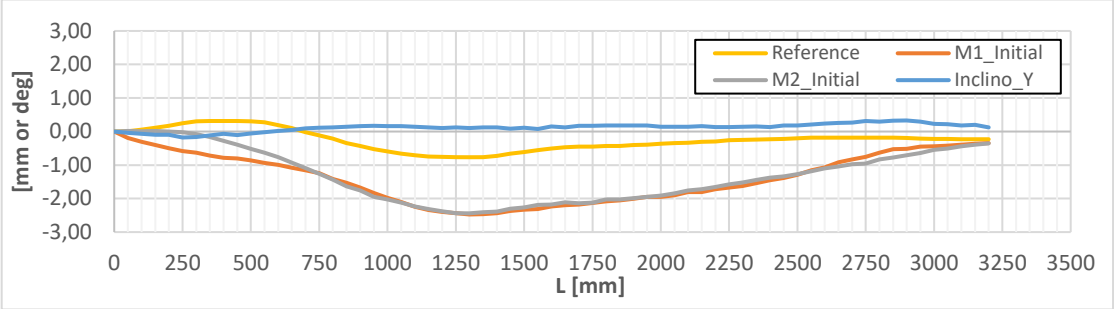

Figure 6.4: Initial measurements of geometrical imperfections for Sp15-face B

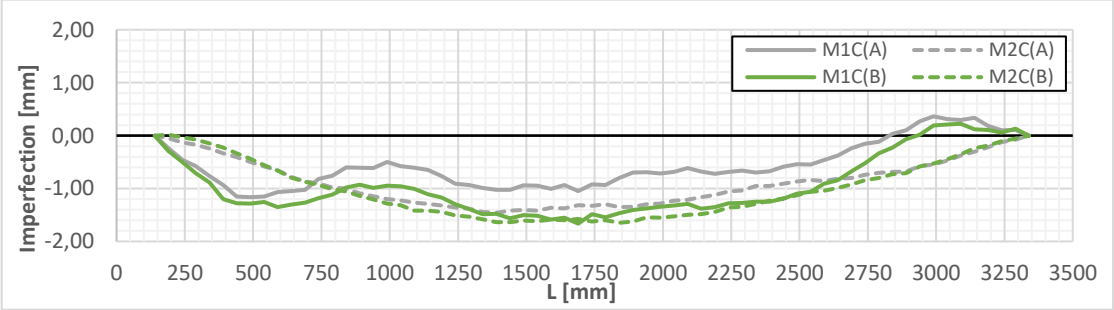

Figure 6.5: Initial geometrical imperfections of both faces along specimen Sp15

An accurate comparison between the actual measured imperfections of the specimens and those assumed in the Eurocode is difficult to perform as explained here after. The European norm EN 1090-2 [35] prescribes that the deviation from straightness should be $\Delta \leq L[mm]/750$ while, in prEN 1993-1-14 [29], it is stated that 80% of the geometric fabrication tolerances given in [35] should be applied. This leads to an initial bow imperfection of magnitude approximately equal to $L[mm]/1000$ and, usually, a deformation shape similar to the first member instability mode is assumed. However, in reality, the shape is more complex. For this reason, only a rough comparison can be done at this level (see Table 6.3) through the evaluation of an experimental estimated value $|Max|_{imperf}$ obtained by taking into account the maximum value [M_{1CA}, M_{1CB} , M_{2CA} , M_{2CB}] and by assuming that it is the same in both faces:

$$|Max|_{imperf} = \max\{M_{1CA}, M_{2CA}, M_{1CB}, M_{2CB}\} \cdot \sqrt{2} \qquad \text{(Eq. 6.1)}$$

where:

M_{1CA} is the M_1 maximum final corrected measurement on face A for specimen i;

M_{2CA} is the M_2 maximum final corrected measurement on face A for specimen i;

M_{1CB} is the M_1 maximum final corrected measurement on face B for specimen i;

M_{2CB} is the M_2 maximum final corrected measurement on face B for specimen i.

Table 6.3: Maximum values of the actual initial imperfections of the specimens compared with those prescribed by the European regulations [29]-[35]

ID of specimen	L/1000 [mm]	$\|Max\|_{imperf}$ [mm]
Sp11	2,5	0,4
Sp12	2,5	1,2
Sp13	3,0	1,3
Sp14	3,0	0,8
Sp15	3,5	2,4
Sp16	3,5	3,0
Sp21	3,0	1,6
Sp22	3,0	2,7
Sp23	3,5	1,7
Sp24	3,5	2,8
Sp25	4,0	1,5
Sp26	4,0	1,8

From this table, it can be observed that the measured imperfections are smaller than the geometrical tolerances prescribed in European regulations for all specimens.

6.2.3 Coupon tests for the material properties

Coupon tests have been performed in accordance with ISO 6892-1 [36]. The samples for the tensile tests have been extracted from one of the extremities of the angle member (see Figure 6.6) after the buckling tests, based on ISO 377 [37].

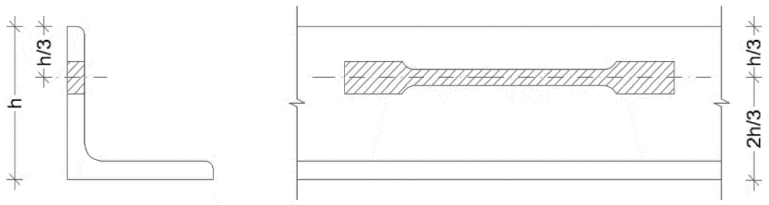

Figure 6.6: Location of tensile samples for coupon tests based on [37]

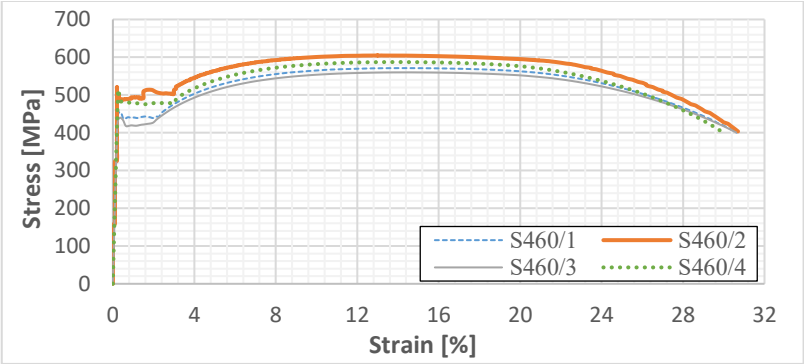

Figure 6.7: Stain-stress curves from the coupon tests

Figure 6.7 shows the strain-stress curves obtained from few tensile tests and Table 6.4 provides the characteristic values for all. The yield stress f_y (engineering stress) is determined by the value of the yield plateau in the curves and defers from the upper value yield stress *ReH*. It may be observed that

while the actual ultimate stress was above the nominal values for all specimens, this was not the case for the yield stress.

Table 6.4: Coupon test's results

ID of material	E [MPa]	Measured yield stress f_y [MPa]	Measured ultimate stress f_{ult} [MPa]	Measured strain at failure [%]	Nominal yield stress $f_{y,nom}$ [MPa]	$f_y/f_{y,nom}$ [-]	Characterized specimens
S 460/1	203155	425,8	572,50	14,3	460,0	0,93	Sp12, Sp13, Sp14, Sp15, Sp16
S 460/2	208947	487,6	604,64	13,7	460,0	1,06	Sp21, Sp22, Sp23, Sp25, Sp26
S 460/3	197317	417,2	560,87	14,3	460,0	0,91	Sp11
S 460/4	203797	472,6	587,21	13,8	460,0	1,03	Sp24

6.2.4 Measurements during the test

The tests have been carried out in an Amsler 500 testing machine, with a compression capacity of 5000 kN. The specimens are pin ended in the testing rig, since the rotations about the minor and major axes can develop freely, but no twist or warping is able to occur at the extremities. During the tests, the following displacements illustrated in Figure 6.8 were measured:

- the vertical displacement C_1 (using two transducers: one at the front and one at the back side of the specimen);
- four horizontal displacements C_2, C_3, C_4 and C_5 at the mid cross-section (1st position);
- four horizontal displacements C_6, C_7, C_8 and C_9 at the cross-section located at ¼L from the bottom (2nd position).

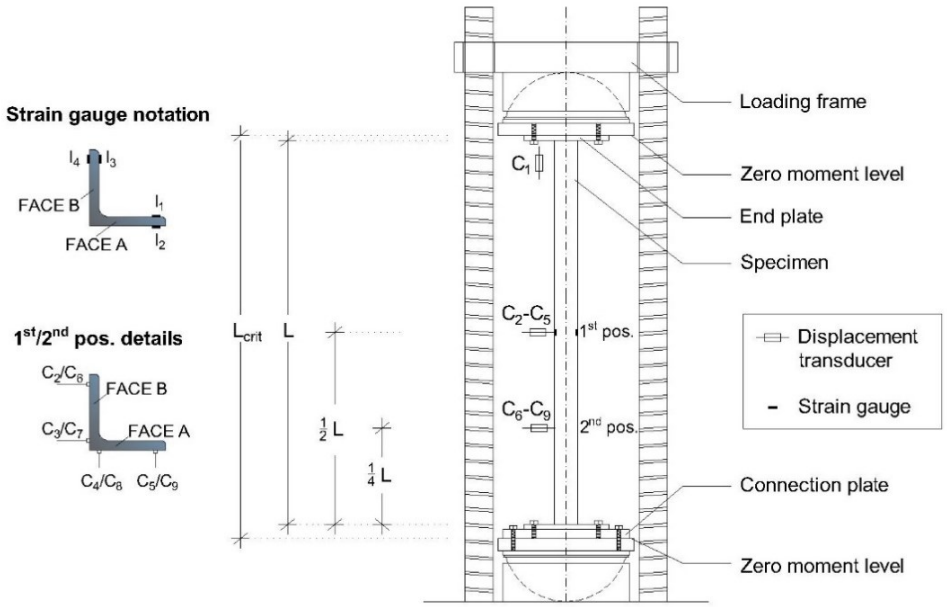

Figure 6.8: Schemes of the Amsler 500 test machine and of the measurements during a test

All the displacement transducers have been placed 30 mm from the edges/corner of all cross-sections and profiles. The set-up allowing the record of those displacements is illustrated in Figure 6.9. In addition, four strain gauges (I_1 to I_4) have been placed at the mid-height cross-section of each column

in order to check local yielding. The strain gauges have been positioned as close as possible to the leg extremities, accounting for the curvature of the latter.

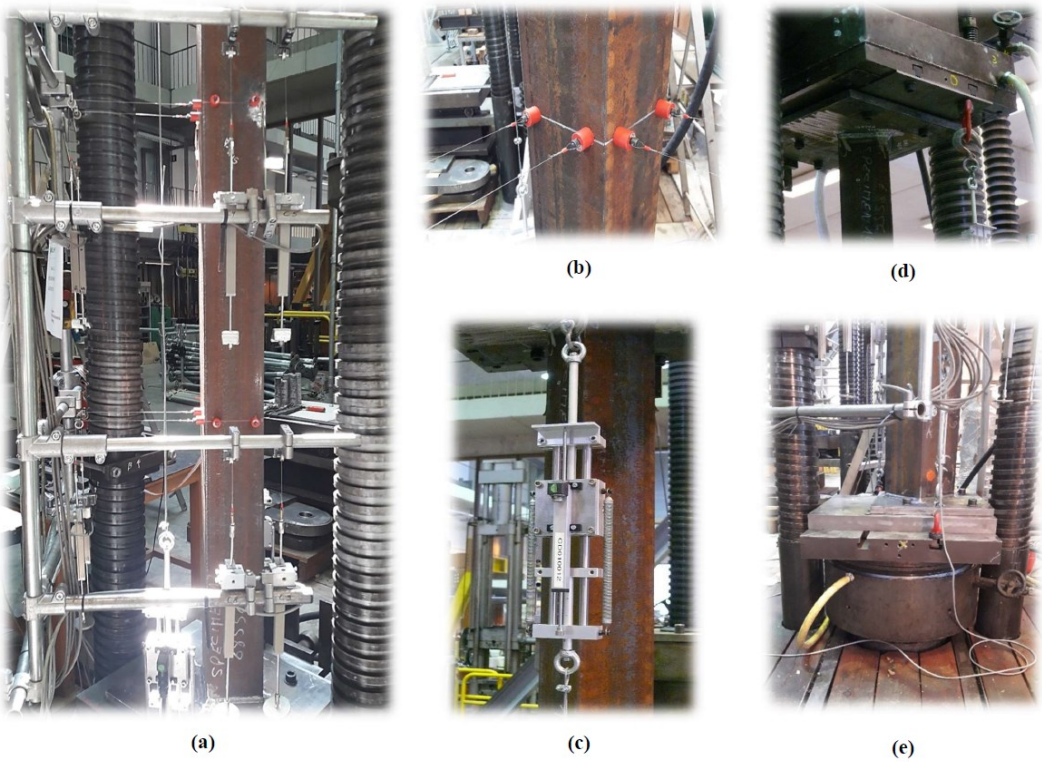

Figure 6.9: (a) General view of test rig with the measurement devices, (b) connection points of displacement transducers on the cross-section, (c) vertical displacement transducer, (d) detail of the top bearing plate and (e) detail of the bottom bearing plate

6.2.5 Mathematical interpretation of the measurements

The displacements of the corner of the angle (O point) as well as the twist of the cross-section, that are reported in the graphs of section §6.3, have been evaluated using the following formulae (for the definition of the axes and symbols, see Figure 6.10 left):

$$y_O = C_3 + 30 \cdot \frac{C_3 - C_2}{d}\ [mm] \qquad \text{(Eq. 6.2)}$$

$$z_O = C_4 - 30 \cdot \frac{C_5 - C_4}{d}\ [mm] \qquad \text{(Eq. 6.3)}$$

$$\theta = \frac{1}{2}\left(atan\left(\frac{C_3 - C_2}{d}\right) + atan\left(\frac{C_5 - C_4}{d}\right)\right) \cdot 1000\ [mrad] \qquad \text{(Eq. 6.4)}$$

where *d = 90* or *140* [mm] for L150x150x18 or L200x200x16 respectively.

The formulae are given for the middle cross-section, but they may also be used for the lower one, by replacing C_2, C_3, C_4 and C_5 by C_6, C_7, C_8 and C_9 respectively.

To transform the displacements from the geometrical axes to the principal ones (see Figure 6.10 right), the following equations have been used:

$$u_i = y_i cos\theta + z_i sin\theta = (y_i + z_i) \cdot \frac{\sqrt{2}}{2} \qquad \text{(Eq. 6.5)}$$

$$v_i = z_i cos\theta - y_i sin\theta = (z_i - y_i) \cdot \frac{\sqrt{2}}{2} \qquad \text{(Eq. 6.6)}$$

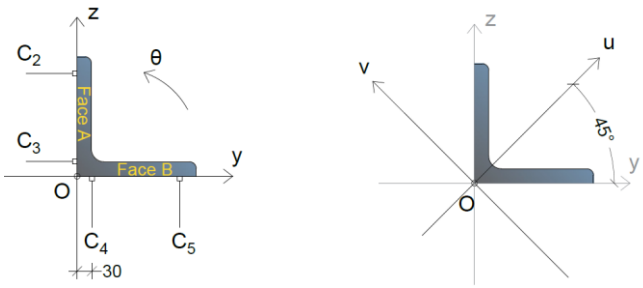

Figure 6.10: Definition of axis and symbols for the mathematical interpretation

The axial deformation of the specimen has been evaluated as the mean value of both vertical transducers.

6.3 Results of the experimental tests

The results of the experimental tests are presented below through graphs and tables. Figure 6.11 and Figure 6.12 show the load-axial displacement (shortening) curves for the profiles L150x150x18 and L200x200x16 respectively. All the measurements (initial geometrical imperfections, rotations, strains and deflections) for each specimen are available in the relevant technical report [34].

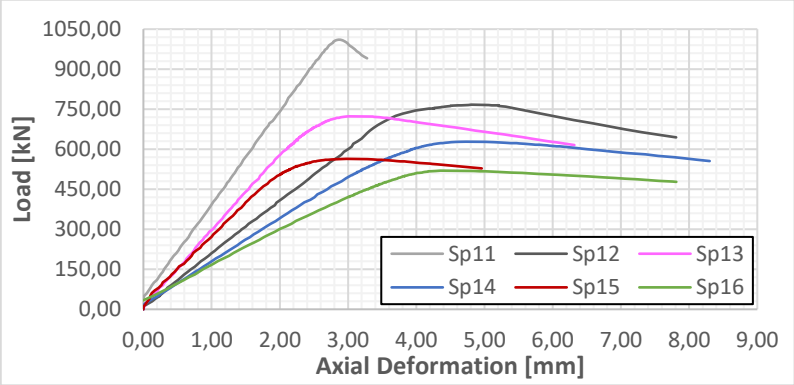

Figure 6.11: Load vs axial deformation of tested profiles L 150x150x18

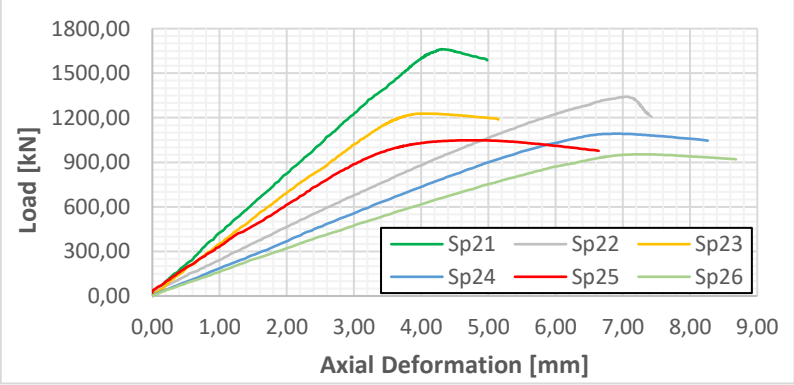

Figure 6.12: Load vs axial deformation of tested profiles L 200x200x16

Both figures indicate that the results obtained by experimentation are in line with the expectations when the test campaign was defined, in particular in terms of influence of the member length and of the eccentricity on the member stiffness and resistance.

Amongst the specimens without nominal load eccentricity, three (Sp11, Sp15, Sp25) showed nearly zero deflections transverse to the weak axis and three (Sp13, Sp21, Sp23) showed very small ones (see Figure 6.13). For the latter, it may indicate that some limited unintentional eccentricity resulting from installation tolerances were introduced as explained later. Nevertheless, for all these tests, the deflections according to the weak axis increased significantly with the load until failure was reached by weak axis buckling; towards the heel of the cross section for Specimens Sp13, Sp15, Sp25 (negative value of u – see Figure 6.10) and in the opposite direction for Sp11, Sp21 and Sp23 (positive value of u – see Figure 6.10). It can be concluded that specimens Sp11, Sp13 and Sp15 failed in a pure flexural buckling mode (see Figure 6.15(a)), while for specimens Sp21, Sp23 and Sp25, twist rotations were recorded (see Figure 6.14) in addition to weak axis deflections, indicating a flexural torsional buckling mode.

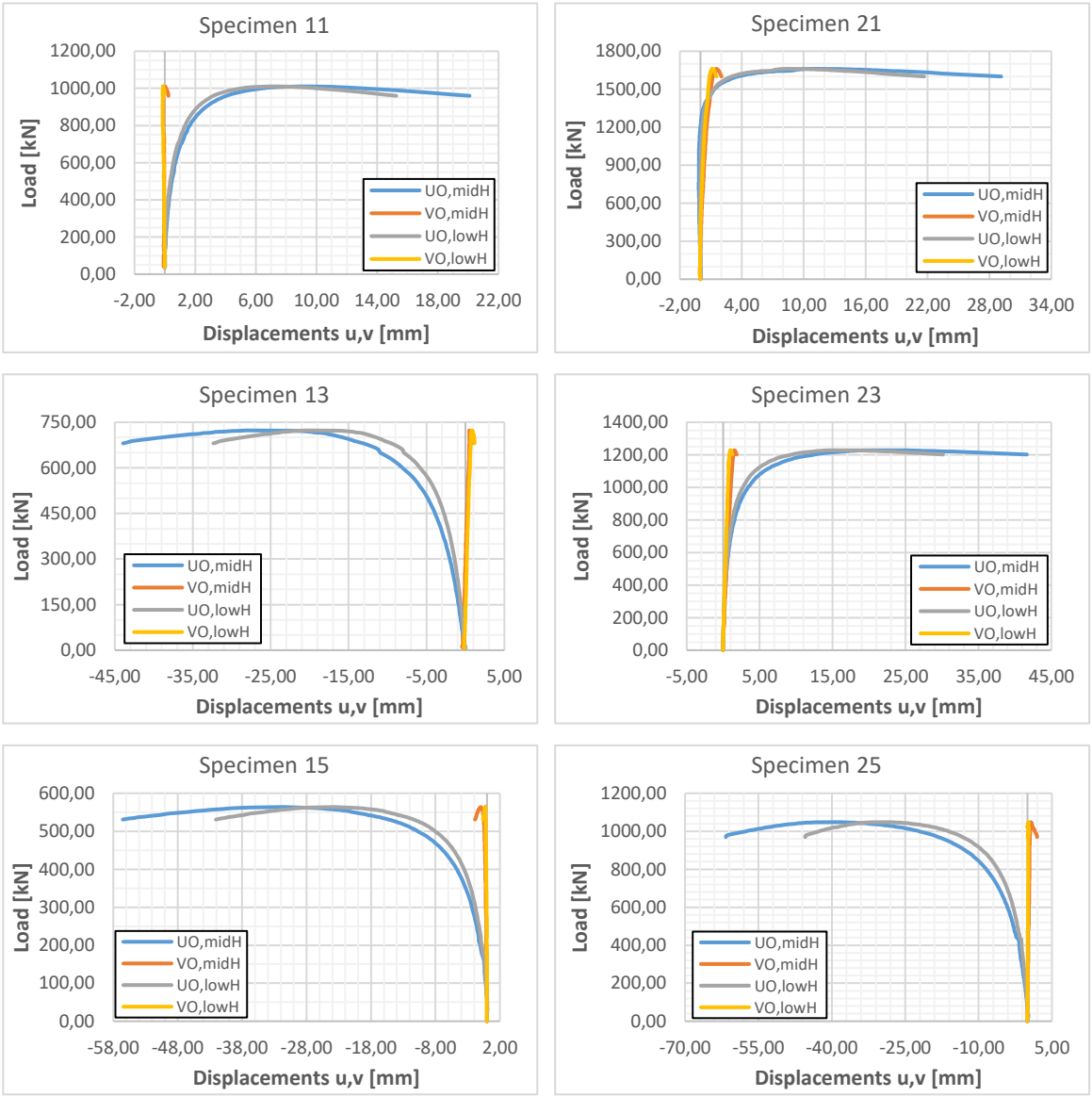

*$U/V_{O,midH}$ is the displacement of the corner point O of the mid – height cross-section along u/v principal axis
*$U/V_{O,lowH}$ is the displacement of the corner point O of the low – height cross-section along u/v principal axis

Figure 6.13: Load-deflection curves for centrally loaded specimens

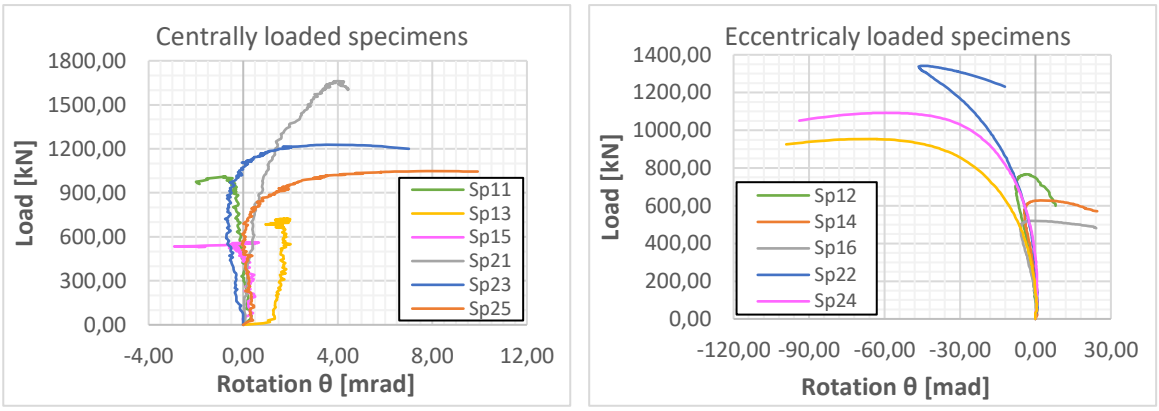

Figure 6.14: Load-twist curves at mid-height cross-section for centrally loaded (left) and eccentrically loaded (right) specimens

Figure 6.15: Final deformed shape of (a) Sp15 with a pure flexural buckling mode, (b) Sp26 with a flexural-torsional failure buckling mode and (c) Sp14 with a mixed mode between flexural and flexural torsional buckling

The eccentrically loaded specimens were initially subjected to compression and strong axis bending. At low load levels, the deflections transverse to the strong axis were high while they were very small in the other principal direction (see Figure 6.16 and green cross-sections in Figure 6.17); this was opposite to the tendency of the angles to fail by weak axis buckling. At higher load levels, deflections transverse to the weak axis grew quickly and prevailed at failure (in Figure 6.17, the red cross-section corresponds to the ultimate load and the blue cross-section is after buckling). In specimens Sp22, Sp24 and Sp26, these deflections were accompanied by significant twist rotations indicating clearly

a failure with a flexural-torsional buckling mode (see Figure 6.15(b)). On the contrary, twist rotations were small for specimens Sp12, Sp14 and Sp16 indicating a mixed mode between flexural and flexural torsional buckling (see Figure 6.15(c)). The most stressed mid-height cross section was subjected to compression and bi-axial bending. In fact, strong axis bending was primarily due to the eccentric loading and weak axis bending due to second order effects.

The absence of visible local buckling in all specimens should be also mentioned, although all Sp2# specimens are categorized as class 4 according to the existing provisions of EN 1993-1-1; with the proposed classification system they are also classified in class-4 for compression but in class-2 for bending ($c/\varepsilon t = 14,6$).

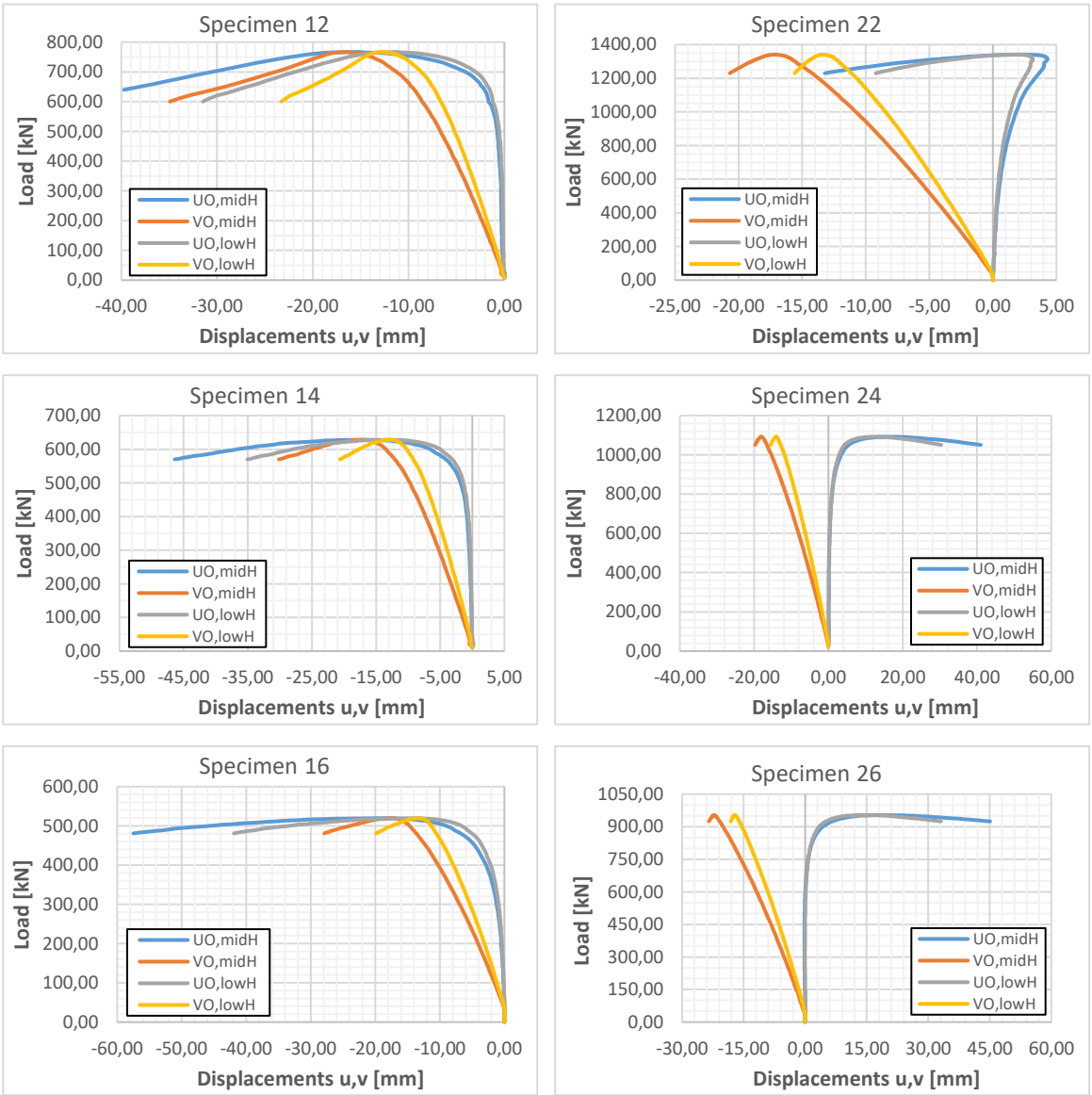

*U/VO,midH is the displacement of the corner point O of the mid – height cross-section along u/v principal axis
*U/VO,lowH is the displacement of the corner point O of the low – height cross-section along u/v principal axis

Figure 6.16: Load-deflection curves for eccentrically loaded specimens

Finally, Table 6.5 presents, for each specimen the measured failure load (N_{exp}) as well as the deflections about minor (v_O) and major (u_O) principal axes and the twist at the mid-height cross-

section, all at the failure load. The sign of the deflections and the twist is in accordance with Figure 6.10.

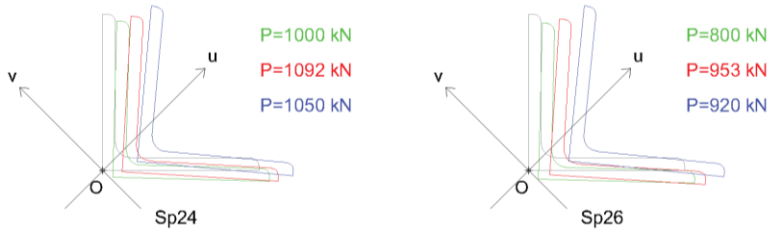

Figure 6.17: Schematic movement of the mid-height cross-section along the loading for specimens Sp24 and Sp26

Table 6.5: Deflections and twist at the mid-height cross-section at the failure load

ID of Specimen	Profile	N_{exp} [kN]	u_O [mm]	v_O [mm]	θ [mrad]
Sp11	150x150x18	1010,6	8,88	-0,01	-0,82
Sp12		767,3	-15,28	-16,39	-3,94
Sp13		723,2	-28,22	0,53	1,71
Sp14		628,3	-16,35	-17,05	2,05
Sp15		563,9	-31,53	-0,95	0,39
Sp16		519,8	-17,78	-17,03	-1,81
Sp21	200x200x16	1661,5	10,89	1,52	3,96
Sp22		1341,4	2,48	-17,07	-44,92
Sp23		1228,0	20,49	1,53	3,51
Sp24		1092,3	16,87	-18,09	-59,51
Sp25		1048,1	-38,43	0,62	7,77
Sp26		953,6	16,31	-22,11	-62,95

6.4 Comparison with FEM analyses

Subsequently, numerical simulations considering relevant imperfections as well as geometrical and material non-linearities were performed and compared with the results of the experimental tests. The numerical analyses were performed with the FINELG non-linear finite element software using beam elements. The choice of beam elements is acceptable and justified from the fact that no local buckling took place during the tests. Only the column has been modelled while the end plates at the extremities have been considered indirectly: the length (L) of each column has been increased by 107 mm, what corresponds to the thickness of the end plates of the specimens as well as the connection plate, so as to simulate the actual buckling length (L_{crit}) of the column (length between the zero moment levels in Figure 6.8). Each column has been meshed in twenty beam finite elements along the member length. This is an optimal mesh as the difference of member's response (ultimate load and deflections) is less than 1% ether the member is meshed in fifteen elements or thirty. The columns were assumed as pin-end members with free rotations at their extremities, except the rotation that leads to torsion along the length axis, which was blocked. All the other DOF at the extremities were blocked, except u_x at the node of the applied load. Therefore, the experimental boundary conditions were rather well represented by the model.

The FINELG finite element analyses adopting the GMNIA method were performed considering:

- An initial member imperfection (shape and magnitude in accordance with the measured ones).
- Residual stresses resulting from the hot-rolling procedure; the selected pattern (Figure 6.18) is chosen from previous studies [38]-[39] in which appropriate measurements had been realized. It was shown that the residual stresses in hot rolled steel angle sections are independent of the steel grade and therefore a magnitude of 70 MPa (corresponding to $0{,}3 \cdot f_y$, for steel grade S235) is used. The selected pattern is applied automatically by the software to each beam element along the member length.
- A material law in accordance with the measured one (see Table 6.4).

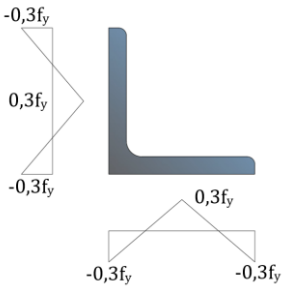

Figure 6.18: Assumed distribution pattern of residual stresses based on [38]-[39] with f_y fixed to 235 MPa whatever is the actual steel grade

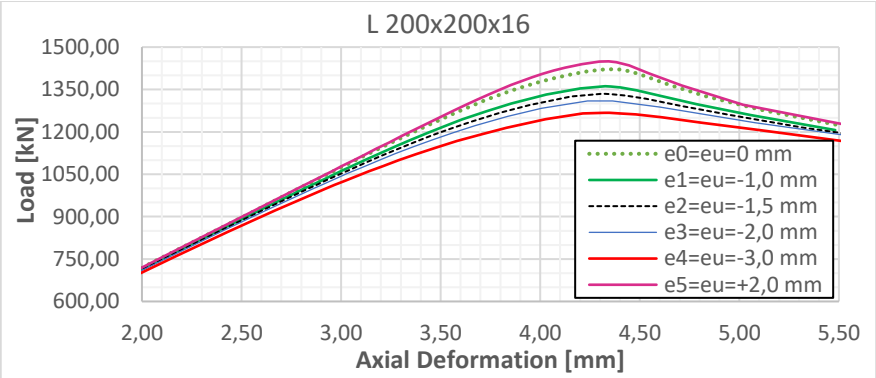

Figure 6.19: Influence of eccentricity at the ultimate resistance of member (excerpt of the full graph)

A tolerance on the position of the applied load from up to 2,0 mm has been adopted for the numerical simulations in order to calibrate the results. It has been found that even a small eccentricity could affect significantly the ultimate resistance and the stiffness of the member in comparison to the perfectly "no loading eccentricity" case. Figure 6.19 shows that an eccentricity equal to 1,5 mm (for the angle section L200x200x16) changes the ultimate resistance by approximately 6%. The influence of this small eccentricity of the applied load on the stiffness and the ultimate resistance has been also observed in [40]. The eccentricity has been applied in u direction as it has been found, through the numerical simulations, that the influence on the response of an eccentricity in the v direction is negligible (see Figure 6.1 for the definition of the axes). The adoption of such a tolerance can be justified as by the two following reasons:

- the nominal position of the load has been designed to coincide with the centre of the end plates and, accordingly, with the centre of gravity of the cross section. In reality, due to small differences in the cross-section geometry, the real centre of gravity does not coincide exactly with the loading point;

- the positioning of the specimen in the testing rig may also induce a small and unexpected eccentricity.

Figure 6.20 and Figure 6.21 show the axial deformations (shortening) of the specimens versus the load for both experimental tests (solid lines) and numerical simulations (dotted lines). Table 6.6 summarizes and compares the ultimate experimental and numerical resistances. One can see from the graphs and the table that there is a very good agreement between numerical simulations and experimental tests in terms of axial stiffness and load carrying capacity. The mean value of the ratio N_{exp} / N_{FEM} is equal to 0,98 with a COV of 1%.

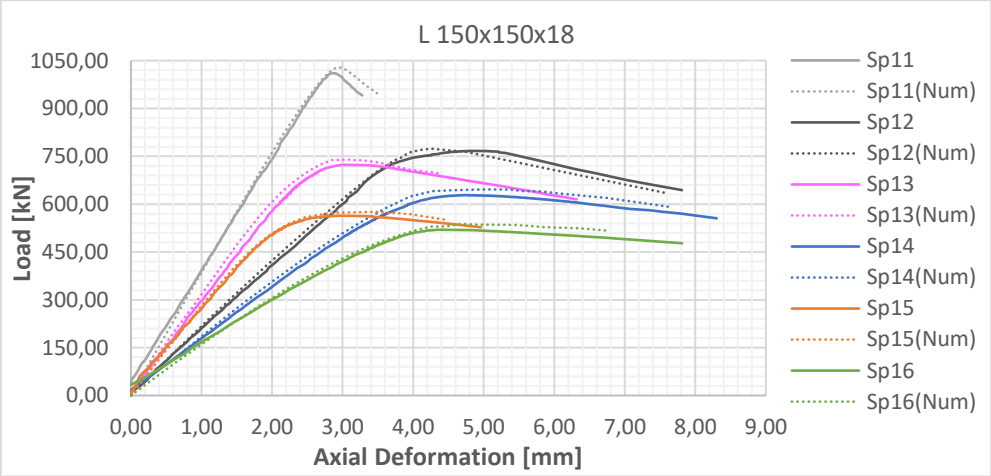

Figure 6.20: Comparison between test and FEM results for Sp1#

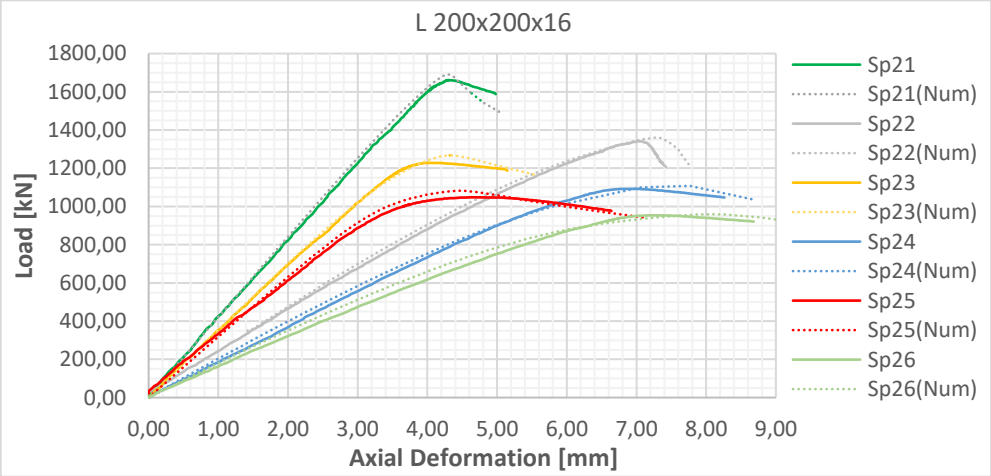

Figure 6.21: Comparison between test and FEM results for Sp2#

Figure 6.22 and Figure 6.23 show some characteristic load-deflections curves of the specimens for both experimental tests and numerical simulations.

The numerical results provide similar responses for most of the specimens without nominal loading eccentricity (same as Specimen Sp15 in Figure 6.22), as well as a good correspondence with the tests. However, for two specimens (Sp21, Sp23), the numerical response appears to be more flexible than the test one, at least in the initial phase of the test; but close to the failure, a rather good agreement with the experiment is contemplated.

Table 6.6: Ultimate resistances obtained by experimental tests and numerical models

ID of Specimen	Profile	Buckling length in GMNIA [mm]	Actual load eccentricities [mm]	Additional assumed eccentricities in GMNIA [mm]	N_{exp} [kN]	N_{FEM} [kN]	N_{exp}/N_{FEM}
Sp11	150x150x18	2607	0,00	$e_u = 1,50$	1010,6	1028,6	0,98
Sp12		2607	$e_v = 48,71$	$e_u = 0,50$	767,3	774,1	0,99
Sp13		3107	0,00	$e_u = -2,00$	723,2	739,3	0,98
Sp14		3107	$e_v = 48,72$	$e_u = -1,10$	628,3	645,9	0,97
Sp15		3607	0,00	$e_u = -2,00$	563,9	575,8	0,98
Sp16		3607	$e_v = 48,70$	$e_u = -1,00$	519,8	536,0	0,97
Sp21	200x200x16	3107	0,00	$e_u = -1,50$	1661,5	1690,6	0,98
Sp22		3107	$e_v = 66,60$	$e_u = -0,80$	1341,4	1361,0	0,99
Sp23		3607	0,00	$e_u = -2,00$	1228,0	1267,4	0,97
Sp24		3607	$e_v = 66,65$	$e_u = -0,50$	1092,3	1107,6	0,99
Sp25		4107	0,00	$e_u = -1,70$	1048,1	1082,2	0,97
Sp26		4107	$e_v = 66,63$	$e_u = 0,00$	953,6	959,1	0,99

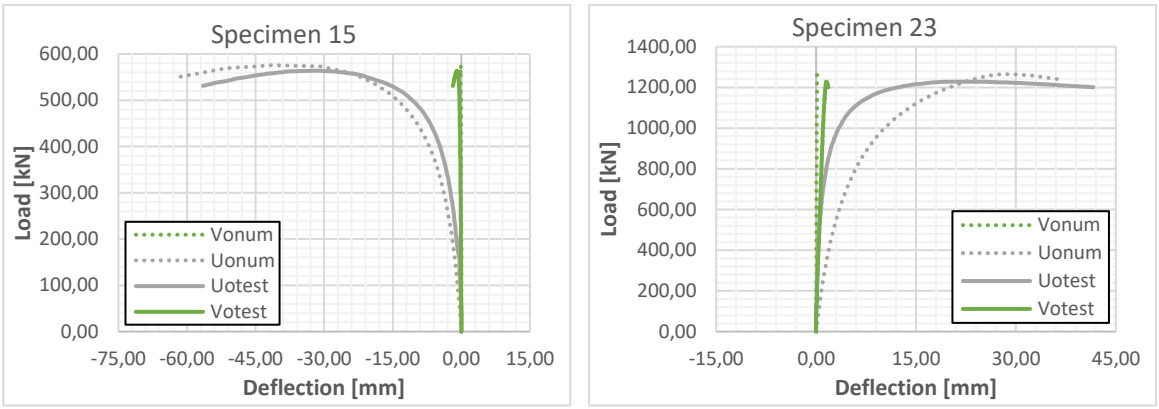

Figure 6.22: Characteristic load-deflection curves at mid-height cross-section for centrally loaded specimens

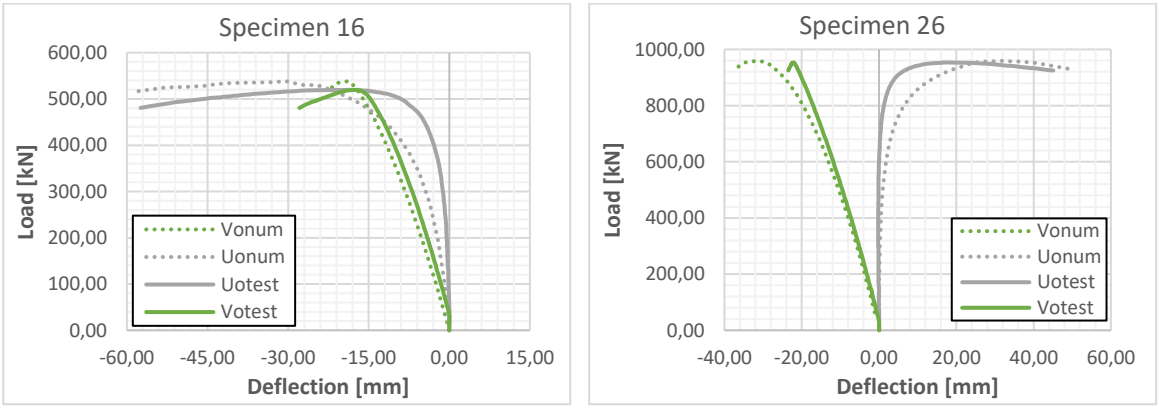

Figure 6.23: Characteristic load-deflection curves at mid-height cross-section for eccentrically loaded specimens

Similar results, in terms of lateral flexibility of the columns, have been observed for eccentrically loaded specimens (see Figure 6.23). This additional flexibility could be explained by the fact that the end plates at the extremities of the angle members have been modelled indirectly (additional length

and restraints at the extremities of the member), as well as by the consideration of the unintentional eccentricities. The prevailing of weak axis buckling near the failure load has been observed also through the numerical simulations for the eccentrically loaded specimens.

6.5 Conclusions

The stability of columns made of large angle profiles in high strength steel and subjected to centric and eccentric compression loads is investigated through experimental tests and numerical simulations. The experimental campaign consists of twelve tests on columns with large angle cross-sections (L150x150x18 and 200x200x16) made of S460 or S420 steel grade. Accompanying numerical studies have been carried out, considering relevant geometrical imperfections as well as geometrical and material non-linearities. From the present study, the following conclusions may be drawn.

- The centrically loaded specimens (Sp11, Sp13, Sp15) and the eccentrically loaded specimens (Sp22, Sp24, Sp26) failed very clearly in a pure weak axis flexural buckling mode and correspondingly flexural torsional buckling mode.
- The centrically loaded specimens (Sp21, Sp23, Sp25) and the eccentrically loaded specimens (Sp12, Sp14, Sp16) failed mostly in a flexural torsional buckling mode, which was more pronounced.
- For the eccentrically loaded specimens that subjected to compression and strong axis bending, it has been seen that at low levels of loading the deflections transverse to the strong axis were high while they were very small in the other principal direction, but at higher load levels, deflections transverse to the weak axis grew quickly and prevailed at failure, this is in line with the tendency of angles to buckle along weak axis.
- Local buckling was not visibly observed in any specimen, although all Sp2# specimens are categorised as class 4 according to the existing provisions of EN 1993-1-1; with the proposed classification system they are also classified in class-4 for compression but in class-2 for bending.
- A very good agreement between the numerical GMNIA simulations performed with FINELG and the experimental results in terms of axial stiffness and ultimate resistances has been achieved, through the consideration of an unintentional small eccentricity. Indeed, a small eccentricity of the position of the applying load can affect the ultimate resistance of the member in comparison with the perfect “no loading eccentricity” case. For the current study, an eccentricity equals to 1,5 mm may reduce the ultimate resistance by about 6%. At the end of this comparative study, it may be concluded that the FINELG is appropriate numerical tool to predict the response of angle profiles subjected to combined axial load and bending moments.

7. DESIGN RULES FOR MEMBERS MADE OF ANGLES

The particularities of angles explain that existing design rules for other types of sections, mostly doubly symmetric ones, cannot safely cover angles, what inevitably leads to the need for the development of specific design provisions for angle sections. Such specific design rules and recommendations can be found in various parts of Eurocode 3. More specifically, EN 1993-1-1 [1] as well as its forthcoming new version named prEN 1993-1-1 [26] provides general rules for angles, while EN 1993-3-1[2] provides rules for the buckling resistance of angles as members in towers when connected eccentrically with bolts on one leg. Another European specification, the CENELEC standard EN 50341-1 [5] provides specific rules for lattice towers used in the field of overhead electrical lines, addressing specific problems linked to such application but it also provides specific rules for the verification of lattice towers and their constituting parts, including members made of angles. However, all these rules are not necessarily compatible and so their validity is questionable.

In the following, formulae about the design resistance and stability of equal leg angle members are proposed, highlighting the differences with the existing provisions of Eurocode 3. The proposed rules were fully validated through numerical investigations and experimental tests. The extensive numerical parametrical studies were performed by the full non-linear software ABAQUS. Experimental results are coming from tests carried out in the framework of the thesis, as well as from previous experimental investigations found in literature. Experimental results were also compared to existing Eurocode 3 provisions for sake of comparison.

7.1 Design rules and recommendations

7.1.1 Buckling resistance to compression

The buckling design resistance for axial compression may be determined from:

$$N_{b,Rd} = \begin{cases} \chi_{min} \frac{Af_y}{\gamma_{M1}} & \text{for class 1,2 and 3 profiles} \\ \chi_{min} \frac{A_{eff} f_y}{\gamma_{M1}} & \text{for class 4 profiles} \end{cases} \quad \text{(Eq. 7.1)}$$

where A_{eff} is the area of the effective cross-section that equals:

$$A_{eff} = A - 2ct(1-\rho) \quad \text{(Eq. 7.2)}$$

The reduction factor ρ for outstand plated elements due to local buckling is given in EN 1993-1-5 as below:

$$\rho = \begin{cases} 1{,}0 & \text{for } \bar{\lambda}_p \leq 0{,}748 \\ \frac{\bar{\lambda}_p - 0{,}188}{\bar{\lambda}_p^2} & \text{for } \bar{\lambda}_p > 0{,}748 \end{cases} \quad \text{(Eq. 7.3)}$$

considering the relative plate slenderness of legs equal to:

$$\bar{\lambda}_p = \sqrt{\chi_{min}} \frac{\frac{c}{t}}{18{,}6\varepsilon} \quad \text{(Eq. 7.4)}$$

The buckling reduction factor χ_{min} is determined as a function of the relative slenderness $\bar{\lambda}$ of the compression member for the flexural buckling modes only:

$$\chi_{min} = min\{\chi_u; \chi_v\} \quad \text{(Eq. 7.5)}$$

The value of the buckling reduction factors χ_u, χ_v are computed for the appropriate relative slenderness $\overline{\lambda_u}, \overline{\lambda_v}$ and considering buckling curve b for steel grades S235-S420, or buckling curve a for higher steel grades (≥ S460).

The relative slenderness $\overline{\lambda_u}$ and $\overline{\lambda_v}$ should be taken as:

$$\overline{\lambda_u} = \sqrt{\frac{Af_y}{N_{cr,u}}} \quad \text{and} \quad \overline{\lambda_v} = \sqrt{\frac{Af_y}{N_{cr,v}}} \qquad \text{(Eq. 7.6)}$$

where,

$N_{cr,u}$ is the elastic critical force for the flexural buckling mode about u-u axis, based on the gross cross-sectional properties;

$N_{cr,v}$ is the elastic critical force for the flexural buckling mode about v-v axis, based on the gross cross-sectional properties.

> Comparison with EN 1993-1-1 and prEN 1993-1-1 provisions

EN 1993-1-1 recommends the use of buckling curve b whatever is the steel grade while, in the forthcoming new version of this normative document, prEN 1993-1-1, curve b is still used for steel grades S235-S420 but curve a is proposed for higher steel grades (≥S460). For the purposed of the thesis, the selection of the buckling curves follows the provisions of prEN 1993-1-1. However, both versions recommend the use the "elastic critical load for the relevant buckling mode" for the evaluation of the non-dimensional slenderness, i.e. the minimum eigenvalue amongst all flexural and flexural-torsional buckling modes. As explained in §3.1, a pure torsional mode cannot be obtained for a centrally loaded angle column. Through numerical studies on angles in compression (see §7.2.2) considering various profiles, lengths and steel grades, it is seen that weak axis flexural buckling always prevail at failure even for angles exhibiting a flexural-torsional elastic critical instability mode as minimum eigenvalue. Therefore, it seems reasonable to calculate the member resistance of rolled angles by using the slenderness for flexural buckling only and not by referring to the "relevant buckling mode" which may include torsional effects, as EN 1993-1-1 and prEN 1993-1-1 prescribe.

Additionally, the interaction between local and global buckling are considered in the definition of the relative plate slenderness $\bar{\lambda}_p$ via the term $\sqrt{\chi_{min}}$, unlike in EN 1993-1-1.

7.1.2 Lateral torsional buckling resistance to strong axis bending

The bending resistance of laterally unrestrained beams is determined by application of a reduction factor, accounting for effects of lateral torsional buckling, to the relevant resistance of the same beams assumed to be laterally restrained. It is reminded here that the bending resistance of laterally restrained beams was derived in chapter 4, considering a linear transition between plastic and elastic bending resistances, adopting thus the procedure for double symmetric cross-sections that was proposed by SEMI-COMP [33].

The design buckling resistance moment $M_{u,Rd}$ of a laterally unrestrained beam may accordingly be determined from:

$$M_{u,Rd} = \chi_{LT} W_u \frac{f_y}{\gamma_{M1}} \qquad \text{(Eq. 7.7)}$$

where W_u is the section modulus about the u axis equals to:

$$W_u = \alpha_{i,u} W_{el,u}\ , \ \text{i} = 2, 3, 4 \qquad \text{(Eq. 7.8)}$$

where,

$\alpha_{2,u} = 1{,}5$ for class 1 or 2 (Eq. 7.9)

$\alpha_{3,u} = \left[1 + \left(\frac{26{,}3\varepsilon - c/t}{26{,}3\varepsilon - 16\varepsilon}\right) \cdot (1{,}5 - 1)\right]$ for class 3 (Eq. 7.10)

$\alpha_{4,u} = W_{eff,u}/W_{el,u} = \rho_u^2$ for class 4 (Eq. 7.11)

ρ_u is the reduction factor for plate buckling, evaluated through eq. (7.3), considering a reduced plate slenderness of the legs equal to:

$$\bar{\lambda}_p = \sqrt{\chi_{LT}} \frac{\frac{c}{t}}{35{,}58\varepsilon} \quad \text{(Eq. 7.12)}$$

The reduction factor for lateral torsional buckling χ_{LT} should be determined as a function of the relative slenderness $\overline{\lambda_{LT}}$ of the member:

$$\overline{\lambda_{LT}} = \sqrt{\frac{W_u f_y}{M_{cr}}} \quad \text{(Eq. 7.13)}$$

where the elastic critical moment for lateral-torsional buckling M_{cr} is given by the following equation [7], in combination with Table 7.1:

$$M_{cr} = C_b \frac{0{,}46 \cdot E \cdot h^2 \cdot t^2}{l} \quad \text{(Eq. 7.14)}$$

The value of the buckling reduction factor χ_{LT} for the relative slenderness $\overline{\lambda_{LT}}$ should be derived from buckling curve a, which can be determined using eq. (6.57) of EN 1993-1-1:§6.3.2.3(1) for lateral-torsional buckling, using $\bar{\lambda}_{LT,0} = 0{,}4$ and $\beta = 1{,}00$ (see equations below).

$$\chi_{LT} = \frac{1}{\Phi_{LT} + \sqrt{\Phi_{LT}^2 - \bar{\lambda}_{LT}^2}} \quad \text{but} \begin{cases} \chi_{LT} \leq 1{,}0 \\ \chi_{LT} \leq 1/\bar{\lambda}_{LT}^2 \end{cases} \quad \text{(Eq. 7.15)}$$

$$\Phi_{LT} = 0{,}5\left[1 + a_{LT}\left(\bar{\lambda}_{LT} - 0{,}4\right) + \bar{\lambda}_{LT}^2\right] \quad \text{(Eq. 7.16)}$$

However, following the recommendations of EN 1993-1-1, lateral torsional buckling may be ignored ($\chi_{LT} = 1{,}0$) when one of the following conditions apply:

$$\bar{\lambda}_{LT} \leq \bar{\lambda}_{LT,0} \text{ (where } \bar{\lambda}_{LT,0} = 0{,}4) \quad \text{or} \quad \frac{M_{Ed}}{M_{cr}} \leq \bar{\lambda}_{LT,0}^2$$

Table 7.1: Determination of the C_b-factor for LTB [7]

General case:

$$C_b = \frac{12{,}5 M_{max}}{2{,}5 M_{max} + 3M_A + 4M_B + 3M_C} \leq 1{,}5$$

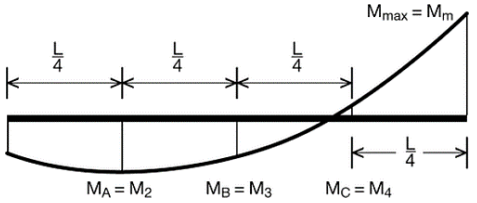

For linear moment distribution:

$C_b = \frac{12{,}5}{7{,}5 + 5\psi}$ with $-1 \leq \psi = \frac{M_2}{M_1} \leq 1$

> Comparison with EN 1993-1-1 and prEN 1993-1-1

The lateral torsional buckling resistance is in line with EN 1993-1-1 eq. (6.55) or prEN 1993-1-1, eq. (8.79). However, like in flexural buckling, the interaction between local and global buckling are

considered through the relative plate slenderness $\bar{\lambda}_p$ and not through the global slenderness $\bar{\lambda}_{LT}$. Buckling curve d is recommended by both normative documents while, a is adopted in the thesis as a result of the validation procedure based on numerical studies (see §7.2.3).

The transition between elastic and plastic bending resistances adopts the proposals of SEMICOMP in contrast with the existing version of Eurocode 3, but in line with the forthcoming one, at least for doubly symmetric sections.

7.1.3 Resistance to weak axis bending

As already shown, the cross-section resistance of angles subjected to weak axis bending depend on whether the tip is in tension or in compression, but not on the member length. Therefore, the member resistance coincides with the cross-section resistance as provided in §5.4.

7.1.4 Buckling resistance to bending and axial compression

Following the procedures of EN 1993-1-1 and prEN 1993-1-1, two conditions for buckling around one or the other principal axis should be satisfied for angle members subjected to compression and biaxial bending. Torsional buckling is not checked separately but is included in the local buckling check.

- strong axis check

$$\left(\frac{N_{Ed}}{N_{bu,Rd}} + k_{uu}\frac{M_{u,Ed}}{M_{u,Rd}}\right)^{\xi} + k_{uv}\frac{M_{v,Ed}}{M_{v,Rd}} \leq 1 \qquad \text{(Eq. 7.17)}$$

- weak axis check

$$\left(\frac{N_{Ed}}{N_{bv,Rd}} + k_{vu}\frac{M_{u,Ed}}{M_{u,Rd}}\right)^{\xi} + k_{vv}\frac{M_{v,Ed}}{M_{v,Rd}} \leq 1 \qquad \text{(Eq. 7.18)}$$

where k_{ij} are the interaction factors provided in Table 7.2;

Table 7.2: Determination of k_{ij} factors

k_{ij} factors	
$k_{uu} = \frac{C_u}{1-\frac{N_{Ed}}{N_{cr,u}}}$	$k_{uv} = C_v$
$k_{vu} = C_u$	$k_{vv} = \frac{C_v}{1-\frac{N_{Ed}}{N_{cr,v}}}$
$C_u = 0{,}6+0{,}4\psi_u$	$C_v = 0{,}6+0{,}4\psi_v$
$-1 \leq \psi_u = \frac{M_{2u}}{M_{1u}} \leq 1$	$-1 \leq \psi_v = \frac{M_{2v}}{M_{1v}} \leq 1$

The ξ-factor that depends on the cross-section class, is expressing a plastic, intermediate or elastic design and may be determined accordingly as follows:

$c/t \leq 16\varepsilon$: $\xi = 2$ (Eq. 7.19)

$16\varepsilon < c/t < 26{,}3\varepsilon$: $\xi = \left[1 + \left(\frac{26{,}3\varepsilon - \frac{c}{t}}{26{,}3\varepsilon - 16\varepsilon}\right)\cdot(2-1)\right]$ (Eq. 7.20)

c/t > 26,3ε: $\xi = 1$ (Eq. 7.21)

> Comparison with EN 1993-1-1 and prEN 1993-1-1

The procedure exhibits similarities, but also differences with EN 1993-1-1,6.3.3 (4) and prEN 1993-1-1, 8.3.3 (5). In both procedures there are two equations, respectively for buckling around one and the other principal axis, the equations have three terms (one for compression, two for bending around the principal axes), lateral torsional buckling is included in the strong axis bending term while local buckling is included through the properties of the effective section.

In contrast, in the proposed check, the factor ξ is introduced that makes the interaction between the three terms non-linear (as in Eurocode 3, despite they appear as linear). The quadratic term with $\xi=2$ tries to cover the cross-section resistance check of class-2 cross-sections as derived in Vayas et al. in [8]. Furthermore, simpler expressions for the terms C_i and $k_{i,j}$, straightforwardly derived from the stability theory, are proposed.

7.1.5 General method for angles

The general method proposed in EN 1993-1-1 and prEN 1993-1-1 for the evaluation of the stability of structural members or parts of structures applies to lateral and lateral torsional buckling for structural components with mono symmetric cross-sections, built-up or not, uniform or not, with complex support conditions or not, which are subjected to compression and/or uni-axial bending in the plane, but which do not contain rotated plastic hinges.

The general method can be interpreted as follows, for members with equal leg angles. The out-of-plane buckling resistance of the member is checked if the following equation satisfied:

$$\chi_{op} \cdot \frac{\alpha_{ult,k}}{\gamma_{M1}} \geq 1{,}0 \qquad \text{(Eq. 7.22)}$$

where,

χ_{op} is the reduction factor corresponding to the non-dimensional slenderness $\overline{\lambda_{op}}$ and aimed at accounting for weak axis buckling only, as it is the predominant failure mode for angles. The selection of the buckling curve is based on prEN 1993-1-1.

$\alpha_{ult,k}$ is the minimum load factor to be applied to the design loads to reach the characteristic resistance of the most critical cross-section of the structural component considering its in plane behaviour without accounting for lateral or lateral torsional buckling, but accounting for all effects due to in plane geometrical deformation and imperfections, global and local, where relevant. It can be derived from the following equation:

$$\frac{1}{\alpha_{ult,k}} = \frac{\sigma_{max}}{f_y} = \frac{\sigma_N}{f_y} + \frac{\sigma_{e_0}}{f_y} + \frac{\sigma_{M_u}}{f_y} + \frac{\sigma_{M_v}}{f_y} \qquad \text{(Eq. 7.23)}$$

in which:

- the first term relates to the stress under pure compression;
- the second, to the second order maximum stress resulting from the amplification of the first order moment $N_{Ed} \cdot e_{0,EC3}$ ($e_{0,EC3}$ is the in-plane equivalent imperfection as defined in prEN 1993-1-1), i.e. the moment $N_{Ed} \cdot e_{0,EC3}[1/(1-N_{Ed}/N_{cr,u})]$;

- the third one relates to the second order maximum stress resulting from the amplification of the first order moment $N_{Ed} \cdot e_v$ (e_v is the in-plane load eccentricity), which can be estimated as $N_{Ed} \cdot e_v [1/(1-N_{Ed}/N_{cr,u})]$;
- the fourth term relates to the first order bending moment $N_{Ed} \cdot e_u$ (e_u is the out-of-plane load eccentricity).

The global relative slenderness $\overline{\lambda_{op}}$ for the structural component should be determined from the equation below, in which the term $\alpha_{cr,op}$ is the minimum load factor for the design loads to reach the elastic critical load of the structural component associated to weak axis buckling ($\alpha_{cr,op} = \alpha_{cr,v}$).

$$\overline{\lambda_{op}} = \sqrt{\frac{\alpha_{ult,k}}{\alpha_{cr,op}}} \qquad \text{(Eq. 7.24)}$$

In case that the angle is connected by the leg, the "in-plane" instability effects may be considered as negligible, 2nd order effects may be disregarded ($1/(1-N_{Ed}/N_{cr,u}) = 1$) and e_0 may be taken equal to zero (in recognition of the rather limited impact of this parameter in regard to the load eccentricity).

The cross-section resistance in bending may be evaluated by using eq. (7.8). Conservatively, the elastic cross-section resistance (W_{el}) may be also used.

> Comparison with EN 1993-1-1 and prEN 1993-1-1

The difference with the present and forthcoming code versions lies in the definition of the reduction factor which aims to take into account only the weak axis buckling (instead of lateral and lateral torsional buckling. The term $\alpha_{cr,op}$ is therefore adapted accordingly.

7.2 Numerical validation

The validation of the proposed formulae for the prediction of the carrying capacity of members with equal leg angle sections is based on comparisons with the results of numerical simulations conduced considering a wide range of parameters. The profile sizes, the member lengths and the steel grades have been selected in order to obtain a large number of samples with properties that are commonly used in steel towers (see Table 7.3). It has to be mentioned that the classification system used hereafter follows the proposals of chapter 4.

Table 7.3: Cross-sections commonly used in steel lattice towers

Chords				Braces			
Cross-section	**Use**	**Length [m]**	**Steel grade**	**Cross-section**	**Use**	**Length [m]**	**Steel grade**
L70x70xt	Smallest cross-section for upper levels	1,0-2,0	S355 S460	L80x80xt	For low levels	1,0-2,0	S355 S460
L150x150xt	Standard cross-section	2,0-3,0	S355 S460	L70x70xt	For middle levels	1,0-2,0	S355 S460
L250x250xt	For high pylons at low levels	2,0-3,0	S355 S460	L45x45xt	For upper levels	1,0-2,0	S355 S460

7.2.1 Description of the numerical models

The numerical models have also been performed with the finite element software ABAQUS. The angle members were considered as pin-ended and have been modelled using at least three (3) volume

elements over the leg thickness, while fictitious end plates have been introduced through a specific constraint at the extremities. In all the numerical simulations, all the applied loads increasing simultaneously up to failure (or at least until reaching a maximum-ultimate load). In the cases where second order effects are significantly affecting the response, the ultimate load is defined as in §3.6. The model is similar to the one used in the numerical studies for classification, presented in §4.1.

The finite element analyses were performed considering:

- An initial bow imperfection of magnitude approximately equal to *L[mm]/1000* with a deformation shape similar to the first member instability mode.
  This value combines (i) the recommendation from the European norm EN 1090-2 [35], which prescribes that the deviation from straightness should be $\Delta \leq L[mm]/750$, with (ii) the provisions of prEN 1993-1-14 [29], which states that 80% of the geometric fabrication tolerances given in Ref. [35] should be applied.
- Residual stresses resulting from the hot-rolling procedure as shown in Figure 6.18 .

Due to some technical difficulties to introduce residual stresses in the ABAQUS model, it has been decided to use an equivalent imperfection e_0 that will represent the effect of the combined action of both residual stresses and initial imperfections. To calibrate the value of the equivalent imperfection e_0, some analyses have been performed with FINELG finite element software, using beam elements. The angle members were considered as pin-ended with fictitious end plates at the extremities. The selection of the FINELG software has been done due to its easy and automatic way of introducing accurately residual stresses in the model. The profiles and the material and geometrical properties of the studied samples are shown in Table 7.3.

Table 7.4: Details and results concerning the analyses to determine the equivalent imperfection e_0

No	Cross-Section	Length L [mm]	Steel grade	e_0 [mm] from eq. (7.25)	e_0=L/700 [mm]	N_{ult} [kN]	N_{ult^*} [kN]	N_{ult}/N_{ult^*} [-]
1	L70x70x5	1000	S355	1,34	1,42	182,41	188,45	0,97
2	L70x70x5	1000	S460	1,26	1,42	217,71	216,77	1,00
3	L70x70x5	2000	S355	2,69	2,86	64,04	64,77	0,99
4	L70x70x5	2000	S460	2,52	2,86	64,61	65,62	0,98
5	L80x80x8	2000	S355	2,74	2,86	144,31	142,03	1,02
6	L80x80x8	2000	S460	2,58	2,86	148,54	146,35	1,01
7	L150x150x13	2000	S355	2,89	2,86	1029,72	1077,83	0,96
8	L150x150x13	2000	S460	2,73	2,86	1259,42	1267,67	0,99
9	L250x250x20	2000	S355	2,87	2,86	3156,6	3236,49	0,98
10	L250x250x20	2000	S460	2,67	2,86	4005,27	3939,71	1,02

First, a full-non-linear analysis has been performed using FINELG software considering an initial imperfection (L/1000), an elastic perfectly plastic material behaviour law, as well as residual stresses (using the pattern shown in Figure 6.18) for each of the 10 different samples provided in Table 7.3. Through these analyses, the ultimate resistance N_{ult} has been predicted. By introducing this value (N_{ult}) in equation (7.25), a rough estimation of the equivalent imperfection e_0 to be introduced in ABAQUS can be found; a value of $e_0 = L/700$ is fixed.

$$\sigma_{max} = \frac{N_{ult}}{A} + \frac{N_{ult} e_0}{\left(1 - \frac{N_{ult}}{N_{cr,v}}\right) W_v} = f_y \qquad \text{(Eq. 7.25)}$$

Then, a second full-non-linear analysis has been performed using again FINELG software, considering this time the equivalent imperfection (L/700) and an elastic perfectly plastic material law for each of the 10 samples; the ultimate resistance N_{ult*} has been recorded and reported in Table 7.4. The mean value of the ratio N_{ult}/N_{ult*} is equal to 0,99 with a COV of 2,0% which seems to demonstrate the adequacy of the adopted alternative modelling approach.

Finally, a third full-non-linear analysis, considering the equivalent imperfection (L/700), has been performed with ABAQUS using solid elements. The mean value of the ratio $N_{ult,abaqus}/N_{ult}$ is equal to 0,96 with a COV of 3,3%, which can be acceptable considering the different types of finite elements used in the two models (beam elements in FINELG vs. solid element in ABAQUS). Therefore, the equivalent imperfection $e_0 = L[mm]/700$ accounting for both geometric imperfections and residual stresses is finally used in the analyses performed with ABAQUS to validate the member resistance formulae.

7.2.2 Members in axial compression

The profiles, lengths and steel grades have been selected from Table 7.3, but the thicknesses have been chosen so as to have samples of different classes (class 1 and 4) but also different elastic buckling modes as flexural or flexural-torsional. The details are summarized in Table 7.5, including also the ratio between the elastic critical load for flexural-torsional buckling and the minimum one obtained for flexural buckling.

Table 7.5: Details of the samples subjected to a uniform compression load

No	Cross-Section	L [mm]	f_y [N/mm^2]	Class	Eigenmode deformed shape	$N_{cr,FT}/minN_{cr,F}$ [-]
1	L70x70x5	1000	355	1	Flexural	1,05
2	L70x70x5	1000	460	4	Flexural	1,05
3	L70x70x5	2000	355	1	Flexural	2,64
4	L70x70x5	2000	460	4	Flexural	2,64
5	L70x70x6	1000	355	1	Flexural	1,43
6	L70x70x6	1000	460	1	Flexural	1,43
7	L70x70x6	2000	355	1	Flexural	3,01
8	L70x70x6	2000	460	1	Flexural	3,01
9	L70x70x7	1000	355	1	Flexural	1,82
10	L70x70x7	1000	460	1	Flexural	1,82
11	L70x70x7	2000	355	1	Flexural	3,25
12	L70x70x7	2000	460	1	Flexural	3,25
13	L70x70x10	1000	355	1	Flexural	2,71
14	L70x70x10	1000	460	1	Flexural	2,71
15	L70x70x10	2000	355	1	Flexural	3,53
16	L70x70x10	2000	460	1	Flexural	3,53
17	L150x150x13	2000	355	1	Flexural	1,29
18	L150x150x13	2000	460	1	Flexural	1,29
19	L150x150x13	3000	355	1	Flexural	2,25

20	L150x150x13	3000	460	1	Flexural	2,25
21	L150x150x14	2000	355	1	Flexural	1,46
22	L150x150x14	2000	460	1	Flexural	1,46
23	L150x150x14	3000	355	1	Flexural	2,44
24	L150x150x14	3000	460	1	Flexural	2,44
25	L150x150x15	2000	355	1	Flexural	1,63
26	L150x150x15	2000	460	1	Flexural	1,63
27	L150x150x15	3000	355	1	Flexural	2,61
28	L150x150x15	3000	460	1	Flexural	2,61
29	L150x150x18	2000	355	1	Flexural	2,11
30	L150x150x18	2000	460	1	Flexural	2,11
31	L150x150x18	3000	355	1	Flexural	2,98
32	L150x150x18	3000	460	1	Flexural	2,98
33	L250x250x17	2000	355	4	Flexural-torsional	0,32
34	L250x250x17	2000	460	4	Flexural-torsional	0,32
35	L250x250x17	3000	355	4	Flexural-torsional	0,69
36	L250x250x17	3000	460	4	Flexural-torsional	0,69
37	L250x250x20	2000	355	1	Flexural-torsional	0,45
38	L250x250x20	2000	460	4	Flexural-torsional	0,45
39	L250x250x20	3000	355	1	Flexural-torsional	0,99
40	L250x250x20	3000	460	4	Flexural-torsional	0,99
41	L250x250x22	2000	355	1	Flexural-torsional	0,54
42	L250x250x22	2000	460	1	Flexural-torsional	0,54
43	L250x250x22	3000	355	1	Flexural	1,11
44	L250x250x22	3000	460	1	Flexural	1,11
45	L250x250x26	2000	355	1	Flexural-torsional	0,75
46	L250x250x26	2000	460	1	Flexural-torsional	0,75
47	L250x250x26	3000	355	1	Flexural	1,48
48	L250x250x26	3000	460	1	Flexural	1,48

The samples have been modelled as explained in §7.2.1. However, for those where the first elastic eigenmode is a flexural-torsional one, three cases were considered in terms of initial imperfections:

a. equivalent imperfection $e_{0,FT} = L/700$ with a deformation shape similar to the first member instability mode, i.e. the flexural-torsional one (which correspond to $N_{ult(a)}$);
b. equivalent imperfection $e_{0,F} = L/700$ with a deformation shape similar to the first flexural instability mode (which correspond to $N_{ult(b)}$);
c. equivalent imperfection $e_0 = e_{0,FT} + e_{0,F}$ (which correspond to $N_{ult(c)}$): $e_{0,FT} = L/700$ with a deformation shape similar to the first member instability mode (flexural-torsional) and $e_{0,F} = L/700$ with a deformation shape similar to the first flexural instability to counterbalance the fact that, in most of these cases, the torsional component predominates in the flexural-torsional mode. The combination of both modes is done automatically through the software.

Even though, in case c, there is (i) a twist of the cross-section and (ii) an initial flexural deflection a bit higher than in case b, the difference between the values $N_{ult(b)}$ and $N_{ult(c)}$ is negligible (less than 0,5%).

Figure 7.1 illustrates the numerical results compared with the reference buckling curves a and b as reported in prEN 1993-1-1. The buckling reduction factor χ_{num} of the numerically tested samples has been evaluated as $\chi_{num} = N_{ult}/N_{pl}$ and the slenderness using eq. (7.6) For the samples with a flexural-torsional eigenmode, two cases are distinguished in Figure 7.1: the numerical results reported with blue/orange points have been evaluated using $N_{ult} = min\{N_{ult(a)}, N_{ult(b)}, N_{ult(c)}\}$, while the results presented with green points using $N_{ult} = N_{ult(a)}$.

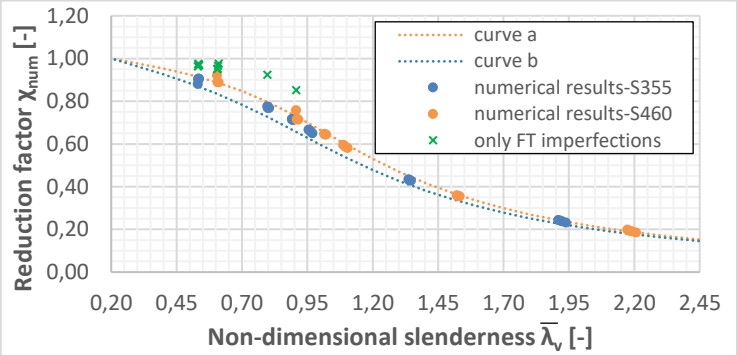

Figure 7.1: Comparison of numerical results with buckling curves of prEN 1993-1-1

According to prEN 1993-1-1, the obtained numerical results for the S355 steel grade should be compared with curve b while with curve a for S460. It can be easily observed that all the results referred to curve b are above the curve, while the results referred to curve a are in line, above or just a bit lower, which is acceptable given the 2% deviation that is considered. Regarding the results obtained using only an equivalent imperfection based on the 1st eigenmode (i.e. the flexural-torsional one), it is obvious that they are much higher even when compared with curve a. Through this comparison, it can be easily observed that the slenderness should be calculated using only the minimum elastic critical force for the flexural buckling mode as reported in §7.1.1.

7.2.3 Members in strong axis bending

For this load case, the profiles, lengths and steel grades have been again selected from Table 7.3, while the thicknesses have been chosen to have samples of different classes (1 and 3). The details are summarized in Table 7.6. As there are no hot-rolled angle profiles with S355 or S460 steel grades that are categorized as class 4, a few analyses have been additionally considered (marked with * in the mentioned table) with higher steel grades and member lengths so as to study some more slender members. For each non-linear analysis, an initial imperfection of magnitude *L/700* has been applied with a deformation shape proportional to the first member instability mode to introduce a twist imperfection at the middle cross-section (see Figure 7.2). It should also be noted that the application of eq. (7.14) was checked numerically with satisfactory results. Indeed, the mean value of the ratio $M_{cr,num}/M_{cr,anal}$ is equal to 0,989 with a COV of 4%.

Figure 7.3 illustrates the numerical results compared with the buckling curves a and a_0 for LTB as they are defined in §7.1.2, eq. (7.15) and eq. (7.16). The reduction factor for lateral torsional buckling $\chi_{LT,num}$ of the numerical samples has been evaluated by the equation $\chi_{LT,num} = M_{ult,u}/W_u f_y$ and the slenderness using eq. (7.13).

Table 7.6: Details for the samples subjected to a major axis bending moment

No	Cross-Section	L [mm]	f_y [N/mm^2]	Class	No	Cross-Section	L [mm]	f_y [N/mm^2]	Class
1	L 45x45x3	1000	355	1	29	L 250x250x17	2000	355	1
2	L 45x45x3	1000	460	3	30	L 250x250x17	2000	460	3
3	L 45x45x3	2000	355	1	31	L 250x250x17	3000	355	1
4	L 45x45x3	2000	460	3	32	L 250x250x17	3000	460	3
5	L70x70x5	1000	355	1	33	L 250x250x20	2000	355	1
6	L70x70x5	1000	460	1	34	L 250x250x20	2000	460	1
7	L70x70x5	2000	355	1	35	L 250x250x20	3000	355	1
8	L70x70x5	2000	460	1	36	L 250x250x20	3000	460	1
9	L70x70x6	1000	355	1	37	L 250x250x22	2000	355	1
10	L70x70x6	1000	460	1	38	L 250x250x22	2000	460	1
11	L70x70x6	2000	355	1	39	L 250x250x22	3000	355	1
12	L70x70x6	2000	460	1	40	L 250x250x22	3000	460	1
13	L 80x80x5	2000	355	1	41	L 250x250x22*	4000	355	1
14	L 80x80x5	2000	460	3	42	L 250x250x22*	4000	460	1
15	L 80x80x5	3000	355	1	43	L 250x250x22*	5000	355	1
16	L 80x80x5	3000	460	3	44	L 250x250x22*	5000	460	1
17	L150x150x13	2000	355	1	45	L 250x250x22*	4000	550	1
18	L150x150x13	2000	460	1	46	L 250x250x22*	4000	690	3
19	L150x150x13	3000	355	1	47	L 250x250x22*	5000	55	1
20	L150x150x13	3000	460	1	48	L 250x250x22*	5000	690	3
21	L150x150x14	2000	355	1	49	L 250x250x26	2000	355	1
22	L150x150x14	2000	460	1	50	L 250x250x26	2000	460	1
23	L150x150x14	3000	355	1	51	L 250x250x26	3000	355	1
24	L150x150x14	3000	460	1	52	L 250x250x26	3000	460	1
25	L150x150x15	2000	355	1					
26	L150x150x15	2000	460	1					
27	L150x150x15	3000	355	1					
28	L150x150x15	3000	460	1					

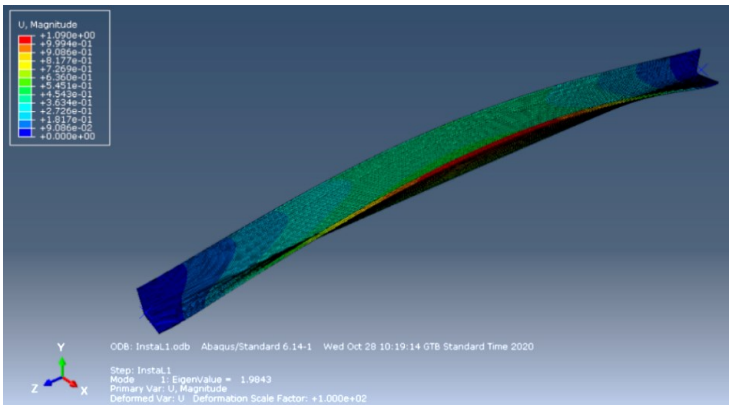

Figure 7.2: Typical shape of initial imperfection for a member subjected to strong axis bending

Figure 7.4 shows the ratio between the numerical member resistance ($M_{ult,u}$) and the analytical resistance ($M_{u,Rd}$), versus the non-dimensional slenderness. The analytical resistance has been evaluated by using the formulas proposed in §7.1.2 and validated through the numerical results.

It is seen in Figure 7.3 that all the results are above curve a and below curve a_0, and this validates the proposed in §7.1.2 buckling curve for LTB of angle sections. However, it seems that the resistance of some class-3 profiles is above curve a_0. This could be explained by the fact that these cross-sections are classified as class 3 but with a *c/εt* ratio quite close to the class-2 limit. So, they are treated as class 3 sections while, in reality, they reach their plastic resistance. On the contrary, due to the integration of the SEMICOMP concept, a profile classified as Class 3, but very close to Class 2, should be characterized by a section resistance close to M_{pl}. To set this clear, one should have in mind that a profile with a *c/εt* approximately equal to 16, could have a ratio $M_{ult,u}/M_{pl}$ from 0,95 to 1,0 (see Figure 4.5). This justifies the small increased value of the numerical results. It should be also noticed that for higher *c/εt* ratios, the results conform to curve a.

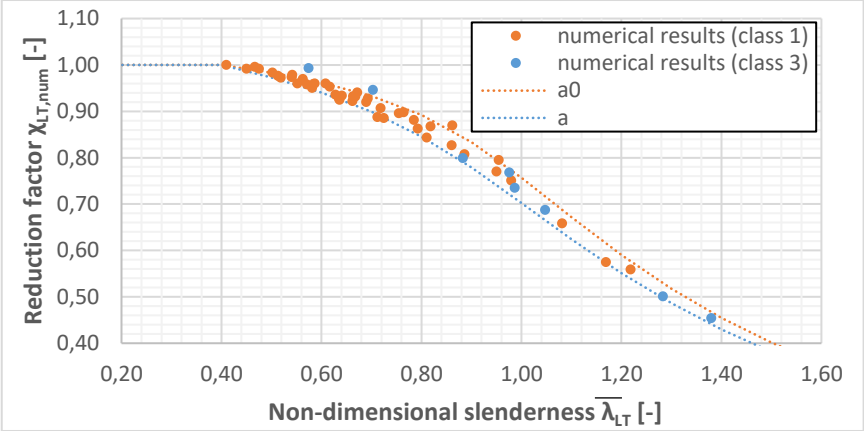

Figure 7.3: Comparison of numerical results with buckling curves for LTB of EN 1993-1-1

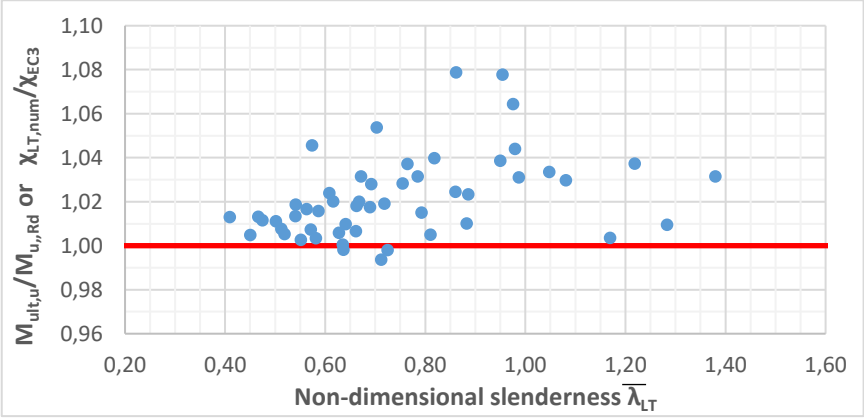

Figure 7.4: Comparison between numerical and analytical results for the resistance of members subjected to strong axis bending, related with the non-dimensional slenderness

7.2.4 Members in weak axis bending

The design resistance of angle cross-sections to weak axis bending M_v, either with the tip is in tension or in compression, is independent of the member's length. Therefore, just a few analyses have been performed to validate the proposed formulas additionally with the analyses presented in §5.4. Again, the profiles, lengths and steel grades have been chosen from Table 7.3, and the details are summarized in Table 7.7.

Figure 7.5 and Figure 7.6 shows the ratio between the numerical results for the member resistance ($M_{ult,v}$) and the analytical resistance ($M_{v,Rd}$) when the tip is in compression and in tension respectively. It can be seen that the analytical approach for the resistance of a member subjected to weak axis

bending is successfully validated when compared to the numerical results, by accepting a 2% deviation.

Table 7.7: Details for the samples subjected to a weak axis bending moment

Tip in compression					Tip in tension				
No	**Cross-Section**	**L [mm]**	**f_y [N/mm²]**	**Class**	**No**	**Cross-Section**	**L [mm]**	**f_y [N/mm²]**	**Class**
1	L70x70x5	1000	355	1	1	L45x45x3	1000	355	1
2	L70x70x5	1000	460	3	2	L45x45x3	1000	460	1
3	L70x70x5	2000	355	1	3	L45x45x3	2000	355	1
4	L70x70x5	2000	460	3	4	L45x45x3	2000	460	1
5	L150x150x14	2000	355	1	5	L70x70x6	1000	355	1
6	L150x150x14	2000	460	1	6	L70x70x6	1000	460	1
7	L150x150x14	3000	355	1	7	L70x70x6	2000	355	1
8	L150x150x14	3000	460	1	8	L70x70x6	2000	460	1
9	L250x250x17	2000	355	3	9	L250x250x20	2000	355	1
10	L250x250x17	2000	460	3	10	L250x250x20	2000	460	1
11	L250x250x17	3000	355	3	11	L250x250x20	3000	355	1
12	L250x250x17	3000	460	3	12	L250x250x20	3000	460	1

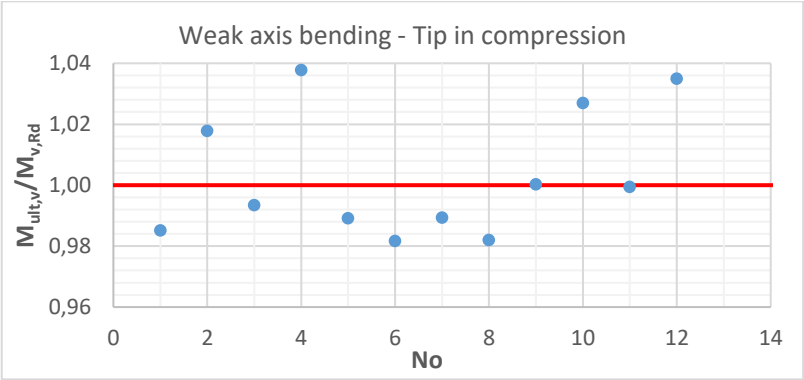

Figure 7.5: Comparison between numerical and analytical results for the resistance of members subjected to weak axis bending with the tip in compression

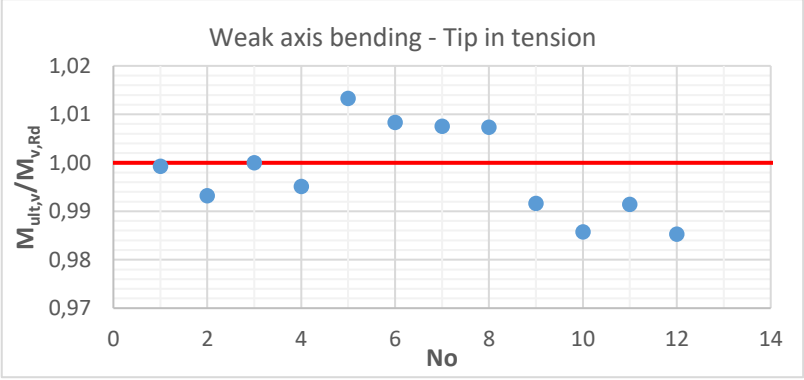

Figure 7.6: Comparison between numerical and analytical results for the resistance of members subjected to weak axis bending with the tip in tension

7.2.5 Members in bending and axial compression

For the numerical studies, three cases have been considered in terms of bending moments: weak axis bending, strong axis bending and bi-axial bending, always in combination with an axial compression force. The results are presented in the following sub-sections.

7.2.5.1 Axial force and weak axis bending

The numerical investigations have been performed considering a constant weak axis moment along the member length caused by an eccentric axial force. The eccentricity is in u-u axis (point P_1 in Figure 7.7(a)), and ranges between 5 and 35 mm; the value have been chosen randomly for each sample. The details of the numerical samples are presented in Table 7.8. All the analyses are for the tip in compression, which is more critical than the tip in tension.

Table 7.8: Details for the samples subjected to an eccentric axial force causing a weak axis moment

No	Cross-Section	L [mm]	f_y [N/mm^2]	e_u [mm]	No	Cross-Section	L [mm]	f_y [N/mm^2]	e_u [mm]
1	L 45x45x3	1000	355	10	17	L150x150x14	2000	355	12
2	L 45x45x3	1000	460	10	18	L150x150x14	2000	460	12
3	L 45x45x3	2000	355	10	19	L150x150x14	3000	355	20
4	L 45x45x3	2000	460	10	20	L150x150x14	3000	460	20
5	L70x70x5	1000	355	5	21	L150x150x18	2000	355	10
6	L70x70x5	1000	460	5	22	L150x150x18	2000	460	10
7	L70x70x5	2000	355	20	23	L150x150x18	3000	355	32
8	L70x70x5	2000	460	20	24	L150x150x18	3000	460	32
9	L70x70x6	1000	355	35	25	L 250x250x17	2000	355	8
10	L70x70x6	1000	460	35	26	L 250x250x17	2000	460	8
11	L70x70x6	2000	355	35	27	L 250x250x17	3000	355	12
12	L70x70x6	2000	460	35	28	L 250x250x17	3000	460	12
13	L 80x80x5	2000	355	25	29	L 250x250x22	2000	355	5
14	L 80x80x5	2000	460	25	30	L 250x250x22	2000	460	5
15	L 80x80x5	3000	355	25	31	L 250x250x22	3000	355	5
16	L 80x80x5	3000	460	25	32	L 250x250x22	3000	460	5

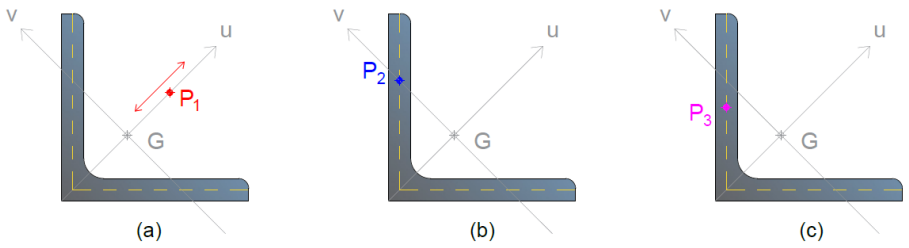

Figure 7.7: Position of the load application point for the samples subjected to N+M_v (b) N+M_u (c) N+M_u+M_v

Figure 7.8 presents the ratio between numerical and analytical (§7.1.4) resistance loads according to the weak axis non-dimensional slenderness $\overline{\lambda_v}$. The analytical load is determined by the maximum

load that satisfies both eq. (7.17) and eq. (7.18), without safety factors. For all the samples, the weak axis check was the critical one.

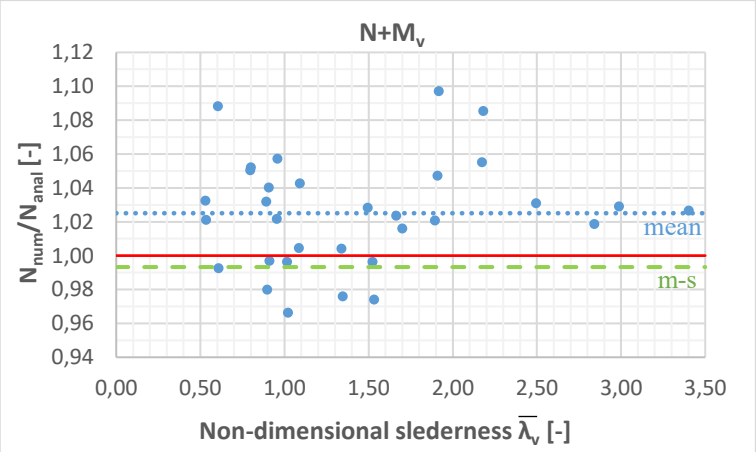

Figure 7.8: Ratio between numerical and analytical loads for $N+M_v$

The mean value (m) of the ratio N_{num}/N_{anal} is equal to 1,03 with a standard deviation of 3,18%. The analytical approach is validated by accepting a 2% deviation from the numerical results.

7.2.5.2 Axial force and strong axis bending

The details (profiles/lengths/steel grades) of the numerical samples that have been used are the same than those presented in Table 7.8. The axial force is applied at the intersection point of the minor principal axis v-v with the middle line of the leg thickness (point P_2 in Figure 7.7(b)) and ranges between 14,57 and 84,00 mm, depending on the profile geometry.

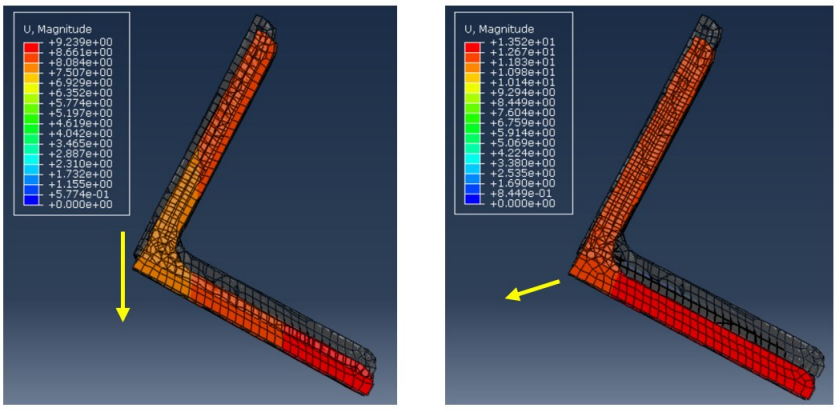

(a) (b)

Figure 7.9: Movement of a profile subjected to an axial force and strong axis bending: (a) during initial loading steps and (b) at the failure load

Figure 7.10 presents the ratio between numerical load resistances and the analytical ones derived through the current proposal using the weak axis slenderness $\overline{\lambda_v}$. For all samples, weak axis check was again the critical one, as the member finally buckles along weak axis. Analytically, lateral torsional buckling was ignored ($\chi_{LT} = 1,0$) due to one of the four conditions described in §7.1.2, and therefore the member buckles due to the axial load. Numerically, it can be shown from Figure 7.9 that the member starts to move laterally (along strong axis) but finally buckles towards weak axis. This again justifies the tendency of angles to buckle along weak axis. The mean value of the ratio

N_{num}/N_{anal} is equal to 1,05 with a standard deviation of 5,90%, and the validation of the analytical approach is effective if one accepts a 2% deviation from the numerical results.

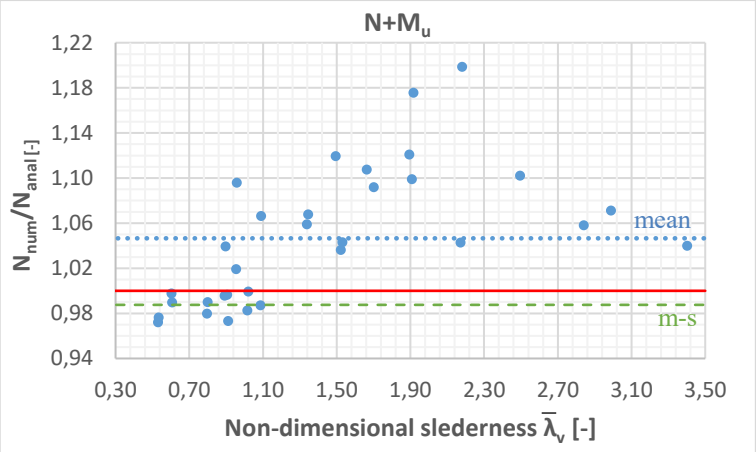

Figure 7.10: Ratio between numerical and analytical loads for $N+M_u$

7.2.5.3 Axial force and bi-axial bending

In this case, the axial force is applied at the mid-height of the leg at the middle line of the leg thickness (point P_3 in Figure 7.7(c)). This point could represent rather well the position of the connecting bolt for angles in structures. The details of the numerical samples that have been used, are the same as in the previous cases. Figure 7.11 illustrates the ratio between numerical and analytical (§7.1.4) resistance loads according to the weak axis slenderness $\overline{\lambda_v}$. The weak axis check was the critical one for this loading case too, and the member buckles towards weak axis.

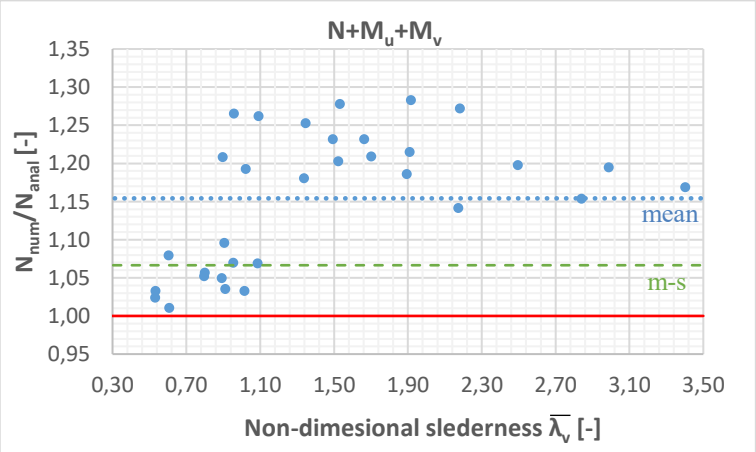

Figure 7.11: Ratio between numerical and analytical loads for $N+M_u+M_v$

The mean value of the ratio N_{num}/N_{anal} is equal to 1,15 with a standard deviation of 8,77%; these values are higher than for the previous studied cases, but it can be observed on Figure 7.11 that all the analytical predictions are on the safe side. Accordingly, the analytical approach for the combined resistance can be assumed as validated.

7.2.6 General method for angle sections

The validation of the proposed method has been done through comparison with numerical results obtained using the same analyses than those performed in §7.2.5.3. Therefore, the axial force is applied at the mid-height of the leg at the middle line of the leg thickness.

Three cases were considered for the validation:

A. Case 1:
   - "In-plane" 2nd order effects and bow imperfections are accounted for, in $\alpha_{ult,k}$;
   - e_0 is taken from prEN 1993-1-1:2019-§7.3.3.1 for relevant buckling curve (elastic verification);
   - elastic cross-section resistance is used (W_{el}).
B. Case 2:
   - "In-plane" instability effects are considered as negligible;
   - 2nd order effects are disregarded ($k_u=1/(1-N_{Ed}/N_{cr,u})=1$) and e_0 is taken equal to zero (in recognition of the rather limited impact of this parameter) - such an assumption should be limited to angles connected by one leg as, in this case, the strong axis moment and its influence remains limited;
   - elastic cross-section resistance is used (W_{el}).
C. Case 3:
   - Same assumptions as in Case 2, but taking into account the actual cross-section resistance using $W_u=\alpha W_{el,u}$, as defined in §7.1.2.

Figure 7.12 presents the ratio between numerical and analytical resistances obtained for the three different cases as a function of the weak axis slenderness $\overline{\lambda_v}$. The analytical resistance corresponds to the maximum load that satisfies eq. (7.22). Each case is represented by a colour and the relative horizontal line illustrates the mean value minus the standard deviation for each case.

It may be seen that the analytical approach for all the three cases is on the safe side, with Case 1 to be the safest. Therefore, each one may be used but the 3rd is closer to the numerically determined actual behaviour.

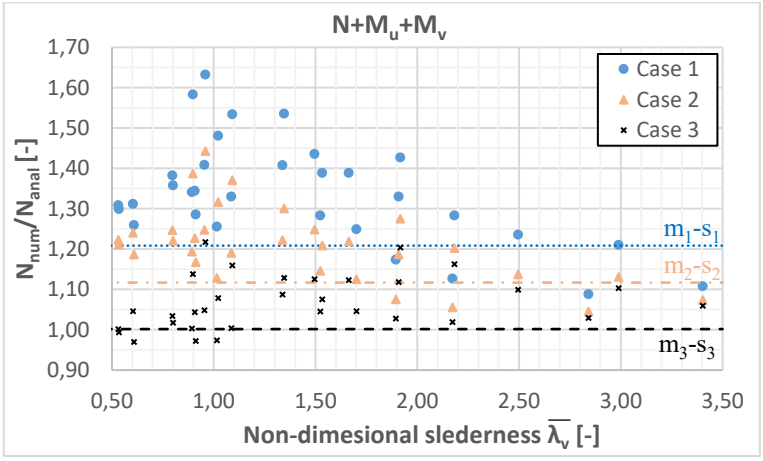

Figure 7.12: Ratio between numerical loads and the analytical ones, obtained through the general method, for N+Mu+Mv

7.3 Experimental validation

In the following, the design formulas given in §7.1 are checked against tests that have been performed by various universities and are available in the literature, as well as with the tests performed in the framework of the present thesis. For all the tests, the analytical load was determined using the actual geometrical and material properties without safety factors. A comparison with Eurocode 3 provisions is also reported.

7.3.1 Centric compression tests at Tsinghua University

At Tsinghua University, 66 tests were carried out on axially loaded pin-ended columns from equal angle sections and reported in Ref. [13]. The cross-sections ranged from L125x125x8 to L200x200x14 and the material was high strength steel (HSS) S420. All the profiles were categorized as class 4. For each section, the nominal slenderness of the angle columns, defined as the ratio of the column length to the gyration radius of cross-section around the principal minor axis, were selected as approximately 30, 40, 50, 60 and 80.

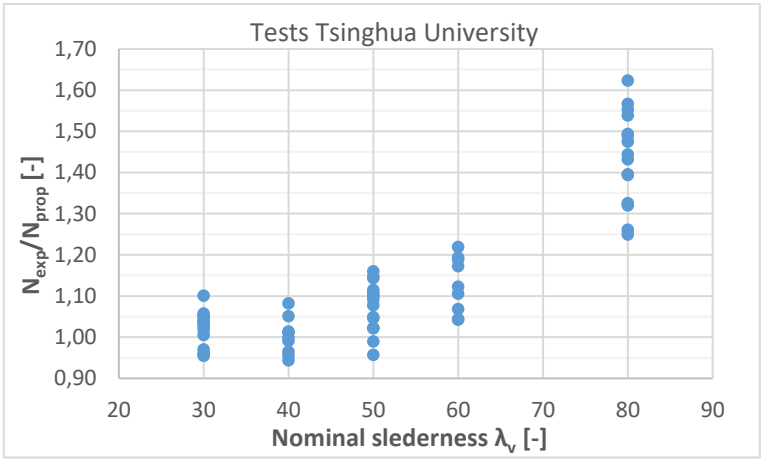

Figure 7.13: Ratio between experimental and analytical load for the Tsinghua University tests

Figure 7.13 presents the ratio between the experimental resistances and the analytical ones obtained using current proposal (see §7.1.1) according to the weak axis nominal slenderness λ_v. Figure 7.14 presents the mean value of the ratio between the experimental load resistances and the ones predicted by prEN 1993-1-1 and by the current proposal, as well as the mean minus one standard deviation value. For the evaluation of both analytical resistances, curve b has been used for all specimens except for one group of samples (L160x160x10) that exhibited a yield strength of 460,7 MPa; so curve a has been selected for the latter. It may be seen that the current proposal gives a better prediction of the resistance compared to the Eurocode 3. The conservative character of prEN 1993-1-1 may be explained by the fact that, in this case, the non-dimensional slenderness is determined from the weakest buckling mode (which is a flexural-torsional one in most of the cases according to the experimental tests), while, in the proposed model, the non-dimensional slenderness is always determined from the flexural mode.

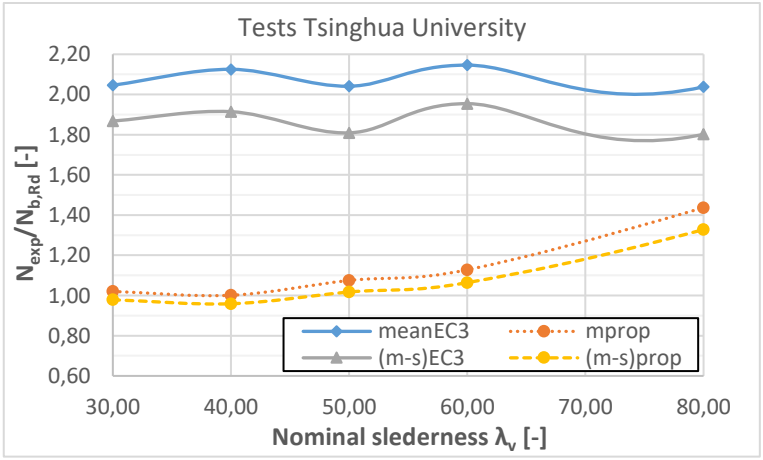

Figure 7.14: Ratio between experimental and analytical loads for the Tsinghua University tests, mean values

7.3.2 Centric and eccentric compression tests at ULiège

At the University of Liege, 12 tests were carried out on axially loaded pin-ended columns with or without eccentricity in the framework of the present thesis; they are reported in detail in chapter 7. The cross-sections were L150x150x18 and L200x200x16 with three different lengths. The material was high strength steel (HSS) S420 and S460. The load was introduced through supports that correspond to fully hinged boundary conditions, allowing free rotation in- and out-of-plane.

The ratio between the experimental load and the buckling resistance from prEN 1993-1-1 (noted as EC3 in the graph) as well as the resistance of the current proposal (see §7.1.1) for the tests without eccentricity are reported in Figure 7.15. As for all centrally loaded specimens, the first instability mode was a flexural one, the value for the computed non-dimensional slenderness is the same for both procedures. Therefore, the difference of the ratios reported in Figure 7.15 which are only observed for class 4 cross-sections are due to the evaluation of the plate slenderness for class 4 profiles, which differs in both procedures.

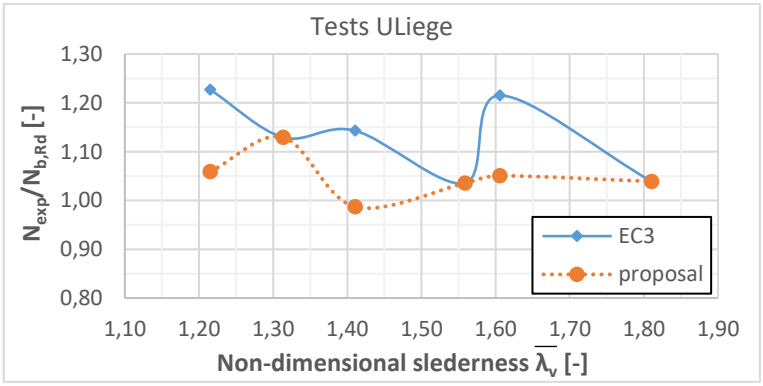

Figure 7.15: Ratio between experimental and analytical loads for the Liege University tests

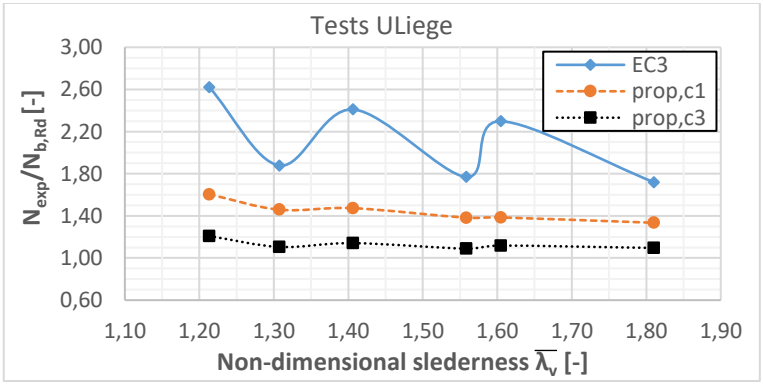

Figure 7.16: Ratio between numerical loads and the analytical ones, obtained through the general method, for Liege University tests

In the following, the general method, adapted for angles (see §7.1.5), is applied for the eccentrically loaded specimens and compared with the provisions of prEN 1993-1-1. The results are illustrated in Figure 7.16; two cases (Case 1 and Case 3 as defined in §7.2.6) were considered for the determination of the analytical load, based on the current proposal. It may be seen that the analytical method provides less conservative and safe side predictions for all test subjected to compression and bending. It should be noted that the specimens Sp22, Sp24 and Sp26 are categorized in class 4 according to prEN 1993-1-1 and therefore the W_{eff} value is used for the determination of the maximum stress. In

contrast, according to the current proposal, all the profiles reach their elastic resistance in bending and so the W_{el} value is used.

7.3.3 Eccentric compression tests at NTUA

At the National Technical University of Athens, 33 tests were carried out on axially loaded pin-ended columns with or without eccentricity and reported in Ref. [14]. The cross-sections were equal angle profiles L70x70x7 in S275 steel. The profile was categorized in class 1. The load was introduced through supports that correspond to fully hinged boundary conditions, allowing free rotation in- and out-of-plane. The experimental results are compared with the resistance formulae of the current proposal as outlined in section 7.1.4, as well as with the resistance formulae for members as described in prEN 1993-1-1, eq. (8.88)-(8.89), in combinations with Annex C where interaction factors for mono-symmetric sections are given.

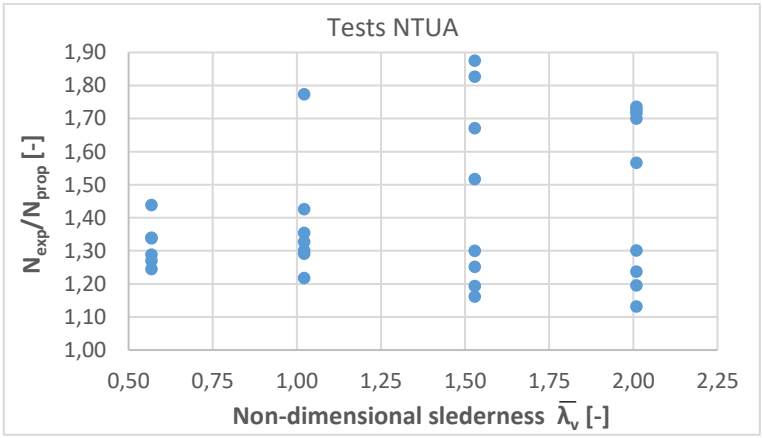

Figure 7.17: Ratio between experimental and analytical loads for the NTUA tests

Figure 7.17 presents, for all tests (except one for which the achieved experimental load was higher than its critical load) the ratio between the experimental resistances and the analytical ones obtained using current proposal (see §7.1.4) according to the weak axis non-dimensional slenderness.

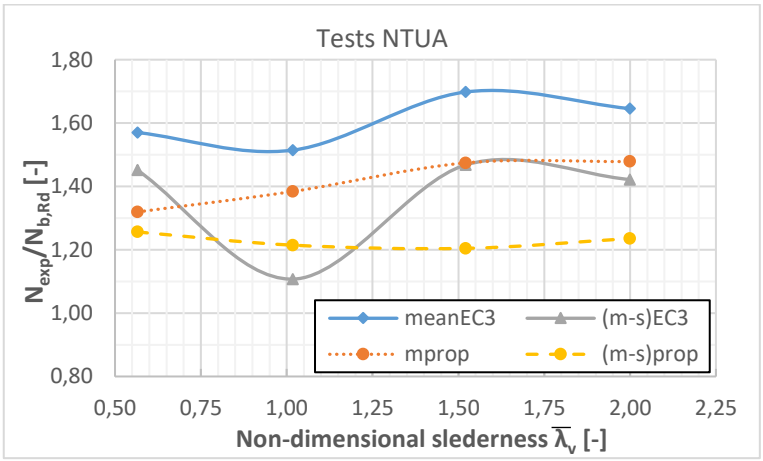

Figure 7.18: Ratio between experimental and analytical loads for the NTUA tests, mean values

Figure 7.18 presents the mean value of the ratio between the experimental loads and the analytical loads as determined by the above methods, and the mean minus one standard deviation value. It can be seen that the current proposal gives a better prediction for the column capacity compared to the existing version of prEN 1993-1-1 and is always on the safe side.

7.3.4 Eccentric compression tests at TU Graz

At the Technical University of Graz, 27 compression tests were carried out and reported in Ref. [11] on equal angle sections: 24 on L80x80x8 and 3 on L120x120x12 profiles. The material was S275. The boundary conditions varied from clamped supports (series BC1), to knife supports allowing rotation in the loading plane (series BC2) and fully hinged support allowing free rotation in- and out-of-plane (series BC3). The load was introduced to the profile through one leg by a bolted connection; the introduction point is the centre of the hole for connection with one bolt, or the centre between the two holes for connection with two bolts.

For this experimental campaign, the member capacity was calculated firstly by the proposed method, checking the angle profile to compression and biaxial bending that results from the loading eccentricity. The buckling length was set equal to the system length L_{sys}, for all cases except for support conditions BC1 with connection by two bolts, where the buckling length was set equal to $L_{sys}/2$.

The results of the current proposal are compared with the provisions of EN 1993-3-1 and not the ones of prEN 1993-1-1 as before, so as to account for the effect of the bolted connection. In this case, the member is checked to compression through an effective slenderness that takes into account both the eccentric loading and the end restraints brought by the bolted connection. Buckling is checked in respect to the weak (v) and geometric (y) axes. The relevant effective slenderness is determined from the following equations:

$$\bar{\lambda}_{eff,v} = 0{,}35 + 0{,}7 \cdot \bar{\lambda}_v \qquad \text{(Eq. 7.26)}$$

$$\bar{\lambda}_{eff,y} = \begin{cases} 0{,}40 + 0{,}7 \cdot \bar{\lambda}_y & \text{for connection with 2 bolts} \\ 0{,}58 + 0{,}7 \cdot \bar{\lambda}_y & \text{for connection with 1 bolt} \end{cases} \qquad \text{(Eq. 7.27)}$$

The design resistance, where $\chi = min\{\chi_v, \chi_y\}$, may be obtained as follows:

$$N_{b,Rd} = \begin{cases} \dfrac{\chi A f_y}{\gamma_{M1}} & \text{for connection with 2 bolts} \\ 0{,}8 \cdot \dfrac{\chi A f_y}{\gamma_{M1}} & \text{for connection with 1 bolt} \end{cases} \qquad \text{(Eq. 7.28)}$$

The member resistance is the lowest between the resistances according to the v- and y-axes.

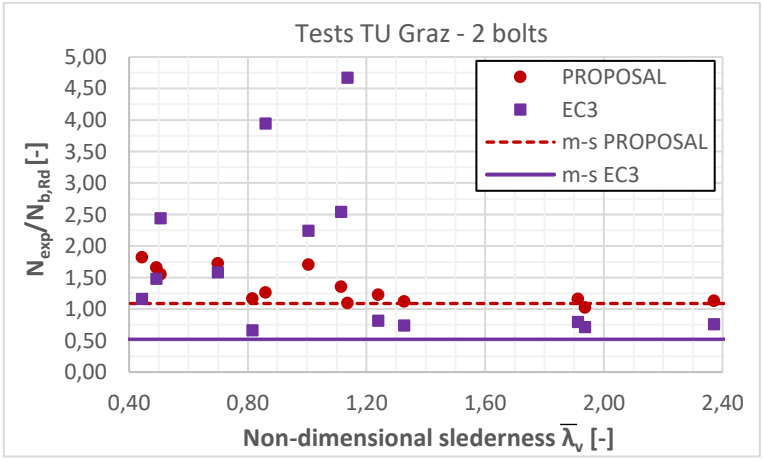

Figure 7.19: Ratio between experimental and analytical loads for the TU Graz tests with two bolts

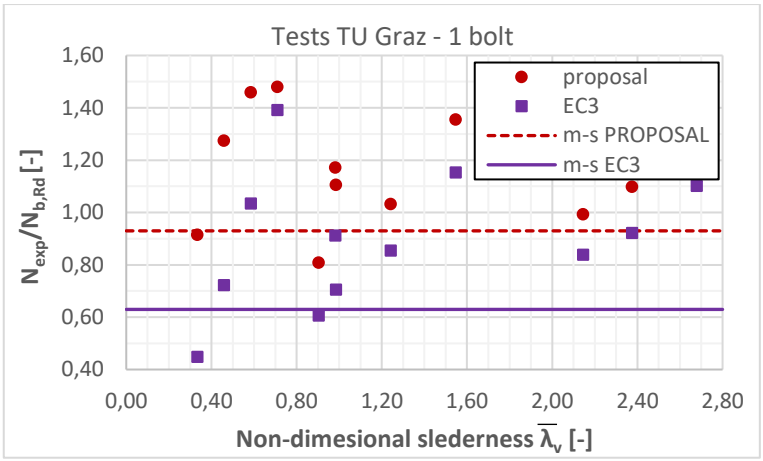

Figure 7.20: Ratio between experimental and analytical loads for the TU Graz tests with one bolt

Figure 7.19 and Figure 7.20 illustrate the ratio between the experimental and the analytical loads for connection with two bolts and one bolt respectively and provide the mean minus one standard deviation value for all tests. It may be seen that the EN 1993-3-1 method largely overestimates the angle capacities and is on the unsafe side. The conclusion of the authors in Ref. [11] is therefore confirmed who recommends, in absence of appropriate design formulae, to design through a 2nd order system analysis accounting for member imperfections. In contrast, the proposed method provides safe predictions for all tests with two bolts, and all but 3 tests with one bolt. Consequently, further investigations are still required to better account for the effect of the connections at the extremities of the angle; this could be a perspective for future research.

7.3.5 Eccentric compression tests at TUBraunschweig

At the Technical University of Braunschweig, 40 compression tests were carried out and reported in Ref. [15] on equal leg angle L50x50x5 profiles. The specimen lengths were 300, 600, 900, 1200 and 1500 mm, while the material was S355. The end support conditions were defined as clamped and hinged, and the load was introduced through one bolt M12.

Figure 7.21 presents, for all tests, the ratio between the experimental resistances and the analytical ones obtained using current proposal (see §7.1.4) according to the weak axis non-dimensional slenderness $\overline{\lambda_v}$.

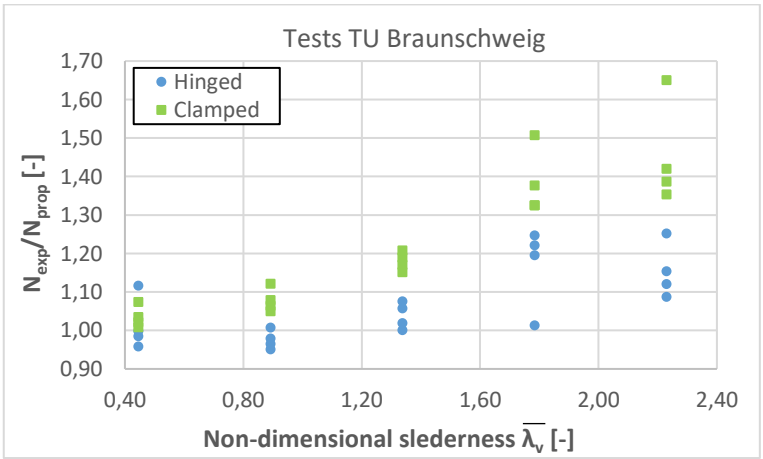

Figure 7.21: Ratio between experimental and analytical loads for the TU Braunschweig tests

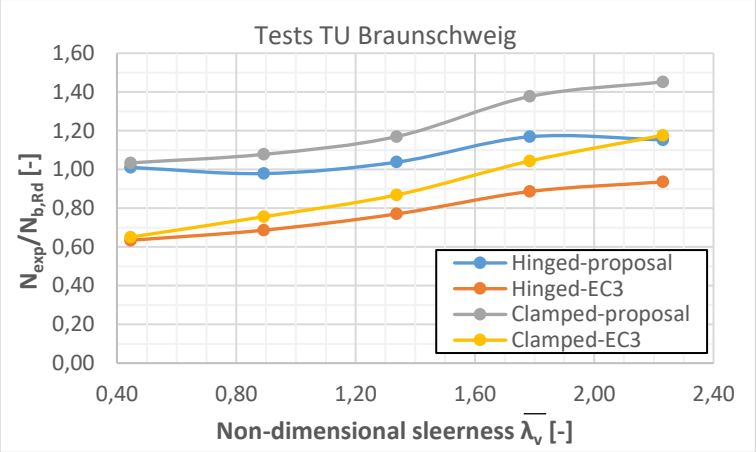

Figure 7.22: Ratio of experimental to analytical loads as determined by the proposed method and the provisions of EN 1993-3-1, mean minus one standard deviation values

Figure 7.22 presents the ratio (mean minus one standard deviation) of the experimental to analytical loads as a function of the relative weak axis slenderness. Similarly to the previous section, the analytical load was determined by the proposed method, under consideration of the moments that result from the loading eccentricity, and by the provisions of EN 1993-3-1. The buckling length was set in all cases equal to the system length as for the TU Graz tests, since all the specimens are connected through one bolt at their extremities. It may be seen that the proposed method gives best results for the hinged support conditions while, for the clamped support, the buckling capacity at larger slenderness is underestimated. In contrast, the provisions of EN 1993-3-1 appear to overestimate the capacity, especially for hinged support conditions. The conclusion of the authors in Ref. [15] is therefore confirmed that: "….the simplified method of EN 1993-3-1 for the one screw joint in the existing form is not wise to be used in practice".

7.4 Conclusions

This chapter presents design rules to predict the stability and resistance of members made of rolled equal leg angle profiles subjected to combined forces and moments. The main features of the proposed design rules are as follows:

- Existing Eurocode provisions are adapted for angle profiles.
- Appropriate European buckling curves for flexural and lateral torsional buckling of angles are detected.
- The proposed rules account directly for the presence of applied moments resulting from the connection eccentricities.
- The rules are generic for the referred profiles and do not apply only for lattice towers.
- They are written respecting the format of the existing Eurocode 3 specifications.
- They are simple to apply and are derived from basic rules of the stability theory.
- The proposed design rules were validated through comparisons to extensive numerical analyses and numerous experimental tests. Experimental results were also compared to existing Code provisions. It was shown that the proposed method allows a safe prediction of the member capacity with an accuracy which is much better than the one obtained with the present Code provisions. Accordingly, the current proposal may be used as an alternative to existing Code provisions.

8. STRUCTURAL TYPOLOGIES OF TRANSMISSION TOWERS

Transmission towers have been being built since the very beginning of the 20th century with the upcoming need to transport electrical energy from the production location to the consumers. The first regular transmission tower in Europe was erected in 1905 between Moosburg and Munich in Germany. A transmission tower consists in a tall self-supporting structure, which carries electrical overhead lines. These lines are part of high-voltage CD or AC systems. The function of the supporting structures consists on one hand in the safe transfer of the conductor loads to the ground and on the other hand in ensuring a safety distance between the conductors and the ground as well as between the conductors. The height of the towers or pylons depends on the voltage of the power lines and generally varies in a range between 15 m for low voltage (≤ 1 kV) and 70 m for extra-high voltage lines (> 110 kV). However, for special purposes as to span obstacles in the axis of the power line such as forests or rivers, supporting structures exceeding a height of 100 m are realized. The tallest transmission towers in Europe, with a height of 227 m, are a group of four lattice transmission towers in Schleswig-Holstein (Germany), known as the Elbe Crossing 2.

The typologies and the functions of transmission towers, and the typologies of lattice towers and the relevant terminology are briefly presented in this chapter.

8.1 Typologies of transmission towers

The supporting structures of overhead lines can be made of different materials, and they can have several typologies: tubular steel towers, lattice steel towers, wooden and concrete pylons (Figure 8.1). The selection of the type of the transmission tower is mainly based on the voltage circuit (low, medium, high or extra-high voltage) that it should support. Lattice towers are used for all ranges of voltages and therefore they are the most common types of towers for high-voltage transmission lines.

(a) **(b)** **(c)** **(d)**

Figure 8.1: Typical structure for a (a) wooden pylon, (b) concrete pylon, (c) tubular steel pylon and (d) lattice tower

8.2 Functions of transmission towers

The transmission towers can be categorized by the way they support the line conductors as suspension or dead-end towers. In reality, the line grid is composed of transmission towers with different functions to ensure a safe support of the line conductors.

A suspension tower has vertical hanging isolators that carry the conductors (Figure 8.2 left). The tower is subjected to gravity loads coming from the conductors and the tower itself as well as transverse forces caused by wind loading. As the tower does not get any tension forces from the conductors, its design results in lighter structures than for dead-end towers.

Figure 8.2: Suspension tower (left) and dead-end tower (right)

Dead-end towers are located at the extremities of the power line, for long spans, at the places where the line changes its direction and in regular distance of a straight line to reduce the cascading tower failures after an unexpected conductor failure. A dead-end tower uses horizontal strain insulators at the end of the conductors (Figure 8.2 right). As dead-end towers are subjected to tension loads obtained from the conductors additionally to the self-weight and wind loads, their structures are heavier and more expensive than those required for suspension towers.

8.3 Steel lattice towers

8.3.1 The tower's structure

Steel lattice towers for transmission lines are mainly made of hot-dip galvanized steel angle profiles that are used as single members and/or as parts of built-up members. The galvanization of the angle profiles ensures a corrosion protection over the whole lifetime of the tower, generally from 80 to 100 years.

Figure 8.3: Modular construction with bolted connections.

The bolted connections and gusset plates allow a modular construction (Figure 8.3) of the tower and simplify its erection at the construction site. First, the different modules are preassembled in lying

position, then lifted with a crane and finally bolted by assembly operators. Alternatively, the whole tower can be mounted in lying position and then be raised by cable pull. This operation requires a big assembling area, and it is therefore only rarely applied. In mountains area, the different modules are often placed by helicopter since the mounting area is too confined for cranes. Welded connections are not used in lattice towers, as they would complicate its erection.

In general, the tower structure can be subdivided into four main parts which are described in detail below.

(α) The tower body

The body is the main structure of the tower. It is consisted, in general, of 4 leg members connected together through a primary and a secondary bracing system in the vertical and horizontal plane (Figure 8.4).

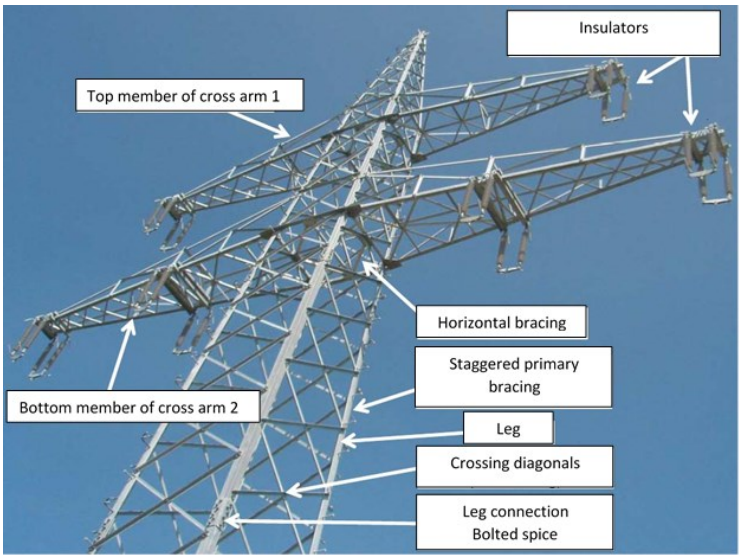

Figure 8.4: Tower body with description of the different elements

The legs, made of single equal leg angle profiles or built-up ones in star-battened configuration, run from the foundations to the top of the tower. They mainly transfer the self-weight of the structure and therefore the profile size continuously decreases from the lower to the upper modules. Over the height, the tower body is subdivided into several modules/segments, which are connected between their leg profiles by bolted splices. This allows a reduction of the delivery length of the leg profiles and a modular mounting of the tower.

The primary bracing system is constituted of diagonals often made of single equal or unequal angle profiles and built-up angle profiles in a back-to-back configuration. It reduces the buckling length of the legs and helps stabilizing the framework structure (e.g. triangulation) of the tower. It also transfers the horizontal forces coming from the wind forces acting on the tower body. The secondary bracing members are also redundant members; they are used to reduce the unsupported length of the main legs and of primary bracing members, so increasing their buckling stability. In addition, they increase the stiffness of the tower structure. They are commonly made of small equal or unequal angle profiles. The type of primary and secondary vertical bracing systems depends on the loads and on the tower's height, and commonly varies over the height of the tower. Different layouts are given in Figure 8.5. For standard tower geometries as used in Europe, the K-bracing and X-bracing are usually applied for the bottom and the second section of the tower respectively. The upper modules are often

braced by a crossing diagonal system. The advantage of the crossing diagonal system is that the compression diagonal is stabilized by the tension one, as the lateral displacement of the latter is avoided.

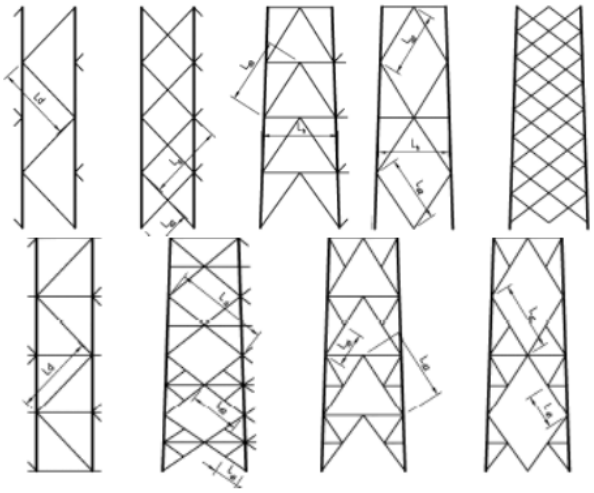

Figure 8.5: Different primary and secondary vertical bracing systems as illustrated in EN 1993-3-1

Between two modules the tower is usually stiffened by a horizontal bracing system (Figure 8.6), also called diaphragm bracing. This system takes the horizontal forces from wind loading on the tower and transfers it to the legs. In addition, the horizontal bracing system absorbs the torsional moments generated by an accidental unbalanced loading on the structure (e.g. rupture of one conductor).

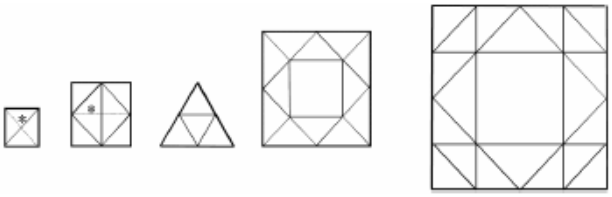

Figure 8.6: Common horizontal bracing systems as illustrated in EN 1993-3-1

Figure 8.7: Cross arms of a lattice tower

(β) The cross arms

The cross arms (Figure 8.7) support the insulators and the conductors of the power line and transfer their loads to the tower body. Depending on the type of tower, one, two or even more than three cross arms on the left and right sides of the tower are necessary. The length of the cross arms depends on

the type of tower and operating voltage. For high voltage circuits, the clearance between the conductors must be increased and the cross arms become longer. For instance, if the three phases of a 380-kV circuit are installed on one single cross arm, the length of the cross arm is about 22 m. This leads to a total width of the transmission tower of approximately 45 m.

The cross arm is constituted of a top and bottom angle member, each being connected by bolts to the tower legs. These members are braced by a vertical and horizontal system of angle profiles. The size of the angle profiles strongly depends on the tower type and the conductor loads.

(γ) The earth wire support

The earth wire support is the top module of a transmission tower which carries the earth wire. The main role of the earth wire is the protection against lightning, and in some cases when it is made of an optical fibre, is also used as an information transmitter.

The usual heights of the support, where the legs taper, vary between 5,0 m and 8,0 m in function of the tower height and operating voltage of the line. The legs are commonly braced by a single lattice staggered systems of small single angle profiles.

(δ) The foundations

The foundation of the tower depends on the form of the tower, the loading, the type of the soil and the available space. The types which are mainly used in practice are strip or step foundations, pile or driven pipe pile foundations (Figure 8.8). The legs are anchored by friction or by separate elements into the concrete. The elements are usually sticking angles made of common angle profiles.

Figure 8.8: Step foundation of a lattice tower

8.3.2 Typologies of lattice towers

Depending on the terrain typology, different lattice tower structures are used to overcome the several obstacles (e.g. forests, rivers, railways, etc) encountered along the grid. Different typologies of lattice towers are currently used all over the world. The typology differs between the continents and the corresponding operating voltage of the power lines. In this section, on overview of the different types of lattice towers used on the European market is given. The different configurations are illustrated in Figure 8.9 and described below:

(a) Anchor portal tower

Anchor portal towers are gantry structures supporting the conductor in a switchyard. The internal cross arms are supported by at least two tower bodies. The structure of anchor portal towers is adapted to the high tensions forces in the conductors that need to be anchored in the switchyard. Anchor

portal towers are also used to span over railways as they are less sensitive to vibrations than cross span structures.

(b) Delta tower

In a Delta tower, the cross arm is supported by a V-shaped fork, which offers space for a conductor in the centre line of the tower. They are commonly used to support one single circuit (i.e. 3 phases). The delta tower is widely spread in the US, Canada, France, Spain and Italy. The name originates from the fact that the fork with the cross arm resembles the shape of an inverted Delta.

(c) Fir tree tower

A fir tree tower belongs to the three plane tower typologies. It has three cross arms arranged in three planes on two sides of the tower body. The lower cross arm is longer than the one in the middle, which is again longer than the upper cross arm. This form is reminiscent of a fir tree. The tower generally carries two circuits whereupon the conductors of each circuit are supported on each side of the cross arms. Fir tree towers are tall and the span of the cross arms is reduced. For a 380-kV circuit for instance, the standard height is about 60 m and the span of the cross arm is approximately 20 m. The required width of the protection strip (i.e. the strip of land set aside for a safety corridor distance between the power line and nearby structures and vegetation and which is used to construct, maintain or repair the power line) is only 50 m compared to 70 m or 120 m of other tower typologies. Therefore, fire tree towers are mainly erected in areas where the distance of the conductors to the soil is increased and where the width of the protection strip needs to be small (e.g. forests).

(d) Single plane tower

Single plane towers only have one single cross arm and carry one or two circuits. The phases are supported by the cross arm on the two sides of the tower body. The Single Plane tower is used in areas with reduced height prescription like airports. The disadvantage of the tower typology is the wide span of the cross arm (e.g. 40 m) which results in a wide protection strip (e.g. 120 m) and therefore in a huge environmental intervention.

(e) Danube tower

The Danube tower is the most widely spread tower typology in Europe for 220-kV and 380-kV circuits. The tower has two cross arms arranged in two planes. The lower cross arm is usually longer then the upper one. In general, they support two circuits whose phases are ordered in a triangular shape. The upper cross arm carries one phase while the lower one carries two phases.

(f) Barrel tower

Barrel towers have a similar typology than Fir Tree towers. They have three cross arms in three planes and they commonly carry two circuits. The median cross arm is longer than the lower and upper cross arms and each cross arm supports 2 phases on each side of the tower body. As for Fir Tree towers, Barrel towers are tall with a reduced span of the cross arms, and they are applied in areas where big heights and reduced protection strips widths are required (e.g. forests). It is the standard tower typology in the UK National Grid.

(a) Anchor portal tower

(b) Delta tower with one circuit

(c) Fir tree tower

(d) Single plane towers at the airport of Karlsruhe, Germany

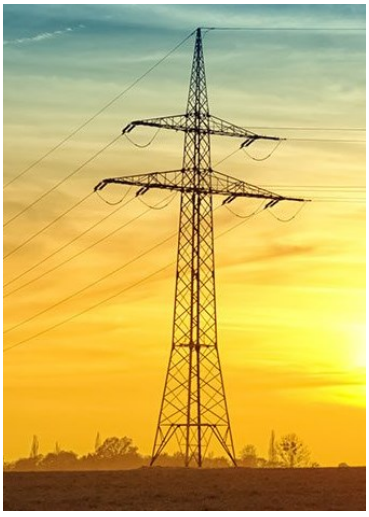

(e) Danube tower

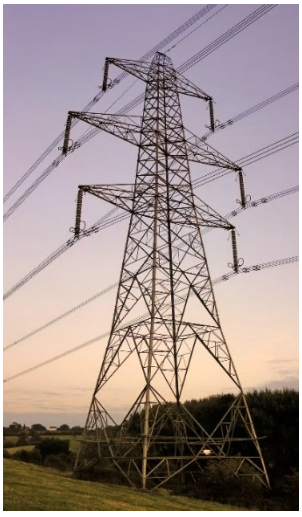

(f) Barrel tower

Figure 8.9: Different typologies of transmission towers

9. ASSESSMENT OF THE DESIGN OF A TRANSMISSION TOWER

In Europe, the design of transmission towers for overhead electrical lines is carried out according to EN 1993-3-1, in combination with EN 1993-1-1 which providing general rules, and for electrical lines exceeding 1 kV, according to the CENELEC standard EN 50341. Based on these normative documents, the tower is modelled as a simple truss structure where all the steel element connections are considered as hinged and the forces are only applied to the truss nodes. Such models do not adequately reflect the actual tower behaviour of the structure, as loads and especially wind ones are directly imposed on the entire member length and introduce bending moments in members. Furthermore, the design of lattice towers is classically carried out through a first order linear elastic analysis, neglecting the significant second order effects developing in these structures.

In this chapter, a typical electric transmission steel lattice tower made of angle section members has been selected. The tower has been initially designed by means of the commercial software TOWER [41], in accordance with the current normative requirements, based on a first-order linear elastic structural analysis of a truss structure. For the assessment of the design, the tower is then simulated with FINELG non-linear finite element software using beam elements, considering relevant imperfections as well as geometrical and material non-linearities. In this model, every single member has been properly simulated, in terms of orientation and eccentricities at its extremities.

Both software were firstly compared by the results of the frame analysis in the elastic range. Then, and to have a global overview of the actual tower's response, an elastic instability analysis has been performed and was complemented-validated by a second order linear elastic one. The importance of considering second order effects in the analysis is underlined. However, as material and geometrical non-linearities combined with imperfections (member out-of-straightness and structural out-of-plane) are affecting the response of the tower, a full non-linear analysis has been performed to check the validity, in terms of resistance and stability, of the initial design made with the TOWER software. The results of all the analyses are presented and discussed in the following.

9.1 Details of the studied tower

The Danube tower is the most spread tower typology for transmission lines in Europe. Moreover, many transmission lines are currently in planning throughout Europe, in the framework of the conversion from 220 kV to 380 kV lines, where this typology of tower is the preferable one of both designers and owners. As a result, the Danube tower (Figure 9.1) is the typical typology for current and future transmission lines and is therefore selected for the case study presented in this chapter.

Figure 9.1: Danube tower for a transmission line of 380 kV

9.1.1 Geometry of the tower and the line

The considered tower is a suspension one (i.e. hanging insulators), with a height of 50 m, made of steel equal-leg angle profiles; its geometry is shown in Figure 9.2. The structure is supposed to be erected in Erzgebirge in Saxony (Germany) and is part of a straight transmission line.

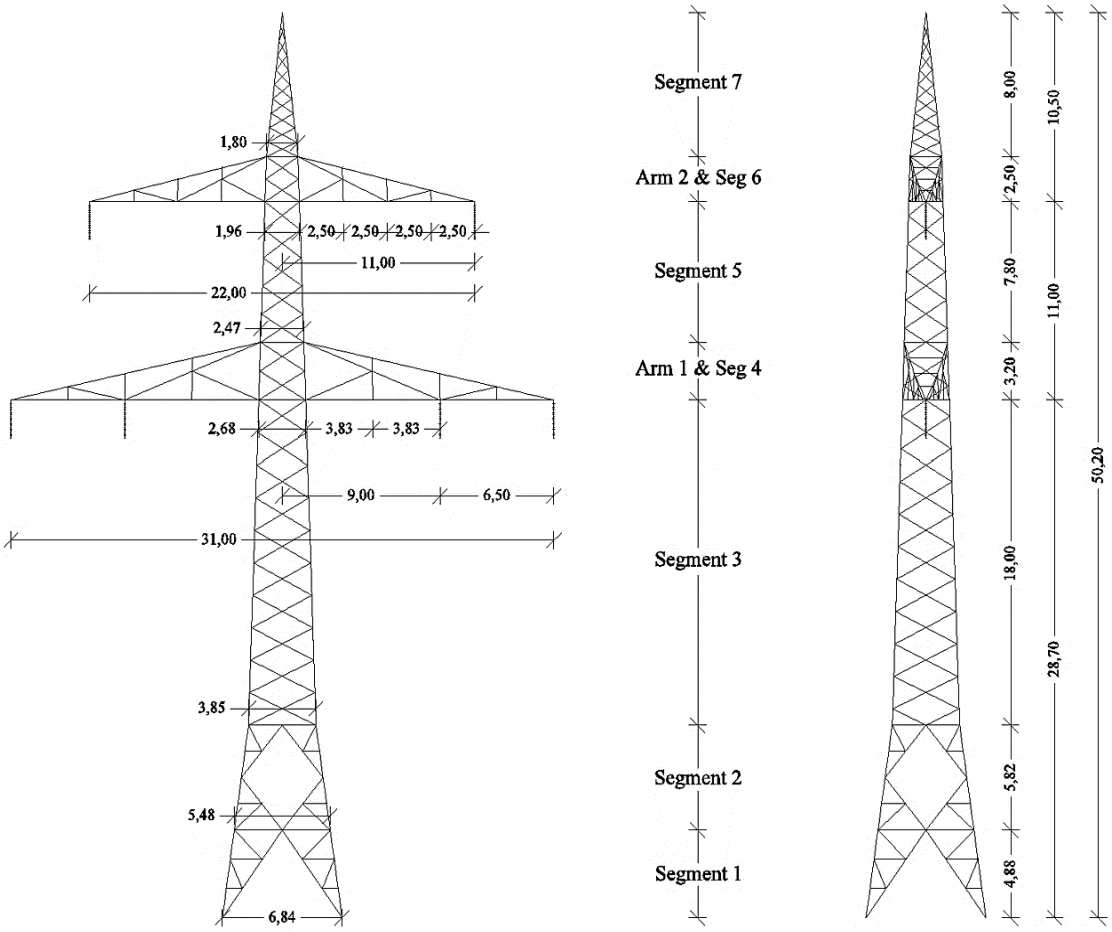

Figure 9.2: Geometry and annotation of the different segments of the studied Danube tower

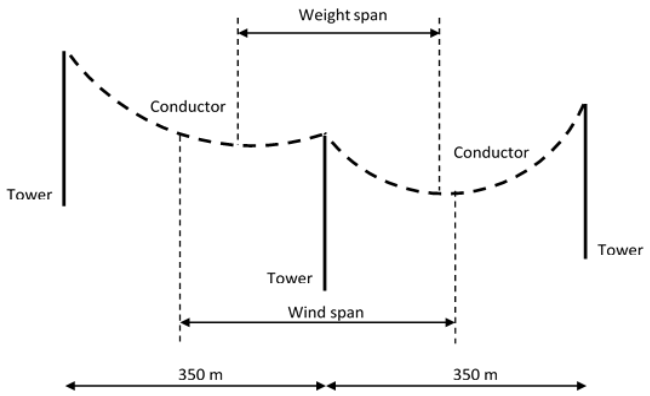

Figure 9.3: Definition of wind span and weight span

Even if only one lattice tower is considered, the design requires some basic information of the line, in order to quantify the conductor loads acting on the pylon. Thus, the studied tower is part of a 380-kV straight transmission line with a distance between the towers of 350 m. The segment of the line

is in a mountain area with significant height differences, what leads to the following line spans (Figure 9.3):

- Wind span: L_w = 350 m
- Weight span: L_g = 1,5·350 m = 525 m (according to [42])

The wind span is equal to the mean value of the two neighbouring spans of the tower while the weight span is equal to the distance between the two lowest points of the conductors in the two neighbouring spans of the tower.

9.1.2 Conductors and insulators

The tower carries two 380 kV circuits, each one consisting in 3 phases. Each phase is made of a bundle of 4 conductors which is supported by a suspension insulator. On its top, the tower carries one single earth wire for lightening protection. The conductors and the earth wire are made of steel fibres enveloped by several fibres of aluminium (Figure 9.4-a). The steel fibres reinforce the conductors and allow a safe transfer of the conductor loads while the aluminium fibres increase the conductivity of the conductor. Based on EN 50182 [43], the following conductors have been selected:

- 4*264-AL1/34-ST1A for the conductors;
- 1*94-AL1/15-ST1A for the earth wire.

Important mechanical data of the conductors and the earth wire can be found in Table 9.1.

(a)

(b)

Figure 9.4: (a) Aluminium-steel conductor, (b) Quadri*Sil insulator

Table 9.1: Mechanical data for the conductors

Code	Areas		No. of wires		Wire diameter		Mass per unit	Final modulus	Coefficient of linear
	Al [mm²]	Total [mm²]	Al [-]	Steel [-]	Al [mm]	Steel [mm]	[kg/gm]	[N/mm²]	1/K
94-AL1/15-ST1A	94,4	109,7	26	7	2,15	1,67	380,6	77000	1,89E-05
264-AL1/34-ST1A	263,7	297,7	24	7	3,74	2,49	994,4	74000	1,96E-05

Each conductor is connected to a suspension insulator, which transfers the conductor loads to the cross arms of the lattice tower. The insulators (Figure 9.4-b) are made of silicone rubber (Quadri*Sil Insulator from the company Hubbell); their length is about 5 m to ensure a safe distance between the conductors and the tower structure.

9.1.3 Initial design of the studied tower

The initial design of the tower has been done by TOWER finite element software, which is dedicated to the design of transmission and telecommunication steel lattice towers, according to different international standards. The tower has been designed under gravity and wind loads following mainly the recommendations and requirements of EN 50341-1 and EN 50341-2-4 [44]. The design is carried out through a first order linear elastic analysis of a truss structure.

The angle profiles are made of steel grade S355J2; the steel material law is linear elastic without any plastic yield plateau (nominal values). The eccentricities of the connections are not modelled, but their influence is considered via an effective non-dimensional slenderness λ_{eff} in the member buckling checks. More details about the design of the tower can be found in [45] and [46].

The cross-sections resulting from the design checks based on a linear elastic global analysis performed by TOWER are presented in Table 9.2. For the annotations of the different segments of the tower, see Figure 9.5. The total weight of the structure is 166,73 kN.

Table 9.2: Angle profiles for the different sections of the tower

Group name	Cross-Section	Steel grade
Bottom-legs	L 150x150x13	S355J2
Segment 2	L 140x140x15	S355J2
Segment 3	L 120x120x16	S355J2
Segment 4	L 80x80x10	S355J2
Segment 5	L 80x80x6	S355J2
Segment 6	L 75x75x4	S355J2
Segment 7	L 45x45x3	S355J2
Diagonal 1	L 75x75x4	S355J2
Diagonal 2	L 75x75x4	S355J2
Diagonal 3	L 90x90x5	S355J2
Diagonal 4	L 90x90x6	S355J2
Diagonal 5	L 60x60x4	S355J2
Diagonal 6	L 45x45x4	S355J2
Cross 1 – bottom	L 150x150x12	S355J2
Cross 1 – top	L 120x120x7	S355J2
Cross 1 – base	L 130x130x8	S355J2
Horizontal 1	L 80x80x5	S355J2
Horizontal 2	L 90x90x5	S355J2
Horizontal 3	L 100x100x7	S355J2
Horizontal 4	L 76x76x4,8	S355J2
Horizontal 5	L 75x75x6	S355J2
Horizontal 6	L 65x65x4	S355J2
Horizontal 1 base	L 80x80x5	S355J2
Horizontal 2 base	L 80x80x5	S355J2
Horizontal 3 base	L 76x76x4,8	S355J2
Horizontal 4 base	L 60x60x4	S355J2
Cross – Horizontal	L 45x45x3	S355J2
Cross 2 – bottom	L 120x120x7	S355J2
Cross 2 – top	L 75x75x5	S355J2
Cross 2 – base	L 90x90x5	S355J2
Redundant 1	L 90x90x5	S355J2
Redundant 2	L 60x60x4	S355J2
Redundant 3	L 90x90x5	S355J2

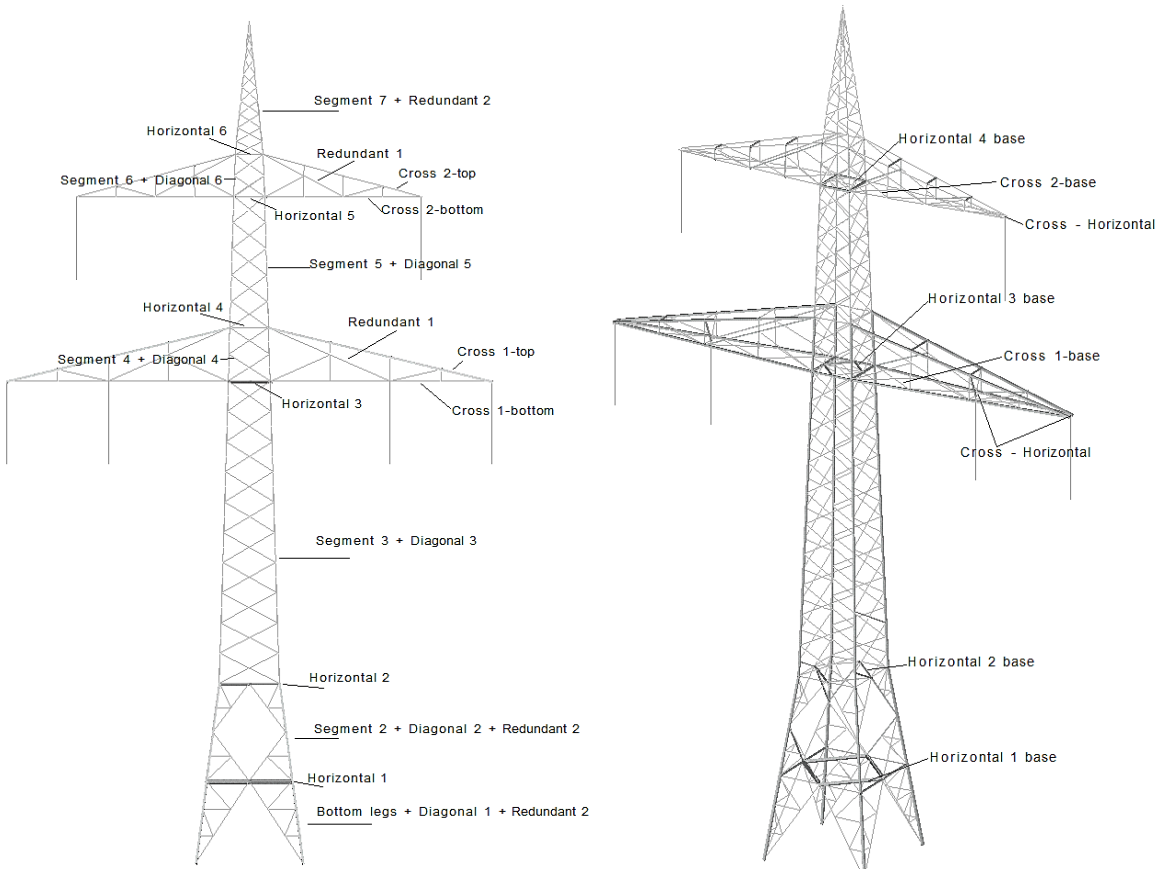

Figure 9.5: Annotations of the different segments of the tower

9.2 Numerical simulation of the tower with FINELG

9.2.1 Description of the finite element model

For the validation and the assessment of the initial design, the tower has been simulated with FINELG finite element software, using beam elements with 7 degrees of freedom, as plate buckling phenomena in the angle legs are not to be contemplated. The model of the tower is represented in Figure 9.6. It is worth noting that FINELG has been already successfully used in the past to simulate a lattice tower [22]; and it has also been used on the framework of the present thesis to predict successfully the failure load of full-scale experimental tests, as they reported in Annex B.

Every element/bar is modelled with its appropriate eccentricity, rotation and orientation in order to simulate the reality as closely as possible. As a result, the elements are not only subjected to axial forces but also to bending moments. At the level of a global analysis, the bolted connections between the diagonals and tower legs as well as the splices in the tower legs are not considered directly in the model, but their global response has been simulated through appropriate hinges/constraints at the ends of the elements. Moreover, their self-weight has been considered as referred in §9.2.2(A1).

The tower structure is modelled using the following assumptions:

- the main legs are modelled considering continuity over their total length;
- the bracing members and horizontal members are considered as pinned at their ends connected to the main legs and to the horizontal members;
- the secondary bracing elements are also considered as pinned at their ends.

For the members that are assumed as continuous over their total length (main tower legs), the 7 DOF are blocked at the extremities of the finite beam elements. For the pin-end members (i.e horizontals, primary and secondary bracings), all the rotations are free, except the torsion about the beam axis which is blocked; all the other DOF are blocked too. The foundations are assumed as pinned.

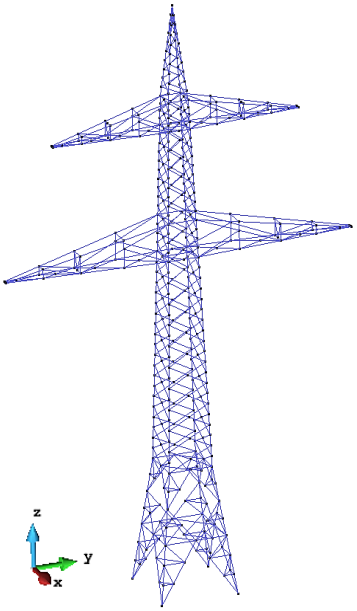

Figure 9.6: 3-D model from FINELG software

All the members of the tower are made of steel grade S355J2. Two cases have been considered in terms of material law: a linear elastic one and a non-linear perfectly plastic one. Nominal values for the material properties have been used (E=210.000 MPa, v=0,3 and ρ=7850 kg/m^3), while the yield stress is taken equal to 345 MPa, as for the initial design checks. For each element, residual stresses originating from hot-rolling are considered in material non-linear analyses; the pattern is in accordance with Ref. [39], as it shown in Figure 6.18 too. Furthermore, for the analyses where initial imperfections have been applied, those are in accordance with the 1st instability mode, calibrated so as to reach an amplitude of *L/1000* (L is the length of the member/segment where instability occurs).

The conductors and the insulators have not been modelled. However, the wind loads acting on them, as well as their self-weight have been calculated apart and introduced in the model as point loads acting at the top of the insulators.

9.2.2 Applied loads

The gravity (self-weight) and wind loads acting on the tower, the conductors, the earth wire and the insulators are presented in the following. Tension loads in the conductors are not considered since it is a suspension tower in a straight line.

A.1 Self-weight of tower

The self-weight of the tower itself is calculated automatically from the analysis program according to the geometry, considering the specific weight of steel $\gamma = 7850\ kN/m^3$. Bolts and gusset plates are not modelled in FINELG, but their self-weight is taken into account by an adjustment factor equal to 1,20 which artificially increases the dead loads of the tower; this approach has been used also for the initial design of the tower. This leads to a total weight of the tower of 172,60 kN.

A.2 Self-weight of conductors, earth wire and insulators

The self-weight $V_{c,i}$ of the conductors and the earth wire cable are evaluated according to EN 50182 [43] and summarized in Table 9.3.

Table 9.3: Self-weight of conductors and earth wire

Type / Code	m_l [kg/km]	L_g [m]	$g_c = m_l \cdot g$ [N/m]	No of bundles n_b	$V_{c,i} = n_b \cdot g_c \cdot L_g$ [kN]	No of conductors n_c	$V_{c,tot} = n_c \cdot V_{c,i}$ [kN]
1 Conductor 264-AL1/34-ST1A	994,4	525	9,755	4	20,49	6	122,91
Earth wire 94-AL1/15-ST1A	380,6	525	3,734	1	1,96	1	1,96

The weight of one insulator is about 0,087 kN. Consequently, for the six insulators which have been used, the total weight equals 0,522 kN.

B.1 Wind loads at the tower's body

The calculation of the wind loads on the tower is based on EN 1993-3-1/Annex B and EN 1991-1-4 [47]. The tower is subdivided into several segments, as illustrated in Figure 9.2, and for each segment a mean wind load is evaluated. The mean wind load in the direction of the wind on the tower, for a segment, should be taken as:

$$F_{m,W}(z) = \frac{q_p(z)}{1+7I_v(z)} \sum c_f A_{ref} \quad \text{(Eq. 9.1)}$$

where z is the height above the base at which the load is calculated. All the notations not explained here are provided in chapter 2. The above equation may be transformed to the following one:

$$F_{m,W}(z) = \frac{1}{2}\rho_{air} v_m^2 \sum c_f A_{ref} = q_m(z) \sum c_f A_{ref} \quad \text{(Eq. 9.2)}$$

The mean wind velocity at the height z is:

$$V_m(z) = c_r(z) c_o(z) \left[c_{dir} c_{season} V_{b,0} \right] \quad \text{(Eq. 9.3)}$$

where:

- $c_r(z)$ is the roughness coefficient;
- $c_o(z)$ is the orography coefficient, equal to 1,0 according to EN 1991-1-4/§4.3.3;
- c_{dir} is the directional factor, equal to 1,0 according to EN 1991-1-4/§4.2;
- c_{season} is the season factor, equal to 1,0 according to EN 1991-1-4/§4.2;
- $v_{b,0}$ is the fundamental value of the basic wind velocity, taken as 25,0 m/sec according to the German national annex of EN 1991-1-4 & EN 50341-2-4.

It is assumed that the tower is located in a category II terrain, according to EN 50341-2-4 (in line with the German National Annex); this leads to some characteristic values for the mean wind velocity to considerer in the calculations.

The mean wind loads have been calculated at the mid-height of each segment and for two different wind directions (see Figure 9.7 for the direction):

- wind loads perpendicular to the cross arms W_x (+X direction);
- wind loads in the direction of the cross arms W_y (+Y direction).

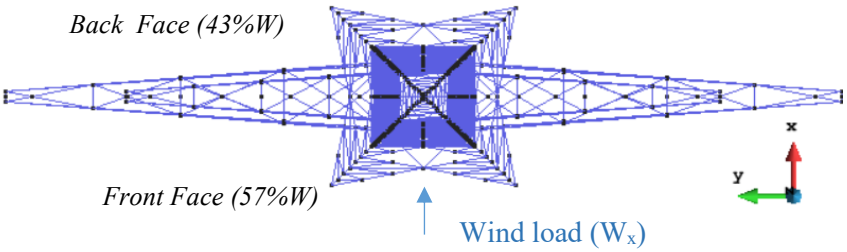

Figure 9.7: Definition of wind direction

Table 9.4: Mean wind loads on the tower body for wind perpendicular to the arms (θ=0°)

Part	z_m [m]	$q_m(z)$ [N/m²]	A_{ref} [m²]	$c_{f,s}$ [-]	$F_{m,wx,front}$ [kN]	$F_{m,wx,back}$ [kN]
Segment 1	2,44	213,137	3,21	2,77	1,080	0,815
Segment 2	7,79	359,422	4,07	2,71	2,261	1,706
Segment 3.down-mid	15,20	460,901	6,09	2,97	4,756	3,588
Segment 3.mid-up	24,20	538,936	5,29	2,93	4,769	3,597
Segment 4	30,30	578,843	1,99	2,76	1,810	1,366
Segment 5	35,80	609,375	3,23	2,99	3,358	2,533
Segment 6	40,95	634,548	0,92	2,95	0,983	0,742
Segment 7	46,20	657,574	1,59	2,85	1,694	1,278
Arm 1 (lower arm)	29,77	575,638	6,09	2,74	5,480	4,134
Arm 2 (upper arm)	40,53	632,614	3,51	2,70	3,424	2,583

Table 9.5: Mean wind loads on the tower body for wind parallel to the arms (θ=90°)

Part	z_m [m]	$q_m(z)$ [N/m²]	A_{ref} [m²]	$c_{f,s}$ [-]	$F_{m,wy,front}$ [kN]	$F_{m,wy,back}$ [kN]
Segment 1	2,44	213,137	3,21	2,77	1,080	0,815
Segment 2	7,79	359,422	4,07	2,71	2,261	1,706
Segment 3.down-mid	15,20	460,901	6,09	2,97	4,756	3,588
Segment 3.mid-up	24,20	538,936	5,29	2,93	4,769	3,597
Segment 4	30,30	578,843	0,51	3,61	0,610	0,460
Segment 5	35,80	609,375	3,23	2,99	3,358	2,533
Segment 6	40,95	634,548	0,38	3,51	0,477	0,360
Segment 7	46,20	657,574	1,59	2,85	1,694	1,278
Arm 1 (lower arm)	29,77	575,638	5,74	2,80	5,274	3,978
Arm 2 (upper arm)	40,53	632,614	3,33	2,76	3,310	2,497

Given that the tower being symmetrical, the directions –X and –Y and +X and +Y are respectively the same (geometry and loads) and they are not considered as different load cases. Then, the mean wind load in each direction is distributed on the front and back face of the tower – which vary obviously according to the wind direction. It is assumed that the front face of each segment is supporting 57% of the total wind load, and the back face 43% (see Figure 9.7). At the end, the wind

load acting on a face is distributed to each bar according to its normal area, as a constant linear load along each bar, in order to achieve a realistic simulation of the action.

Table 9.4 and Table 9.5 summarise the mean wind loads acting on the tower body and the cross arms, for both wind directions (W_x and W_y) and for the two faces of the tower (front and back faces).

B.2 Wind loads on the conductors and the insulators

The calculation of the wind loads on the conductors is based on EN 1993-3-1/Annex B. The maximum wind loading on the cables in the direction of wind $F_c(z)$ should be taken as:

$$F_c(z) = \frac{q_p(z)}{1+7I_v(z)} \sum c_{f,G} A_G \left[1 + \frac{[1+7I_v(z)]c_s C_d - 1}{c_o(z)}\right] \quad \text{(Eq. 9.4)}$$

where z is the height above the base of the support of the conductor/cable and $c_s c_d$ is the structural factor that equals 1,0 according to EN 1991-1-4/§6. Table 9.6 shows the calculation of the wind load on the conductors/earth wire for both different wind directions.

Table 9.6: Wind loads on the conductors

Wind direction	ψ [°]	z [m]	$q_m(z)$ [N/m²]	$C_{f,G,0}$ [-]	$I_v(z)$ [-]	d [mm]	In direction $F_{cy}(z)$ [kN]	Perpendicular $F_{cx}(z)$ [kN]
Parallel to the cross-arm axis	0	28,70	569,081	1,10	0,157	22,4	20,631	0
		39,70	628,696		0,150		22,212	0
		50,20	673,663		0,145	13,6	7,100	0
Perpendicular to the cross-arm axis	90	28,70	569,081	1,10	0,157	22,4	0	0
		39,70	628,696		0,150		0	0
		50,20	673,663		0,145	13,6	0	0

According to EN 1993-3-1/Annex B, the wind loads on the insulators are these reported in Table 9.7.

Table 9.7: Calculation of wind loads on the insulators

Position of insulator	z [m]	$q_m(z)$ [N/m²]	$C_{f,G,0}$ [-]	C_c	A_{ins} [m²]	Each direction $F_{ins}(z)$ [kN]
Insulator at the lower arm	28,70	569,081	1,20	1,0	0,150782	0,216
Insulator at the upper arm	39,70	628,696	1,20	1,0	0,150782	0,233

One could argue here that, as the wind loads have been evaluated with different standards in TOWER and FINELG, no comparison is possible. Indeed, there are some differences between both standards but the total acting wind force per direction does not differ so much; according to EN 50341-2-4 wind loads are bigger for the tower's body but are smaller for the conductors. However, the way that the loads are applied on the pylon (i.e linear loads along the bars in FINELG in comparison with the concentrate forces at the nodes used in TOWER) influences more the response of the tower; and for sure the assumption made in FINELG simulation is much closer to the reality.

9.2.3 Load combinations

Twelve different load combinations regarding the wind direction and the definition of the actions (favourable/unfavourable) have been considered for the initial design of the tower. Amongst them, the two most critical ones have been here selected for the assessment, which correspond to unfavourable actions:

- **X direction**: gravity loads (G) and wind forces perpendicular to the cross arms (W_x).
- **Y direction**: gravity loads (G) and wind forces parallel to the cross arms (W_y).

The design action is therefore the following one:

$$E_d = \gamma_G G_K + \gamma_W Q_W \quad \text{(Eq. 9.5)}$$

where:

Ed total loads;

G_K dead loads of conductors, insulators and body of the structure;

Q_W wind forces.

Same safety load factors have been used for the applied loads as the ones used in the initial design of the pylon, i.e $\gamma_G = \gamma_W = 1,35$ for unfavourable actions according to EN 50341-2-4. For all the analysis, gravity loads are applied first, and then in the deformed due to gravity loads tower, wind loads are increased [$1,35G+\alpha(1,35W)$] until failure occurs. This load sequence simulation is closer to the reality.

9.3 Comparison of FINELG and TOWER models in the elastic range

Before validating and drawing conclusions about the initial design of the tower, it is important to compare the model created by FINELG with the initial model created through the TOWER software. First of all, the self-weight of the structure has been compared to the one provided by TOWER. Then, the maximum displacements for three different load cases have been evaluated, again in view of this comparison.

As already referred in section 9.1.3, the total weight of the structure reported from TOWER is 166,73 kN. It should be noted that the total weight includes the weight of the angle profiles, the weight of the insulators and the weight of the bolts and gussets which is estimated through a load adjustment factor of 1,2. The corresponding value for total weight load from FINELG software is 172,60 kN. The difference between two models is 3,40%, while both self-weights should be a priori the same. This can be justified by the eccentricity of each bar and its actual position in FINELG, which changes slightly the length of the bar, while in TOWER all the members are connected centrally. This small length difference can explain the difference of both self-weight evaluations.

Table 9.8: Maximum displacements for linear elastic analysis

Load case	Node with maximum displacement	Direction of displacement	Maximum displacement from TOWER software [m]	Maximum displacement from FINELG software [m]
1,35G	Edge of lower arm	Z (vertical)	$-8,14 \cdot 10^{-3}$	$-9,61 \cdot 10^{-3}$
$1,35G+1,35W_x$	Top of the tower	X (horizontal)	0,301	0,164
$1,35G+1,35W_y$	Top of the tower	Y (horizontal)	0,514	0,596

The maximum displacements are summarized in Table 9.8. It should be noted that:

- load case 1,35G includes only the self-weight of the tower without the conductors and insulators;
- the wind load calculations in TOWER and FINELG being based on different norms (EN 1993-3-1 for FINELG and EN 50341-1 for TOWER), it is normal to see a difference between those displacements;
- the wind loads in FINELG are introduced as linear loads along the bars while in TOWER they are introduced as loads at the nodes;
- the wind loads on the body of the tower are bigger according to EN 50341-1 than EN 1993-3-1, what justifies the difference in load case $1{,}35G + 1{,}35W_x$;
- the wind loads on the conductors are smaller according to EN 50341-1 than EN 1993-3-1, what explains why the difference in load case $1{,}35G + 1{,}35W_y$ is smaller than in load case $1{,}35G + 1{,}35W_x$.

Regarding those values, one notices that they are high. However, the displacements are appearing at the failure limit state (applying loads with 1,35 load factors) and not at the service limit state (applying loads without load factors). Additionally, there is no special indication or limitation specified in both main norms (EN 1993-3-1 or EN 50341-1) in terms of maximum displacement at service limit state. The only reason to provide displacements here is to compare the order of magnitude – not even the exact value – between TOWER and FINELG software. However, due to the big difference of the maximum displacements of both software, complementary analyses have been performed to investigate the stiffness of the two models. The comparison has been achieved through a first order linear elastic analysis, where a horizontal load of 1 kN has been applied (i.e. the same loading in TOWER and FINELG) at the top of the tower in the two following situations:

- the load is applied perpendicularly to the cross-arm axis (X direction);
- the load is applied parallelly to the cross-arm axis (Y direction).

The results are summarized in Table 9.9. The difference between the displacements is less than 5%, what means that both models have almost the same stiffness. This seems to indicate that a simplified modelling of the members at their extremities (as in TOWER) could be accurately contemplated for a first order analysis.

Table 9.9: Displacements on the top of the tower from linear elastic analyses

Load case	Direction of load and displacement	Displacement from TOWER software [m]	Displacement from FINELG software [m]	Difference [%]	Stiffness of FINELG model [kN/m]
F_x=1 kN	X	$9{,}019 \cdot 10^{-3}$	$9{,}455 \cdot 10^{-3}$	4,61	105,76
F_y=1 kN	Y	$9{,}021 \cdot 10^{-3}$	$9{,}438 \cdot 10^{-3}$	4,42	105,95

9.4 Numerical results

In order to investigate the tower response and validate the initial design method, different types of complementary analyses have been performed by means of FINELG and the results are presented in the next paragraphs.

9.4.1 Elastic instability analysis

The critical load multipliers α_{cr} are summarised in Table 9.10, while the deformation shape of the first instability mode is shown in Figure 9.8 and Figure 9.9 for wind loads acting on X and Y direction respectively.

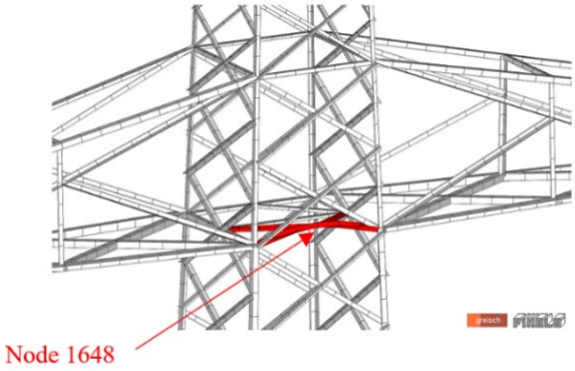

Figure 9.8: First buckling mode for load combination 1,35G+ α_{cr}1,35W_x

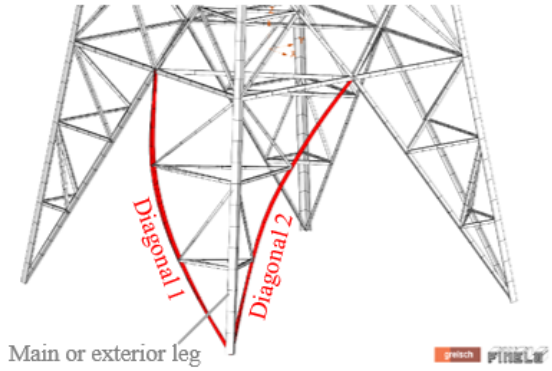

Figure 9.9: First buckling mode for load combination 1,35G+ α_{cr}1,35W_y

Table 9.10: Results from elastic instability analysis

Load combination	**1,35G+ α_{cr}1,35W_x**		**1,35G+ α_{cr}1,35W_y**	
No of mode	**Load factor α_{cr}**	**Type of instability**	**Load factor α_{cr}**	**Type of instability**
1st	3,056	Member	1,015	Segment
2nd	5,853	Member	1,179	Member
3rd	6,764	Member	1,205	Member

The instability mode observed in Figure 9.9 has been baptized as “segment instability” and is further investigated in chapter 10, where two analytical prediction models are proposed.

9.4.2 Second order elastic analyses

A geometrically non-linear elastic analysis with elastic material law but without considering initial imperfections has been performed, to complement-validate the elastic buckling analysis. The results are summarized, for each direction, below.

For the load combination *1,35G+ $\alpha_{cr,nl}$1,35W_x*, the load-displacement curve is reported in Figure 9.10. The first branch of the curve represents the loading with the gravity loads while the second one, with

the wind loads. The abscissa represents the global vertical displacement (see Figure 9.6 for the definition of the axis), while the horizontal dot line corresponds to the critical load multiplier a_{cr} resulting from the elastic buckling analysis. For both analyses, instability occurs in the same bar (see Figure 9.8).

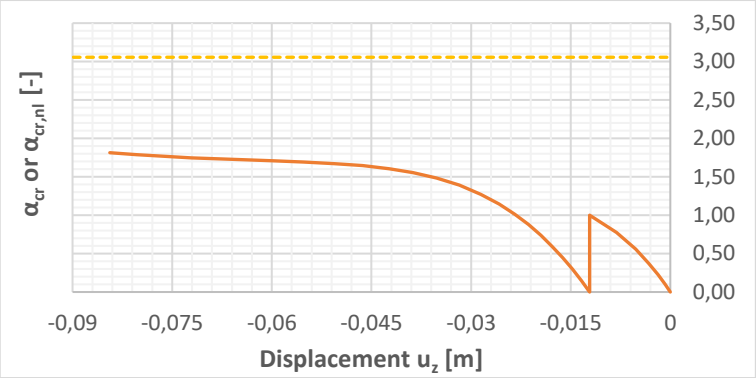

Figure 9.10: Displacement u_z versus load factor for different types of analyses - wind perpendicular to the arms (X direction)

Table 9.11: Internal forces at node 1648, for the two analyses

Internal forces/Type of analysis	Elastic instability analysis	2nd order linear elastic analysis without initial imperfection
Axial N [kN]	-266,92	-177,10
Torsion M_T [kNm]	0,05	0,413
Bending M_u [kNm]	3,56	10,19
Bending M_v [kNm]	-0,24	-5,08
Load factor α_{cr} or $\alpha_{cr,nl}$	3,06	1,71

It is a priori surprising to see that the critical load obtained by the instability analysis ($\alpha_{cr} = 3{,}056$) is significantly higher than the maximum load factor obtained by the geometrically non-linear elastic analysis ($\alpha_{cr,nl} \approx 1{,}71$). When checking the internal forces at the middle node of the bar (node 1648) in both cases (see Table 9.11), one realises that the failure occurs for two different triplets of relative axial force and bending moments. Indeed, in the second order linear elastic analyses, the second order effects are significantly influencing the internal forces in the members. This has been also observed for isolated angle members in §3.6, but now the complexity and the scale of the structure are really amplifying the *P-δ* phenomena. This explains why the buckling load multiplier is so much smaller than the one obtained through the elastic instability analysis.

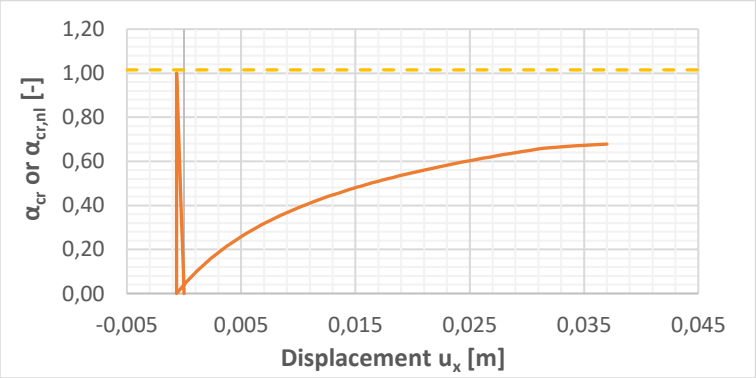

Figure 9.11: Displacement u_x versus load factor for different types of analyses - wind parallel to the arms (Y direction)

When the wind forces acting on Y direction, a segment instability again appears, as shown in Figure 9.9. The graph in Figure 9.11 shows the horizontal displacement u_x (direction of global X axis - Figure 9.6) at the middle of diagonal 2 versus the load factor. The horizontal dot line represents the critical load multiplier obtained from the elastic instability analysis. The difference between the critical instability load factor and the maximum one reached through a 2nd order linear elastic analysis, that is about $\alpha_{cr,nl} \approx 0,68$, could again be explained by the different loading situations (relative axial force and bending moments) in the critical bars.

9.4.3 Full non-linear analyses

The validation of the initial design requires a full non-linear analysis, considering an elastic-perfectly plastic material, distributions of residual stresses and an initial imperfection of the structure in accordance with the 1st instability mode. The details are presented in §9.2.1.

Figure 9.12 represents the vertical displacement u_z (direction of global Z axis) at the node 1648 versus the load factor for the load combination $1,35G+ \alpha_u 1,35W_x$. The failure occurs in the same bar as in the previous analyses due to combined plasticity (see Figure 9.13) and instability. The load factor ($\alpha_u = 1,17$) for this load combination is bigger than 1,0 with comparison to the design factored loads. As a result, the initial design appears to be safe. Furthermore, it is observed that the tower remains elastic for load factors $\alpha_u \leq 1,0$, so confirming the TOWER design assumptions.

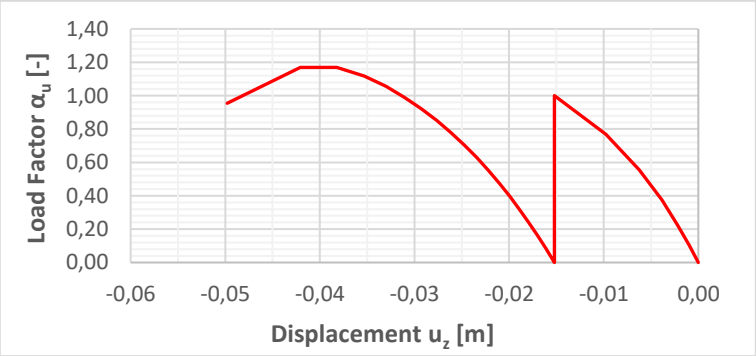

Figure 9.12: Displacement versus ultimate load factor – 1,35G+1,35W_x (X direction)

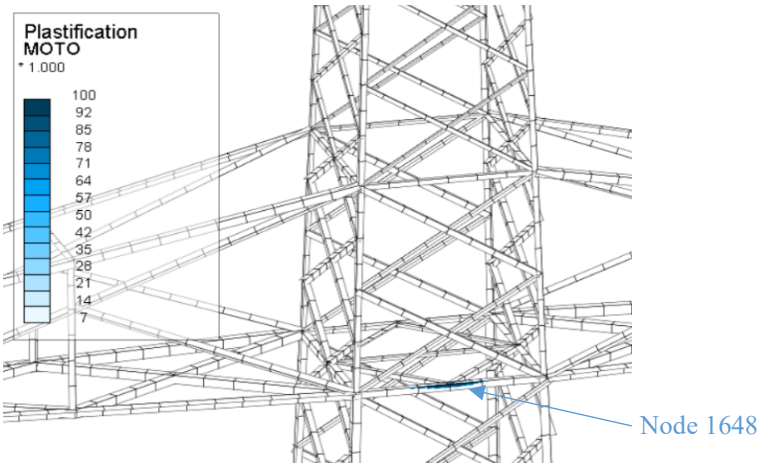

Figure 9.13: Results (plasticisation) from the 2nd order non-linear plastic analysis (X direction)

Figure 9.14 shows the horizontal displacement u_x (direction of global X axis) at the middle of diagonal 2 (see Figure 9.9) versus the load factor, for the load combination $1,35G+ \alpha_u 1,35W_y$. It can be seen that the load factor is about $\alpha_u \approx 0,66$. Contrary to what is seen before, the maximum load

factor remains here far lower than 1,0. The initial design of the tower by TOWER software for this direction is therefore seen as insufficient and unconservative. This may be explained by the development, in reality, of an instability mode in one of the main tower legs, called “segment instability” and which is not covered by TOWER; but more importantly, it is also not addressed properly by the reference European normative documents EN 1993-3-1 and EN 50341 (more information are provided in chapter 10).

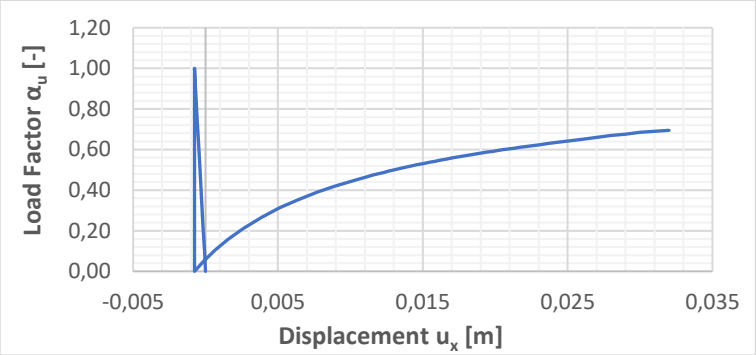

Figure 9.14: Displacement versus ultimate load factor – 1,35G+1,35Wy (Y direction)

9.5 Conclusions

An assessment of the current design approach used for lattice transmission towers has been achieved through numerical studies, and from the results, the following conclusions may be drawn:

- There are different norms for the design of transmission towers, mainly EN 1993-3-1 & EN 50341-1. For some aspects, for instance the amplitude of the wind loads, both norms provide slightly different recommendations. In the present chapter, EN 1993-3-1 has been used for evaluation of the wind loads.
- There is no special indication or limitation in the norms (EN 1993-3-1 & EN 50341-1) about the maximum displacements of the tower at the serviceability limit state.
- A reasonable agreement is seen between FINELG and TOWER elastic analyses. The differences may be explained by modelling aspects.
- The buckling load obtained by a 2nd order elastic analysis is smaller than the critical one obtained by an elastic instability analysis. The reason is that the forces acting on the members in both cases differ, so affecting the member buckling load in the case of non-symmetrical cross-sections. Moreover, these effects are amplified by consideration of actual member support conditions (eccentricities for instance).
- The second order effects should be considered in the analysis as they affect the global response of the tower and its ultimate limit state.
- The initial design of the tower appears to be rather good in the case of application of the wind loads in one direction, but it is quite unconservative for the application of wind loads in the other direction. The reason is due to the development in the second case of an instability mode that is not properly recommended to be checked by the present norms.

10. THE SEGMENT INSTABILITY MODE

In chapter 9, an instability mode for lattice towers not properly covered by the norms, that has been named “segment instability”, was observed through numerical simulations. In the following, two analytical models for the prediction of the critical load of the new buckling mode are proposed, accompanying by their numerical validation. Comparisons with the existing norms are also provided.

10.1 Definition of segment instability

A “segment instability” is defined as a global instability mode associated to the buckling of more than one member forming a segment. As shown in Figure 10.1, the instability is associated to the buckling of the two diagonals of the leg in the present case, and therefore could also be named “leg-segment instability”. More precisely, the leg is made of three vertically orientated members: the main or “exterior” leg and the two diagonals that are connected with a number of horizontal bars and bracing members forming “triangles”. In fact, each of the two diagonals and the exterior leg constituting the segment are stable individually and can resist to the applied maximum forces, as they have been initially designed for that. However, the simultaneous buckling of the diagonals over the whole leg height, involving a longitudinal rotation of the main leg member, represents a “new mode” which has been seen to be relevant in various usual design situations.

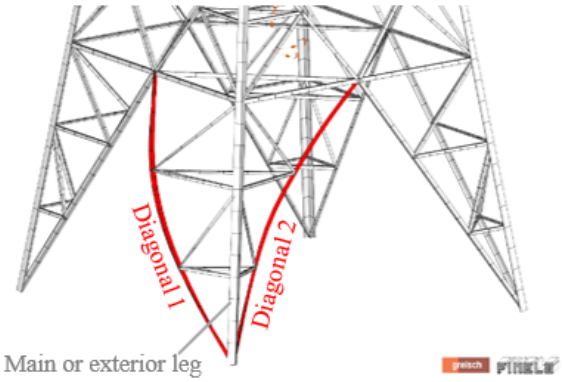

Figure 10.1: Segment elastic instability mode

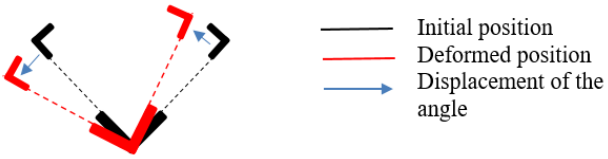

Figure 10.2: Deformation of the members through a horizontal cut in the leg

Figure 10.2 shows a horizontal cut in the leg and indicates how the constitutive elements deform in the instability mode. It is seen that:

- The diagonals move laterally and bend about an axis parallel to one of their angle legs.
- The main leg rotates about its longitudinal axis.
- The elements which form the “horizontal leg triangles” (not represented on the picture in Figure 10.2) do not undergo any deformation; they are just translated.

10.2 Proposed analytical models

Two models, a simplified one and a refined one, to predict the critical loads of the segment instability mode are first presented. Then, a model to predict the buckling resistance of the leg is described.

10.2.1 Simplified model

The equivalent model illustrated in Figure 10.3 has been built, in order to represent physically what is observed in the leg. The two parallel vertical members represent the two diagonals and the horizontal pinned members, the elements forming the horizontal leg triangle. Both diagonals are assumed to be made of the same profile, as it happens in practice in most of the cases. The extremities of the vertical members are assumed to be pinned; this is what is expected at the foundation level, while the very small restraining effect resulting from the actual continuity of the diagonals at the top is neglected. The modal deformed shape of the system is illustrated on the right side of Figure 10.3.

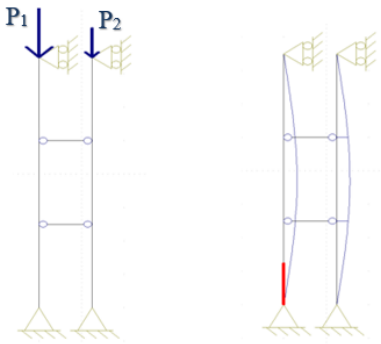

Figure 10.3: Equivalent model of the leg (left) and modal deformed shape (right)

For the simplified model, the critical load may be given by the following equation:

$$N_{cr} = \frac{2\pi^2 E I_{y,d}}{L^2} \qquad \text{(Eq. 10.1)}$$

where,

$I_{y,d}$ is the moment of inertia about y-y geometrical axis of the diagonal's cross-section;

L is the buckling length of the diagonal.

Thus, the critical load multiplier may be determined as follows:

$$a_{cr} = \frac{N_{cr}}{P_1 + P_2} \qquad \text{(Eq. 10.2)}$$

where,

N_{cr} is the critical load given by eq. (10.1);

P_1, P_2 are the axial compression forces at the diagonals (see Figure 10.3).

This model is independent of the number of horizontal "rigid triangles", and therefore may be generally used for segments with pyramidal configuration.

10.2.2 Refined model

In the proposed refined model, the beneficial effect of the torsional stiffness of the exterior leg, which has been disregarded in the simplified one, is considered. When the segment instability occurs, the exterior member is assumed to be locally stable. If it would not be the case, then the buckling of the

exterior leg determines the failure and limits the pylon resistance. Therefore, considering the fact that the buckling resistance of an individual member in compression follows a flexural mode and not a torsional one, it can be reasonably assumed that the axial force in the exterior leg is not influencing its torsional stiffness.

When the leg instability develops, the exterior member is activated in torsion at the 1/3 and the 2/3 of the exterior leg length (L_{ext}) where the "triangles" are here assumed to be located. The first step consists in the evaluation of the torsional restraint offered by the rigidity of the exterior leg member in torsion.

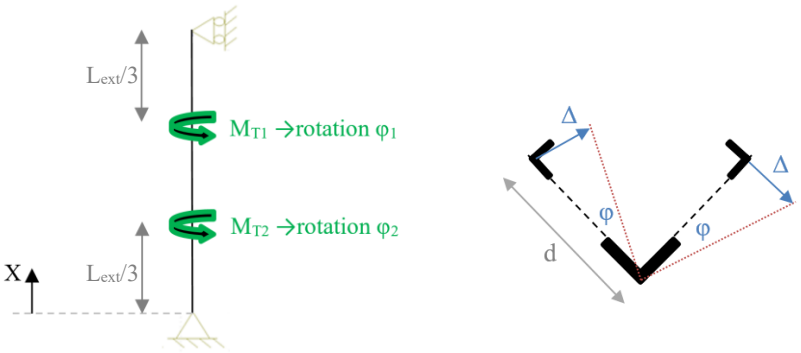

Figure 10.4: Schemes for the calculation for the torsional restraint brought by the exterior member

The torsional moments (see Figure 10.4) can be evaluated as follows, considering that M_{T1} and M_{T2} are equal to M_T:

$$\varphi = \int_0^{\frac{L_{ext}}{3}} \frac{M_T}{C} dx \quad \Rightarrow \quad M_T = \frac{3C}{L_{ext}}\varphi \qquad \text{(Eq. 10.3)}$$

The torsional rigidity C of the cross-section is given in Annex A. Then:

$$\left.\begin{matrix} M_T = \frac{3C}{L_{ext}}\varphi \\ M_T = 2Fd \end{matrix}\right\} \Rightarrow \frac{3C}{L_{ext}}\varphi = 2Fd \overset{F=R\Delta}{\Longrightarrow} \frac{3C}{L_{ext}}\varphi = 2R\Delta d \overset{\Delta=d\varphi}{\Longrightarrow} \frac{3C}{L_{ext}}\varphi = 2Rd^2\varphi \qquad \text{(Eq. 10.4)}$$

where F is a force applied at each diagonal in direction of Δ and which causes torsional moment at the exterior member of the leg ($M_T=2Fd$ where d is defined in Figure 10.4), while R is the lateral restraint of the diagonal ($R=F/\Delta$). By solving eq. (10.4), the lateral restraint of the diagonal is obtained:

$$R = \frac{3C}{2L_{ext}} \cdot \frac{1}{d^2} \qquad \text{(Eq. 10.5)}$$

The torsional restraints evaluated at 1/3 or at 2/3 of the member length (where the rigid triangles act) are different as different values of d are met at these locations, what implies different values for M_{T1} and M_{T2} in Figure 10.4 and invalidates de facto the use of eq. (10.3). But, for sake of simplicity, the actual values of R at $L/3$ and at $2L/3$ are substituted by a mean value of R_{mean} defined as follows:

$$R_{mean} = \frac{3C}{2L_{ext}} \cdot \frac{1}{n}\sum_{i=1}^{n}\frac{1}{d_i^2} \qquad \text{(Eq. 10.6)}$$

This is illustrated in Figure 10.5. To simplify it further, both restraints are merged into a single one called K_T, as illustrated in the right sketch of Figure 10.5. For this case, Gardner proposes in Ref. [48] an analytical expression of the critical load for a column of flexural inertia I:

$$N_{cr} = \frac{\pi^2 EI}{L^2} + \frac{3}{16}K_T L \qquad \text{with} \quad K_T < \frac{16\pi^2 EI}{L^3} \qquad \text{(Eq. 10.7)}$$

If K_T reaches a value of $\frac{16\pi^2 EI}{L^3}$, the column will buckle in the second eigenmode (two half sine waves); further increases of the K_T values will not produce a corresponding increase in the critical load. The column therefore effectively becomes restrained at its mid-height, and $N_{cr,2} = \frac{4\pi^2 EI}{L^2}$ (see Figure 10.6). In the specific case of pylons, the restraints remain quite low, and for sure much lower than $\frac{16\pi^2 EI}{L^3}$.

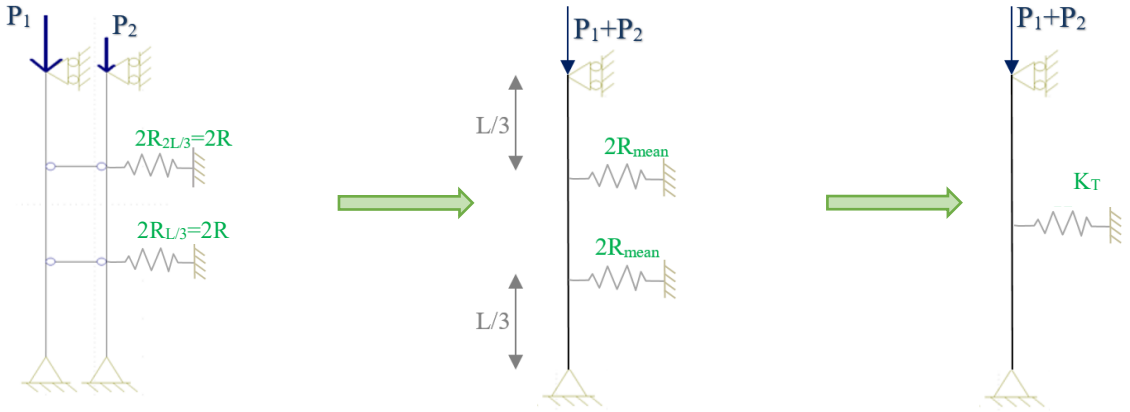

Figure 10.5: Initial (left), intermediate (middle) and final (right) proposed design model

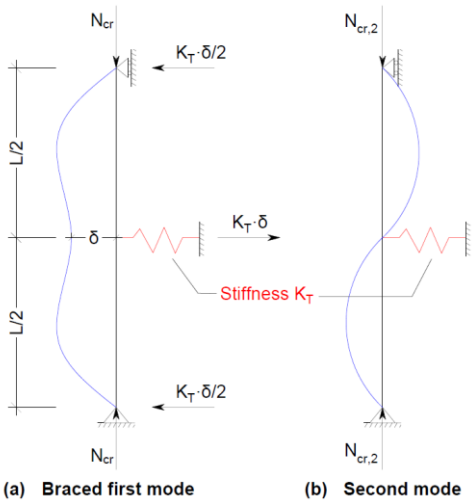

Figure 10.6: Column with a single discrete restrain [48]

The determination of the spring stiffness K_T may be contemplated referring to the literature (p.474-475 of Ref.[31]), from which it may be deduced that, for few discrete supports, the term $m\frac{C}{EI}l^3$ is constant. In this expression, m is the number of zones of length $l = L/m$ separated by rigid triangles in the leg, $C = 2R_{mean}$ and $EI = 2EI_y$ where I_y is the value of the flexural rigidity of one diagonal.

$$m\frac{C}{EI}l^3 = const \quad \Rightarrow \quad m \cdot 2R_{mean} \cdot \left(\frac{L}{m}\right)^3 = 2 \cdot K_T \cdot \left(\frac{L}{2}\right)^3 \qquad \text{(Eq. 10.8)}$$

This being, the equivalent spring stiffness K_T may be evaluated as follows:

$$K_T = \frac{4}{m^2}(2R_{mean}) \qquad \text{(Eq. 10.9)}$$

The critical load of the equivalent column is finally given by:

$$N_{cr} = \frac{\pi^2 E I_{y,tot}}{L^2} + \frac{3}{16} K_T L \quad \text{(Eq. 10.10)}$$

where,

$I_{y,tot}$ is the total moment of inertia about y-y geometrical axis of both diagonals (i.e $I_{y,tot}=2I_{y,d}$);

L is the buckling length of the diagonal;

K_T is the stiffness of the unique spring restraint, equal to $\frac{4}{m^2}(2R_{mean})$;

R_{mean} can be evaluated using eq. (10.6);

m is the number of zones of length *l* in the leg (*l = L/m* separated by rigid horizontal triangles in the leg); the accuracy of the formulae for K_T is sufficient for a value of $m \leq 6$ (i.e for maximum 5 horizontal rigid triangles in the leg);

d_i is the horizontal distance of the longitudinal axis of one diagonal from the longitudinal axis of the main leg, where i is the index for the horizontal level (see Figure 10.4).

Finally, the critical load multiplier can be evaluated using eq. (10.2).

10.2.3 Ultimate resistance of the leg

The ultimate buckling resistance of the leg may be determined by the current provisions of EN 1993-1-1, as follows:

$$N_{b,Rd} = \begin{cases} \chi \frac{A_d f_y}{\gamma_{M1}} & \text{for class 1,2 and 3 profiles} \\ \chi \frac{A_{d,eff} f_y}{\gamma_{M1}} & \text{for class 4 profiles} \end{cases} \quad \text{(Eq. 10.11)}$$

where the effective area of the diagonal is given using eq. (7.2). The buckling reduction factor χ is determined as a function of the relative slenderness:

$$\overline{\lambda_{seg}} = \sqrt{\frac{2N_{pl}}{N_{cr}}} \quad \text{(Eq. 10.12)}$$

where,

N_{cr} is the critical load of the segment determined by one of the proposed models (simplified or refined);

N_{pl} is the plastic design resistance of one diagonal ($N_{pl}=A_d \cdot f_y$).

The value of the buckling reduction factor χ can be determined from the European buckling curve d for any steel grade. It is suggested to safely use the lowest buckling curve due to the lack of studies showing that a higher one could be safely used. The selection of the buckling curve could be further investigated in the future.

10.3 Validation of the proposed models

The validation of the proposed formulae (simplified and refined) has first been achieved through comparisons to results obtained through 2D numerical simulations of the proposed models (illustrated in Figure 10.3 and Figure 10.5-right) by means of the OSSA2D software [49], and then through the use of the whole tower model described in chapter 9, using FINELG software. The

reference codes for the constitutive elements of the tower leg simulated in FINELG are illustrated in Figure 10.7, while details about the members are reported in Table 10.1.

For the refined model, the mean value of the lateral restraint R of the diagonals and the stiffness K_T of the spring are:

$$R_{mean} = \frac{3C}{2L_{ext}} \cdot \frac{1}{n}\sum_{i=1}^{n}\frac{1}{d_i^2} = \frac{3 \cdot 1{,}69761 \cdot 10^{10}}{2 \cdot 5000} \cdot \frac{1}{2}\left(\frac{1}{913^2} + \frac{1}{1827^2}\right) = 3{,}82\ N/mm$$

$$K_T = \frac{4}{m^2}(2R_{mean}) = \frac{4}{3^2}(7{,}64) = 3{,}39\ N/mm$$

Table 10.1: Details of the leg members

Member	CS code	Cross-section	Length [m]
Diagonal 1 (left)	13	75x75x4	6,00
Diagonal 2 (right)	13	75x75x4	6,00
Main leg	12	150x150x13	5,00
Horizontal level 2	14	60x60x4	1,827
Horizontal level 3	14	60x60x4	0,913

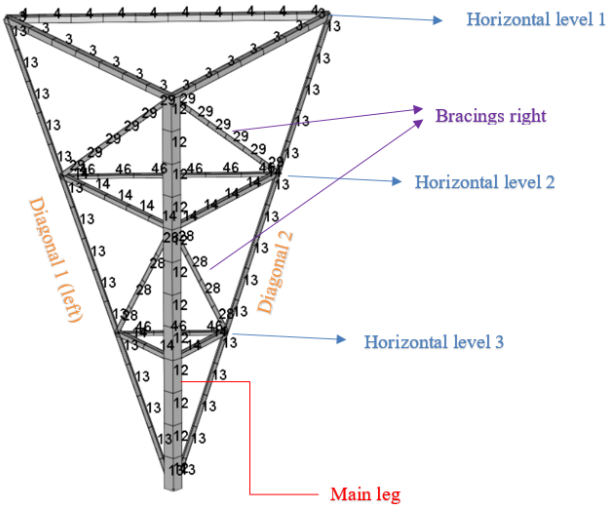

Figure 10.7: Notations of the constitutive elements of the tower leg

By using the OSSA2D software and performing an elastic buckling analysis, the values of the critical load multipliers ($\alpha_{cr,OSSA2D}$) for both models are obtained and reported in Table 10.2. The corresponding analytical values $\alpha_{cr,anal} = N_{cr}/(P_1+P_2)$ are also reported ($\alpha_{cr,anal,s}$ and $\alpha_{cr,anal,r}$ for the simplified and refined models respectively) and fit quite well with the numerical ones. Obviously, the lower values obtained with the simplified model when compared to the refined one, results from the fact that the rotational restraint of the main leg, as well as the continuity of the diagonals above the leg level, are disregarded.

Further numerical estimations of α_{cr} have been achieved for the transmission tower through an elastic instability analysis performed on the whole tower model, subjected to different actual external load combinations so as to vary the loading on the leg (in the exterior member and in the two diagonals). In Table 10.3, the obtained numerical results ($\alpha_{cr,FIN}$) are compared with the analytical ones for both proposed models.

Table 10.2: Results obtained through the OSSA2D software and the analytical prediction models

P_1 [kN]	P_2 [kN]	Simplified model		Refined model	
		$\alpha_{cr,OSSA2D}$ [-]	$\alpha_{cr,anal,s}$ [-]	$\alpha_{cr,OSSA2D}$ [-]	$\alpha_{cr,anal,r}$ [-]
30	0	1,19	1,21	1,33	1,33
30	15	0,80	0,80	0,90	0,89
30	20	0,72	0,72	0,81	0,80
30	30	0,59	0,60	0,67	0,67

Table 10.3: Results obtained for the whole tower model through FINELG and the analytical models

Load combination	P_1+P_2 [kN]	$\alpha_{cr,FIN}$ [-]	No of eigenmode	$\alpha_{cr,s}$ [-]	$\alpha_{cr,r}$ [-]	$\alpha_{cr,s}/\alpha_{cr,FIN}$ [-]	$\alpha_{cr,r}/\alpha_{cr,FIN}$ [-]
$G+W_y$	30,00	1,37	1	1,21	1,33	0,881	0,973
$G+W_x$	9,77	4,28	4	3,70	4,10	0,866	0,957
G_{tower}	1,83	23,99	12	19,75	21,84	0,823	0,910
Wx	7,15	6,42	1	5,06	5,60	0,788	0,872
Wy	33,05	1,48	1	1,10	1,21	0,740	0,818
Mean value	---	---	---	---	---	0,820	0,906

The safe character of the simplified approach may be seen. The refined design model in which the rotational restraint of the main leg member is taken into account gives better results than the simplified one as expected, but is still on the safe side. Obviously, one should compare the ultimate resistances and not only the critical ones in order to put a definitive judgement on the level of safety of the approach. By using the simplified model for the evaluation of the critical load, the leg slenderness is $\bar{\lambda} = \sqrt{\frac{2 \cdot 204,585}{N_{cr}}} = 3,363$, while, with the refined one, the slenderness slightly changes $\bar{\lambda} = 3,198$, but remains significantly high. With so high slenderness values, the ultimate resistance of the leg is almost equal to its critical one. So, in this specific situation, even if the comparisons between both models and FINELG would be done based on the ultimate resistances, the safe character would remain.

10.4 Existing recommendations of the normative documents

As referred in the introduction, two main documents are used to design steel lattice transmission towers: EN 1993-3-1 and the CENELEC document EN 50341-1. In the latter, it is said that compression members shall be designed using the provisions of Annex G and Annex H of EN 1993-3-1, or in accordance with the provisions of Annex J.4 of EN 50341, only if full-scale tests are performed. In practise, full scale tests on towers are rarely performed and so the use of Annex J.4 of EN 50341 is rarely met. Accordingly, the remaining question is to see if the above-mentioned annexes of EN 1993-3-1 cover segment instability design check.

In fact, EN 1993-3-1, Annex H, clause H.3.7 recommends a buckling check of two members (one in each of two adjacent faces) against the algebraic sum of the loads in the two members connected by the diagonal brace over length L_{d4} (see Figure 10.8) on the transverse axis, for cross bracing systems. For this case, the total resistance should be calculated as the sum of the buckling resistances of both members in compression.

This design check looks to correspond to the simplified model proposed here. However, even if it seems clear for X bracings, it is not sufficiently clearly addressed for K bracings and therefore it is not sure that it is properly applied in practice. Besides that, in figure H.2, the member could also

buckle along $L_{d,}$ what means that the two extremity points of the bar with length equal to L_{d4} are not laterally fixed, which leads to a more complex situation. Subsequently, the proposed models fill a gap in the provisions of the existing norms, clearly indicate the required check and recommend easy-to-apply design models.

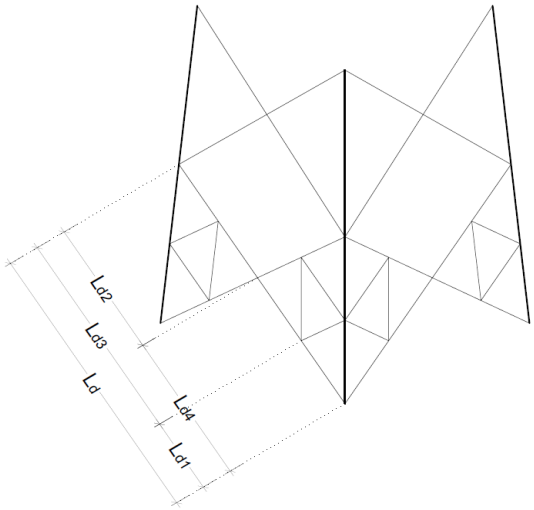

Figure 10.8: Figure H.2(b) from EN 1993-3-1

10.5 Application of the design models

In the following, an example illustrating the application of the design rules to the segment instability of the studied transmission tower is presented. The load sequence has been defined in §9.2.3, where *1,35G* is applied first and then the wind load parallel to the cross arms is progressively increased *1,35αWy* (*α* being the load factor).

Table 10.4 summarizes the load multipliers and the critical loads that have been evaluated by an elastic first order critical instability analysis or analytical calculations. The segment instability mode that is illustrated in Figure 10.1 appears far before the instability mode that would be detected according to EN 1993-3-1, i.e. the member instability of a single individual element (this instability takes place in diagonal 2 for $\alpha_{cr} = 1,66$ and in the main leg for $\alpha_{cr} = 4,30$), and therefore is tends to be rather relevant.

Table 10.4: Load factors and critical loads for elastic critical instability

Elastic critical instability	Buckling mode	Load factor α_{cr} [-]	Corresponding compression load [kN]	Level of accuracy
FINELG ($\alpha_{cr,FIN}$)	Segment	1,02	41,88	EN 1993-3-1: $\alpha_{cr,EC3} / \alpha_{cr,FIN} = 1,66$ Proposed simplified model: $\alpha_{cr,anal,s} / \alpha_{cr,FIN} = 0,86$ Proposed refined model: $\alpha_{cr,anal,r} / \alpha_{cr,FIN} = 0,96$
FINELG ($\alpha_{cr,FIN,diag}$)	Diagonal in between restraints – weak axis	1,66	66,30	
EN 1993-3-1 ($\alpha_{cr,EC3}$)		1,69	67,41	
Segment inst. models: Simpl. model ($\alpha_{cr,anal,s}$) Refined model ($\alpha_{cr,anal,r}$)	 Segment Segment	 0,87 0,97	 36,19 40,01	

Table 10.5 presents the ultimate load factors and the corresponding ultimate resistances that have been obtained from a full second-order elastoplastic GMNIA analysis (by progressively increasing

the value of α). The ultimate resistance of the segment has been evaluated analytically with the two proposed models using the European buckling curve d for the determination of the buckling reduction factors. Then, the load factor has been derived numerically from a second order elastic analysis without initial imperfections to correspond to a force in the diagonals just equal to the ultimate one.

Table 10.5: Load factors and ultimate loads at the ultimate state

Ultimate state	Buckling mode	Load factor α_u	Corresponding compression load [kN]	Level of accuracy
FINELG ($\alpha_{u,FIN}$)	Segment	0,66	(4,49+31,55)=36,04	EN 1993-3-1: $\alpha_{u,EC3}/\alpha_{u,FIN}$ = unknown Proposed simplified model: $\alpha_{u,,anal,s} / \alpha_{u,FIN} = 0,86$ Proposed refined model: $\alpha_{u,anal,r} / \alpha_{u,FIN} = 0,92$
EN 1993-3-1 ($\alpha_{u,EC3}$)	Diagonal in between restraints – weak axis	See comment below.[1]		
Segment inst. models: Simpl. model ($\alpha_{u,anal,s}$) Refined model ($\alpha_{u,anal,r}$)	 Segment Segment	 0,57 0,61	 0,072·409,17=29,46 0,079·409,17=32,32	

[1]This value cannot be evaluated through a second order elastic analysis, as the segment instability occurs before the diagonal buckles. But it may be seen that, when segment instability occurs ($\alpha_u = 0,66$), the force in diagonal 2 is equal to 31,50 kN while the ultimate buckling resistance between intermediate restraints according to EN 1993-3-1 (using buckling curve b for a slenderness 1,742) is equal to $N_{Rd}=\chi N_{pl}=0,27\cdot 204,59=55,24$ kN. Subsequently, the unconservative character of the present EN 1993-3 is seen to be rather significant.

By performing a first order linear elastic analysis ($\alpha = 1,0$), the compression force in the main leg of the segment equals 535,3 kN, while in diagonals 1 and 2 are 0,80kN and 40,50kN respectively. It is seen that those internal forces are much higher than the real ones obtained at the ultimate state, highlighting once again the influence of the second order effects on the response of the pylon and clearly indicating the need for their consideration in the structural analysis. Furthermore, it can be seen that both prediction models for the segment instability working well and on the safe side, with the simplified one to be more conservative as expected.

10.6 Conclusions

A new buckling instability mode named “segment instability” and involving more than one member has been detected, defined and characterised. It has been demonstrated that this instability mode is not properly covered by the present norms.

In particular, two analytical models (a simplified and a refined one) for the prediction of the critical load of the new buckling mode have been proposed and validated numerically. The proposed design models are easy to apply, and fill the gap in the existing provisions of the European normative documents. The latter could be contemplated for a direct implementation of the future draft of the Eurocodes.

11. GENERAL CONCLUSIONS AND PERSPECTIVES

11.1 Conclusions

Angle profiles, and more specifically equal leg ones investigated in the present thesis, exhibit some properties that clearly distinguish them from the well-known profiles. It is known that, for a double-symmetric cross-section, the critical load is not affected by the load eccentricity while the buckling modes are always decoupled and the critical one is flexural. However, this is not the case for angle sections, as they mostly buckle along their weak axis with a flexural or a flexural-torsional mode, depending on the load eccentricity. The full decoupling of the buckling modes happens only for a very specific case, where the member is loaded at the shear centre; this is also the only case for which a pure torsional buckling mode can appear. Furthermore, the critical load is affected by the type of loading; an instability can even occur for an eccentric tensile load, depending on the cross-section geometry.

These particularities shows that existing design rules for other types of sections, mostly doubly symmetric ones, cannot straightforwardly and safely cover angles, what inevitably leads to the need for the development of specific design provisions for angle sections. A need that is clearly enhanced by the lack of unified consistent rules for angles in the existing European normative documents; design rules for angles can be currently found in EN 1993-1-1, EN 1993-3-1, EN 1993-1-5 and EN 50341-1 as explained in the introduction, but all these documents are sometimes in contradiction. In the thesis, the existing European specifications on rolled equal angle sections were reviewed and a complete and consistent set of design rules covering all aspects of design have been developed and fully validated scientifically, clearing the design process for angles in contrast to the existing code approaches.

A proposal for the classification of equal leg angle profiles, fully consistent with the Eurocode normative documents, have been developed and validated through extensive numerical investigations and analytical methods. The numerical investigations have been performed with the full non-linear software ABAQUS using volume elements and are in very good agreement with the analytical developments. Angle cross-sections have been classified separately for compression, strong and weak axis bending, while the classification boundaries from class 3 to 4 have been determined through the slenderness of the compression leg and not the torsional instability mode as usually considered for other common profiles. Additionally, rules for cross-sections design resistances including all important loading conditions (compression, weak and strong axis bending), have been developed and validated numerically. These rules allow a smooth transition between cross-section classes, removing any artificial stepwise prediction of resistance, as already proposed in the new draft of Eurocode 3 for doubly symmetric sections which is presently under finalisation; they are also less conservative than the current design rules proposed by Eurocode 3.

Design rules to predict the stability and resistance of members made of rolled equal leg angle profiles subjected to combined normal forces and moments have also been proposed and validated through numerical investigations and experimental tests. The extensive numerical parametrical studies were again performed with ABAQUS software using volume elements. Experimental results are coming from tests carried out in the framework of the thesis on large angle profiles made of S460 high strength steel, as well as from previous experimental investigations found in literature. Appropriate European buckling curves for flexural and lateral torsional buckling of angles have been detected and proposed. From the experimental results, it has been shown that the proposed method allows a

safe prediction of the member capacity with an accuracy which is much better than the one obtained with the present Code provisions.

An assessment of the current design approach used for lattice transmission towers has also been achieved through numerical studies. From the numerical results, it can be seen that the buckling load obtained by a 2nd order elastic analysis is smaller than the critical one obtained by an elastic instability analysis. The reason is that the forces acting on the members in both cases differ, so affecting the member buckling load in the case of non-symmetrical cross-sections. Moreover, these effects are amplified when considering the actual member support conditions. Consequently, the second order effects should be considered in the analysis as they affect the global response of the tower but also its ultimate limit state. In addition, an instability mode for lattice towers not properly covered by the norms has been detected and defined. Two analytical models (a simplified and a refined one) for the prediction of the critical load of the new buckling mode have been proposed and validated numerically. Both proposed design models are easy to apply, clearly indicate the required check to perform and fill the gap in the existing provisions of the European normative documents. The current provisions of Eurocode 3 have been used for the prediction of the resistance of the member associated with this instability mode.

Concluding, all the proposed design rules and methods are simple to apply and have been written in the format of the existing Eurocode 3 specifications. Nevertheless, they are referring only to equal leg angle profiles mainly used in pylons; they are generic for the referred profiles.

11.2 Research contribution and innovation

The innovations and contributions of the present dissertation to the advancement of engineering science and design practice can be summarized as following:

− Results of experimental tests on large angle high strength steel columns were presented, providing qualitative understanding and quantitative evaluation of the member response.

− Detailed numerical simulations of the experimental tests were performed, demonstrating useful modelling features that can prove beneficial for researchers.

− Existing European specifications on hot-rolled equal angle sections were critically reviewed, highlighting the inconsistencies and the lack in the design approaches in these normative documents.

− A complete and full consistent set of design rules covering all aspects of design for angles was developed, clearing thus the design process. They include cross section classification, cross section resistance for all types of loading as well as rules for member design to individual and combined internal normal forces and bending moments.

− Extensive experimental, analytical and numerical studies were conducted to validate the proposed set of design rules. The validated rules can be directly applied in structural engineering design practice involving angle profile members.

− Appropriate buckling formulas and corresponding buckling curves were proposed for flexural and lateral-torsional buckling of angles. The buckling formulas and curves can be reliably implemented in the structural design practice according to modern structural design standards.

− An assessment of the current design approach used for lattice transmission towers was achieved through numerical studies. Results can be useful for designing appropriate lattice towers.

− An instability mode for lattice towers not properly covered by the norms was detected and defined. Two analytical models for the prediction of the critical load of the new buckling mode were developed and validated numerically. Both design models are easy to apply, clearly indicate the required check to perform and fill the gap in the existing provisions of the European normative documents.

− All the developed rules of the present dissertation were written in Eurocode 3 format to allow a direct possible inclusion in forthcoming drafts.

11.3 Perspectives for future research

Based on the present dissertation, some suggestions for future research are summarized next:

− Numerical parametrical studies to find out if the application of the proposed design rules developed for equal-leg angles, could be extended to unequal leg angles too.

− Investigations are still required to better account for the beneficial effect of the restrains due to bolted connections at the extremities of the angle members, that is currently covered by the provisions of EN 1993-3 through the definition of an equivalent bucking length.

− The segment instability mode detected here need further examination. First, the selection of the buckling curve could be improved, as now it is suggested to use the lowest one (curve d) due to the lack of studies showing that a higher one could be safely used.

− The segment instability mode detected in the framework of the thesis, was associated with a certain tower configuration and has been observed in the tower's leg. Consequently, further numerical and experimental investigations are needed to check if a similar instability mode could occur in other parts of the tower (for instance in the arms), and how this could be affected by the configuration of the tower. Finally, the accuracy of the proposed models for other possible segment instabilities may be checked.

12. ANNEX A: GEOMETRICAL PROPERTIES OF ANGLE PROFILES

Annex A includes formulae for the geometrical properties of angle cross-sections that are not reported at the commercial cross-section catalogues, such as the elastic and plastic modulus about strong and weak axis and the torsional and warping constants.

12.1 Elastic and plastic modulus about strong axis

The elastic modulus about u axis, $W_{el,u}$, can be derived from the following formula:

$$W_{el,u} = \frac{I_u}{0{,}5h\sqrt{2}} \quad \text{(Eq. 12.1)}$$

The plastic modulus about u-u axis can be evaluated equal to $W_{pl,u} = 1{,}5 \cdot W_{el,u}$. The factor of 1,5 is on the safe side as the mean value for all available angle profiles is 1,58 with a standard deviation of 2%. The exact analytical expression for the plastic modulus about u-u axis can be found in Ref. [50].

12.2 Elastic and plastic modulus about weak axis

For the angle cross-section, due to its asymmetry, the $W_{el,v}$ is different for a top fibre (at the tip) or a bottom fibre (at the toe). For the design of the cross-section, the most distant fibre from centroid is considered when calculating the elastic modulus (i.e at the toe of the leg), which results in higher stress calculations. Therefore, the elastic modulus about v axis can be derived from the following formula:

$$W_{el,v} = \frac{I_v}{x_G\sqrt{2}} \quad \text{(Eq. 12.2)}$$

The plastic modulus about v axis can be estimated through the following equation by assuming that the radius at the toe of the cross-section is equal to zero ($r=0$). The notation of the following formulas are supplemented by Figure 12.1 below.

$$W_{pl,v} = \frac{A}{2} \cdot (c + d) \quad \text{(Eq. 12.3)}$$

where,

c is the distance between the centre of gravity of the sub-cross-section 2 and the plastic neutral axis (pna), and it can be calculated by the equation:

$$c = \sqrt{2} \cdot (\frac{h_2}{2} - y_{G_2}) \quad \text{(Eq. 12.4)}$$

d is the distance between the centre of gravity of the sub-cross-section 1 and the pna, and it equals:

$$\text{d} = \sqrt{2} \cdot (y_{G_1} - \frac{h_2}{2}) \quad \text{(Eq. 12.5)}$$

$h_2 = h - h_1$ is the width of the sub-cross-section 2 (Eq. 12.6)

$h_1 = A/4t$ is the width of the sub-cross-section 1 (Eq. 12.7)

y_{G_1} is the distance between the centre of gravity of the sub-cross-section 1 and the point O(0,0) along y' axis and it can be estimated by the equation:

$$y_{G_1} = \frac{h_1}{4} + \frac{h_2}{2} + \frac{t}{4} \quad \text{(Eq. 12.8)}$$

y_{G_2} is the distance between the centre of gravity of the sub-cross-section 2 and the point O(0,0) along y' axis and it given by the equation:

$$y_{G_2} = \frac{h_2^2 + h_2 t - t^2}{4h_2 - 2t} \quad \text{(Eq. 12.9)}$$

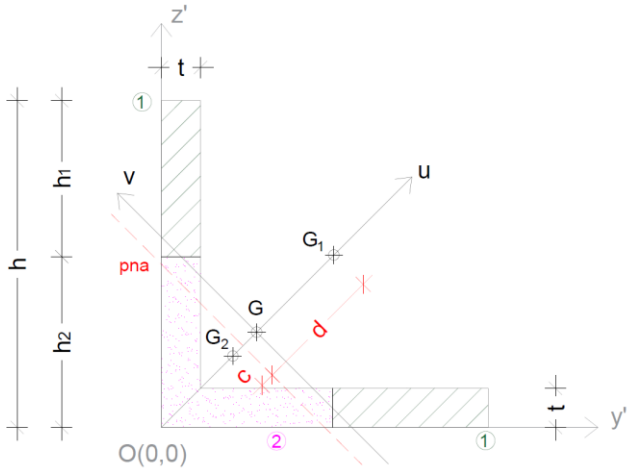

Figure 12.1: Notation for the calculation of the plastic modulus about v axis

Formulae, in which the radius at the toe of the cross-sections is taken into account, can be found in Ref. [50].

12.3 Torsional and warping constant

The torsional constant C_T of the cross-section is approximately equal to:

$$C_T = \frac{G}{3}\sum ht^3 = \frac{G}{3} \cdot 2 \cdot (h - 0{,}5t)t^3 \quad \text{(Eq. 12.10)}$$

The warping constant C_w of the cross-section is approximately equals:

$$C_w = \frac{(h-0{,}5t)^3 t^3}{18} \quad \text{(Eq. 12.11)}$$

13. ANNEX B: NUMERICAL SIMULATION OF FULL-SCALE TESTS

In this annex, FINELG finite element software is used to predict the ultimate resistance and the failure mode of full-scale tests performed on lattice towers at the National Technical University of Athens and reported in Ref. [51] and [52].

13.1 Details of the tests

The experimental program consists of six full-scale tests on cell network telecommunication lattice towers subjected to horizontal forces at their tops, increased gradually until failure occurs. Three specimens have been subjected to orthogonal loading and three to diagonal loading as shown in Figure 13.1. In order to transfer the horizontal force evenly to the top level, a 6 mm thick steel plate of 100 kg weight acting as diaphragm was placed and bolted to all the beams of the top level (Figure 13.2). Amongst the tested towers, two have been strengthened with FRP strips; they are not considered here.

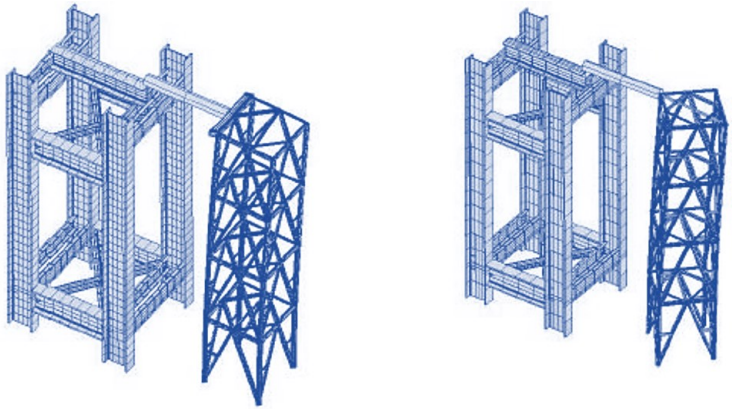

Figure 13.1: Reaction frame and towers of type O (orthogonal) left and type D (diagonal) right [51]

Figure 13.2: Tested tower with diagonal loading [51]

The geometry of the specimen-tower is illustrated in Figure 13.3. The overall external dimensions were 1,44x1,44x6,82 [m], while the axial distance between centroids of the tower legs was 1,40 [m]. The tower is subdivided in 4 levels, each with a height of 1,70 [m]. All the members of the tower are made of single angle profiles and are detailed in Table 13.1; their actual material properties are

summarized in Table 13.2, while, for those that no tensile test has been performed, the nominal values of steel grade S275 are used.

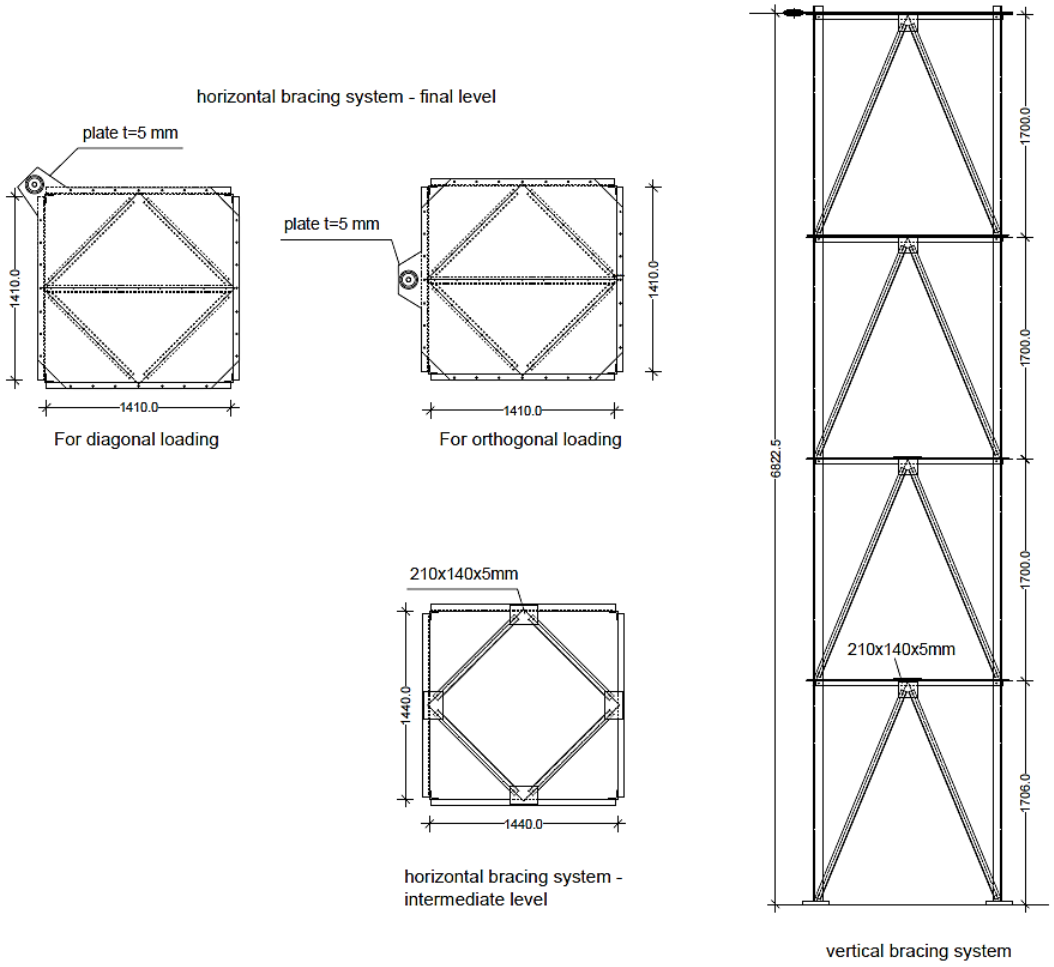

Figure 13.3: Tower dimensions in plan and side view

The columns run continuously over the height of the towers, while the bracing members were bolted at their extremities with one bolt. The horizontal external members were bolted directly to the column legs, the braces directly to the columns at the lower end and to a gusset plate 150x120x5 mm at its top, while the horizontal internal members to gusset plates 210x140x5 mm at both extremities. The experimental failure load and the corresponding mode are reported in Table 13.1.

Table 13.1 Results of the tested towers

Test code	Loading direction	Profiles for legs	Profiles for braces/horizontals	Experimental failure load [kN]	Experimental failure mode
O-1	Orthogonal	L 70x70x7	L 45x45x5	39,00	Buckling of diagonals
O-2	Orthogonal	L 70x70x7	L 65x65x7	106,5	Buckling of lower legs
D-1	Diagonal	L 70x70x7	L 40x40x4	38,50	Buckling of diagonals
D-2	Diagonal	L 70x70x7	L 60x60x6	78,50	Buckling of lower legs

Table 13.2 Measured material properties of the tested angle profiles

No	Profile	Yield strength f_y [Mpa]	Ultimate strength f_u [Mpa]
1	L 70x70x7	308,3	435,7
2	L 45x45x5	286,7	416,7
3	L 40x40x4	325,7	435,4
4	L 60x60x6	280,0	403,9

13.2 Description of the numerical model of the tower

The ultimate resistance and the failure mode of the tested towers are predicted through full non-linear analyses. The tower is modelled with FINELG finite element software [25] using beam elements with 7 degrees of freedom. The members have been considered in their exact position in terms of orientation and eccentricities (Figure 13.4). The main legs have been simulated as continuous elements along their length. The tower is assumed to be clamped at the ground, so as to reflect the actual support conditions of the laboratory tests.

The bracing members were connected through bolts and gusset plates. At the level of the connections, the bolts have been represented by fictitious elements possessing a very low torsional stiffness, as recommended in Ref. [53]. In Figure 13.4(b), one may observe that the gusset plate have been modelled through a beam finite element. Consequently, the eccentricity between the horizontal member and the diagonals is also accounted for. The gusset plates, welded to the horizontal members in the specimens, have been simulated as clamped to the horizontal members. The diagonals have been connected to the gusset plate using fictitious elements with a low torsional stiffness reproducing a pinned “one bolt” connection.

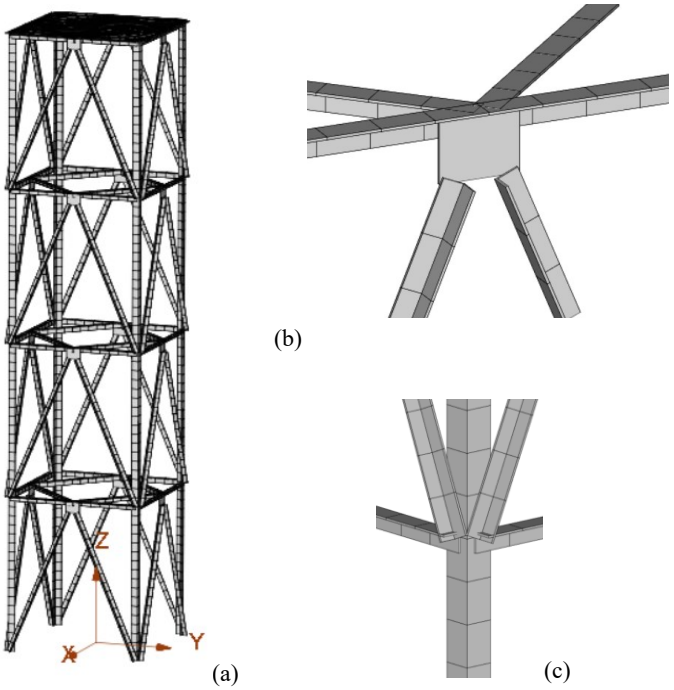

Figure 13.4 (a) 3-D tower model, (b) Detail of the connection between horizontal and vertical bracings, (c) Detail of the connection between vertical bracings and leg

The self-weight of the structure (W) has been calculated automatically by the software, while the horizontal loads (H) were introduced at the extremities of the legs at the top level. The steel plate on

the top level has been modelled with plate elements and its weigh introduced as a uniform surface load. The FINELG finite element analysis adopting the GMNIA method is performed considering:

- an initial imperfection with a shape in accordance with the first buckling mode and an amplitude determined using eq. (7.17) of prEN 1993-1-1-§7.3.6.(1);
- a linear elastic - perfectly plastic material law without strain hardening, based on the measured yield stresses (see Table 13.2).
- residual stresses as shown in Figure 6.18.

13.3 Numerical results

For each specimen, an elastic buckling analysis has been performed so as to determine the buckling mode. Then, a full non-linear analysis is realised, in which the gravity loads (W) are first applied and then the horizontal load is increased up to failure ($W + \alpha_{ult}H$) in full agreement with the experimental loading sequence. The results for all towers are provided in the following figures and tables.

Tower O-1: Table 13.3 provides the results for the Tower O-1. The first buckling mode (shape and critical load) of Tower O-1, associated to a minor-axis flexural buckling of the lower compressed diagonals, is presented in the first column of the table. The following columns represent the deformed shape of the tower at the ultimate limit state, the failure load and the distribution of yielding in the members of the tower. The numerical failure load equals 40,7 kN and is a bit higher (4,17 %) than the one obtained experimentally (see Table 13.1) but is acceptable due to the complexity of the structure as it is remains less than 5%. Finally, failure occurs at the lower compressed diagonals as for the experiment.

Table 13.3 Tower O-1 – numerical results

Elastic instability analysis	Full non-linear analysis	
Shape of 1st Buckling mode	Deformation shape at ULS	Level of yielding
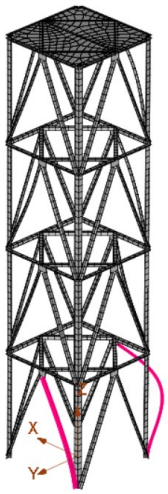	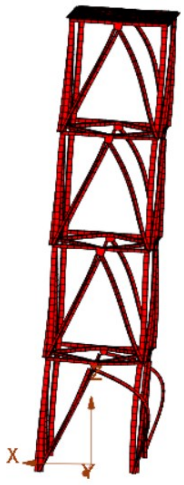	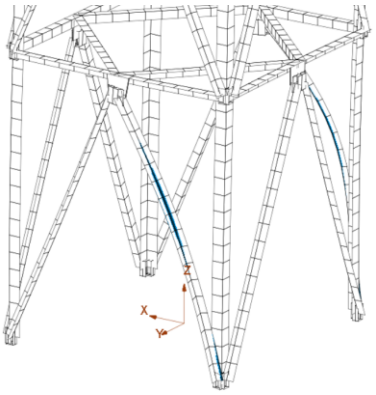
Critical load = 62,01 kN (α_{cr}=1,590)	Failure load= 40,70 kN	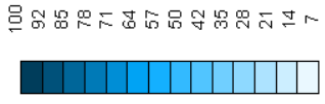

Tower O-2: Table 13.4 represents the results obtained for Tower O-2 failing through a leg buckling. It should be noticed that the tower fails by inward leg buckling during the laboratory test in contrast

with the numerical prediction that shows an outward leg buckling. The failure load is equal to 101,6 kN and is close to the experimental one (106,5 kN).

Table 13.4 Tower O-2 – numerical results

Elastic instability analysis	Full non-linear analysis	
Shape of 1st Buckling mode	Deformation shape at ULS	Level of yielding
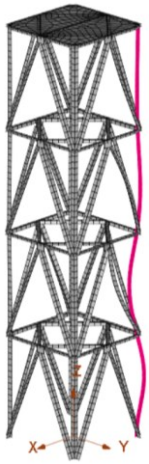	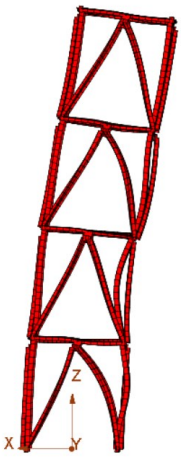	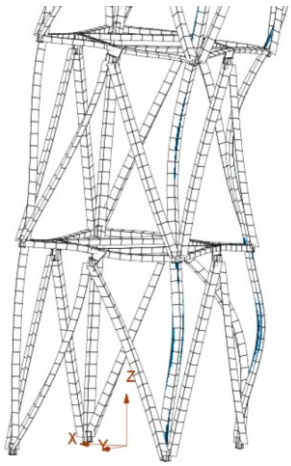
Critical load = 162,41 kN (α_{cr}=1,525)	Failure load= 101,62 kN	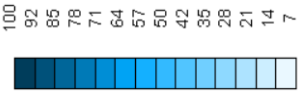

Tower D-1: For the Tower D-1, the results are summarized in Table 13.5. The failure occurs due to a diagonal buckling. The numerical failure load is 38,6 kN and is almost equal to the experimental one.

Table 13.5 Tower D-1 – numerical results

Elastic instability analysis	Full non-linear analysis	
Shape of 1st Buckling mode	Deformation shape at ULS	Level of yielding
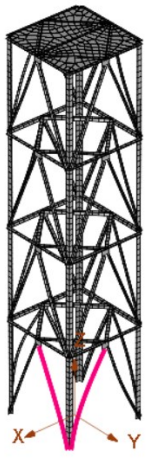	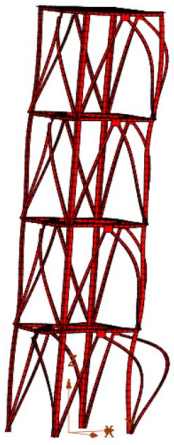	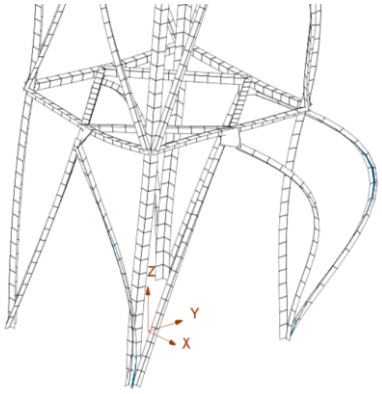
Critical load = 58,83 kN (α_{cr}=1,528)	Failure load= 38,50 kN	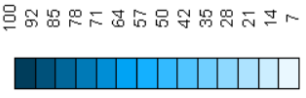

Tower D-2: The results for the Tower D-2 are reported in Table 13.6. The tower fails due to a buckling of the most compressed diagonal for a design load equal to 74,7 kN to be compared to the experimental one equal to 78,5 kN. The buckling is developing to the inside of the tower as observed during the experimental test. It can be observed that analyses predicting a diagonal buckling failure give results rather close to the tests.

Table 13.6 Tower D-2 – numerical results

Elastic instability analysis	Full non-linear analysis	
Shape of 1st Buckling mode	Deformation shape at ULS	Level of yielding
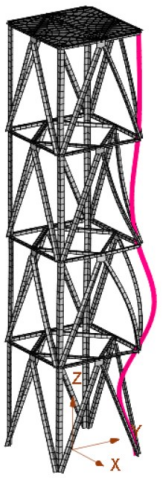	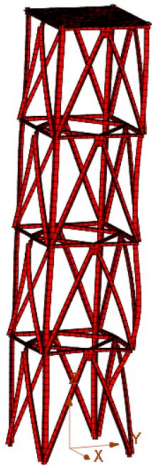	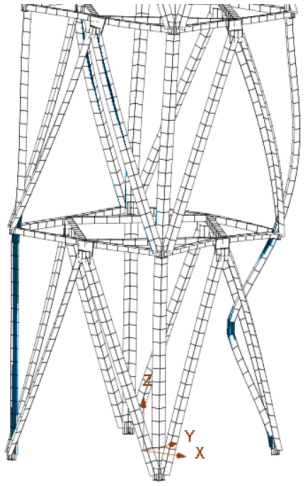
Critical load = 119,16 kN (α_{cr}=1,518)	Failure load= 74,68 kN	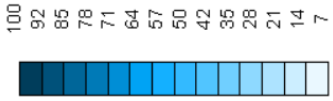

Table 13.7 summarises both experimental and numerical results. It can be seen that the numerical simulation gives very satisfying results that are quite close to the tested ones.

Table 13.7 Results of different design approaches

Tower	**Experimental ultimate load [kN]**	**Experimental failure mode**	**Numerical ultimate load [kN]**	**Numerical failure mode**	**Difference [%]**
O-1	39,00	Buckling of diagonals	40,7	Buckling of diagonals	-4,17
O-2	106,5	Buckling of lower legs	101,6	Buckling of lower legs	4,58
D-1	38,50	Buckling of diagonals	38,6	Buckling of diagonals	-0,34
D-2	78,50	Buckling of lower legs	74,7	Buckling of lower legs	4,86

14. REFERENCES

[1] EN 1993-1-1: Design of steel structures - Part 1-1: General rules and rules for buildings, Brussels, Comité Européen de Normalisation (CEN), 2005.

[2] EN 1993-3-1: Design of steel structures - Part 3-1: Towers, masts and chimneys – Towers and masts, Brussels, Comité Européen de Normalisation (CEN), 2007.

[3] EN 1993-1-8: Design of steel structures - Part 1-8: Design of joints, Brussels, Comité Européen de Normalisation (CEN), 2005.

[4] EN 1993-1-5: Design of steel structures - Part 1-5: Plate structural elements, Brussels, Comité 000.Europeen de Normalisation (CEN), 2006.

[5] EN 50341-1: Overhead electrical lines exceeding AC 1 kV - Part 1: General requirements - Common specifications, 2012.

[6] EN 1990: Eurocode - Basis of structural design, Brussels, Comité 000.Europeen de Normalisation (CEN), 2005.

[7] Load and resistance factor specifications for single-angle members, AISC, 2000.

[8] Vayas I., Charalampakis A., Koumousis V., "Inelastic resistance of angle sections subjected to biaxial bending and normal forces", Steel Construction, vol. 2, no. 2, pp.138-146, 2009.

[9] Trahair N., "Bearing, Shear, and Torsion Capacities of Steel Angle Sections", Journal of Structural Engineering, Vol. 128, No. 11, ASCE, 2002.

[10] Schillo N., Feldmann M., "Buckling resistance of L-profiles in towers, masts and open line Constructions", Stahlbau 84, Heft 12, 946-954, 2015. (in German)

[11] Kettler M., Lichtl G., Unterweger H., "Laboratory tests on bolted steel angles in compression with varying end support conditions", Journal of Constructional steel research Vol.155, pp. 301-315, 2019.

[12] Hussain A., Liu Y.P., Chan S.L., "Finite Element Modelling and Design of Single Angle Member Under Bi-axial Bending", Structures, Vol.16, pp.373-389, 2018.

[13] Ban H.Y, Shi G., Shi Y.J, Wang Y.Q, "Column buckling tests of 420MPa high strength steel single equal angles", International Journal of Structural Stability and Dynamics, Vol.13, Issue 2, pp. 1250069-1–1250069-23, 2013.

[14] Spiliopoulos A., Dasiou M.E., Thanopoulos P., Vayas I., "Experimental tests on members made from rolled angle sections", Steel Construction Design and Research, Volume 11, Issue 1, pp. 84-93, 2018.

[15] Reininghaus M., Skottke M., "Dimensioning of pressed angle steel with one screw joint based on the standards DIN 18800-2 and EN 1993-3-1", Stahlbau 74 H7, p.p.534-538, 2005.

[16] Albermani F.G.A., Kitipornchai S., "Numerical simulation of structural behaviour of transmission towers", Thin-Walled Structures, Vol. 41, pp. 167–177, doi:10.1016/S0263-8231(02)00085-X, 2003.

[17] da Silva J.G.S, da S. Vellasco P.C.G, de Andrade S.A.L, de Oliveira M.I.R., "Structural assessment of current steel design models for transmission and telecommunication towers", Journal of constructional steel research, Vol. 61, pp.1108-1134, doi:10.1016/j.jcsr.2005.02.009, 2005.

[18] Jiang W.Q., Wanga Z.Q., McClure G., Wangc G.L., Gengd J.D., "Accurate modelling of joint effects in lattice transmission towers", Engineering structures, Vol. 33, pp.1817-1827, doi:10.1016/j.engstruct.2011.02.022, 2011.

[19] Kitipornchai S., AlBermani F.G.A., Peyrot A.H., "Effect of bolt slippage on ultimate behaviour of lattice structures", Journal of Structural Engineering, Vol.120, Issue 8, doi.org/10.1061/(ASCE)0733-9445(1994)120:8(2281), 1994.

[20] Nuño J., Miller M., Kempner L., "Historical perspective of full-scale latticed steel transmission tower testing", Electrical Transmission and Substation Structures, pp. 313-322, doi:10.1061/9780784412657.027, 2012.

[21] Ziemian R.D., "Guide to stability design criteria for metal structures", ISBN 978-0-470-08525-7, John Wiley & Sons, Inc., Hoboken, New Jersey, 2010.

[22] de Ville de Goyet V., "L'analyse statique non linéaire par la méthode des éléments finis des structures spatiales formées de poutres a section non symétrique", PhD thesis (in French), University of Liège, 1989.

[23] Vlassov B.Z., "Pièces longues en voiles minces", traduit par SMIRNOFF G., Editions Eyrolles, Paris, 1962

[24] Trahair N.S., "Restrained elastic beam-columns", Journal of the Structural Division, 1969.

[25] FINELG: Non-linear finite element analysis program, User's manual, Version 9.0, Greisch Ingeniere, 2003.

[26] prEN 1993-1-1: Design of steel structures - Part 1-1: General rules and rules for buildings, Brussels, Comité Européen de Normalisation (CEN), 2019.

[27] ABAQUS, User's manual, Version 6.14, Simulia, 2014.

[28] EN 10056-2: Structural steel equal and unequal leg angles - Part 2: Tolerances on shape and dimensions, Brussels, Comité Européen de Normalisation (CEN), 1993.

[29] prEN 1993-1-14 (20XX): XXXX, Brussels. Comité Européen de Normalisation (CEN), 2018.

[30] Eaton K.J., "ESDEP-European Steel Design Education Programme", 3rd Nordic conference on computer aided learning, Finland, ISBN 9512207311, Helsinki University of Technology, 1991.

[31] Petersen C., "Statik und Stabilität der Baukonstruktionen" (in German), ISBN 978-3-528-18663-0, Friedrich Vieweg & Sohn Verlag, Germany, 1982.

[32] Gardner L., Fieber A., Macorini L., "Formulae for Calculating Elastic Local Buckling Stresses of Full Structural cross-sections", Structures, Vol.17, pp. 2-20, 2019.

[33] Greiner R., Lechner A., Kettler M., Jaspart J.P., Weynand K., Oerder R., Dehan V., "Valorisation action of plastic member capacity of semi-compact steel sections: A more economic design (SEMI-COMP+)", RFCS European Research project, Directorate-General for Research and Innovation (European Commission), ISBN 978-92-79-29312-2, 2013.

[34] Bezas M.Z., Jaspart J.P., Demonceau J.F., Labeye N., "Report about the compression tests on large angle columns in high strength steel", Research Program of the Research Fund for Coal and Steel ANGELHY, Grant Agreement Number: 753993, European Commission, University of Liège, 2020.

[35] EN 1090-2: Technical requirements for the execution of steel structures, Comité Européen de Normalisation (CEN), 2008.

[36] EN ISO 6892 – 1: Metallic materials – Tensile testing – Part 1: Method of test at room temperature, Brussels, Comité Européen de Normalisation (CEN), 2016.

[37] EN ISO 377: Steel and steel products – Location and preparation of samples and test pieces for mechanical testing, Brussels, Comité Européen de Normalisation (CEN), 1997.

[38] Zhang L., Jaspart J.P., "Stability of members in compression made of large hot-rolled and welded angles", Research Report, University of Liège, 2013.

[39] Moze P., Cajot L.G., Sinur F., Rejec K., & Beg D., "Residual stress distribution of large steel equal leg angles", Engineering Structures, Vol.71, 35-47, 2014.

[40] de Menezes A.A., da S. Vellasco P.C.G., de Lima L.R.O., da Silva A.T., "Experimental and numerical investigation of austenitic stainless steel hot-rolled angles under compression", Journal of Constructional Steel Research, Vol.152, pp. 42-56, 2019.

[41] TOWER User's Manual – Version1 15.0, ©Power Line Systems Inc, 2017.

[42] Fischer R, Kießling F, "Freileitungen: Planung, Berechnung, Ausführung", 4 Auflage, Springer Verlag, 2013.

[43] EN 50182, Conductors for overhead lines - Round wire concentric lay, 2018.

[44] EN 50341-2-4, Overhead electrical lines exceeding AC 1 kV - Part 2-4: National Normative Aspects (NNA) for Germany (based on EN 50341-1:2012), 2016.

[45] Bezas M.Z., Tibolt M., Jaspart J.P., Demonceau J.F., "Critical assessment of the design of an electric transmission tower", 9th International Conference on Steel and Aluminium Structures, 3-5 July, Bradford UK, 2019.

[46] Beyer A., Bureau A., Vayas I., Thanopoulos P., Bezas M.Z., Tibolt M., Jaspart J.P., Demonceau J.F., Papailiopoulou A., "Report on analysis and design of 6 case studies", Research Program of the Research Fund for Coal and Steel ANGELHY, Grant Agreement Number: 753993, European Commission, NTUA, 2019.

[47] EN 1993-1-4, Actions on structures - Part 1-4: General actions, Wind actions, Comité Européen de Normalisation (CEN), 2005.

[48] Gardner L., "Stability of steel beams and columns in accordance with Eurocodes and UK National Annexes", SCI publication P360, ISBN 978-1-85942-199-4, Berkshire, UK, 2011.

[49] OSSA2D: Finite element analysis program, User's manual, Version 3.4, University of Liege, 2020.

[50] Charalampakis A.E., "Full plastic capacity of equal-angle sections under biaxial bending and normal force", https://doi.org/10.1016/j.engstruct.2011.02.044, Engineering Structures, Vol.33, Issue 6, pp. 2085-2090, 2011.

[51] Vayas I., Vlachakis K., Palantzas G., Lignos X., Giquel Y., Reygner S, "Report on full scale experimental tests for complete towers", Research Program of the Research Fund for Coal and Steel ANGELHY, Grant Agreement Number: 753993, European Commission, NTUA, 2019.

[52] Vlachakis K., Beyer A., Vayas I., "Tragverhalten von Fachwerkmasten aus Winkelprofilen", Stahlbau 90, Issue 6, pp 425-440, https://doi.org/10.1002/stab.202000059, 2021.

[53] Beyer A., Bureau A., Vayas I., Thanopoulos P., Vamvatsikos D., Vlachakis K., Bezas M.Z., Dasiou M.E., "Guidance on analysis models for complete towers", Research Program of the Research Fund for Coal and Steel ANGELHY, Grant Agreement Number: 753993, European Commission, NTUA, 2020.